Galactic massive star forming regions near and far: a (sub)millimeter study of the Orion Molecular Cloud 1 and W49A

Dissertation
zur
Erlangung des Doktorgrades (Dr. rer. nat.)
der
Mathematisch-Naturwissenschaftlichen Fakultät
der
Rheinischen Friedrich-Wilhelms-Universität Bonn

vorgelegt von
Peng, Tzu-Cheng
aus
Taiwan

Bonn (Mai, 2010)

Angefertigt mit Genehmigung der Mathematisch-Naturwissenschaftlichen Fakultät der Rheinischen Friedrich-Wilhelms-Universität Bonn

Diese Dissertation ist auf dem Hochschulschriftenserver der ULB Bonn
http://hss.ulb.uni-bonn.de/diss_online
elektronish publiziert. Das Erscheinungsjahr ist 2010.

1. Referent: Prof. Dr. K. M. Menten

2. Referent: Prof. Dr. P. Kroupa

Tag der Promotion : 03.09.2010

Abstract

Massive stars play an important role in shaping the structure of galaxies due to the large energy output during their lifetime. However, because of the short evolutionary time scales, the large extinction toward their birth places, and the large distance of massive stars, our understanding of their formation is still sketchy. Hence, the observations of two well-known massive star forming regions in our Galaxy (W49A at 11.4 kpc and Orion Molecular Cloud 1 at 414 pc) were carried out using the IRAM 30 m and APEX telescopes, including large-scale mappings of various molecular line emission, such as CO isotopologues, HCN, HCO^+, and SiO. The results of W49A show that its starburst was triggered by expanding shells, causing fragmentation that lead to the formation of massive stars. The cause of the shell expansion is not clear, but likely due to the stellar feedbacks from a first generation of young massive stars by strong stellar winds and ultraviolet radiation, or the interaction between stars in a cluster, which is possibly related to the large-scale gas ejections found in the W49 complex with a total kinetic energy of few times 10^{50} erg. Apart from W49A, the study in Orion Molecular Cloud 1 reveals a more detailed picture of young massive stars strongly interacting with their local environment. The highly excited CO emission in Orion Molecular Cloud 1 shows two main components: one is the north-south dense ridge where two active star-forming regions (Orion BN/KL and Orion South) are located, and the other one consists of photon-dominated regions (e.g., the Orion Bar and Orion East) spread over the whole area, where gas and dust are heated by ultraviolet photons from the Trapezium cluster. In addition, several outflows are detected in the higher-J transitions of CO, which indicates the important role of shock heating associated with star-forming activities.

To My Parents

Acknowledgements

I have benefited from the inputs and discussion from my colleagues and friends over my study in the Max Planck Institute for Radioastronomy in Bonn. I wish to express my gratitude to Friedrich Wyrowski for his patient supervision and some of his ideas in this thesis. I also thank Professor Karl Mention for his support during my study. I want to thank Floris van der Tak for the help in the radiative transfer modeling and the discussion in W49A. I also want to thank Malcolm Walmsley for his many helpful comments in W49A and the Orion Bar. I would like to thank Luis Zapata for the discussion and inspiration in the study of Orion BN/KL and South. I wish to thank Berengere Parise, Edwige Chapillon, and Peter Schilke for the useful discussion in Orion Bar and the PDR modeling. I want to thank Endrik Krügel for the discussion in the dust mass calculation. I want to thank Kazi Rygl for her help to improve my manuscript. I am also grateful to the International Max Planck Institute Research School for Astronomy and Astrophysics at the Universities of Bonn and Cologne for its support. In the end, I wish to thank my parents in Taiwan and some of my friends in Bonn: Ko-Po Yin, Cho-Chung Huang, Li-Rung Huang, and Oliver Nitchke, for their kindly support and company.

Contents

List of Tables

1 Introduction

1.1 Massive Star Formation

The importance of massive stars in the Universe comes from multifold reasons which are related mostly to the large energy output during their life time, and the energetic events, and heavy elements (chemical elements heavier than the H, He and Li) they produce near and at the end of their lives. The ultraviolet (UV) radiation and the strong stellar winds from massive stars shape the interstellar medium (ISM) in one way, and the supernova explosions violently mix the ISM in another way. Black holes, supernova explosions, gamma-ray bursts (GRBs), the most dramatic events in galaxies are all connected to massive stars. Massive stars, hence, play a key role in shaping the structure and modulating the evolution of galaxies.

The term massive star adopted here is in the same definition used in the recent review paper by Zinnecker & Yorke (2007) that a massive star is an OB star massive enough to produce a type II supernova (> 8 $M_{\odot}$ for solar abundances). In addition, the zero-age main sequence (ZMAS) denotes the stars that have started to burn hydrogen in the center, and the high-mass protostellar objects (HMPOs) are referred to the gaseous objects in hydrostatic equilibrium before hydrogen burning (Zinnecker & Yorke 2007). Due to their high mass, massive stars evolve fast, and their early evolutionary stages are relatively short-lived which makes them difficult to observe in the early highly dust-extincted phase. To date, our understanding of massive star formation is still sketchy. Unlike low-mass stars, high-mass stars are rare and seldomly formed in isolation which increases the complexity of the interaction between forming stars and the local environment. Massive star forming regions are usually associated with giant molecular clouds (GMCs) and infrared dark clouds (IRDCs) on a large scale, and also with hot molecular cores and ultra/hyper-compact (UC/HC) H II regions on a small scale.

The theory of massive star formation is still under development, and has many debates, e.g., whether a high-mass star is formed just like a low-mass star, i.e., by disk accretion. However,

Zinnecker & Yorke (2007) argued that the formation of ZAMS O stars (> 20 $M_\odot$) is not a simple scaled-up version of low-mass star formation, although the formation of early-type B stars may still have high similarity to the formation of low-mass stars. Zinnecker & Yorke (2007) summarized four highly connected phases of massive stars formation, i.e., compression, collapse, accretion, and disruption. In their paradigm, most massive stars form via accretion, which could be either monolithic collapse and disk accretion, or competitive accretion. Before accretion, the ISM must be dense enough to provide the material for a massive star to form in a short time. The parental cloud, therefore, should have phases of compression and collapse in the early evolutionary stages. Since massive stars are practically born on the main sequence, their strong stellar winds, outflows, and UV radiation then channel energy back into the environment. Eventually, supernovae disrupt the cloud. Because most of the massive stars form in clusters (Lada & Lada 2003), those fours phases can occur side-by-side or simultaneously in a cloud, which adds more complexity to massive star formation. For instance, a newly born massive star can still have large amount of gas left to be accreted when it starts to burn hydrogen in the center, so that the late accretion phase and the early disruption phase are overlapped. In addition, the strong stellar winds driven by a massive star or a supernova explosion can trigger massive star formation, which leads to an overlap between the disruption phase and the compression phase, and probably the accretion phase as well.

It seems certain that most massive stars are born in dense interstellar regions of giant molecular clouds with sizes from ~ 20 to ~ 100 pc and masses between $\sim 10^4$ to $\sim 10^6$ $M_\odot$. These dense regions usually refer to starless cores with a mass of ~ 100 $M_\odot$ and a size of $\lesssim 0.1$ pc, or starless clumps with a mass of ~ 1000 $M_\odot$ and a size of the order 0.25–0.5 pc (see Zinnecker & Yorke 2007; Beuther et al. 2007). The core/clump formation is a critical step to form high-mass stars and it involves the interaction among gravity, turbulence, and the magnetic field. Besides, as McKee & Ostriker (2007) pointed out, those three key dynamical processes in star formation are highly nonlinear. The dense clumps inside giant molecular cloud, the hot molecular cores rich in complex molecules, and the UC/HC H II regions with strong recombination lines, together with the stellar feedback of outflows are the most observable objects in Galactic massive star forming regions.

1.1.1 Massive star formation in external galaxies

As for the massive star formation in external galaxies, because of their large distances, massive stars usually dominate the luminosity of galaxies and play an important role in shaping galactic structure. Therefore, massive star formation on the extragalatic scale goes a long way toward explaining the course of star formation history in the Universe. Energetic phenomena like starbursts are thus easy to observe in the local Universe. In the last decades, we have seen much progress in our knowledge about luminous infrared galaxies (LIRGs; $L_{\rm IR} > 10^{11}$ $L_\odot$) and their extreme counterparts, ultraluminous infrared galaxies (ULIRGs; $L_{\rm IR} > 10^{12}$ $L_\odot$), which were first discovered by the IRAS. However, the energy origin of (U)LIRGs is still not clear. Powerful sources such as starbursts and active galactic

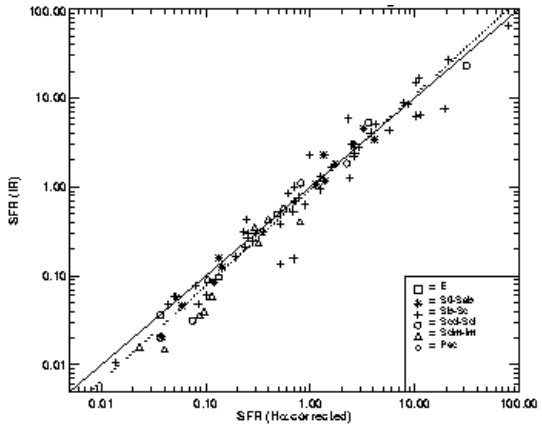

Figure 1.1 The correlation between SFR(IR) and SFR(Hα) from Kewley et al. (2002).

nuclei (AGNs) are believed to be hidden behind dust and gas in (U)LIRGs (see Sanders & Mirabel 1996).

1.1.2 Star Formation Rate

One of the most widely-used parameters for star formation is the star formation rate (SFR). Schmidt (1959) proposed that the SFR is proportional to ρ^2, where ρ is the gas volume density. This gas-density power law is usually expressed in terms of the observable surface densities of gas and the surface density of star formation:

$$\Sigma_{\rm SFR} = A\Sigma_{\rm gas}^{N} \tag{1.1}$$

(e.g., Kennicutt 1998), where A is the absolute SFR efficiency. Kennicutt (1998) showed that star-forming galaxies follow the global Schmidt law with the index $N = 1.4$ from the Hα, H I, and CO measurements of 61 normal spiral galaxies and 36 starburst galaxies. The SFR is usually estimated from the optically visible Hα lines which trace new or young stars. However, in many cases of star-forming regions or galaxies, where lots of young stars formed deeply embedded in gas and dust, Hα lines are not observable, and the infrared, which is generated by UV photons of young stars absorbed by nearby dust, contributes much more luminosity. This led Kewley et al. (2002) to investigate 81 galaxies for the Hα and infrared SFR diagnostics, and they obtained a strong correlation between SFR(IR) and reddening-corrected SFR(Hα) that SFR(IR) $\propto$ SFR(Hα)$^{1.07\pm0.03}$ (Fig. 1.1). Therefore, the far-infrared (FIR) emission from a young stellar population (1–1000 μm) can be used as a good indicator of the SFR. As for the gas density, since a significant fraction of interstellar H is in molecular form, the H_2 density should represent the ISM density in most of the cases. However, H_2 is difficult to observe, and the density of the second most abundant molecule, CO, is usually used to estimate the H_2 density by assuming a fixed abundance ratio between CO and H_2, i.e., [CO]/[H_2]$\sim 2\times10^{-4}$ (e.g., Lacy et al. 1994). Therefore, the Schmidt law can be investigated

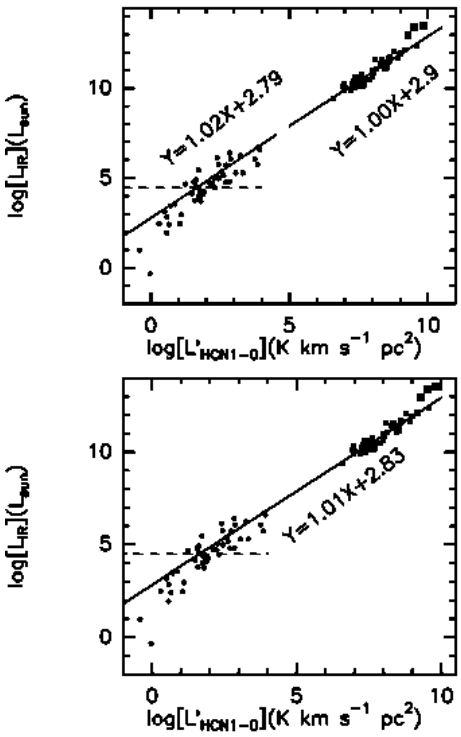

Figure 1.2 The correlation between $L_{\rm IR}$ and $L_{\rm HCN}$ from Wu et al. (2005).

by examining the relation between $L_{\rm IR}$ and $L_{\rm CO}$. However, the relation between $L_{\rm IR}$ and $L_{\rm CO}$ in large samples of IRAS galaxies is not linear, but one observes a general trend of increasing $L_{\rm IR}/L_{\rm CO}$ ratio with increasing $L_{\rm IR}$ (see Sanders & Mirabel 1996). This increasing trend means that the star formation efficiency does not increase with higher $L_{\rm IR}$ in galaxies, and that CO probably fails to trace the gas relevant to the star formation (Wu et al. 2005). In addition, Gao & Solomon (2004) found a tight correlation between $L_{\rm IR}$ and the luminosity observed in the high density tracing HCN molecule, $L_{\rm HCN}$, and interpreted it as strong evidence in favor of star formation as the dominant powering source in (U)LIRGs. The same correlation has been also extended to Galatic dense clumps by Wu et al. (2005), which means star formation in external galaxies is, in essence, the same as in the Galaxy, and we can thus understand extragalactic star formation by studying Galactic star-forming regions (see Fig. 1.2).

In recent years, the wealth of molecular data on starburst galaxies has increased rapidly, even the first unbiased line survey toward a nearby starburst galaxy NGC 253 has been performed (Martín et al. 2006). More and more molecules are detected at high redshifts (García-Burillo et al. 2006; Risacher et al. 2006). It is clear that a thorough understanding of Galactic sources is needed to

bridge the gap between Galactic and extragalactic molecular observations, and only a few studies in recent years addressed this issue (e.g., Wu et al. 2005). Besides, it is important to clarify the energy origin of (U)LIRGs, and investigate the connection between starbursts and AGNs which are believed to be embedded in many (U)LIRGs. Starbursts and AGNs are different in their main radiation fields. Starburst-dominated galaxies are featured by a large amount of photon-dominated regions (PDRs) caused by young stellar clusters, but AGN-dominated galaxies are mainly powered by a central black hole (BH) around which the strong X-ray emission produces X-ray dominated regions (XDRs). For instance, Kohno (2005) used their high resolution interferometer data of CO, HCN, and HCO^+ to distinguish between AGNs and starbursts in nearby Seyfert galaxies. They proposed elevated HCN emission originating from XDRs close to the active nuclei and used the HCO^+/HCN ratio as a diagnostics. On the other hand, PDRs are produced by young stellar populations in starburst galaxies, and can be probed by tracers such as HOC^+, CO^+, [C II] 158μm, and [O I] 63μm. Recently, some models have been constructed to diagnose the effects of PDRs and XDRs, e.g., Loenen et al. (2008); Meijerink, Spaans, & Israel (2007); Meijerink & Spaans (2005).

1.2 Molecular and Dust Emission

Since the early evolutionary stages of massive star formation are obscured in the optical, the best wavelength region for ground-based telescopes to observe massive star forming regions are the millimeter (mm), submillimeter (submm), and X-ray regimes with a limitation of the atmospheric absorption.

Most of the molecules detected in the ISM have their rotational transitions at mm or submm wavelengths, and can thus be observed by ground-based telescopes. However, different molecular lines trace different physical conditions in the ISM. For instance, low-J CO emission can be used to probe the amount of low-density gas in the ISM, because of the small dipole moment of CO (e.g., μ = 0.11 D), which results in a low critical density. The critical density ($n_{\rm crit}$) is defined as the density at which the collisional de-excitation rate equals the radiatively de-excitation rate :

$$n_{\rm crit} \equiv \frac{A_{ul}}{\Sigma_{u \neq l} C_{ul}} \propto \nu^3 \mu^2 T_{\rm ex}^{1/2}, \tag{1.2}$$

where A_{ul} is the Einstein A (spontaneous emission) coefficient and C_{ul} is the collisional de-excitation rates. The critical density depends on the frequency (ν) of the transition, molecular dipole moment μ, and the excitation temperature ($T_{\rm ex}$). HCN and HCO^+, molecules have larger dipole moments, and consequently the energy levels giving rise to emission from their lines require a higher density to be excited, given the collisional cross sections do not change greatly between different molecular line transitions. Therefore, HCN and HCO^+ lines are better tracers (e.g., $n_{\rm crit}(J = 1 - 0) > 10^5$ $\rm cm^{-3}$) for dense gas than the low-J CO lines. The $n_{\rm crit}$ values for different transitions of HCO^+, HCN, HNC, and CO are summarized in Table 1.1, and Figures 1.3 and 1.4. In the massive star forming region where dense and turbulent warm gas dominates, the mid/high-J CO emissions (e.g.,

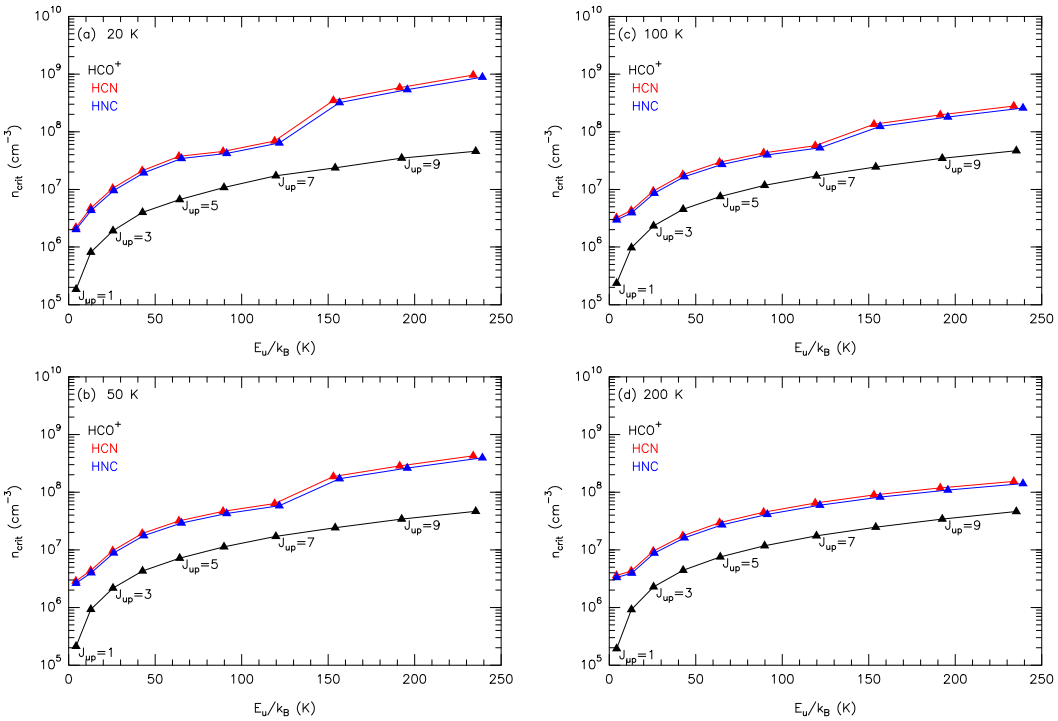

Figure 1.3 Critical densities for HCN, HCO^+, and HNC at 20 K, 50 K, 100 K, and 200 K. Molecular data were taken from the Leiden Atomic and Molecular Database (LAMDA).

$n_{\rm crit}(J = 6-5) > 10^5$ cm^{-3}) in the submm wavelength can also give us more information about the excitation temperature and the density of the environment than the low-J CO lines.

Additionally, in star forming regions in which plenty of stellar feedbacks or activities occur, a shock/outflow tracer like SiO can help us to investigate the kinematic details of a source. The SiO abundance is enhanced in the shock regions or in a high temperature environment where SiO molecules are products of the silicate containing dust grains destroyed by shock waves (see e.g., Ziurys, Snell, & Dickman 1989). The SiO emission is often associated with molecular outflows from young stellar objects (Bachiller et al. 2001; van der Tak 2005), but is also observed on a large scale, e.g., the Galactic center, where strong shocks cause the SiO abundance to increase in the gas phase, and result in a spatial correlation between the Fe 6.4 keV and SiO emissions (Martín-Pintado et al. 2000). Moreover, the SiO emission has also been used to study large-scale molecular shocks in extragalatic starbursts and AGNs (e.g., Usero et al. 2006).

Apart from the molecular line emission, continuum emission in the mm and submm bands reflects a cold dust (< 100 K) distribution, and is usually optically thin. Therefore, the mass of dust can be estimated (see Appendix B), and the total mass of gas can be also estimated by assuming a proper gas-to-dust mass ratio (i.e., 100–150).

Table 1.1. Critical densities of HCO^+, HCN, HNC, CO, and SiO

Transition	HCO^+ (cm^{-3})	HCN (cm^{-3})	HNC (cm^{-3})	CO (cm^{-3})	SiO[b] (cm^{-3})
$J = 1 - 0$	2.4×10^5	3.2×10^6	3.0×10^6	2.1×10^3	5.6×10^4
$J = 2 - 1$	9.8×10^5	4.2×10^6	3.9×10^6	7.1×10^3	2.6×10^5
$J = 3 - 2$	2.3×10^6	9.3×10^6	8.6×10^6	1.8×10^4	6.8×10^5
$J = 4 - 3$	4.5×10^6	1.8×10^7	1.7×10^7	3.9×10^4	1.5×10^6
$J = 5 - 4$	7.5×10^6	2.9×10^7	2.7×10^7	6.9×10^4	2.6×10^6
$J = 6 - 5$	1.2×10^7	4.3×10^7	4.0×10^7	1.1×10^5	4.3×10^6
$J = 7 - 6$	1.7×10^7	5.7×10^7	5.2×10^7	1.7×10^5	6.6×10^6
$J = 8 - 7$	2.4×10^7	1.3×10^8	1.2×10^8	2.3×10^5	9.5×10^6
$J = 9 - 8$	3.4×10^7	2.0×10^8	1.8×10^8	3.2×10^5	1.3×10^7
$J = 10 - 9$	4.7×10^7	2.8×10^8	2.6×10^8	4.3×10^5	1.7×10^7

[a]The critical density, $n_{\rm crit} \equiv A_{ul}/\Sigma\, C_{ul}$ $(u \neq l)$, for different transitions is calculated at 100 K. Molecular data were taken from LAMDA.

[b]Ground vibrational SiO transitions.

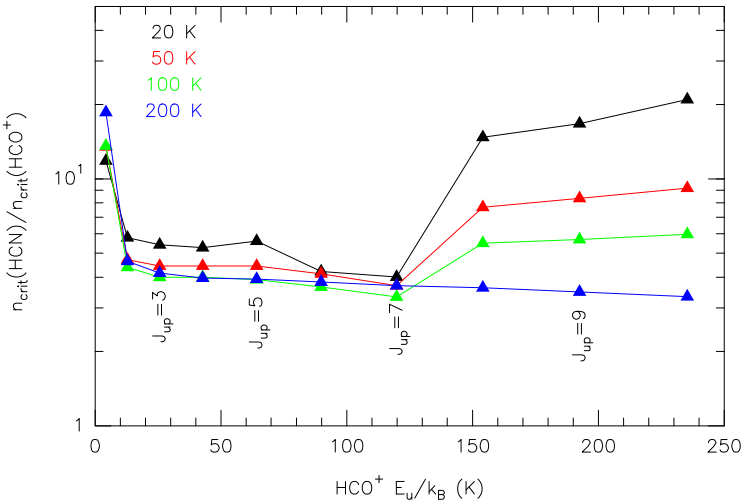

Figure 1.4 Critical density ratios between HCN and HCO^+. Molecular data were taken from LAMDA.

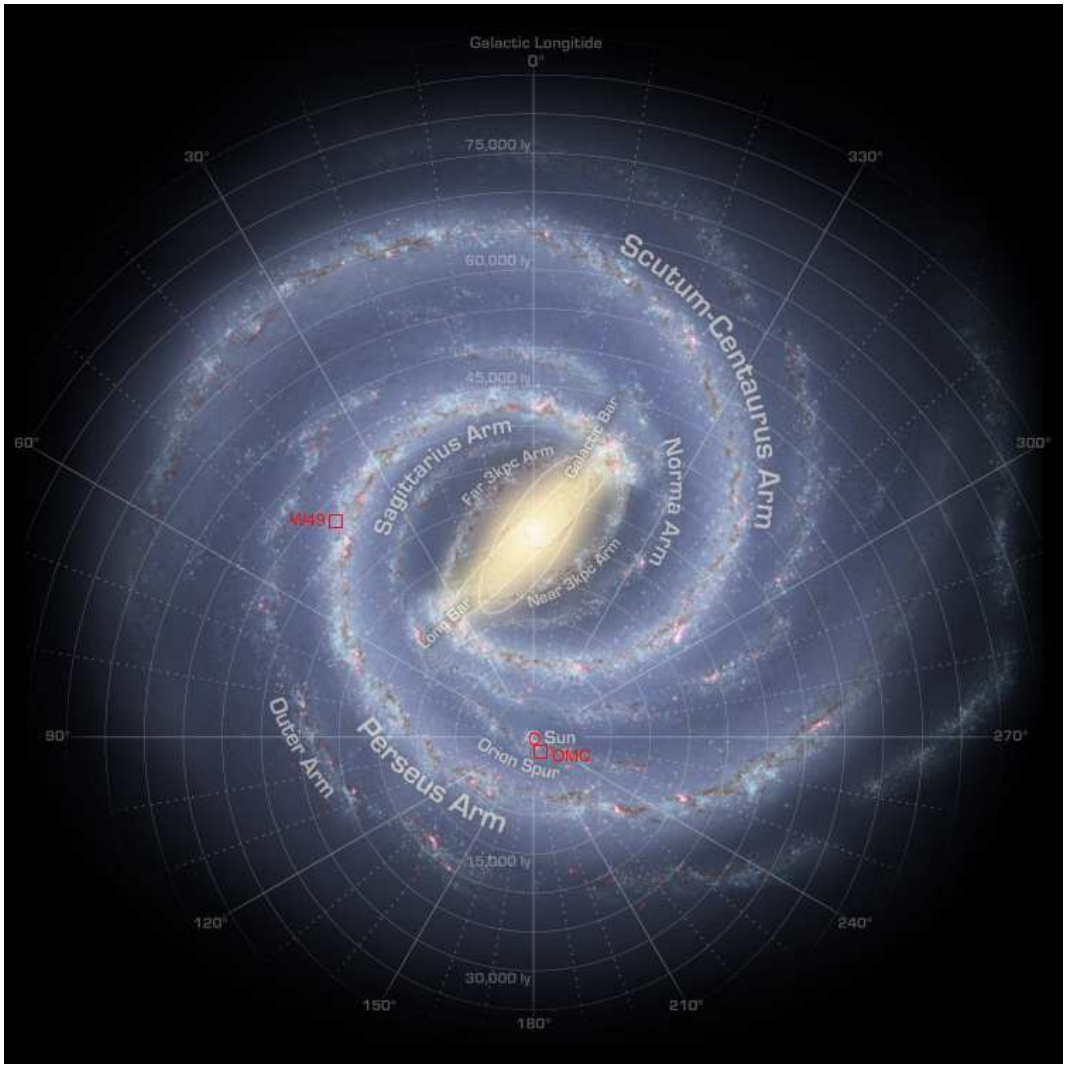

Figure 1.5 The position of W49 and Orion Molecular Cloud in Galaxy. This image is from R. Hurt (NASA/JPL-Caltech/SCC).

1.3 Thesis Motivation & Sources Selection

In order to understand massive star formation in the local Universe, and even the early Universe, a gap must be filled between extragalactic studies and the investigations of Galatic star-forming regions. The Galactic mini-starburst region W49A (11.4 kpc, Gwinn, Moran, & Reid 1992), as we shall see, serves as a good template for the study of starburst phenomena with the angular resolutions provided by current mm and submm telescopes. The observation of spatial scales down to 100–1000 AU at the distance of W49A is still difficult, but can be achieved easily in nearby sources. Therefore, the well-studied Orion Molecular Cloud 1 (414 pc, Menten et al. 2007), is a good candidate for a nearby massive star forming region to study especially the stellar feedbacks and the interaction between young stars and the GMC at higher spatial resolution. In addition, of the merits to choose W49A and Orion Molecular Cloud 1 are their abundant observations in the past and their relatively reliable distance measurements (Fig. 1.5), using the proper motions of H_2O masers in W49A (Gwinn, Moran, & Reid 1992) and the trigonometric parallax of cluster members in the Orion Nebula (Menten et al. 2007), since distance is an essential parameter to determine a source mass and luminosity.

1.3.1 W49A

The giant molecular cloud associated with the powerful radio continuum source W49A (Fig. 1.6) is part of the W49 complex which also includes the supernova remnant W49B. At a distance of 11.4 kpc (Gwinn, Moran, & Reid 1992), W49A includes three main components, i.e., W49A North, W49A South, and W49A Southwest. W49A has an infrared luminosity of $> 10^7$ $L_\odot$ and a total mass of $\sim 10^6$ $M_\odot$ (Sievers et al. 1991). It contains over a dozen of UC H II regions (De Pree, Mehringer, & Goss 1997; De Pree et al. 2000), and also the brightest water maser cluster in our Galaxy ($\sim$1 $L_\odot$ alone in the 22 GHz line, Genzel et al. 1978). The embedded massive cluster found in W49A indicates a somewhat more evolved stage of massive star formation in this region (Alves & Homeier 2003). Basically, none of the W49A sources are optically visible (Alves & Homeier 2003).

Many authors have tried to explain why W49A, a Galactic mini-starburst, has formed so many massive stars on a giant scale in a short time. Welch et al. (1987) proposed a large-scale inside-out gravitational collapse by interpreting two velocity components of HCO^+ spectra measured toward the ring-like configuration of UC H II regions in terms of an infall profile. However, Serabyn, Guesten, & Schulz (1993) argued that the two components of the double-peak line profile seen in CS and $C^{34}S$ come from different clouds, and suggested that massive star formation in W49A is triggered by a large-scale cloud-cloud collision. Recently, it has been argued that one cannot distinguish between a global collapse model of a large cloud and a multiple-cloud model, given the existing HCO^+ and $C^{18}O$ data (Williams, Dickel, & Auer 2004). Hence, the observations and models exist so far do not allow reaching a consensus on this question. In this paper, we present

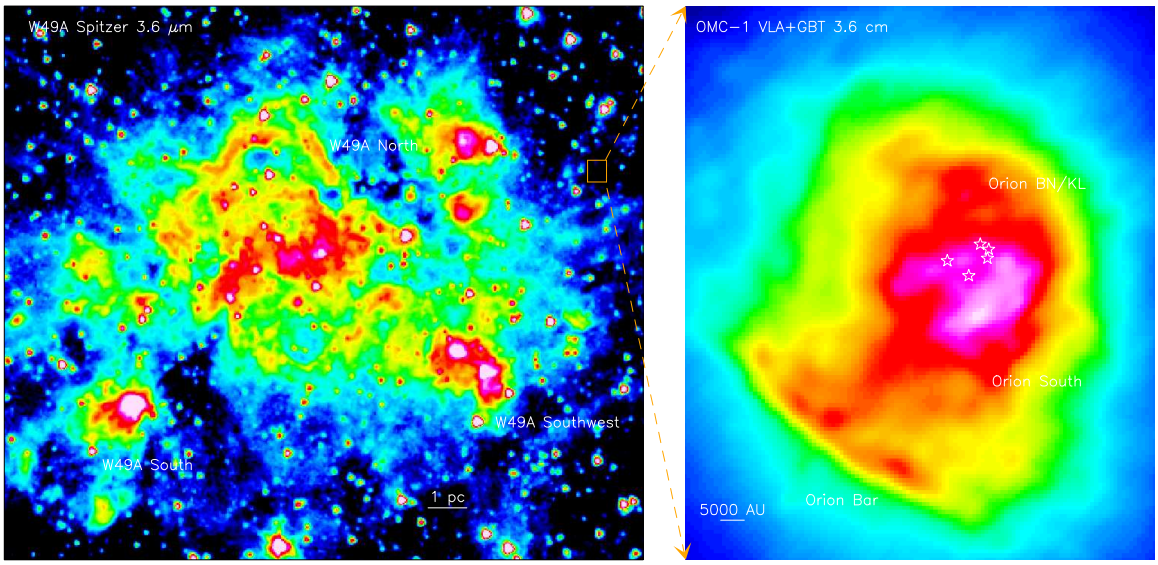

Figure 1.6 The Spitzer 3.6 μm mid-infrared image of W49A (d = 11.4 kpc) and the VLA-GBT 3.6 cm continuum emission image of OMC-1 (d = 414 pc) in pseudo-colors. The orange box indicates the size of OMC-1 if it was located at 11.4 kpc, the distance of W49A.

new evidence of expanding shells in W49A where the dense clumps lie peripherally along the shells, and the expanding shells provide a natural explanation of the observed molecular line profiles, and triggered massive star formation in W49A.

Besides, W49A, as a Galatic starburst template, provides us an opportunity to study similar phonemona in external galaxies in detail.

1.3.2 Orion Molecular Cloud 1

Part of the Orion Molecular Cloud (OMC), OMC-1 (Fig. 1.6) is one of the most-studied astrophysical testbeds in the sky, especially for the research of young clusters and massive star formation. At the distance of 414±7 pc (Menten et al. 2007), OMC-1 is located behind the famous Orion Nebula (M42), which is an H II region ionized by the Trapezium cluster. It includes the Becklin-Neugebauer object and the Kleinmann-Low nebula (Orion BN/KL region), and Orion South (OMC-1 S), the Orion Bar, and Orion East.

The most luminous source, the BN/KL region (Becklin & Neugebauer 1967; Kleinmann & Low 1967), has an IR luminosity of $\sim 10^5$ $L_\odot$ and has been intensively observed in numerous molecular lines and also in various wavelengths. Orion BN/KL harbors the prototypical Orion hot molecular core (HC) with a rich and complex chemistry. In addition, shock and outflow phenomena are also widely present in the Orion BN/KL region. Near-infrared (NIR) observations show H_2 outflows in bullets or finger shapes (Taylor et al. 1984; Allen & Burton 1993) at a wide-angle along a southeast-northwest axis. In radio observations, the powerful outflow is also seen in the high

velocity CO line wings (Kwan & Scoville 1976) together with some hydroxyl (OH) masers which trace shock fronts (Norris 1984; Cohen, Gasiprong, Meaburn, & Graham 2006). Besides, another outflow with lower velocity was detected through proper motions of H_2O masers (Genzel et al. 1981; Gaume et al. 1998) accompanied with SiO masers near the infrared source IRc2 (Greenhill et al. 1998; Doeleman, Lonsdale, & Pelkey 1999). The origin of the wide-angle high-velocity outflow and northeast-southwest low-velocity outflow has been frequently discussed and new debates have came up with updated observations. Zapata et al. (2009) reported explosive CO bullets in high spatial resolution associated with the H_2 fingers, and indicated that the outflows are caused by disintegration of a massive stellar system happened about 500 years ago. Evidence of a close dynamical interaction of a young stellar system is also supported by the proper motions of the Orion BN source, radio source I, and radio source n, which are possibly runaway objects from a dynamically decayed multiple system (Rodríguez et al. 2005; Gómez et al. 2005). Such an event could also produce the energy needed for driving the large-scale outflows in the Orion BN/KL region (Bally & Zinnecker 2005).

In addition, Orion South, a twin massive molecular clump of Orion BN/KL, has roughly same size of the Orion BN/KL cloud ($\sim 2' \times 2'$) but has smaller 1.3 mm bolometric luminosity of $\sim 10^4$ $L_\odot$ which is an order lower in the luminosity than the Orion BN/KL region (Mezger, Zylka, & Wink 1990). Orion South also hosts many outflows which are believed to be associated with star-forming activities, e.g., the famous outflow Ori-S6 extending to the southeastern direction first discovered by Schmid-Burgk et al. (1990). The difference in luminosity indicates that Orion South is probably less evolved than Orion BN/KL, which is also indicated by a comparison of their molecular line emission (McMullin, Mundy, & Blake 1993).

Moreover, the Orion Bar, located at $\sim 2'$ in southeast of the Trapezium cluster, is a well-described PDR where far-ultraviolet (FUV) photons from young massive stars ionize the ISM in different levels, and produce a layer structure between H II regions and neutral molecular clouds (see, e.g., Hollenbach & Tielens 1997; Walmsley, Natta, Oliva, & Testi 2000). Unlike Orion BN/KL and Orion South, the Orion Bar has no evidence of embedded star-forming activities yet, and is offset from the dense ridge. The sharp edge of the Orion Bar indicates that the FUV photons from θ^1 Ori C carve it to the shape we see today.

Therefore, the stellar feedbacks on a larger scale of the whole OMC-1 region, including the UV radiation heating from θ^1 Ori C, and the nearby PDRs, together with the local feedbacks from the on-going star forming regions, including the energetic outflows in Orion BN/KL and Orion South, provide us many diverse cases of young massive stars interacting with their environment. OMC-1, hence, serves as a good nearby object for the study of the stellar feedbacks in detail.

1.3.3 Thesis overview and publication plan

This thesis is arranged in two parts. The first part contains the study of the Galactic starburst template W49A, and the second part contains the study of OMC-1 with the large-scale mappings

of highly excited CO lines.

Part I

The observations toward W49A are presented in §2, and the results are discussed in §3. The detailed radiative transfer modeling is shown in §4. In the study of W49A, we are seeking the answers of the following questions concerning massive star formation:

1. What makes W49A a mini-starburst region where massive stars are formed on a large scale in a short period of time? Is this starburst phenomena unprompted or is it triggered ?
2. Can we conclude a general cloud structure for W49A by examining the molecular spectra ?
3. Can HCO^+/HCN and/or HNC/HCN ratios be used as a diagnostic tool to distinguish between PDRs and XDRs ?
4. What is the relation between the outflows/shocks and the X-ray emission in W49A ?

The first two questions will be discussed in §5.1 where we shall see that the starburst in W49A is triggered by expanding shells, and is associated with the remnant gas ejections on a larger scale (50 pc). The third question will be answered in §5.2 that the intensity ratios of HCO^+/HCN and HNC/HCN do not directly reflect their abundance ratios, and should be used with caution. The fourth question is addressed in §5.3 where we do not find a tight correlation between the emission from the shock tracer SiO and the hard X-ray emission in W49A. The conclusions of the W49A study will be given in §6.

Part II

The APEX observations toward OMC-1 are presented in §7, and the results are discussed in §8. The detailed radiative transfer modeling is shown in §9. In the study of OMC-1, we try to characterize the physical properties of different regions (i.e., Orion BN/KL, Orion South, Orion Bar, and Orion East), and try to understand their connections to the Trapezium cluster:

1. What causes the explosive outflow in Orion BN/KL?
2. What is the relation between the outflows and dense clumps we see in Orion South?
3. Is the stratification also seen in the Orion Bar for the higher-J ^{12}CO, ^{13}CO, and $C^{18}O$ lines?
4. What is the nature of the not so well-known Orion East?

The first question will be discussed in §10.1, where we shall see that the explosive outflows are related to the molecular envelope confined in the Orion BN/KL region. The second question will be addressed in §10.2. The third question will be detailed in §10.3. The fourth question will

be answered in §10.4 that Orion East is probably another PDR region strongly shaped by θ^1 Ori C. The conclusions of the OMC-1 study will be summarized in §11. In the end, the summary of this thesis will be given in §12.

The publication of the W49A study will be divided in three papers. The first paper consists of the discussion of the shell structure and large-scale gas ejections in W49A and has been submitted to A&A. The second and third paper will present the study of HCN, HCO^+, and HNC and SiO and H_2S, respectively. The publication for the Orion study will be presented in two parts. The first part is the overview of the large-scale mapping of OMC-1, and will be published in one paper. The individual sources will be described in detail in the following papers.

Part I

Galactic Starburst Template W49A

2

Observations toward W49A

2.1 IRAM 30 m Observations

The observations of the $J = 1 - 0$ and $J = 3 - 2$ lines of HCN, HCO^+, HNC and their ^{13}C isotopologues together with the SiO ground vibrational state transitions were carried out in 2006 November and 2007 November using the IRAM 30 m telescope on Pico Veleta in Spain. Located at an altitude of 2920 m in the Spanish Sierra Nevada, the IRAM 30 m telescope is a Cassegrain-Nasmyth system with a main reflector of 30 m in diameter which has a surface accuracy of 55 μm.

The focus of the antenna was checked every hour on Uranus, and the pointing was checked every hour on the strong continuum emission from the BL Lac source 1749+096 and Uranus. A cross scan in azimuth and elevation in continuum mode was used to determine the correction of pointing, and the pointing accuracy was $\sim 2'' - 3''$ with a telescope tracking accuracy of $1''$. The chopper-wheel method was used as a standard calibration at the IRAM 30 m telescope to correct atmospheric attenuation where the sky, hot load, and cold load are the calibration sources. The calibrated signals are then generated by subtracting the signals on the cold sky from the ambient temperature absorber.

Table 2.1. The positions of the three clumps in W49A

Source	R.A. (J2000)	Dec. (J2000)	offset ($''$)
W49A North	$19^h10^m13\overset{s}{.}405$	$+09°06'14\overset{''}{.}35$	$(0, 0)$
W49A South	$19^h10^m21\overset{s}{.}575$	$+09°05'00\overset{''}{.}35$	$(+121, -74)$
W49A Southwest[a]	$19^h10^m10\overset{s}{.}907$	$+09°05'15\overset{''}{.}35$	$(-37, -59)$

[a]Including two UC HII sources S and Q.

Table 2.2. The IRAM 30 m observation parameters for the large-scale mapping in W49A

Line	Frequency (GHz)	$\theta_{\rm HPBW}$ ($''$)	$\eta_{\rm MB}$	Receiver	$T_{\rm sys}$ (K)[a]
SiO $(2-1)$ V=0	86.85	28.3	0.81	A100/B100	100
HCN $(1-0)$	88.63	27.8	0.81	A100	100
HCO^+ $(1-0)$	89.19	27.6	0.81	B100	120
HNC $(1-0)$	90.66	27.1	0.81	A100/B100	120
H_2S $(1_{1,0}-1_{0,1})$	168.82	14.6	0.70	C150	330
SiO $(5-4)$ V=0	217.10	11.3	0.60	B230	430
$C^{18}O$ $(2-1)$	219.56	11.2	0.60	HERA	500
^{13}CO $(2-1)$	220.40	11.2	0.60	HERA	620
SiO $(6-5)$ V=0	260.52	9.4	0.51	C270	750
HCN $(3-2)$	265.89	9.3	0.51	HERA	1300
HCO^+ $(3-2)$	267.56	9.2	0.51	HERA	1300
HNC $(3-2)$	271.98	9.0	0.51	HERA	420

[a]System temperatures are averaged from the data.

We used the HEterodyne Receiver Array, HERA (Schuster et al. 2004), to obtain large On-The-Fly (OTF) maps of the HCN, HCO^+, and HNC $J=3-2$ lines together with the ^{13}CO and $C^{18}O$ $J=2-1$ lines. HERA has nine pixels with dual polarizations in a square center-filled 3×3 array, and can be tuned to different sky frequencies with different backends attached, which makes the simultaneous observation of two frequency setups possible. The focus and pointing in the HERA observations were done at the central pixel. The HERA dewar rotation angle of 9.6° was chosen to have Nyquist-sampled maps. The size of $\sim 3\farcm5\times3\farcm5$ has been mapped in the HCN and HCO^+ $J=3-2$ lines with a half power beam width (HPBW) of $\sim 9''$. Every scan in the azimuth direction (λ-scanning) was followed by one in the elevation direction (β-scanning) to reduce strip patterns. The calibration was done for each OTF subscan and reduced in the MIRA software of the GILDAS package[1], and the OFF scans on the reference position ($-600''$, $-600''$) are done before and after each OTF subscan. The Versatile SPectrometer Array (VESPA) was chosen as the backend for HERA configured to a bandwidth of 160 MHz for each receiver element and 0.32 km s^{-1} resolution. The center of the W49A mapping was chosen at the position of W49A North, and the positions of the three main sources are summarized in Table 2.1. The system temperatures during the HERA observations were $\sim 400-1300$ K.

The smaller OTF maps ($\sim 2\farcm5\times2\farcm5$) of HCN $J=1-0$ and HCO^+ $J=1-0$ were observed with the $\lambda=3$ mm single-pixel heterodyne A/B receiver which has an HPBW of $\sim 28''$. Single-

[1]http://www.iram.fr/IRAMFR/GILDAS/

point spectra toward W49A North, W49A South, and W49A Southwest were obtained for the ^{13}C isotopologues of HCN and HCO$^+$ in the $J = 1-0$ and $J = 3-2$ lines. The position-switching mode was used for all spectra in an emission-free reference position at the offset ($-600''$, $-600''$), and the spectral line backend VESPA was mounted for the A/B receiver configured to a bandwidth of 160 MHz bandwidth and 0.32 km s^{-1} resolution. The observation parameters toward W49A using the IRAM 30 m are summarized in Table 2.2.

Spectra and maps were corrected to the main beam temperature $T_{\rm MB}$ unit from the antanna temperatures $T_{\rm A}^*$ (i.e., $T_{\rm MB} = T_{\rm A}^*/\eta_{\rm MB}$), which had only corrected for rear spillover and ohmic losses. The main beam efficiency, $\eta_{\rm MB}$, is given by the ratio between the beam efficiency (named $B_{\rm eff}$; it is 0.78 at 86 GHz and 0.46 at 260 GHz in the IRAM documentation[2]) and the forward efficiency $F_{\rm eff}$ (0.95 at 100 GHz and 0.88 at 270 GHz).

2.2 APEX Observations

Observations of the HCN and HCO$^+$ $J = 4-3$ lines were conducted with the 12 m APEX telescope in 2007 June on Llano de Chajnantor in Chile. The double-sideband heterodyne receiver APEX-2a (Risacher et al. 2006) was used to obtain small maps ($\sim 100'' \times 80''$) toward W49A North with the raster mode. The focus of the antenna was checked every hour on Jupiter, and the pointing was checked every hour on the continuum emission from G34.26 and Jupiter. The five-points mapping in the continuum mode was used to determine the pointing correction, and the accuracy of pointing was $\sim 2''$ with a telescope tracking accuracy of $1''$. The chopper-wheel method was used as a standard calibration in the APEX telescope to correct atmospheric attenuation, radiative loss, rearward scattering, and spillover.

Single-point spectra toward W49A North and South were also observed together with the ^{13}C isotopologic lines of HCN and HCO$^+$ $J = 4-3$. The position-switching mode was used for all spectra in an emission-free reference position at the offset ($-1000''$, $0''$), and the Fast Fourier Transform Spectrometer (FFTS; Klein et al. 2006) backend was mounted for the APEX-2a configured to a bandwidth of 1000 MHz and $\sim$ 0.1 km s^{-1} resolution, which is smoothed to $\sim$ 1 km s^{-1} afterwards. For APEX at 352 GHz, $\eta_{\rm MB} = 0.73$ and $F_{\rm eff} = 0.97$ (Güsten et al. 2006).

The observation of the 870 μm continuum emission toward W49A was carried out using the Large APEX Bolometer Camera (LABOCA; Siringo et al. 2009). The LABOCA instrument has an array of 295 bolometers arranged in an hexagonal pattern, with a field of view of $11\farcm4$ and a two-beam spacing between bolometers. The HPBW at 345 GHz is $19\farcs2$, and the pointing and focus were done on the continuum emission from G34.26 with a pointing accuracy of $\sim 4''$. The data were processed and reduced using the BOlometer array data Analysis (BOA) package (Schuller et al., in prep.). The data were calibated by applying an opacity correction determined from skydips. The data reduction was done by flagging bad pixels, removing the correlated noise, and the map was

[2]http://www.iram.fr/IRAMES

Table 2.3. The APEX observation parameters for the W49A mapping

Line	Frequency (GHz)	$\theta_{\rm HPBW}$ ($''$)	$\eta_{\rm MB}$	Receiver	$T_{\rm sys}$ (K)[a]
^{12}CO $(3-2)$	345.80	17.1	0.75	APEX2a	240
SiO $(8-7)$ V=0	347.33	17.1	0.75	APEX2a	340
HCN $(4-3)$	354.51	16.7	0.75	APEX2a	240
HCO^+ $(4-3)$	356.73	16.6	0.75	APEX2a	340
HNC $(4-3)$	362.63	16.4	0.75	APEX2a	550
HCN $(8-7)$	708.88	8.4	0.47	CHAMP$^+$	3700
HCO^+ $(10-9)$	891.56	6.7	0.45	CHAMP$^+$	1920

[a]System temperatures are averaged from the data.

obtained using a natural weighting. The first image can then be used as a source model to reduce the negative artifacts and recover some fraction of the flux (Schuller et al. 2009). The final flux uncertainty for compact sources is less than 15%.

In 2008 July, we observed W49A North in the 450 μm and 350 μm atmospheric windows using new 2×7 elements heterodyne array CHAMP$^+$ (Kasemann et al. 2006) with the FFTS backend to obtain small maps ($\sim 1' \times 1'$) of the HCN $J = 8-7$ and HCO^+ $J = 10-9$ transition lines. The focus and the pointing were checked on Jupiter every hour with a pointing accuracy of $\sim 2''-3''$. The FFTS backend was used with a velocity resolution of ~ 0.5 km s^{-1}. The single-sideband operation provides a high system sensitivity, and the image sideband is terminated at 20 K. Raster mapping was used to obtain the W49A images in the position-switching mode and the OFF position was chosen at the offset $(-1000'', 0'')$. Single-point spectra toward W49A North were also observed for the HCO^+ $J = 9-8$ transition.

The mapping parameters toward W49A using the APEX telescope are summarized in Table 2.3. All data presented here were reduced using the standard procedures in the GILDAS package.

3

W49A Results

The results of W49A will be presented in this chapter. The molecular emission of CO isotopologues, high density tracers (i.e., HCN, HCO^+, and HNC), and shock/outflow tracers (i.e., SiO and H_2S) will be presented in §3.1, The results of the dust continuum emission and mass estimation will be given in §3.2.

3.1 Molecular line emission

^{12}CO

The ^{12}CO $J = 3-2$ image toward W49A was obtained for the central region of W49A North. Since the low-J ^{12}CO lines trace mostly low-density gas, and have very high optical depth, the ^{12}CO $J = 3-2$ emission in W49A North is probing the outer part of the cloud. The ^{12}CO $J = 3-2$ integrated intensity peaks in Figure 3.1 toward sources G and D. The ^{12}CO line wing emission shown in Figure 3.1 (at -10 km s^{-1} and $+25$ km s^{-1}) is concentrated on the region near sources G, D, and A, indicating a possible outflow originated from this region.

The position-velocity (PV) diagrams of ^{12}CO $J = 3-2$ (Fig. 3.2) clearly show a high-velocity outflow located in the center of W49A North where many UC H II sources accumulate. The PV diagrams and ^{12}CO spectra in Figure 3.2 show two strong absorption features near $6-9$ km s^{-1} and $14-19$ km s^{-1}, and each absorption feature contains even several absorption dips. As we shall see in other molecular lines later, the first absorption at $6-9$ km s^{-1} is due largely to the self-absorption of the clump at ~ 12 km s^{-1}. The second absorption at $14-19$ km s^{-1} is due to the nearby extended gas in a Galactic spiral arm (Fig. 3.3), which is likely the Perseus Arm (Fig. 1.5). In W49A North, the $V_{\rm LSR}$ of the ^{12}CO $J = 3-2$ emission peak is blueshifted to ~ -0.3 km s^{-1} and has a broad line width of ~ 20 km s^{-1}. The blueshifted emission peak is probably due to the optically thick ^{12}CO emission which is seen in the outer part of the cloud. In W49A South (Fig.

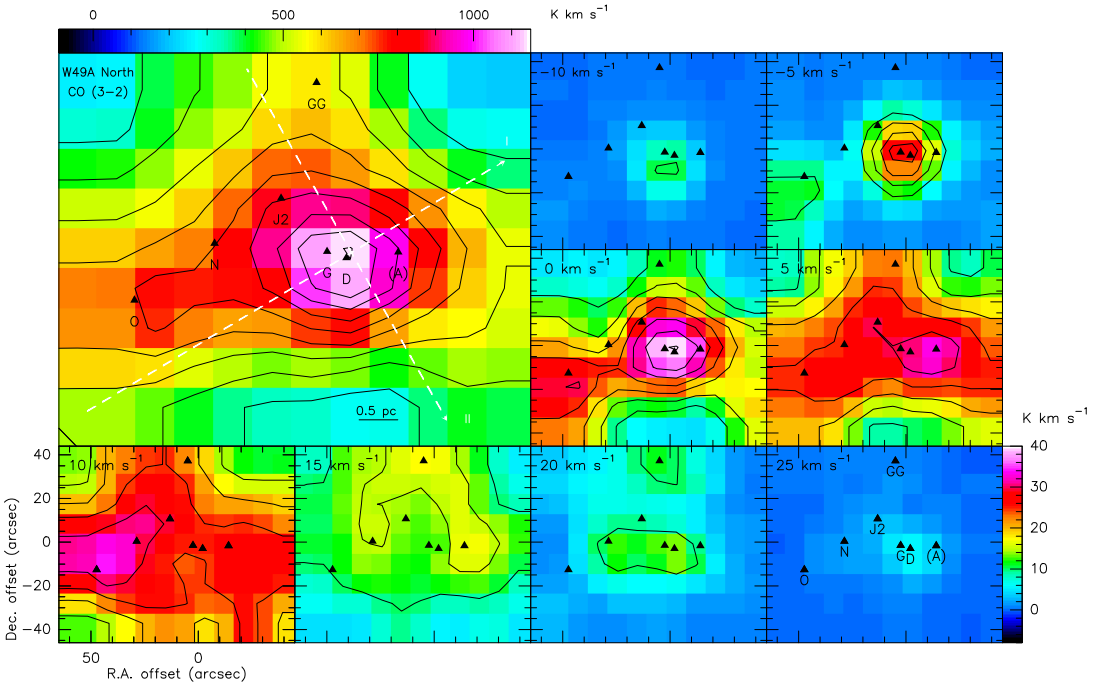

Figure 3.1 The ^{12}CO $J = 3 - 2$ integrated intensity image and the velocity channel maps of W49A North. Upper-left panel is the ^{12}CO $J = 3 - 2$ integrated intensity (from -20 to 30 km s^{-1}) image ($\theta_{\rm HPBW} = 17\farcs1$), and contours are plotted from 350 ($\sim 23\ \sigma$ level) to 1150 K km s^{-1} in steps of 100 K km s^{-1}. The rest panels are the velocity channel maps (5 km s^{-1} interval) in contours running from 10 to 50 K km s^{-1} in steps of 5 K km s^{-1} (3 σ level). The two white dashed lines correspond to the two PV cuts shown in Figure 3.2.

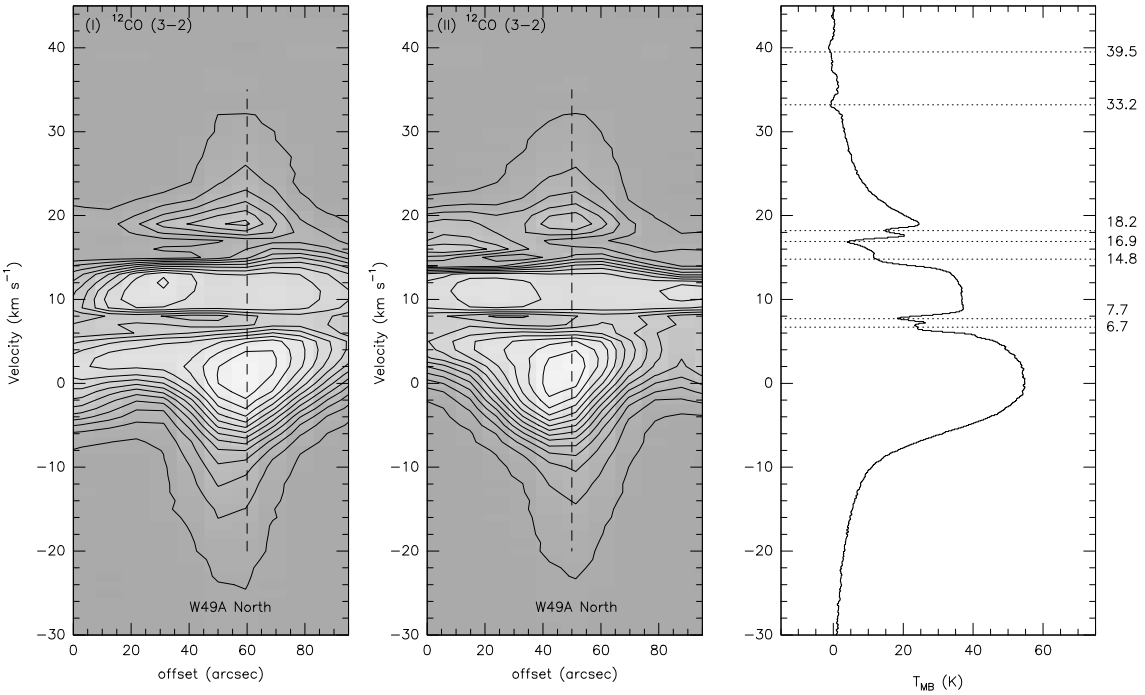

Figure 3.2 The W49A North PV diagrams of ^{12}CO $J = 3 - 2$ corresponding to Cut I and II shown in Figure 3.1. The contours are plotted from 2 to 52 K in steps of 4 K. The spectrum toward W49A North is shown in the right panel where the velocities of the absorption lines are indicated.

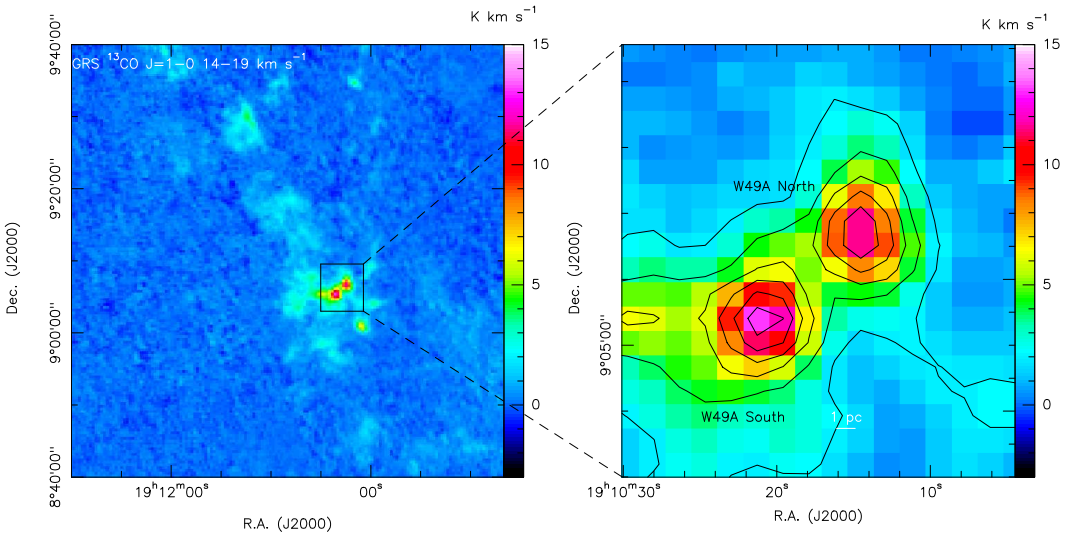

Figure 3.3 Left image shows the Galactic Ring Survey (GRS) ^{13}CO $J = 1 - 0$ integrated intensity (14–19 km s^{-1}) in a large-scale region, and the ^{13}CO emission in this velocity range is likely from the gas of the Perseus Arm. Right image is the zoomed ^{13}CO $J = 1 - 0$ image, and the contours are plotted from 2 to 12 K km s^{-1} in steps of 2 K km s^{-1}.

3.4), the ^{12}CO $V_{\rm LSR}$ of $\sim$ 11 km s^{-1} is also blueshifted with a line width of $\sim$ 15 km s^{-1}. The ^{12}CO $J = 3 - 2$ spectra in W49A South also shows severe absorptions at $\sim$ 15 km s^{-1} and $\sim$ 18 km s^{-1}. The first absorption at $\sim$ 15 km s^{-1} is likely due to self-absorption of its own cloud ($V_{\rm LSR}$ $\sim$ 17 km s^{-1}), and another absorption at $\sim$ 18 km s^{-1} is due to the extended gas in the Perseus Arm. The ^{12}CO measurements are summarized in Table 3.1.

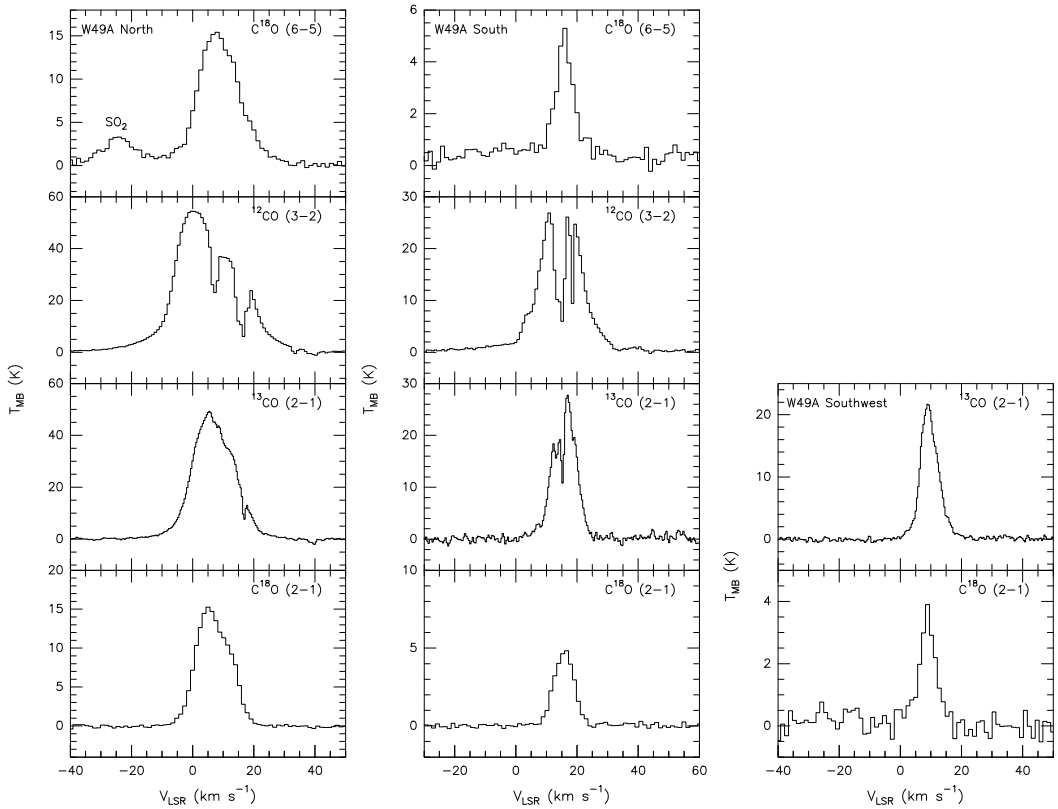

Figure 3.4 The CO isotopologic spectra in W49A. The panel from left to right shows the $C^{18}O$ $J = 6 - 5$, ^{12}CO $J = 3 - 2$, ^{13}CO $J = 2 - 1$ and $C^{18}O$ $J = 2 - 1$ spectra in W49A North, South, and Southwest, respectively.

^{13}CO and C^{18}O

The ^{13}CO and C^{18}O line emission is less optically thick compared with the ^{12}CO line emission. The ^{13}CO and C^{18}O $J = 2 - 1$ lines also trace low-density gas, and appear ubiquitously in W49A. The ^{13}CO $J = 2 - 1$ integrated intensity image and velocity channel maps in Figure 3.5 show clear connection between different clumps in W49A. Apart from these three prominent sources, W49A North, South, and Southwest, the radio source JJ also has strong ^{13}CO $J = 2 - 1$ emission. In addition, faint filamentary emission is revealed. As for C^{18}O $J = 2 - 1$ (Fig 3.6), the faint filamentary emission is less obvious, but the C^{18}O emission is still extended over the whole W49A region. Besides, source JJ also has a strong counterpart in the C^{18}O $J = 2 - 1$ image. The mean intensity image (first moment) of ^{13}CO and C^{18}O (Figs. 3.7 and 3.8) clearly show the faint filamentary emission discussed above. In addition, the velocity images (second moment) indicate a ring/shell structure surrounding the center part of W49A North, and a filament in the NE-SW through source N, source S, and source Q is also seen. Some filaments can be seen in the $V_{\rm LSR}$ images, and their velocity gradients probably result from a shock/outflow activity. In the line width distribution images (third moment), clumps in W49A North have relatively larger line widths, so does the region near source GG and W49A South.

In W49A North (Fig. 3.9), the $V_{\rm LSR}$ of ^{13}CO and C^{18}O $J = 2 - 1$ seems to have two peaks at ~ 5 km s^{-1} and ~ 12 km s^{-1}. As we shall see later in the spectra of the HCN and HCO$^+$ isotopologues, these two peaks are more clear, and correspond to two clumps. However, the $V_{\rm LSR}$ of C^{18}O $J = 6 - 5$ in W49A North is ~ 8 km s^{-1}, which indicates that the heating source for this highly excited C^{18}O line is likely located at ~ 8 km s^{-1}. The line widths of ^{13}CO and C^{18}O lines are $\sim 14 - 15$ km s^{-1} in W49A North. In W49A South (Fig. 3.4), the $V_{\rm LSR}$ of ^{13}CO and C^{18}O is $\sim 16 - 17$ km s^{-1} with line widths ranging from 6 to 9 km s^{-1}. In addition, the $V_{\rm LSR}$ of ^{13}CO and C^{18}O in W49A Southwest is ~ 9 km s^{-1} with a line width of 6 km s^{-1}. The CO isotopologic spectrum comparison toward W49A North, South, and Southwest is shown in Figure 3.4 and their measurements are summarized in Table 3.1.

In Figure 3.4, the CO isotopologic spectra all show asymmetric line profiles in W49A North, which might result from the superposition of two line profiles of two clumps (see also §4.1). In W49A North and South, the ^{12}CO and ^{13}CO lines are self-absorbed. In the detailed comparison of CO isotopologic spectra (Fig. 3.9), the $13 - 19$ km s^{-1} absorption feature is also seen in ^{13}CO and C^{18}O $J = 2 - 1$ due to the extended gas in the Perseus Arm. As for C^{18}O $J = 6 - 5$ at ~ 17 km s^{-1}, it is probably self-absorbed toward W49A North. In the PV diagrams of ^{13}CO and C^{18}O (Fig. 3.10), the ^{13}CO $J = 2 - 1$ emission has obvious connections between W49A North and South at ~ 5 km s^{-1} and 15 km s^{-1}.

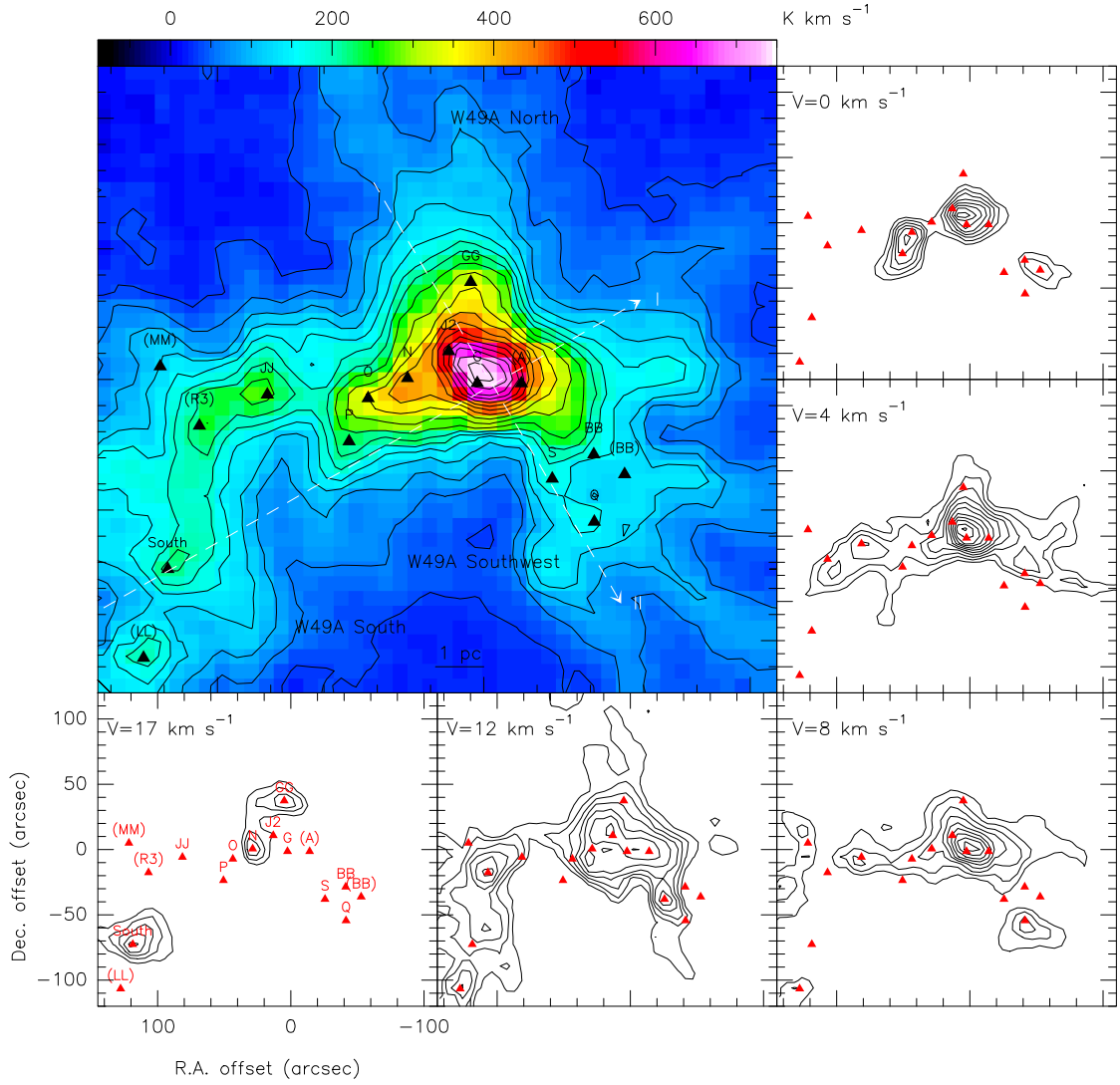

Figure 3.5 The ^{13}CO integrated intensity image and selected velocity channel maps of W49A. Upper-left panel is the ^{13}CO $J = 2 - 1$ image ($\theta_{\rm HPBW} = 11\farcs2$), and contours are plotted from 30 to 210 K km s^{-1} in steps of 30 K km s^{-1} and the subsequent contours are running from 250 to 750 K km s^{-1} in steps of 50 K km s^{-1} for clarity. One σ noise is 3 K km s^{-1} in the ^{13}CO $J = 2 - 1$ map. The rest panels are the five selected velocity channel maps of ^{13}CO $J = 2 - 1$ in contours from 10 to 50 K km s^{-1} in steps of 4 K km s^{-1} (10 σ level). The two white dashed lines correspond to the two PV cuts shown in Figure 3.10.

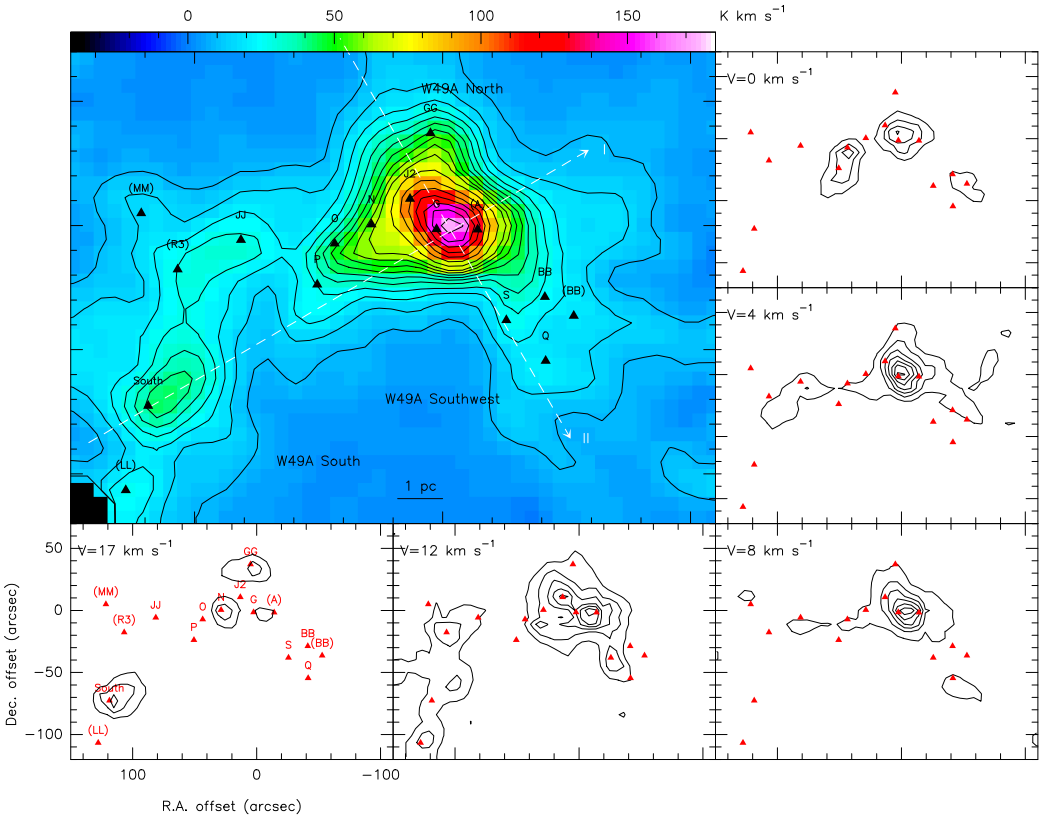

Figure 3.6 The $C^{18}O$ integrated intensity image and selected velocity channel maps of W49A. Upper-left panel is the $C^{18}O$ $J = 2 - 1$ image smoothed with two Gaussian beams ($\theta_{\rm HPBW} = 11\farcs2$), and contours are plotted from 9 to 66 K km s^{-1} in steps of 6 K km s^{-1} and the subsequent contours are running from 75 to 180 K km s^{-1} in steps of 15 K km s^{-1} for clarity. One σ noise is 1 K km s^{-1} for the $C^{18}O$ $J = 2 - 1$ map. The rest panels are the five selected velocity channel maps of $C^{18}O$ $J = 2 - 1$ in contours running from 2 to 14 K km s^{-1} in steps of 2 K km s^{-1} (10 σ level). The two white dashed lines correspond to the two PV cuts shown in Figure 3.10.

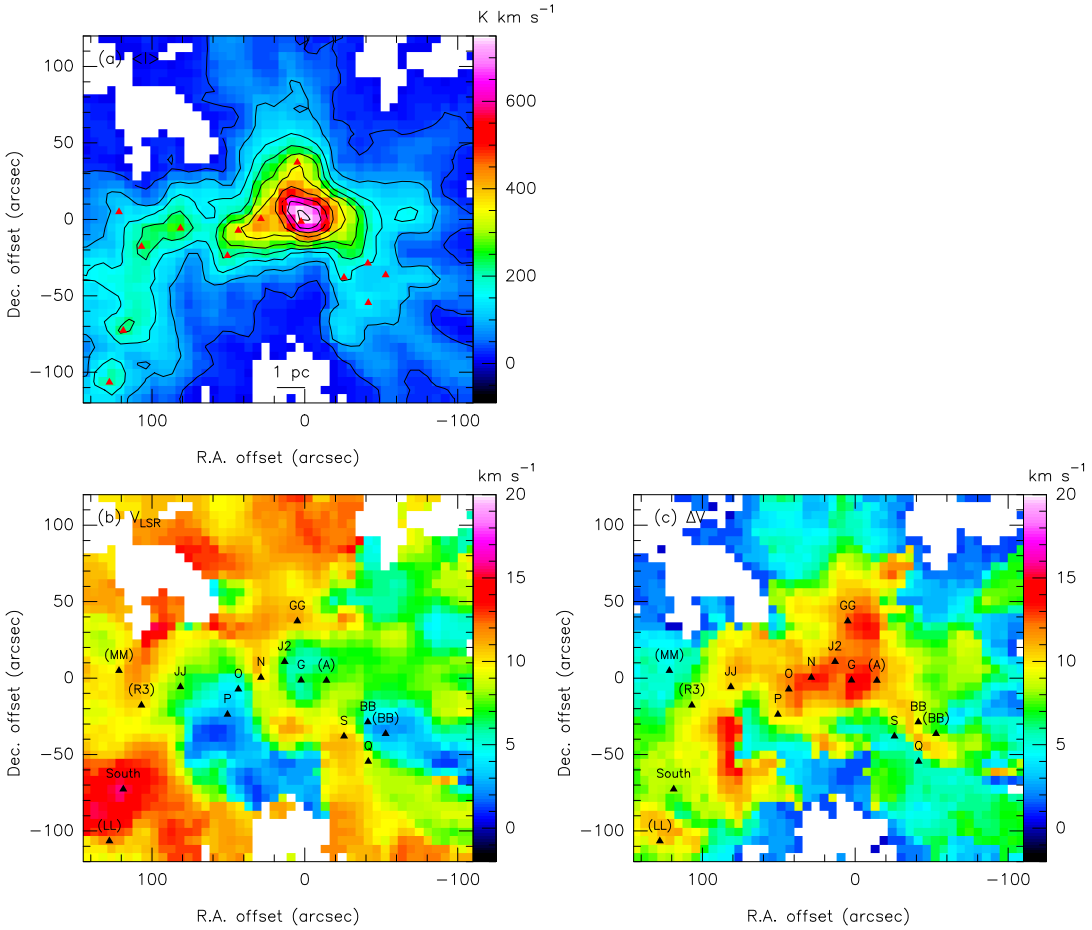

Figure 3.7 The ^{13}CO $J = 2-1$ moment maps of W49A. (a) The mean intensity map is plotted with contours running from 30 to 270 K km s^{-1} in steps of 60 K km s^{-1} and the subsequent contours running from 350 to 750 K km s^{-1} in steps of 100 K km s^{-1}. (b) The second moment of ^{13}CO $J = 2-1$ shows the velocity distribution in W49A. (c) The third moment of ^{13}CO $J = 2-1$ shows the line width distribution in W49A. The pixels whose temperatures are below 3 K are blanked.

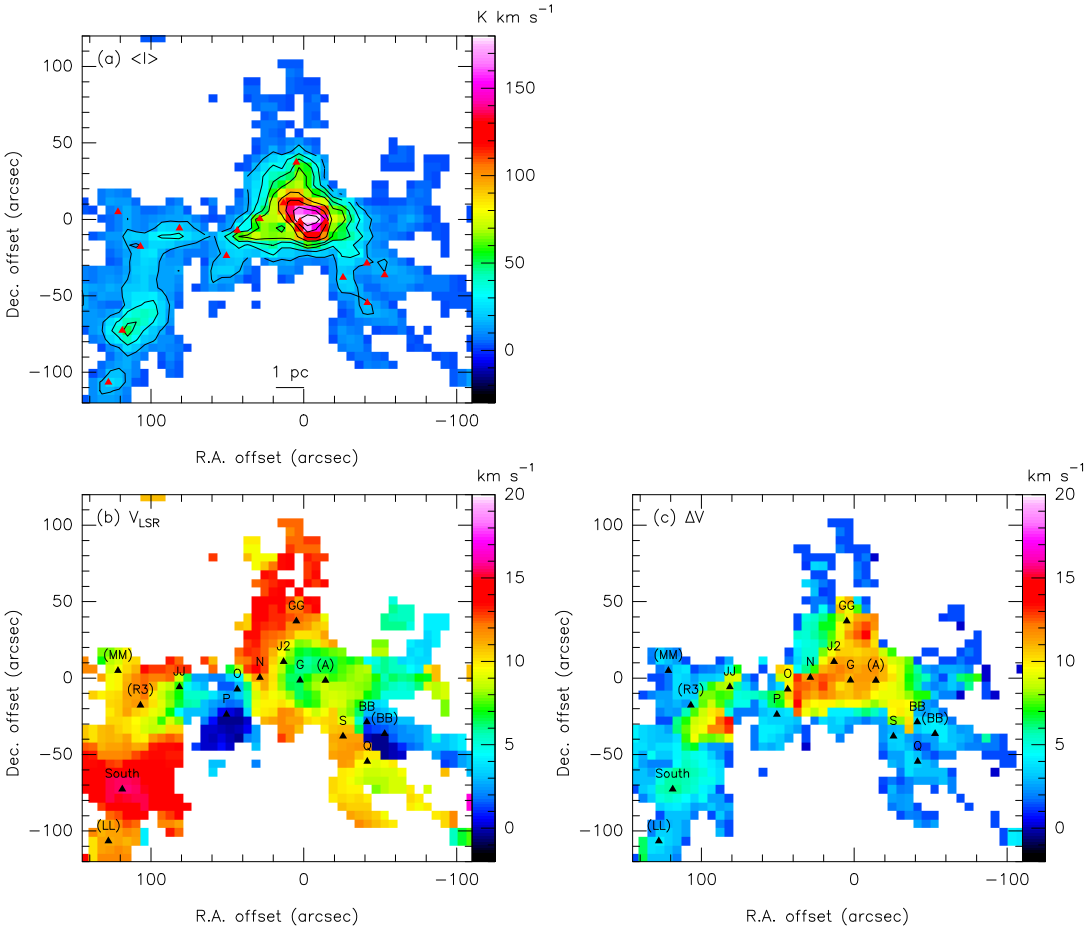

Figure 3.8 The $C^{18}O$ $J = 2-1$ moment maps in W49A. (a) The mean intensity map is plotted with contours running from 30 to 210 K km s^{-1} in steps of 30 K km s^{-1} and the subsequent contours running from 250 to 750 K km s^{-1} in steps of 50 K km s^{-1}. (b) The second moment of $C^{18}O$ $J = 2-1$ shows the velocity distribution in W49A. (c) The third moment of $C^{18}O$ $J = 2-1$ shows the line width distribution in W49A. The pixels whose temperatures are below 1.5 K are blanked.

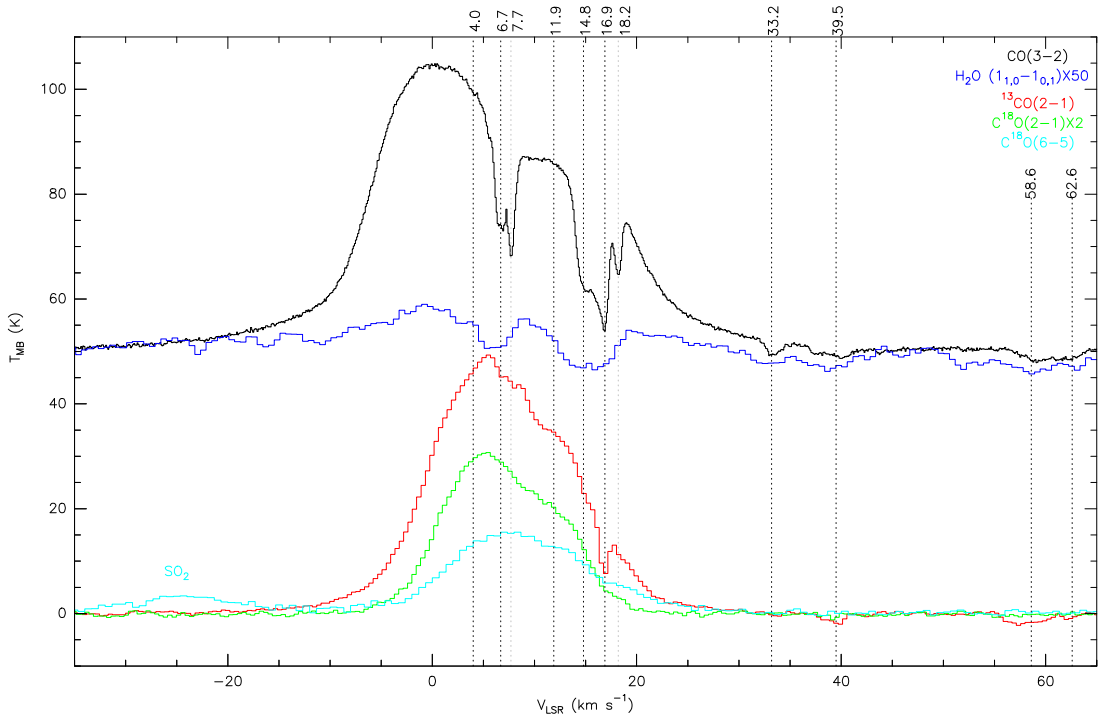

Figure 3.9 The CO isotopologic spectrum comparison in W49A North. The H_2O $1_{1,0} - 1_{0,1}$ spectrum is from the SWAS ($\theta_{\rm HPBW} = 3'.3 \times 2'.5$ at 553 GHz), and was obtained toward the position ($19^{\rm h}10^{\rm m}13^{\rm s}.490$, $+09°06'29''.00$, J2000.0) with an offset $(+1, -15)$ from W49A North. For clarity, the H_2O and ^{12}CO line profiles have been shifted by 50 K.

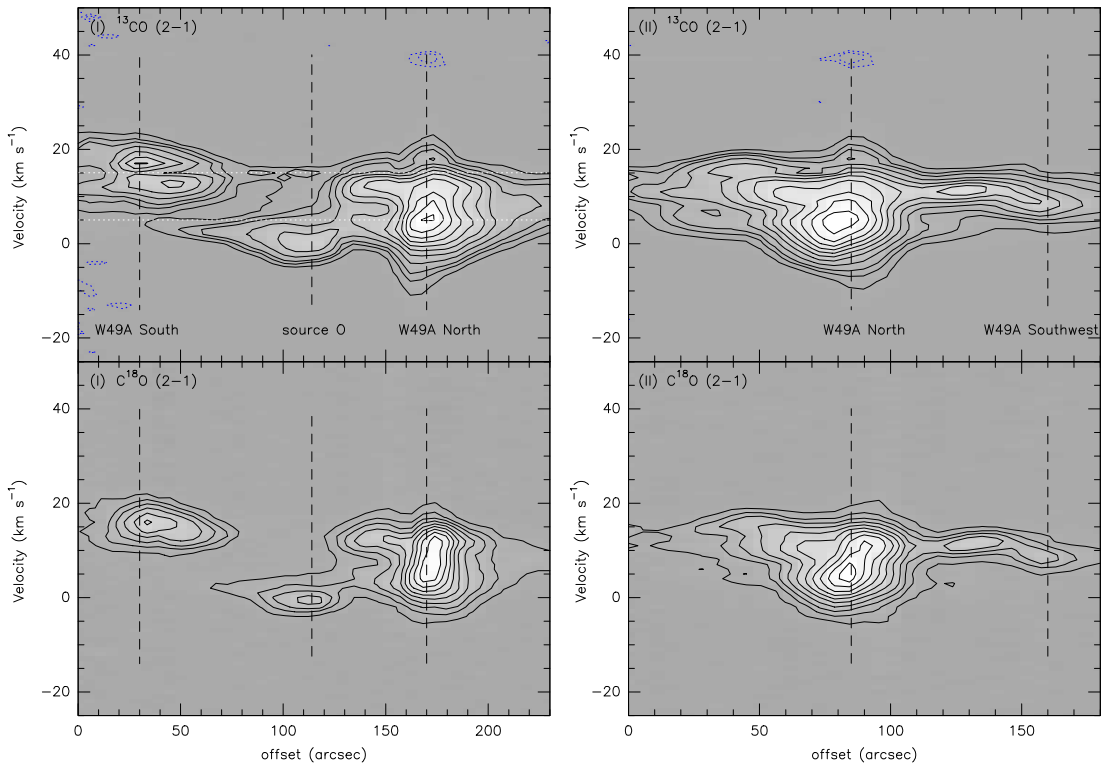

Figure 3.10 The PV diagrams of ^{13}CO and C^{18}O $J = 2 - 1$ of W49A in the positions shown in Figure 3.5. Upper panels show the two cuts of ^{13}CO $J = 2 - 1$. The blue dotted contours represent the absorption of -0.4 and -0.6 K, and the black contours denote the temperature running from 2 to 6 K in steps of 2 K and the subsequent contours running from 10 to 45 K in steps of 5 K. Lower panels show the two cuts of C^{18}O $J = 2 - 1$ in black contours representing 0.75 K, 1.75 K, and 2.75 K and the subsequent contours running from 4 to 13 K in steps of 1.5 K.

Table 3.1. The CO isotopologues measurements in W49A

	W49A North			W49A South			W49A Southwest		
	$T_{\rm peak}$[a] (K)	$V_{\rm LSR}$[b] (km s^{-1})	ΔV[c] (km s^{-1})	$T_{\rm peak}$[a] (K)	$V_{\rm LSR}$[b] (km s^{-1})	ΔV[c] (km s^{-1})	$T_{\rm peak}$[a] (K)	$V_{\rm LSR}$[b] (km s^{-1})	ΔV[c] (km s^{-1})
$C^{18}O$ $(6-5)$	15.4±0.3	8.0	14.7	5.3±0.3	16.0	6.0	···	···	···
^{12}CO $(3-2)$	54.5±0.1	−0.3	20.1[d]	26.9±0.1	10.9	15.2[d]	···	···	···
^{13}CO $(2-1)$	48.7±0.2	5.1	15.3	26.4±0.4	16.5	8.5	21.4±0.2	8.9	6.0
$C^{18}O$ $(2-1)$	15.3±0.1	5.1	14.5	4.8±0.1	16.6	7.7	3.9±0.3	8.9	6.0

[a]Temperatures shown here are corrected to the main beam temperature unit.

[b]$V_{\rm LSR}$ is measured at temperture peaks.

[c]Line widths are measured in FWHM.

[d]All components have been included in the measurement.

HCO^+

HCO^+ is one of the most abundant molecular ions in the ISM. It is usually used to probe the physical properties of molecular clouds, such as density, temperature, and dynamics. HCO^+ has a large dipole moment (i.e., $\mu \sim 3.93$ D) which results in high critical densities, e.g., $n_{\rm cr} \sim 2 \times 10^5$ cm^{-3} in the $J = 1 - 0$ transition. The HCO^+ rotational transition lines, therefore, require a higher density to be excited, and can serve as dense gas tracers. The HCO^+ $J = 1-0$ and $J = 3-2$ images in Figure 3.11 show the three prominent dense components in W49A (W49A North, Southwest and South), and more embedded clumps are revealed in the velocity channel maps. The HCO^+ $J = 4-3$ and $J = 10 - 9$ images of W49A North are shown in Figure 3.12 which is, to our knowledge, the first published HCO^+ $J = 10 - 9$ emission map. The images of HCO^+ $J = 1 - 0$, $J = 3 - 2$, and $J = 4 - 3$ all show very extended and luminous emission in W49A, but the HCO^+ $J = 10 - 9$ emission is compact ($\sim 34'' \times 35''$), and concentrated on source G2, the brightest source in the 3.6 cm continuum emission of source G (De Pree, Mehringer, & Goss 1997). The measurements of the HCO^+ line width, peak temperature, and $V_{\rm LSR}$ for different transitions are summarized in Table 3.2, and the spectrum comparison toward the three main components is shown in Figure 3.13.

In W49A North, the $V_{\rm LSR}$ of main ^{12}C isotopologic lines of HCO^+ varies from -0.9 to 6.5 km s^{-1}, and has an average value of 0.8 km s^{-1} (Table 3.2), where most of the emission peaks are associated with the 4 km s^{-1} clump. The low-J tansition lines of HCO^+ are optically thick in W49A, and come from the outer part of the cloud. The high-J transitions of HCO^+ are probably optically thin already. The $V_{\rm LSR}$ of the high-J HCO^+ lines is ~ 6.7 km s^{-1}, and is probably associated with the 4 km s^{-1} clump. The HCO^+ line widths of the two clumps (at ~ 4 km s^{-1} and ~ 12 km s^{-1}, see also §5.1) in W49A North vary from less than 10 km s^{-1} to 22 km s^{-1} in different transitions, and the large line wing shown in W49A North (Fig. 3.15) indicates an outflow. The optically thin $H^{13}CO^+$ lines have line widths of $\sim 13 - 14$ km s^{-1} with emission peaks at ~ 4 km s^{-1} and ~ 12 km s^{-1}, consistent with the ^{13}CO $J = 2 - 1$ and C^{18}O $J = 2 - 1$ spectra that at least two clumps are present toward the center of W49A North near source G. However, it seems that the emission at 6.7 km s^{-1} also contributes to most of the $H^{13}CO^+$ and high-J HCO^+ lines.

In W49A South, probably because of its less dense environment, the $V_{\rm LSR}$ of the main ^{12}C isotopologic lines of HCO^+ has small deviation compared with the ^{13}C isotopologic lines ($V_{\rm LSR} \sim 16 - 18$ km s^{-1}), but the absorption feature is still strong in the HCO^+ $J = 1 - 0$ transition (Fig. 3.13) at ~ 15 km s^{-1} and ~ 18 km s^{-1}. The line widths for the $V_{\rm LSR}$ of the main ^{12}C lines are $\sim 11 - 12$ km s^{-1}, and $\sim 7 - 11$ km s^{-1} for the ^{13}C isotopologic lines in W49A South. In W49A Southwest, the $V_{\rm LSR}$ of HCO^+ lines is $\sim 8 - 10$ km s^{-1} with relatively small line widths which indicates a relatively quiescent and/or less dense region. At least two clumps can be identified in the HCO^+ $J = 1 - 0$ and $J = 3 - 2$ emission for W49A Southwest, which have been distinguished as three sources (S, R, and Q) by radio recombination lines (De Pree, Mehringer, & Goss 1997) and the NIR observations (Alves & Homeier 2003). Because of the single broad line of HCO^+ $J = 3 - 2$

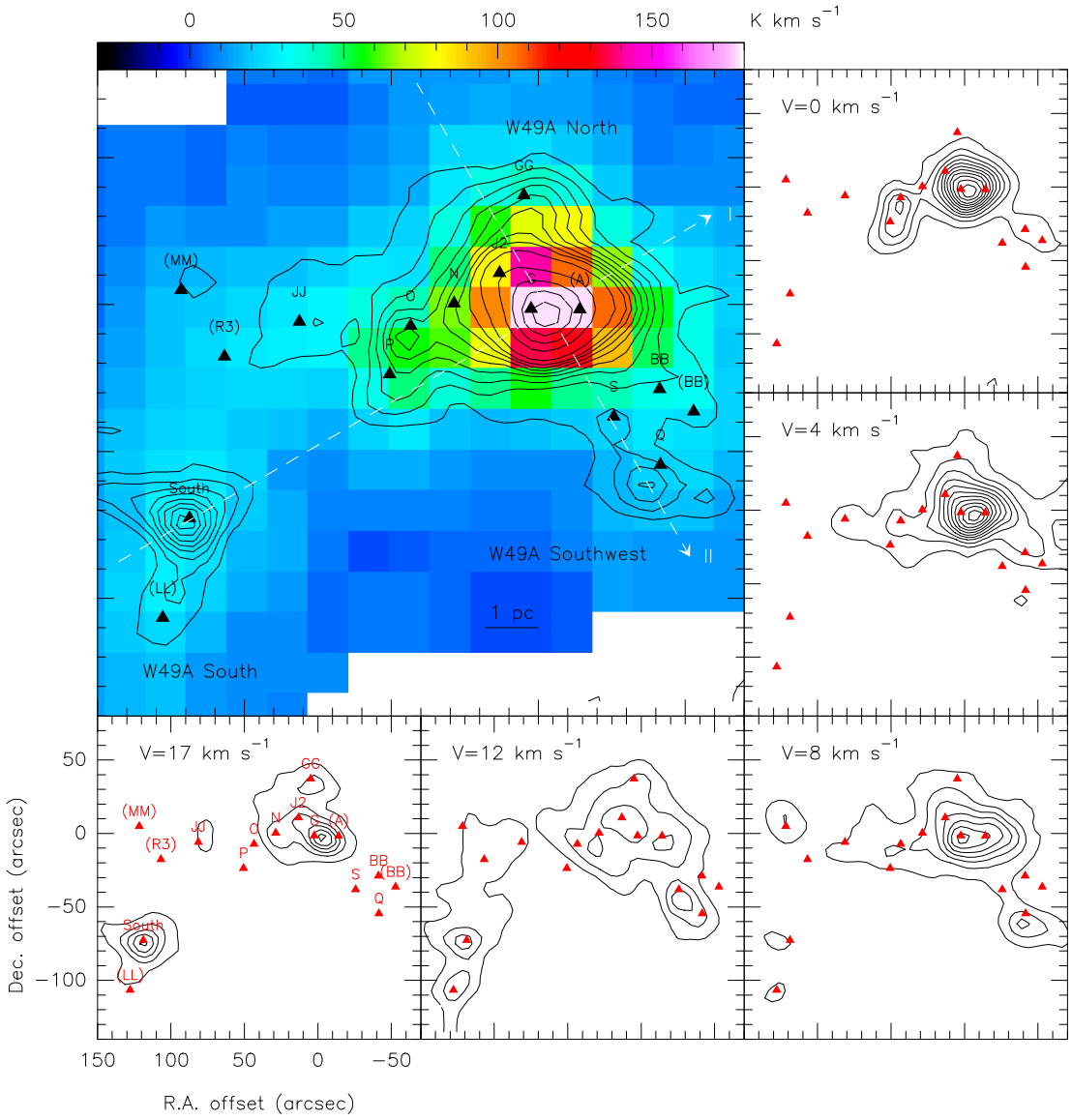

Figure 3.11 The smoothed (two Gaussian beams) HCO^+ integrated intensity image and selected velocity channel maps of W49A. Upper-left panel is the HCO^+ $J = 1 - 0$ image ($\theta_{\rm HPBW} = 27\farcs6$) overlaid with HCO^+ $J = 3 - 2$ contours running from 31.5 to 129.5 K km s^{-1} in steps of 14 K km s^{-1} and the subsequent contours running from 160 to 480 K km s^{-1} in steps of 80 K km s^{-1} for clarity. One σ noise is 7 K km s^{-1} in the HCO^+ $J = 3 - 2$ map ($\theta_{\rm HPBW} = 9\farcs2$). The rest panels are the five selected velocity channel maps of HCO^+ $J = 3 - 2$ in contours running from 2 to 24 K km s^{-1} in steps of 2 K km s^{-1} (10 σ level). The two white dashed lines correspond to the two PV cuts shown in Figure 3.15.

in W49A Southwest, the two components from the HCO^+ $J = 1 - 0$ emission are unlikely resulted from two clumps but due to self-absorption (at 6-8 km s^{-1}) instead.

Figure 3.15 shows two PV diagrams of HCO^+ $J = 1 - 0$ and $J = 3 - 2$ in W49A. In W49A North, two components at ~ 3 km s^{-1}, and ~ 17 km s^{-1} are shown in the HCO^+ $J = 3 - 2$ emission, and the 33 km s^{-1} component corresponds to the SO_2 $13_{3,11} - 13_{2,12}$ line emission. Source O at ~ 0 km s^{-1} is also seen in the both $J = 1 - 0$ and $J = 3 - 2$ trainsitions of the HCO^+ PV diagrams. As for HCO^+ $J = 1 - 0$, two components at ~ 2 km s^{-1} and ~ 10 km s^{-1} are seen, which are probably due to the severe absorption around 7 km s^{-1} and 15 km s^{-1}, caused by self-absorption and the absorption by extended gas from the Perseus Arm, respectively.

Figure 3.16 shows the comparison between the HCO^+ spectra and the H_2O spectrum observed by the Submillimeter Wave Astronomy Satellite (SWAS). The comparison reveals a surprising similarity between the HCO^+ $J = 1 - 0$ spectrum and the ground-state ortho-H_2O $1_{1,0} - 1_{0,1}$ spectrum toward W49A. The 4.0 km s^{-1} absorption feature is due to self-absorption, and is obvious only in the HCO^+ $J = 1 - 0$ and $J = 3 - 2$ spectra. In addition, the 6.7 km s^{-1} self-absorption feature is all seen in HCO^+ $J = 1 - 0$, $J = 3 - 2$, and H_2O lines. The 4.0 and 6.7 km s^{-1} self-absorption features can be also seen at the offsets from the W49A North (Fig 3.18). However, in HCO^+ $J = 10 - 9$ and $J = 9 - 8$, the emission peaks are located at velocities of 6.5 km s^{-1} and 5.9 km s^{-1}, close to the 6.7 km s^{-1} self-absorption feature. Besides, another two absorption features at 14.8 km s^{-1} and 16.9 km s^{-1} appear clearly in the ground-state HCO^+ and H_2O lines due to the extended gas from the Perseus Arm. In the HCO^+ $J = 10 - 9$ and $J = 9 - 8$ transition (Figs. 3.16 and 3.17), the emission from the 12 km s^{-1} clump is relatively weak, and both HCO^+ $J = 10 - 9$ and $J = 9 - 8$ lines show extended line wings. It is worth noting that two emission peaks of HCO^+ $J = 3 - 2$ have V_{LSR} of ~ -1 km s^{-1} and ~ -17 km s^{-1}, and probably correspond to the blue- and redshifted counterparts of the 4 km s^{-1} clump and the 12 km s^{-1} clump, respectively. Several absorption features are seen at 33.2 km s^{-1}, 39.5 km s^{-1}, 60.8 km s^{-1}, and 62.2 km s^{-1} on the line of sight toward W49A intersected with the Sagittarius Arm.

Table 3.2. The HCO^+ measurements in W49A

	W49A North			W49A South			W49A Southwest		
	T_{peak}[a] (K)	V_{LSR}[b] (km s^{-1})	ΔV[c] (km s^{-1})	T_{peak}[a] (K)	V_{LSR}[b] (km s^{-1})	ΔV[c] (km s^{-1})	T_{peak}[a] (K)	V_{LSR}[b] (km s^{-1})	ΔV[c] (km s^{-1})
HCO^+ $(10-9)$	12.3±0.4	6.5	7.9	< 0.5	···	···	< 3.8	···	···
HCO^+ $(9-8)$	13.5±0.7	5.9	9.9	< 1.0	···	···	···	···	···
HCO^+ $(4-3)$	15.2±0.3	1.7	22.2	4.5±0.2	15.6	11.1	···	···	···
$H^{13}CO^+$ $(4-3)$	4.2±0.3	3.7	12.7	0.7±0.2	17.9	10.5	···	···	···
HCO^+ $(3-2)$	23.9±0.3	−0.9	15.8	11.8±0.2	16.6	11.6	8.4±0.4	8.9	7.4
$H^{13}CO^+$ $(3-2)$	5.3±0.4	4.7	14.0	2.8±0.1	16.6	7.6	< 0.4	···	···
HCO^+ $(1-0)$	16.4±0.1	1.7	7.9[d]	3.4±0.1	19.8	12.6	4.0±0.2	9.5	3.9
$H^{13}CO^+$ $(1-0)$	1.5±0.1	4.0	13.8	0.5±0.1	16.1	7.3	0.3±0.1	8.4	2.4

[a]Temperatures shown here are corrected to the mean beam temperature unit.

[b]V_{LSR} is measured at temperture peaks.

[c]Line widths are measured in FWHM.

[d]Only single component has been measured.

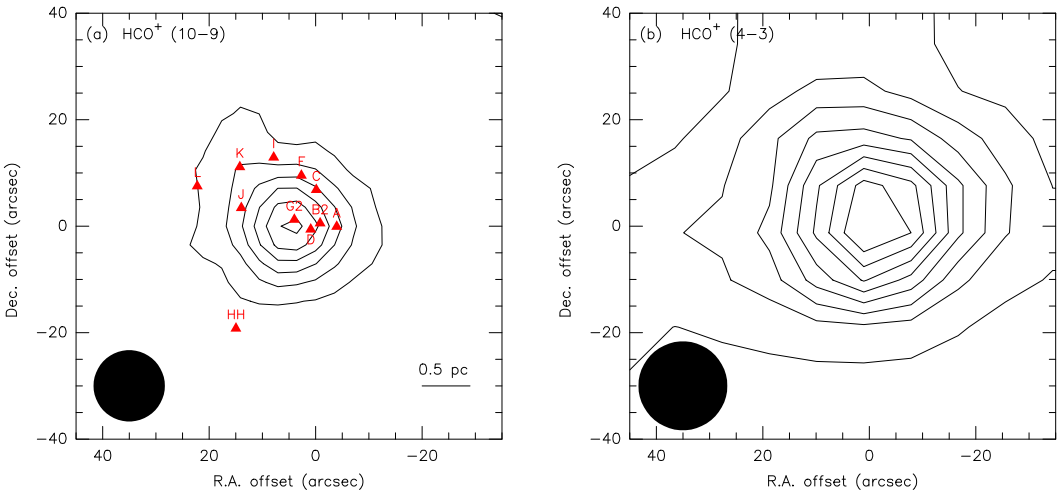

Figure 3.12 The HCO^+ $J = 10 - 9$ and $J = 4 - 3$ images of W49A North. (a) The HCO^+ $J = 10 - 9$ integrated intensity (from -10 to $+30$ km s^{-1}) image smoothed by two Gaussian beams ($\theta_{\rm HPBW} = 6\farcs7$). Contours are plotted from 25 to 175 K km s^{-1} in steps of 30 K km s^{-1} (5 σ level). (b) The HCO^+ $J = 4 - 3$ integrated intensity (from -20 to $+30$ km s^{-1}) image ($\theta_{\rm HPBW} = 16\farcs6$). Contours are plotted from 30 (10 σ level) to 310 K km s^{-1} in steps of 40 K km s^{-1}.

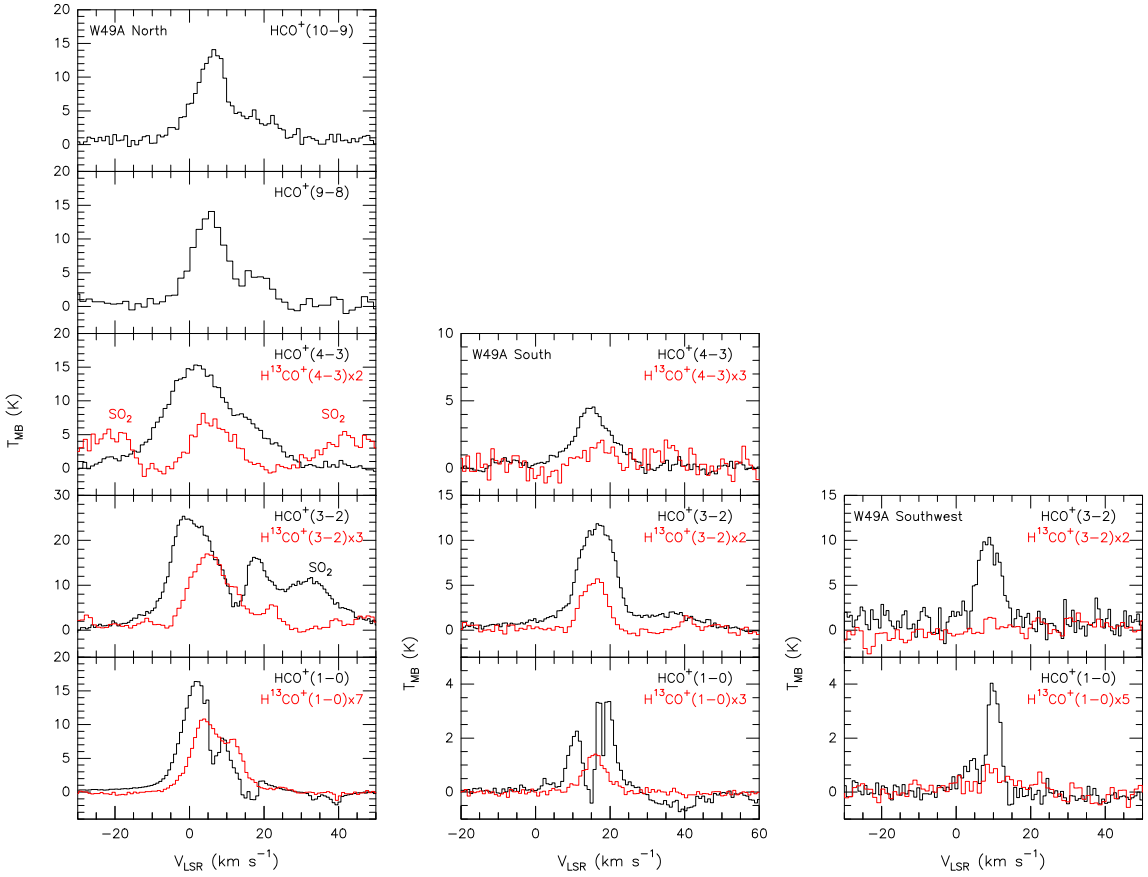

Figure 3.13 The HCO^+ spectra in W49A. Left panel shows the different transitions of the HCO^+ spectra (black) together with the$H^{13}CO^+$ spectra (red) in W49A North. Middle and right panel is the low-J HCO^+ and $H^{13}CO^+$ spectra in W49A South and Southwest, respectively. The absorption features at about 40 km s^{-1} are due to the Sagittarius Arm.

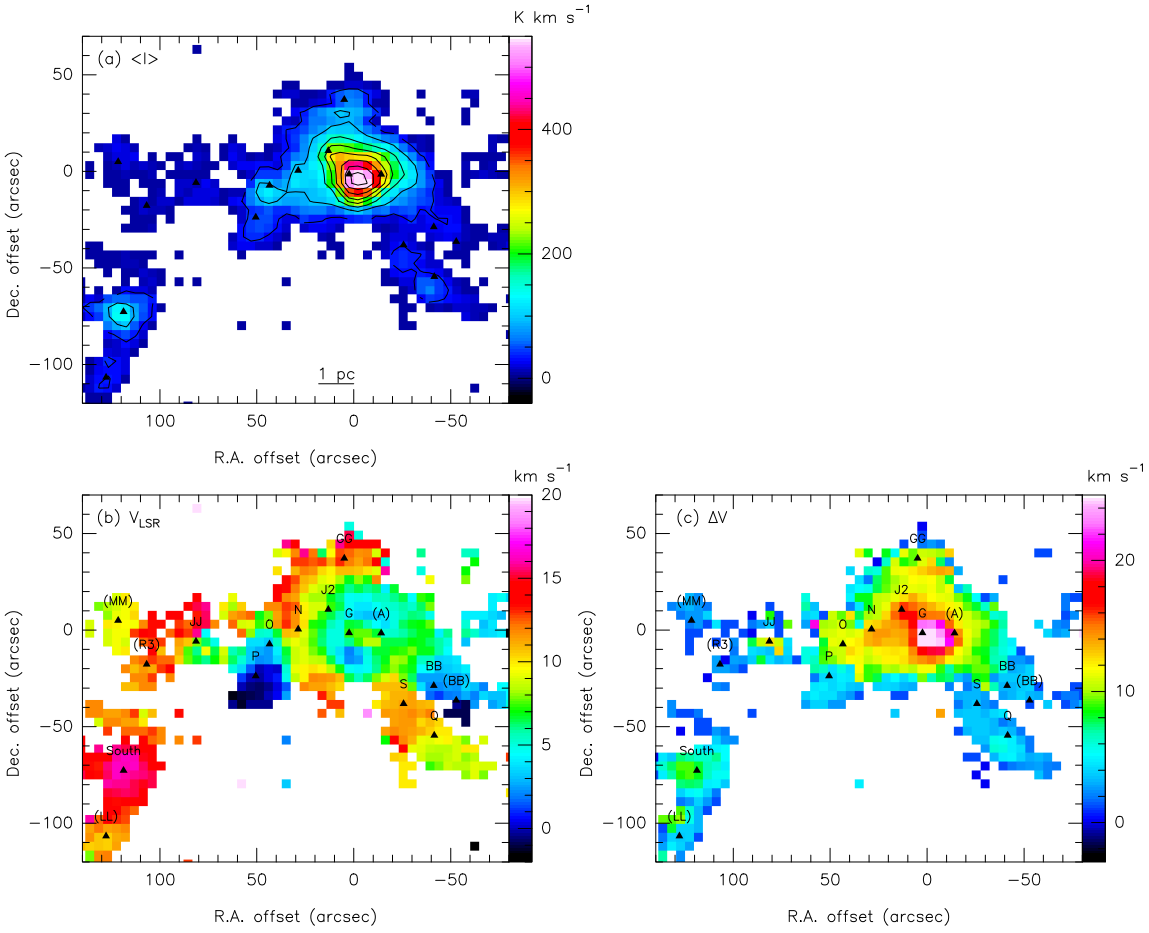

Figure 3.14 The HCO^+ $J = 3 - 2$ moment map in W49A. (a) The mean intensity map is plotted in contours running from 30 to 270 K km s^{-1} in steps of 60 K km s^{-1} and the subsequent contours running from 350 to 550 K km s^{-1} in steps of 100 K km s^{-1}. (b) The second moment of HCO^+ $J = 3 - 2$ shows the velocity distribution in W49A. (c) The third moment of HCO^+ $J = 3 - 2$ shows the line width distribution in W49A. The pixels whose temperatures are below 3 K are blanked.

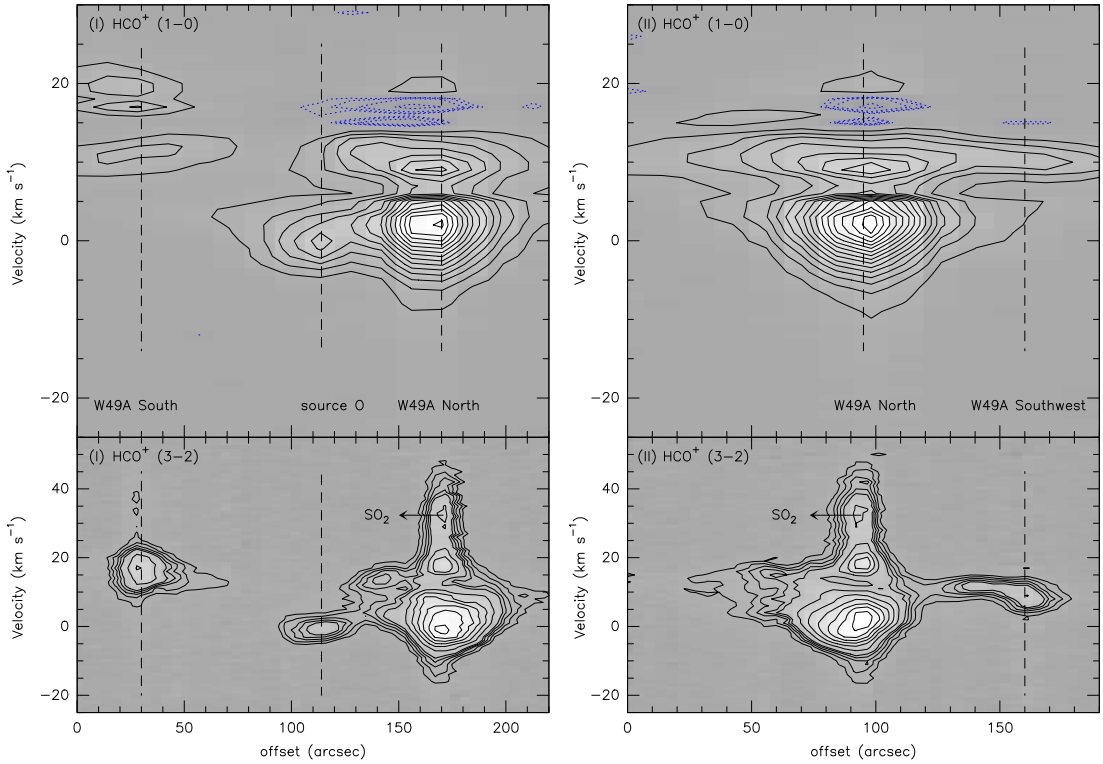

Figure 3.15 The PV diagrams of HCO^+ $J = 1 - 0$ and $J = 3 - 2$ in W49A. The positions of Cut I and II are shown in Figure 3.11. The blue dotted contours represent the absorption of -0.2 K, -0.3 K, -0.5 K, and -1.0 K, and the black contours denote the temperature running from 1 to 15 K in steps of 1 K for HCO^+ $J = 1 - 0$ in the upper panels. For the HCO^+ $J = 3 - 2$ in the lower panels, the black contours are plotted from 2 to 5 K in steps of 1 K and the subsequent contours running from 6 to 27 K in steps of 3 K.

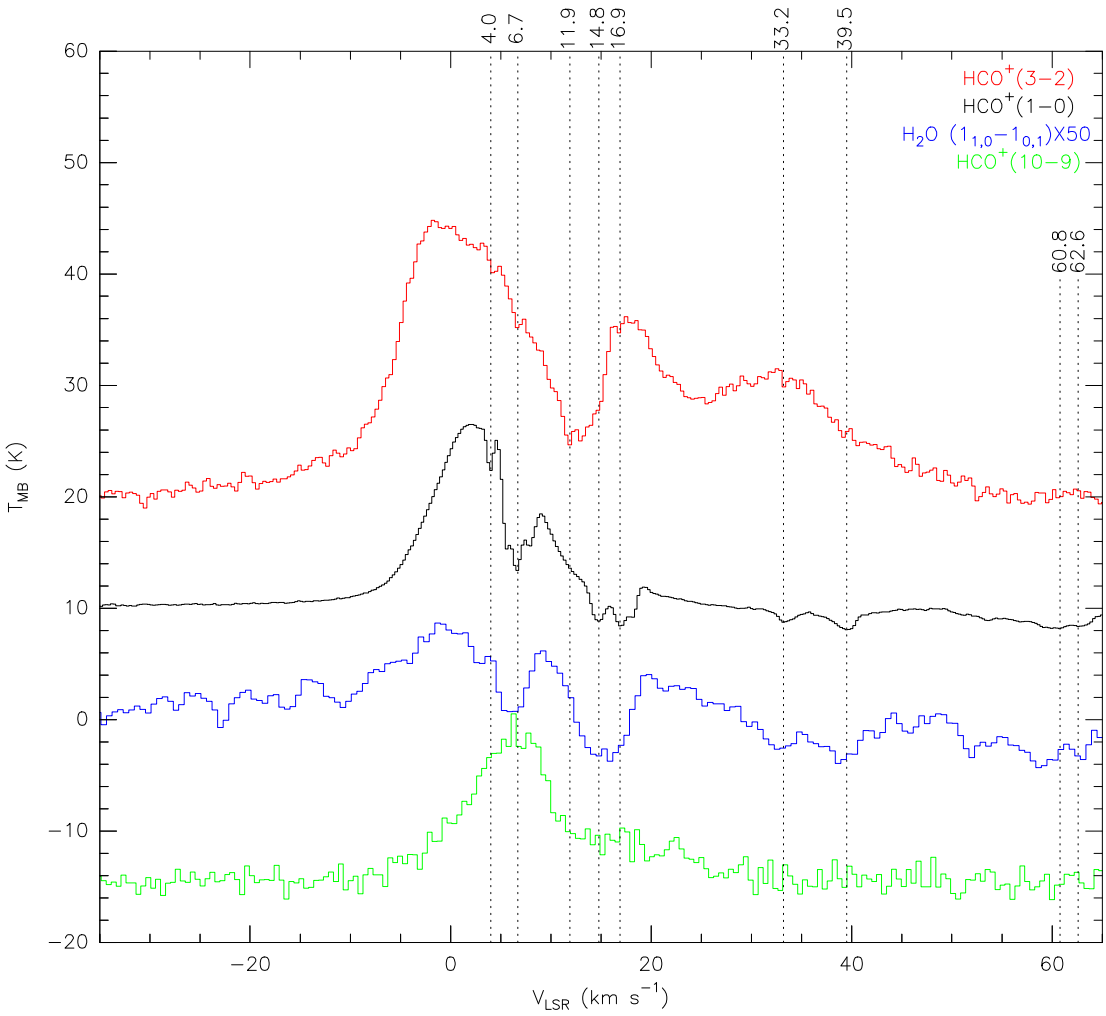

Figure 3.16 The HCO^+ and H_2O spectrum comparison in W49A North. The H_2O $1_{1,0} - 1_{0,1}$ spectrum is from the SWAS ($\theta_{\rm HPBW} = 3\farcm3 \times 2\farcm5$ at 553 GHz). For clarity, the line profiles have been shifted.

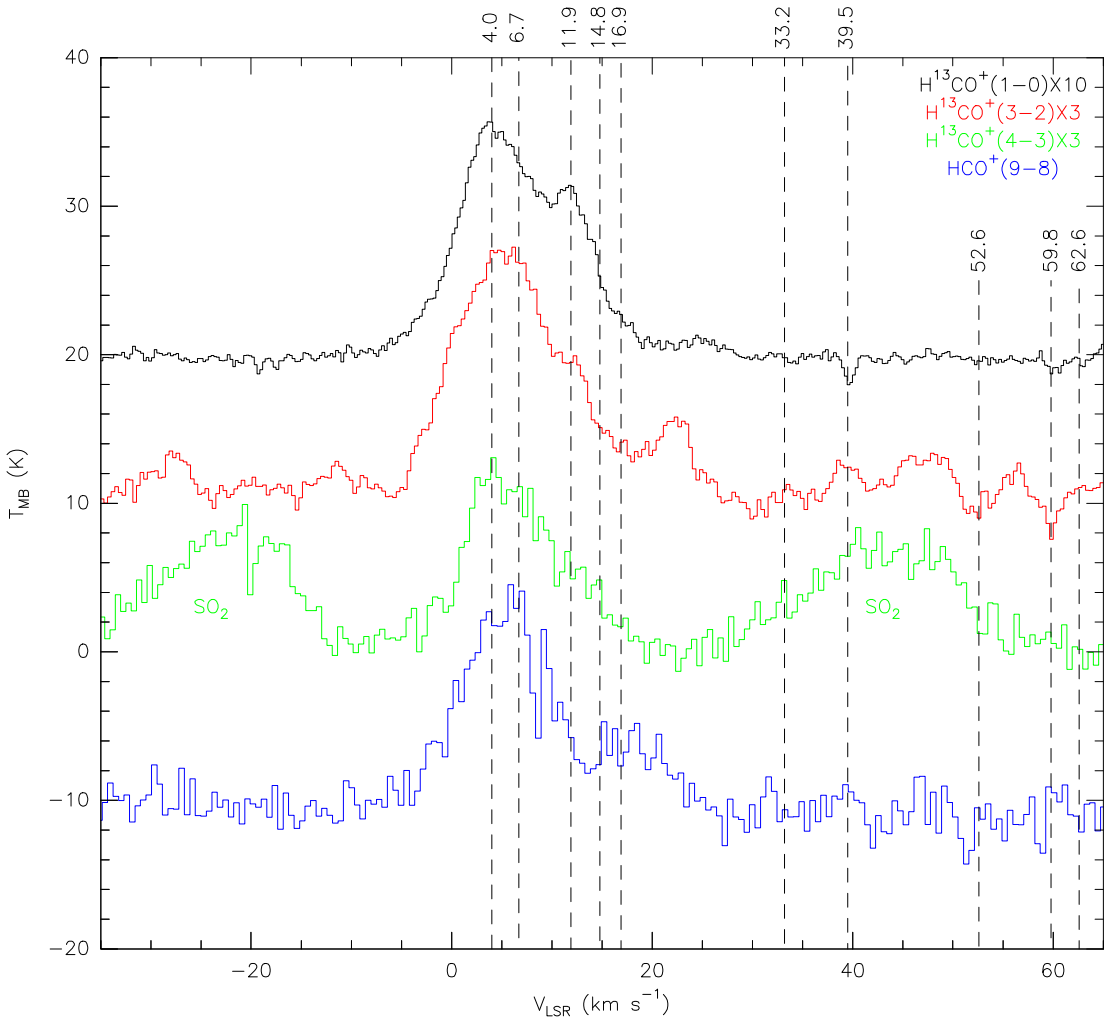

Figure 3.17 The HCO^+ and $H^{13}CO^+$ spectrum comparison in W49A North. For clarity, the line profiles have been shifted.

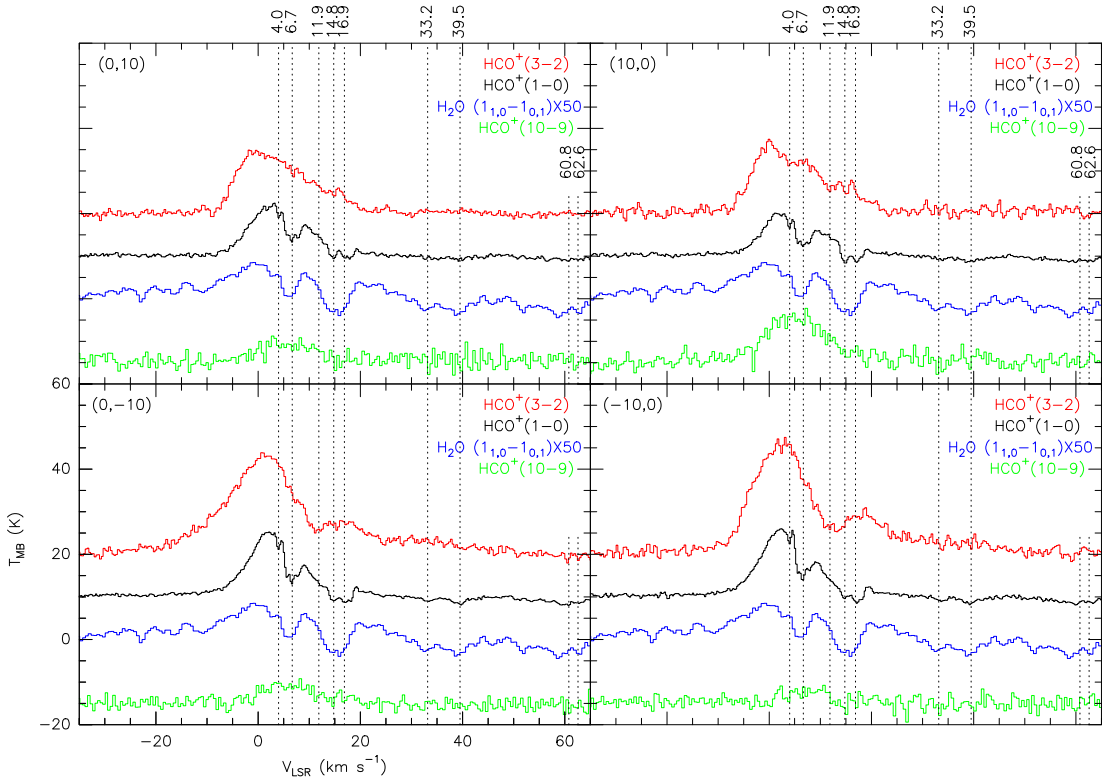

Figure 3.18 The HCO^+ and H_2O spectrum comparison in the different offsets of W49A North. The H_2O $1_{1,0}-1_{0,1}$ spectrum is from the SWAS ($\theta_{\rm HPBW} = 3'.3 \times 2'.5$ at 553 GHz). The offsets in arcsecend are denoted for each panel. For clarity, the line profiles have been shifted.

HCN

With a large dipole moment (i.e., $\mu \sim 2.98$ D), HCN is another important dense gas tracer in the ISM because of its high critical density ($n_{\rm crit} \sim 3 \times 10^6$ cm^{-3} in $J = 1 - 0$). The W49A HCN $J = 1 - 0$ and $J = 3 - 2$ images in Figure 3.19 show a clumpy gas distribution. The HCN $J = 3 - 2$ emission moment maps shown in Figure 3.20 are similar to those of HCO^+. The images of HCN $J = 4 - 3$ and $J = 8 - 7$ are shown in Figure 3.21. The HCN $J = 8 - 7$ emission is also concentrated around source G2 with a size of $\sim 17'' \times 28''$, and extends to the source K. The measurements of the HCN line width, peak temperature, and $V_{\rm LSR}$ for different transitions are summarized in Table 3.3. The comparison of the HCN isotopologic spectra toward the three main clumps is shown in Figure 3.23.

In W49A North (Fig. 3.24), the $V_{\rm LSR}$ of the HCN spectra is similar to what we have seen in the HCO^+ lines that the main ^{12}C low-J lines have diverse $V_{\rm LSR}$ ranging from 0.1 to 3.0 km s^{-1}. The H^{13}CN lines have two peaks at 6.7 km s^{-1} and ~ 12 km s^{-1}, the same as in the HCN $J = 8 - 7$ line. The 4 km s^{-1} emission component is less obvious and weaker in the HCN and H^{13}CN lines. Figure 3.23 shows the HCN and H^{13}CN spectrum comparison toward W49A North, South, and Southwest. The hyperfine lines of HCN $J = 1 - 0$ ($\Delta V = -7.1, 0, +4.8$ km s^{-1}) in W49A North are blended together because of their broad line widths. In W49A South and Southwest, the hyperfine lines are spectroscopically resolved.

One vibrationally excited HCN line ($v_2 = 1$e) has been detected toward source G at 708.8 GHz (Fig. 3.22). Since the first axis-bending state $(0, 1, 0)$ lies at ~ 1000 K above ground state (Ziurys & Turner 1986), it requires a high temperature and density to be excited collisionally. Alternatively, it can be excited by the infrared radiation at 14 μm.

Figure 3.26 shows two PV diagrams of HCN $J = 1 - 0$ and $J = 3 - 2$ in W49A. In W49A North, two components at ~ 1 km s^{-1} and ~ 18 km s^{-1} are seen in the HCN $J = 3 - 2$ emission image. Source O at ~ 0 km s^{-1} is also seen in the both transitions. There is an obvious void between the two components near W49A North, which is similar to the one seen in the HCO^+ PV diagrams (Fig. 3.26). This void is likely due to self-absorption of the 12 km s^{-1} component. As for HCN $J = 1 - 0$, two components at ~ 1 km s^{-1} and ~ 9 km s^{-1} are seen due to self-absorption at 6.7 km s^{-1}, and the absorption by extended gas in the Perseus Arm at ~ 15 km s^{-1}, respectively, which are the same as in the HCO^+ lines.

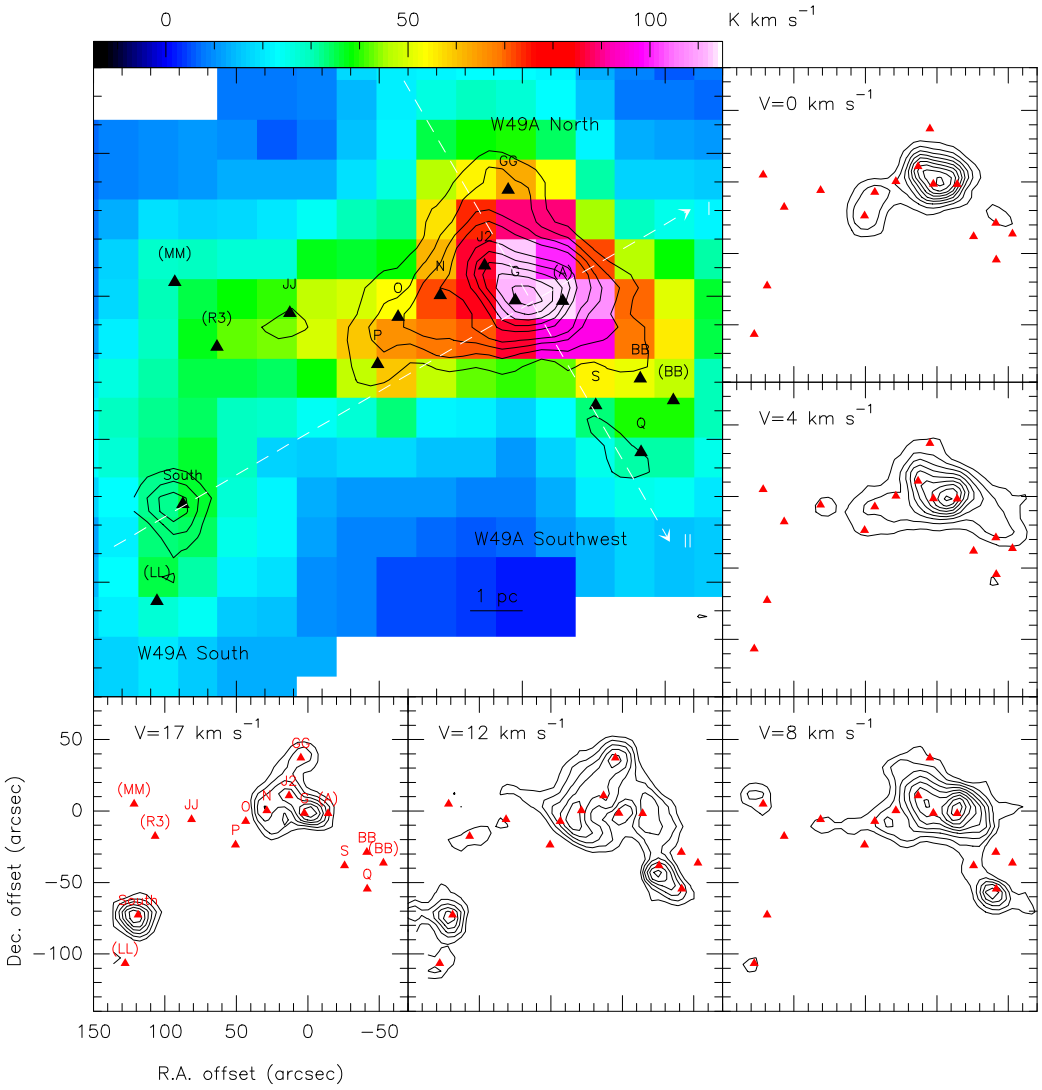

Figure 3.19 The smoothed (two Gaussian beams) HCN integrated intensity image and selected velocity channel maps of W49A. The upper-left panel is the HCN $J = 1 - 0$ image ($\theta_{\rm HPBW} = 27\farcs8$) overlaid with HCN $J = 3 - 2$ contours running from 36 to 84 K km s^{-1} in steps of 16 K km s^{-1} and the subsequent contours running from 120 to 240 K km s^{-1} in steps of 24 K km s^{-1} for clarity. One σ noise is 6 K km s^{-1} for the HCN $J = 3 - 2$ map ($\theta_{\rm HPBW} = 9\farcs3$). The rest panels are the five selected velocity channel maps of HCN $J = 3 - 2$. The first two channel maps at 0 km s^{-1} and 4 km s^{-1} are shown in contours running from 2 to 12.8 K km s^{-1} in steps of 1.2 K km s^{-1} (6 σ level). The contours denoted in the rest three velocity channel maps are from 2 to 7.4 K km s^{-1} in steps of 0.6 K km s^{-1} (3 σ level). The two white dashed lines correspond to the same HCN PV cuts and are shown in Figure 3.26.

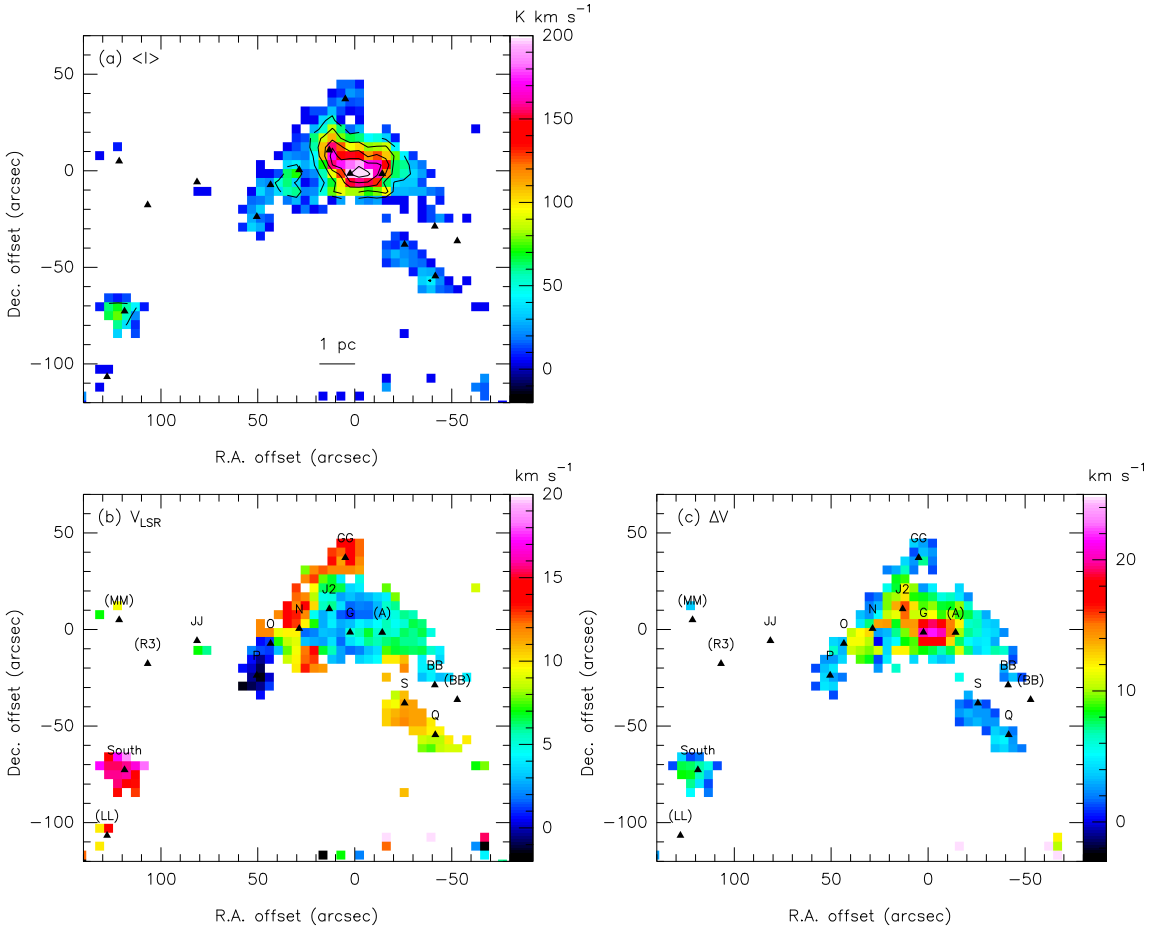

Figure 3.20 The HCN $J = 3 - 2$ moment maps in W49A. (a) The mean intensity map is plotted in contours running from 40 to 200 K km s^{-1} in steps of 40 K km s^{-1}. (b) The second moment of HCN $J = 3 - 2$ shows the velocity distribution in W49A. (c) The third moment of HCN $J = 3 - 2$ shows the line width distribution in W49A. The pixels whose temperatures are below 3.8 K are blanked.

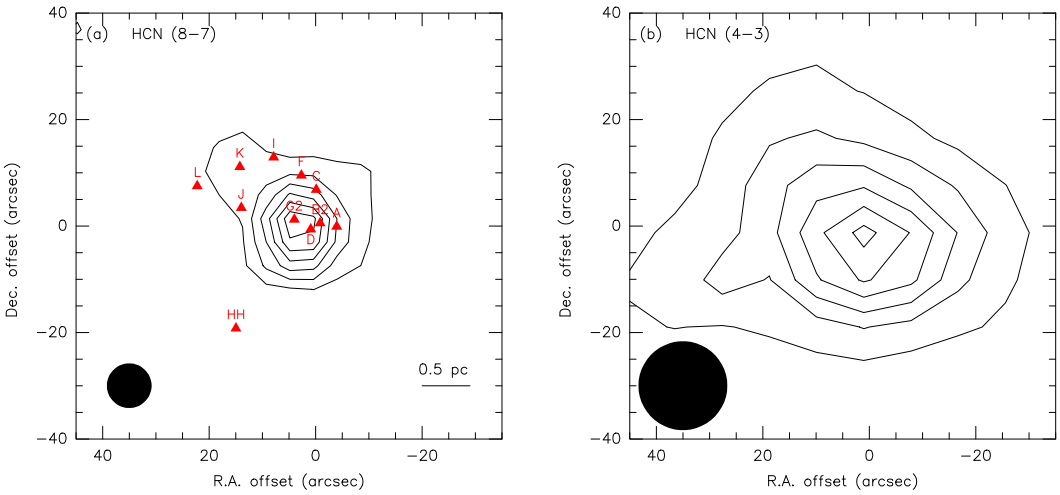

Figure 3.21 The HCN $J = 8 - 7$ and $J = 4 - 3$ images of W49A North. (a) The HCN $J = 10 - 9$ integrated intensity (from -10 to $+30$ km s^{-1}) image ($\theta_{\rm HPBW} = 8\farcs4$). Contours run from 25 to 175 K km s^{-1} in steps of 30 K km s^{-1} (6 σ level). (b) The HCN $J = 4 - 3$ integrated intensity (from -20 to $+30$ km s^{-1}) image ($\theta_{\rm HPBW} = 16\farcs7$). Contours run from 30 to 180 K km s^{-1} in steps of 30 K km s^{-1} (10 σ level).

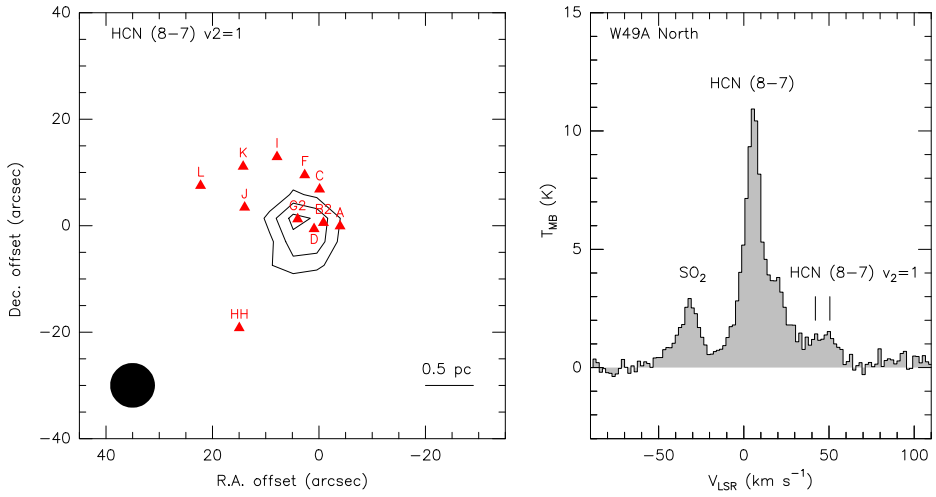

Figure 3.22 Left panel shows the HCN $J = 8 - 7$ vibrationally excited ($\nu_2 = 1$) emission in W49A North. The contours run from 4 (3 σ level) to 13 K km s^{-1} in steps of 7 K km s^{-1}. Right panel shows the HCN $J = 8 - 7$ spectrum together with the HCN vibrationally excited line $(0, 1, 0)$ $l = 1$e at ~ 4 km s^{-1} and ~ 11 km s^{-1}, and the SO_2 $20_{4,16} - 20_{1,19}$ line. The HCN vibrationally excited line at ~ 4 km s^{-1} is blended with the CH_3OH $19_{0,19} - 18_{1,17}$ E line at 708811.374 GHz (37.6 km s^{-1}).

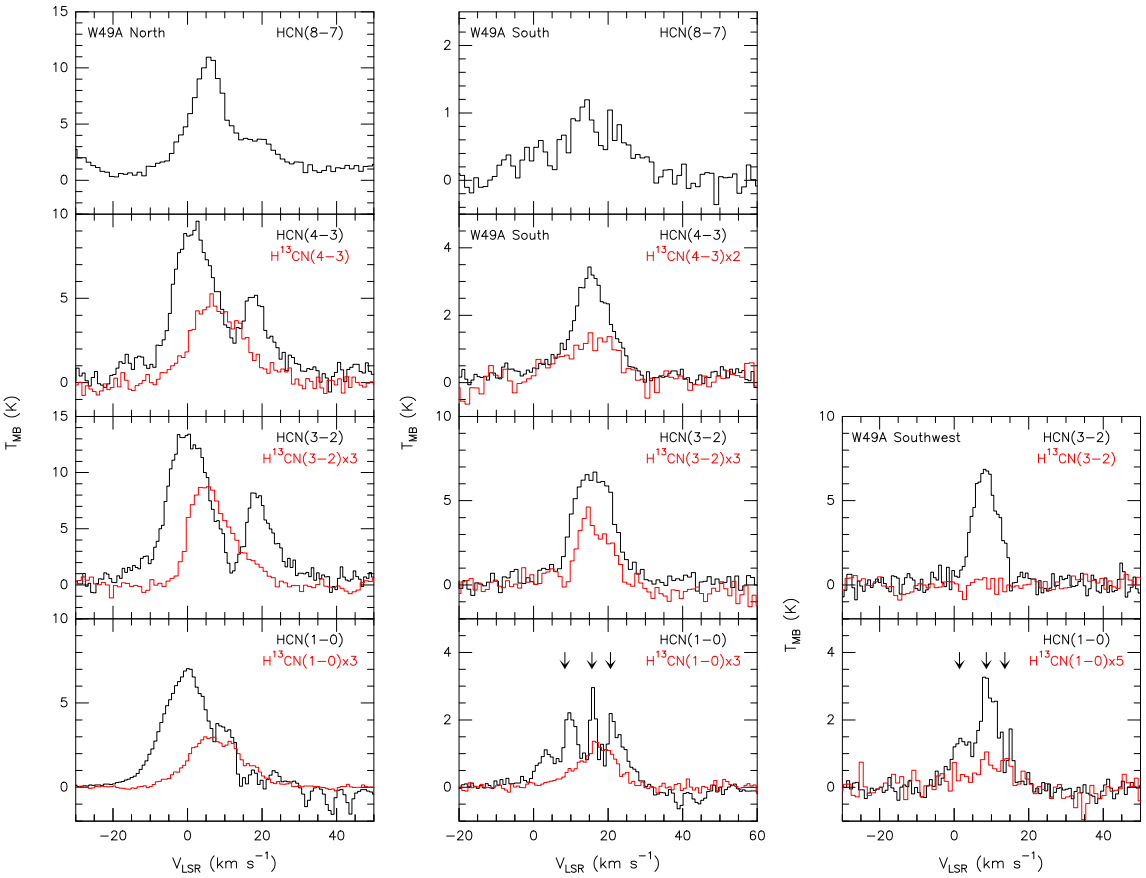

Figure 3.23 The HCN spectra in W49A. Left panel shows different transitions of the HCN spectra (black) together with the $H^{13}CN$ spectra (red) of W49A North. Middle and right panel is the HCN and $H^{13}CN$ spectra of W49A South and Southwest, respectively.

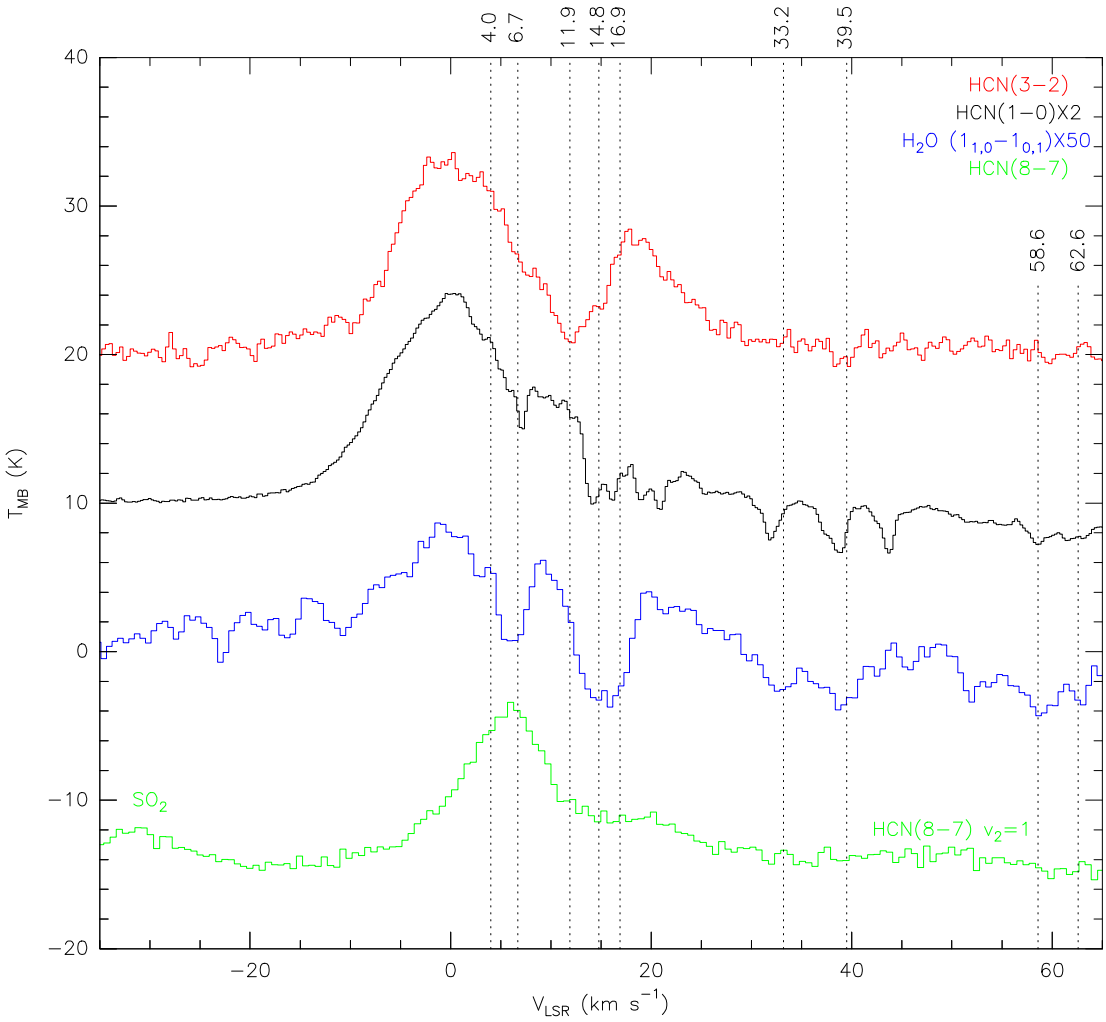

Figure 3.24 The HCN spectrum comparison in W49A North. The H_2O $1_{1,0} - 1_{0,1}$ spectrum is from the SWAS ($\theta_{\rm HPBW} = 3\farcm3 \times 2\farcm5$ at 553 GHz). The HCN hyperfine absorption features at ~ 40 km s^{-1} are due to the Sagittarius Arm. For clarity, the line profiles have been shifted.

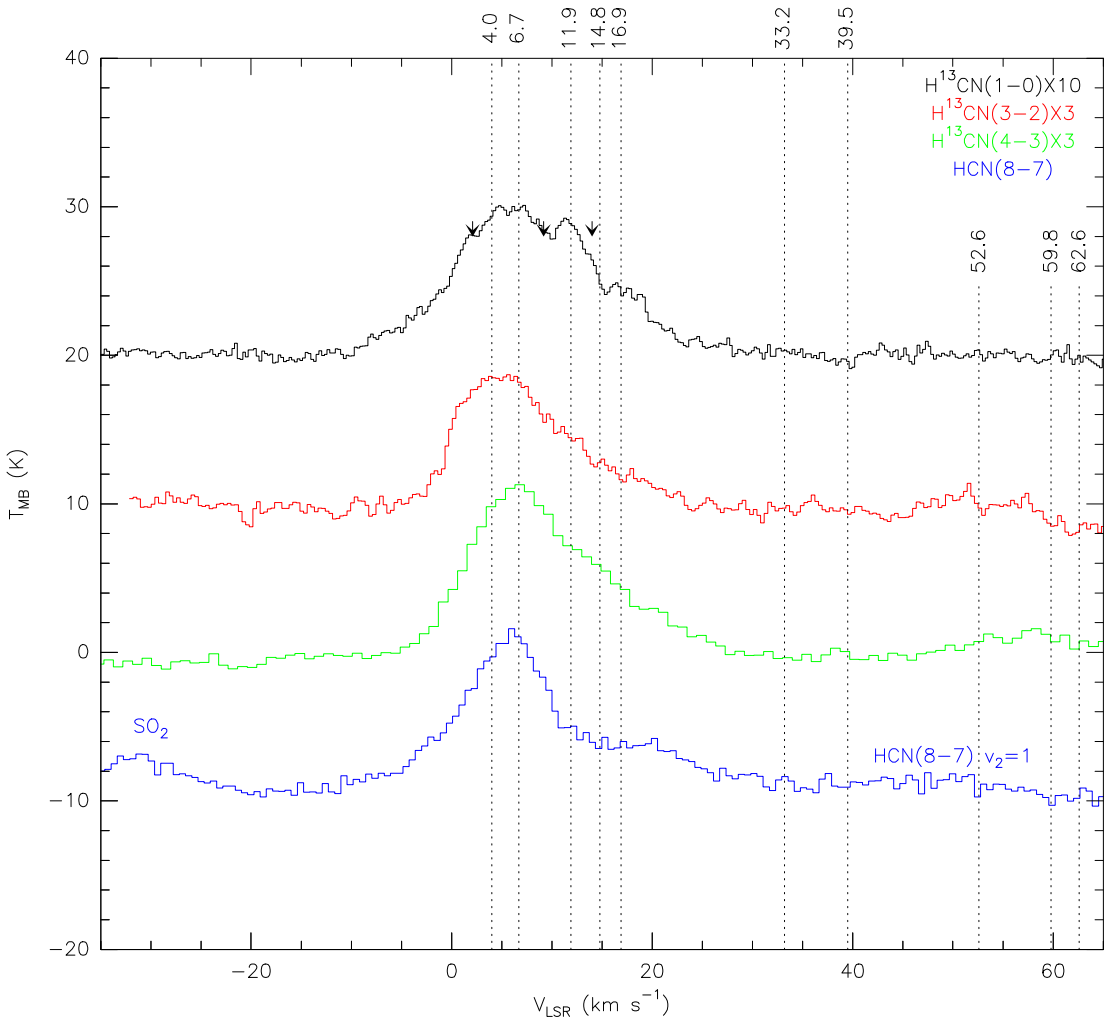

Figure 3.25 The HCN and $H^{13}CN$ spectrum comparison in W49A North. For clarity, the line profiles have been shifted.

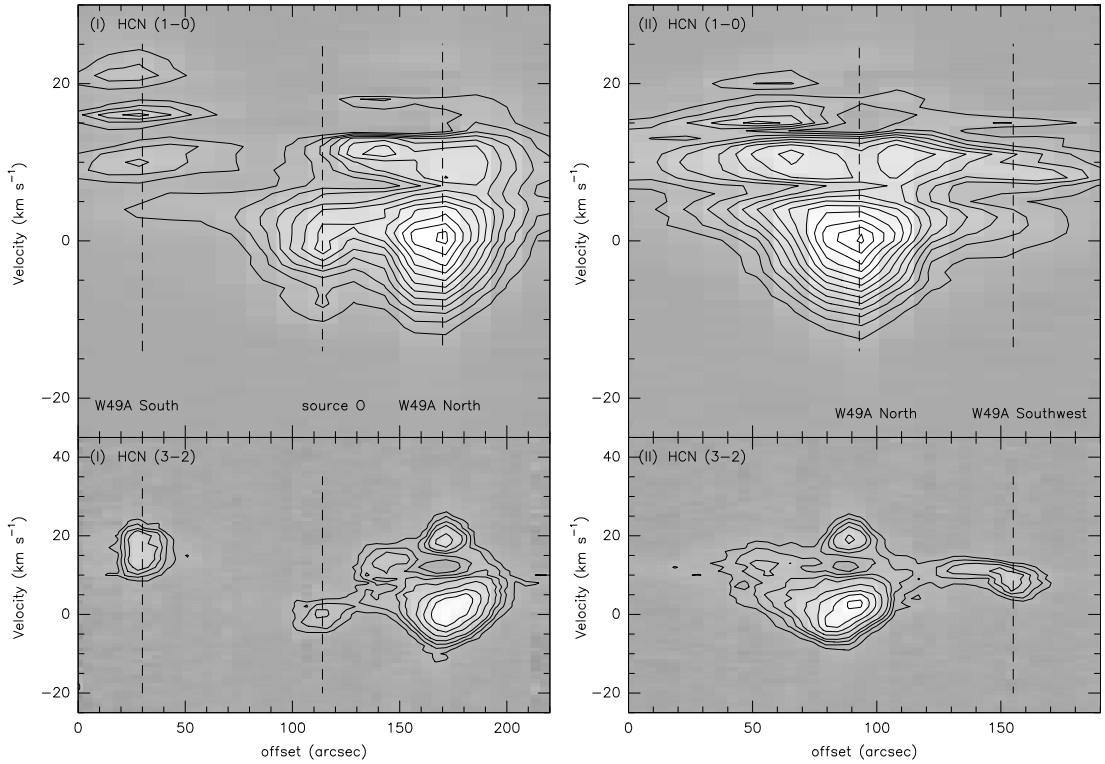

Figure 3.26 The PV diagrams of HCN $J = 1 - 0$ and $J = 3 - 2$ in W49A. The positions of Cut I and II are shown in Figure 3.19. The contours run from 1 to 7 K in steps of 0.5 K for HCN $J = 1 - 0$ in the upper panels. For the HCN $J = 3 - 2$ line in the lower panels, contours run from 2 to 5 K in steps of 1 K, and the subsequent contours run from 7 to 15 K in steps of 2 K.

Table 3.3. The HCN measurements in W49A

	W49A North			W49A South			W49A Southwest		
	$T_{\rm peak}$[a] (K)	$V_{\rm LSR}$[b] (km s^{-1})	ΔV[c] (km s^{-1})	$T_{\rm peak}$[a] (K)	$V_{\rm LSR}$[b] (km s^{-1})	ΔV[c] (km s^{-1})	$T_{\rm peak}$[a] (K)	$V_{\rm LSR}$[b] (km s^{-1})	ΔV[c] (km s^{-1})
HCN $(8-7)$	11.0±0.3	5.7	9.9	1.2±0.2	14.4	11.2	< 0.4	···	···
HCN $(4-3)$	9.3±0.4	3.0	13.0	3.4±0.3	15.0	9.2	···	···	···
$H^{13}CN$ $(4-3)$	5.3±0.5	6.5	15.3	0.7±0.2	15.3	9.5	···	···	···
HCN $(3-2)$	13.3±0.5	0.5	13.7	6.7±0.3	16.5	12.7	5.3±0.3	7.5	8.5
$H^{13}CN$ $(3-2)$	3.0±0.2	5.7	14.1	1.5±0.3	14.7	10.9	< 0.3	···	···
HCN $(1-0)$	7.0±0.1	0.1	14.3	3.0±0.1	16.0	2.4[d]	3.3±0.1	8.0	7.1
$H^{13}CN$ $(1-0)$	1.0±0.1	4.8	15.5	0.5±0.1	16.2	11.4	0.3±0.1	8.7	8.1

[a]Temperatures shown here are corrected to the mean beam temperature unit.

[b]$V_{\rm LSR}$ is measured at temperture peaks.

[c]Line widths are measured in FWHM.

[d]Only the central hyperfine line.

HNC

HNC, an isomer of HCN, has almost identical dipole moments and similar energy spectra as HCN. The high HCN/HNC abundance ratio is usually used as an indicator of a warm dense region assuming that the following key neutral-neutral reactions play the most important role (Schilke et al. 1992):

$$\mathrm{HNC} + \mathrm{O} \rightarrow \mathrm{NH} + \mathrm{CO} \tag{3.1}$$

$$\mathrm{HNC} + \mathrm{H} \rightarrow \mathrm{HCN} + \mathrm{H} \tag{3.2}$$

An activation energy of 200 K is proposed for both reactions by Schilke et al. (1992) which produce more HCN than HNC in a warm cloud. Like HCN, HNC has also hyperfine lines due to the nuclear spin of ^{14}N ($I = 1$). However, the splitting between each line is so small (< 0.2 MHz for HNC $J = 1-0$, Bechtel, Steeves, & Field 2006) that all hyperfine lines blend together in our observations. Because of its high critical densities (e.g., $n_{\rm crit} \sim 3 \times 10^6$ cm^{-3} at the $J = 1 - 0$ transition, see also Fig. 1.1), the HNC emission also originates mainly from dense gas.

The HNC emission in W49A has a similar distribution but weaker intensity compared with the HCN and HCO$^+$ emissions in the three main components. Figure 3.27 shows the HNC $J = 1-0$ and $J = 3 - 2$ integrated intensity image and the velocity channel maps where most HNC emission peaks have counterparts in UC H II regions. Noteworthily, there is a second HNC $J = 3-2$ emission peak at 0 km s^{-1} offset ($\sim 14''$) from the radio source O, which has emission peaks in HCN and HCO$^+$ $J = 3 - 2$. The HNC measurements of W49A North, South, and Southwest are summarized in Table 3.4, and the selected spectra are shown in Figure 3.29.

The $V_{\rm LSR}$ of the HNC emission peaks in W49A North ranges from ~ 3 to 5 km s^{-1}, corresponding to the 4 km s^{-1} component (Fig 3.30). The self-absorption feature at 6.7 km s^{-1} is not very clear in the HNC data. The Perseus Arm features at $\sim 15 - 17$ km s^{-1} are seen in absorption in the $J = 1 - 0$ transition, but are seen in emission in the $J = 3 - 2$ and $J = 4 - 3$ lines. The FWHM line widths range from ~ 13 km s^{-1} for HNC $J = 1 - 0$ to ~ 8 km s^{-1} for HNC $J = 4-3$, which show a different trend than HCN and HCO$^+$ that the HCN and HCO$^+$ lines have narrower line widths in the $J = 1 - 0$ transition due to absorption. The HN^{13}C $J = 1 - 0$ line shown in Figure 3.30 has two velocity components at 4 km s^{-1} and 12 km s^{-1}, the same as in ^{13}CO and C^{18}O $J = 2 - 1$. Peculiarly, the HN^{13}C $J = 3 - 2$ and $J = 4 - 3$ transitions also show two-component line profiles, but both are redshifted ~ 3 km s^{-1} with a same velocity difference (~ 6.5 km s^{-1}) between the two peaks. Since the HN^{13}C $J = 3-2$ and $J = 4-3$ lines are observed by two different telescopes, this shift is unlikely due to a technical problem, but probably because of the low signal-to-noise ratios in the $J = 3 - 2$ and $J = 4 - 3$ transitions.

In W49A South (Fig. 3.29), the average $V_{\rm LSR}$ of the HNC lines is ~ 16 km s^{-1}, and the HNC $J = 3 - 2$ line has an asymmetric line profile, which is as strong as the line of W49A North. In the HNC $J = 1 - 0$ transition, absorption is also seen toward W49A South due to the Perseus Arm. In the less dense W49A Southwest, the HNC $J = 1 - 0$ line also shows a weak self-absorption

feature, similar to the HCN and HCO^+ $J = 1 - 0$ lines. The measurements of the HNC line width, peak termperature, and $V_{\rm LSR}$ for different transitions are summarized in Table 3.4.

The PV diagrams of HNC $J = 1 - 0$ and $J = 3 - 2$ (Fig. 3.32) reveal a similar distribution as HCN and HCO^+. In HNC $J = 1 - 0$, the Perseus Arm absorptions are clearly seen in W49A North and South.

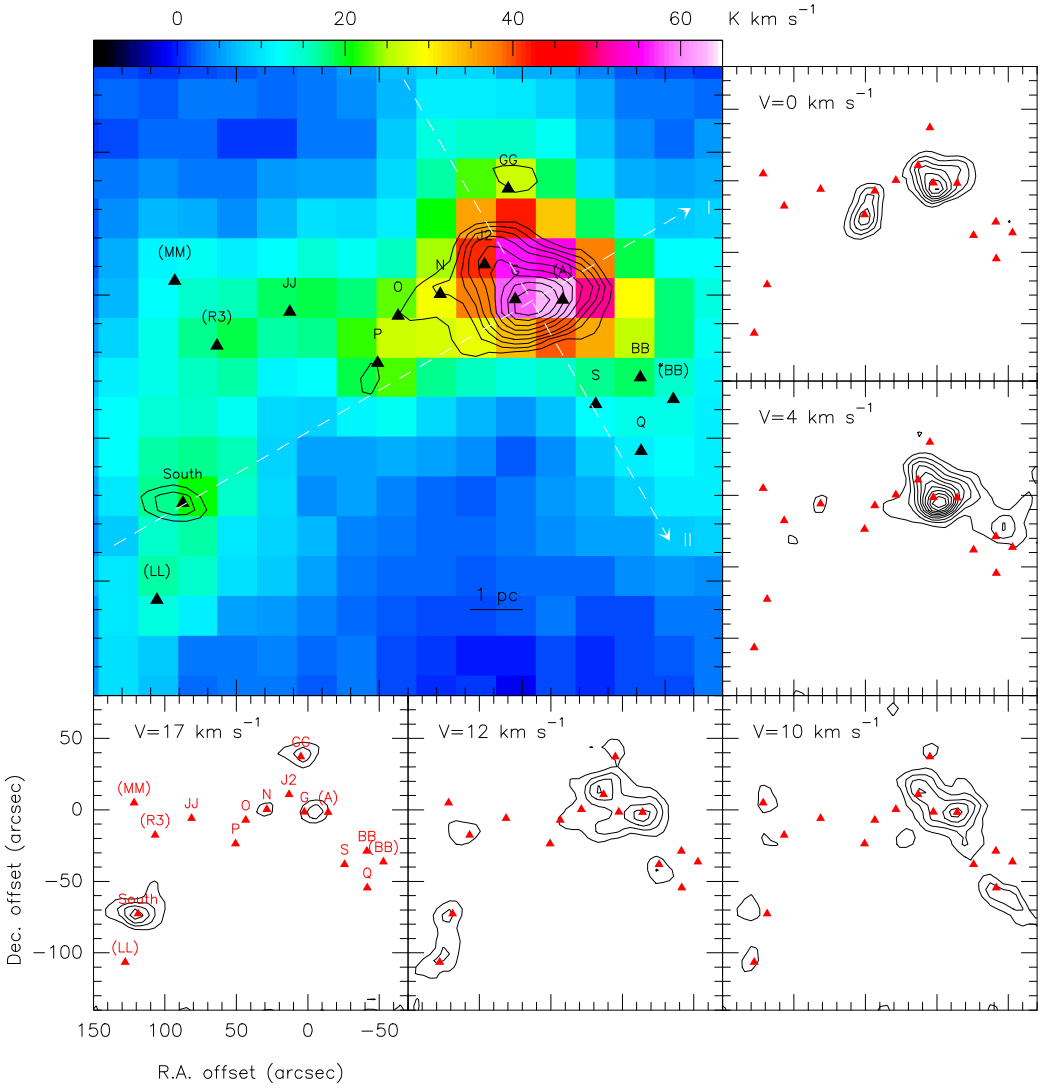

Figure 3.27 The smoothed (two Gaussian beams) HNC integrated intensity image and selected velocity channel maps of W49A. The upper-left panel is the HNC $J = 1 - 0$ image ($\theta_{\rm HPBW} = 27\farcs1$) overlaid with the HNC $J = 3 - 2$ contours running from 19 to 29 K km s^{-1} in steps of 5 K km s^{-1} and the subsequent contours running from 35 to 85 K km s^{-1} in steps of 10 K km s^{-1} for clarity. One σ noise is 3 K km s^{-1} in the HNC $J = 3 - 2$ map ($\theta_{\rm HPBW} = 9\farcs0$). The rest panels are the five selected velocity channel maps of HNC $J = 3 - 2$ shown in contours running from 1 to 6.4 K in steps of 0.6 K (3 σ level). The two white dashed lines correspond to the same HCO$^+$ PV cuts and are shown in Figure 3.32.

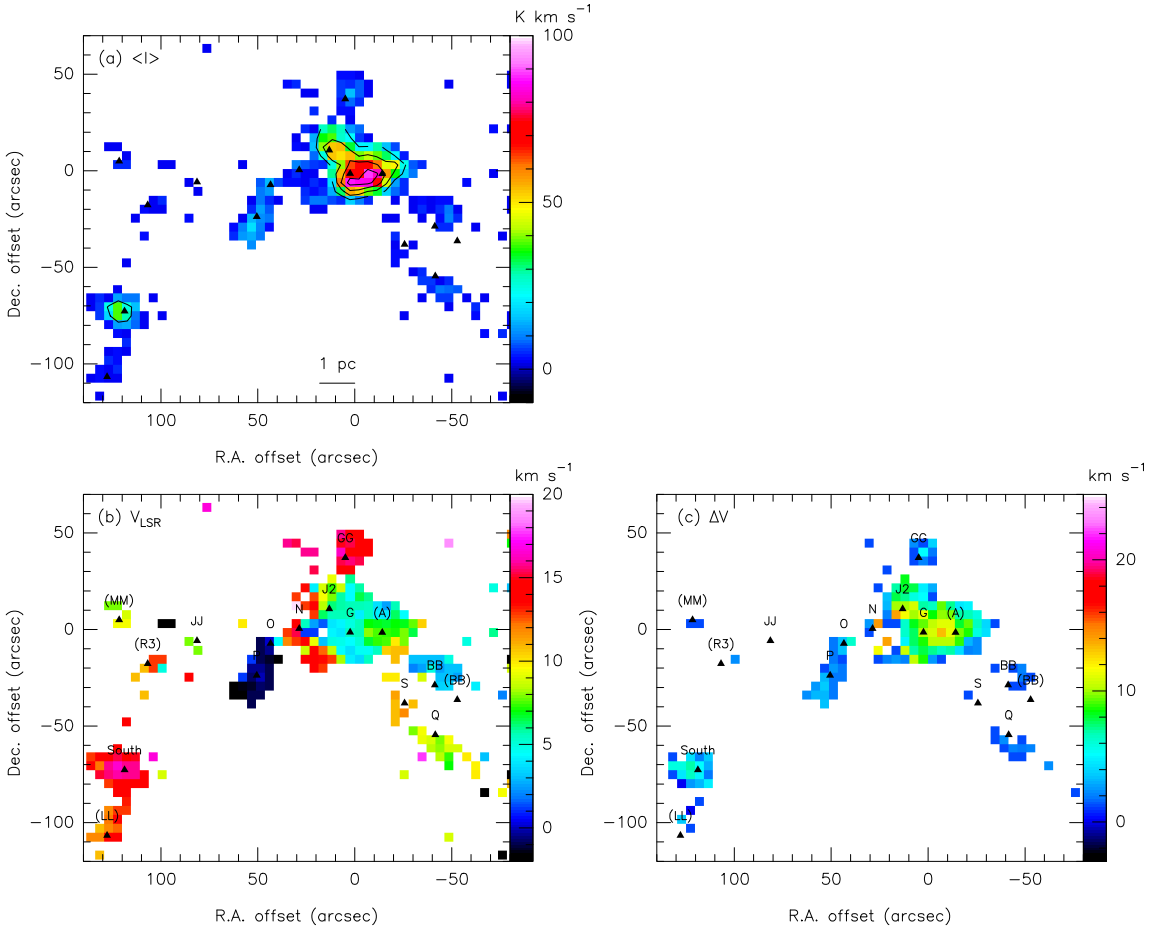

Figure 3.28 The HNC $J = 3 - 2$ moment maps in W49A. (a) The mean intensity map is plotted in contours running from 20 to 200 K km s^{-1} in steps of 20 K km s^{-1}. (b) The second moment of HNC $J = 3 - 2$ shows the velocity distribution in W49A. (c) The third moment of HNC $J = 3 - 2$ shows the line width distribution in W49A. The pixels whose temperatures are below 2 K are blanked.

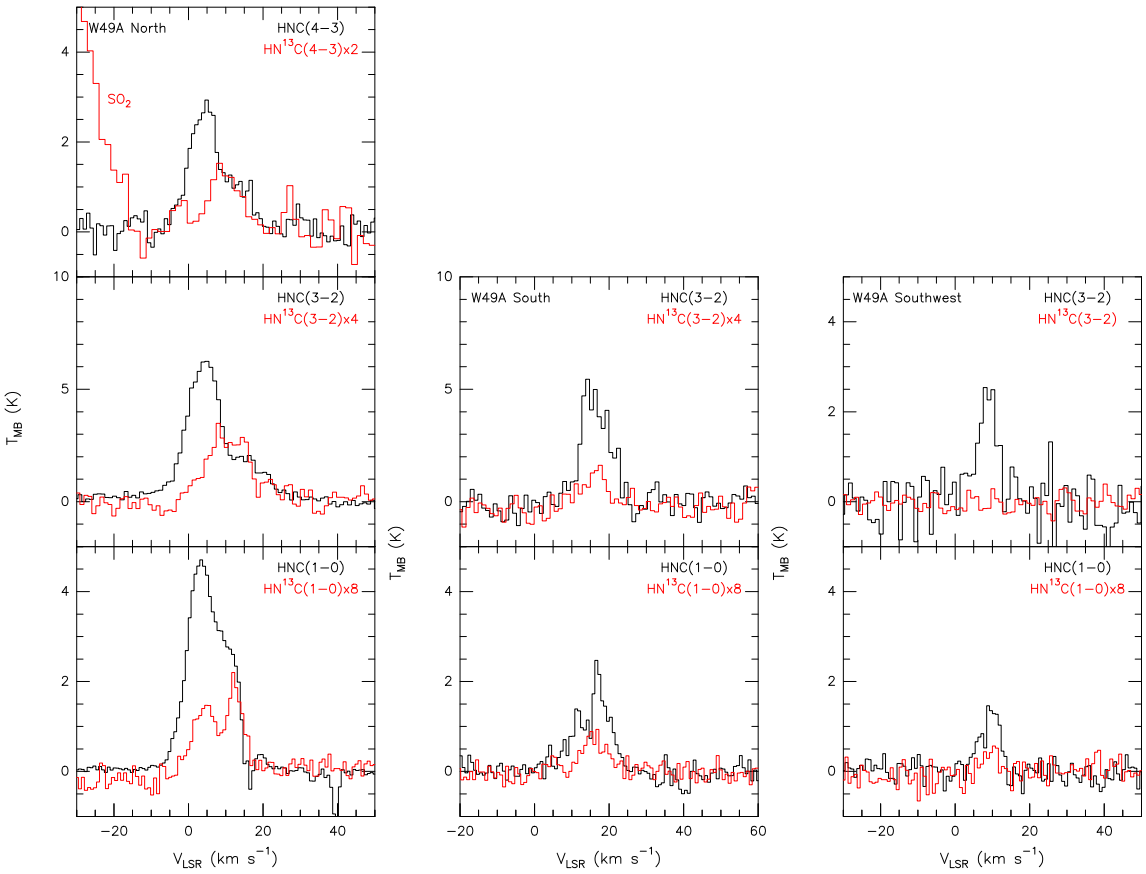

Figure 3.29 The HNC spectra in W49A. Left panel shows different transitions of the HNC spectra (black) together with the $HN^{13}C$ spectra (red) in W49A North. Middle and right panel is the low-J HNC and $HN^{13}C$ spectra of W49A South and Southwest, respectively.

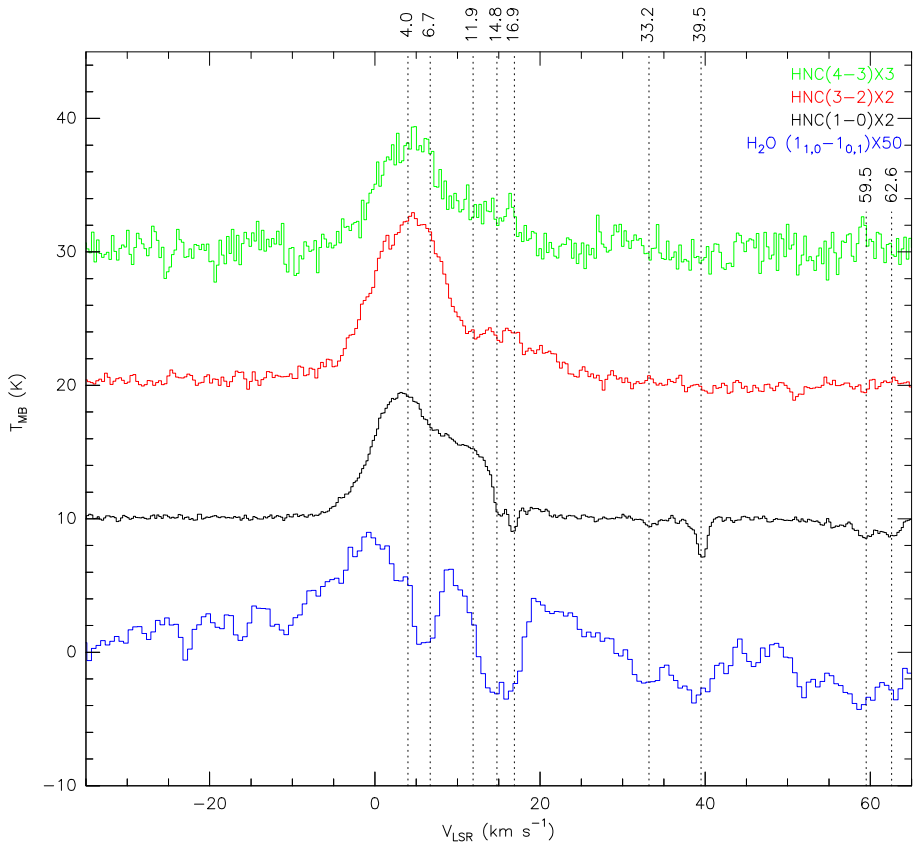

Figure 3.30 The HNC spectrum comparison in W49A North. The H_2O $1_{1,0} - 1_{0,1}$ spectrum is from the SWAS ($\theta_{\rm HPBW} = 3\farcm3 \times 2\farcm5$ at 553 GHz). For clarity, the line profiles have been shifted.

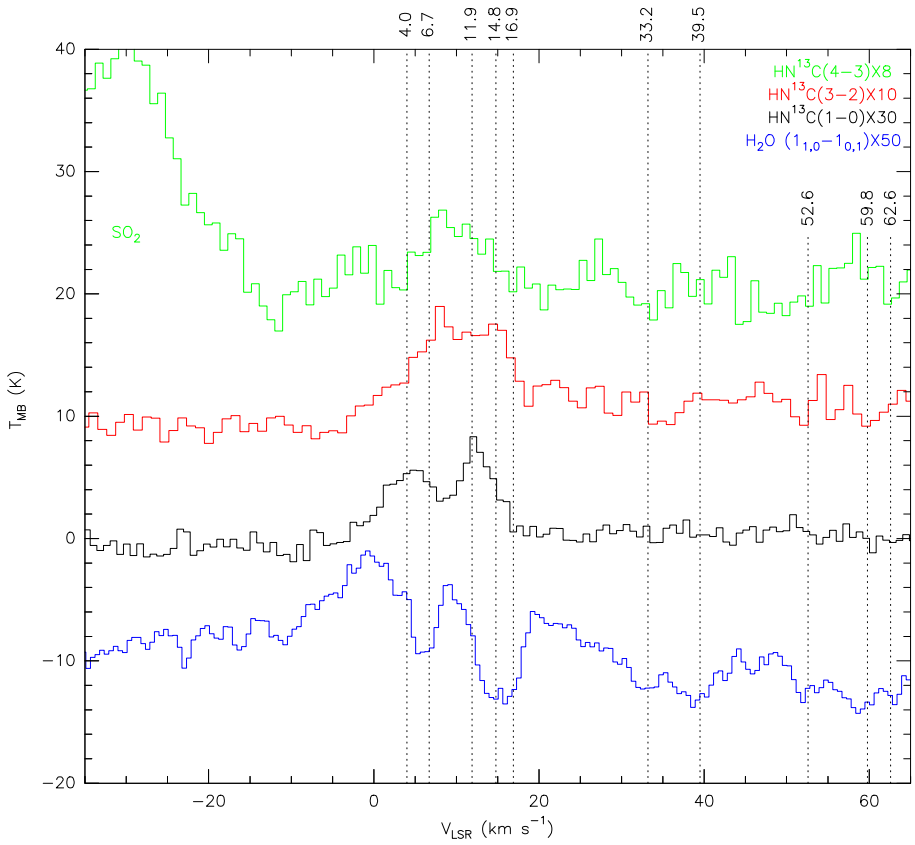

Figure 3.31 The $HN^{13}C$ spectrum comparison in W49A. The H_2O $1_{1,0} - 1_{0,1}$ spectrum is from the SWAS ($\theta_{\rm HPBW} = 3\farcm3 \times 2\farcm5$ at 553 GHz). For clarity, the line profiles have been shifted.

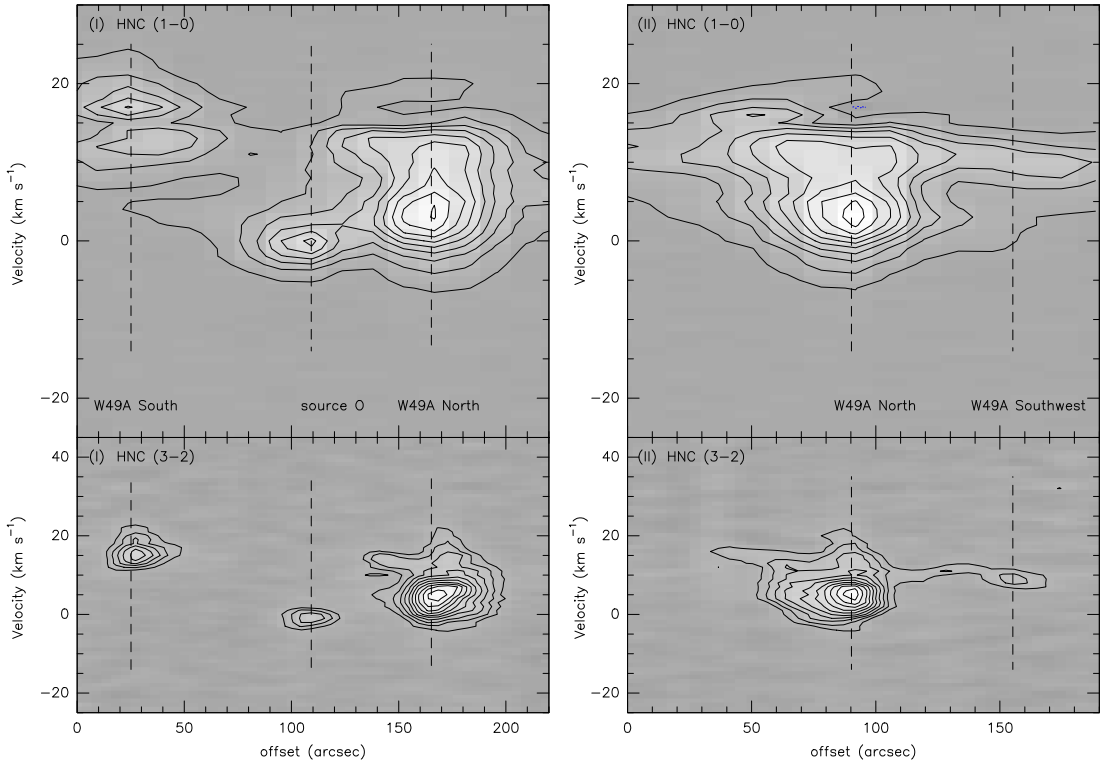

Figure 3.32 The PV diagrams of HNC $J = 1 - 0$ and $J = 3 - 2$ in W49A. The positions of Cut I and II are shown in Figure 3.27. The contours run from 0.2 to 4.2 K in steps of 0.5 K for HNC $J = 1 - 0$ in the upper panels. For the HNC $J = 3 - 2$ line in the lower panels, the contours run from 1 to 7 K in steps of 0.6 K.

Table 3.4. The HNC measurements in W49A

	W49A North			W49A South			W49A Southwest		
	$T_{\rm peak}$[a] (K)	$V_{\rm LSR}$[b] (km s^{-1})	ΔV[c] (km s^{-1})	$T_{\rm peak}$[a] (K)	$V_{\rm LSR}$[b] (km s^{-1})	ΔV[c] (km s^{-1})	$T_{\rm peak}$[a] (K)	$V_{\rm LSR}$[b] (km s^{-1})	ΔV[c] (km s^{-1})
HNC $(4-3)$	2.9±0.2	4.9	8.2	< 0.4	···	···	···	···	···
HN^{13}C $(4-3)$	0.8±0.2	8.3	9.5	< 0.4	···	···	···	···	···
HNC $(3-2)$	6.2±0.2	5.0	11.4	5.4±0.4	14.3	7.2	2.5±0.5	8.1	6.2
HN^{13}C $(3-2)$	0.9±0.1	8.0	11.8	< 0.4[d]	17.7	4.3	< 0.2	···	···
HNC $(1-0)$	4.70±0.05	3.4	13.2	2.47±0.17	16.6	8.5	1.46±0.22	8.9	6.2
HN^{13}C $(1-0)$	0.28±0.03	12.0	13.7	0.12±0.03	16.9	3.2	< 0.07[d]	···	···

[a]Temperatures shown here are corrected to the mean beam temperature unit.

[b]$V_{\rm LSR}$ is measured at temperture peaks.

[c]Line widths are measured in FWHM.

[d]2 σ detection.

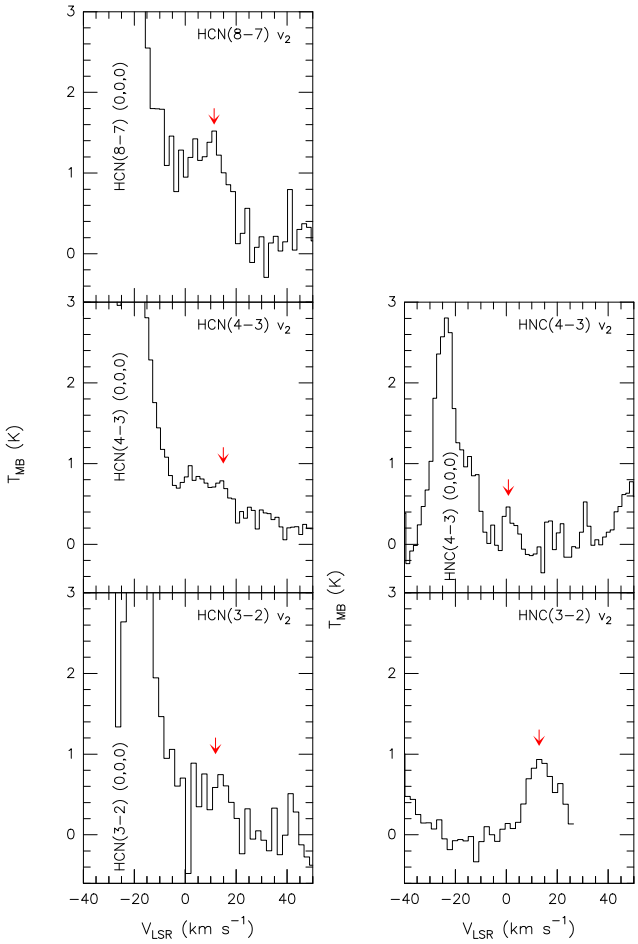

Figure 3.33 The vibrationally excited HCN and HNC spectra ($v_2 = 1e$) in W49A North. Most of the vibrationally excited lines are close to the ground vibrational lines which are indicated in the figures. The cut in the HNC $J = 3 - 2$ spectra is due to the band edge.

Table 3.5. The vibrationally excited HCN and HNC detections in W49A

Line	Frequency (MHz)	$T_{\rm MB}$ (K)	$v_{\rm LSR}$ (km s^{-1})	$\int T_{\rm MB} dV$ (K km s^{-1})	$\frac{T_{\rm MB}(0,0,0)}{T_{\rm MB}(0,1,0)}$ [a]
HCN $(8-7)$ $v_2 = 1e$	708785.86	1.5±0.2[b]	11.3	22.1±2.9	7.33±1.00
HCN $(4-3)$ $v_2 = 1e$	354460.43	0.8±0.2[b]	14.9	14.8±3.7	11.63±2.95
HNC $(4-3)$ $v_2 = 1e$	362595.91	0.5±0.2[c]	0.8	1.9±0.8	5.80±2.35
HCN $(3-2)$ $v_2 = 1e$	265852.71	0.8±0.2[b]	11.9	8.8±2.2	14.13±3.59
HNC $(3-2)$ $v_2 = 1e$	271924.16	0.9±0.1	12.9	10.8±1.2	6.89±0.80

[a]The main beam temperature ratios between the ground vibrational state lines and vibrationally excited lines.

[b]Blended line

[c]2σ detection

SiO

SiO is much more abundant in the shock/outflow or high temperature regions than in quiescent clouds where most SiO is depleted on dust grains. Therefore, SiO is usually used as a shock/outflow tracer in the ISM, and its emission is often associated with molecular outflows from young stellar objects (see e.g., Bachiller et al. 2001; van der Tak 2005). Four ground vibrational transitions of SiO have been observed toward W49A. The SiO emission is concentrated mostly on W49A North, and has a very compact emission distribution (Fig. 3.34). The morphology of the SiO emission is very different from the clumpy and extended HCN and HCO^+ emission. The FWHM size of the SiO emission is estimated to be $\sim 41'' \times 38''$, $\sim 21'' \times 20''$, $\sim 15'' \times 16''$, and $\sim 23'' \times 24''$, for the $J = 2-1$, $J = 5-4$, $J = 6-5$, and $J = 8-7$ transition, respectively. In addition, the PV diagrams of the SiO emission do not show any structure.

The SiO spectra in W49A North (Fig. 3.35) share a similar line width of $\sim 12 - 16$ km s^{-1}. The $V_{\rm LSR}$ of SiO lines is ~ 6 km s^{-1}, similar to the ^{13}C isotopologic lines of HCN, HCO^+, and HNC, except for the SiO $J = 8 - 7$ line (~ 9 km s^{-1}) which is probably due to the noise in the peak temperature measurement. Therefore, the SiO emission is likely associated with the 4 km s^{-1} clump in W49A North. In W49A South, the SiO emission is relatively weak and has $V_{\rm LSR}$ of ~ 16 km s^{-1} and line widths of $\sim 10 - 14$ km s^{-1}. The SiO measurements in W49A are summarized in Table 3.6.

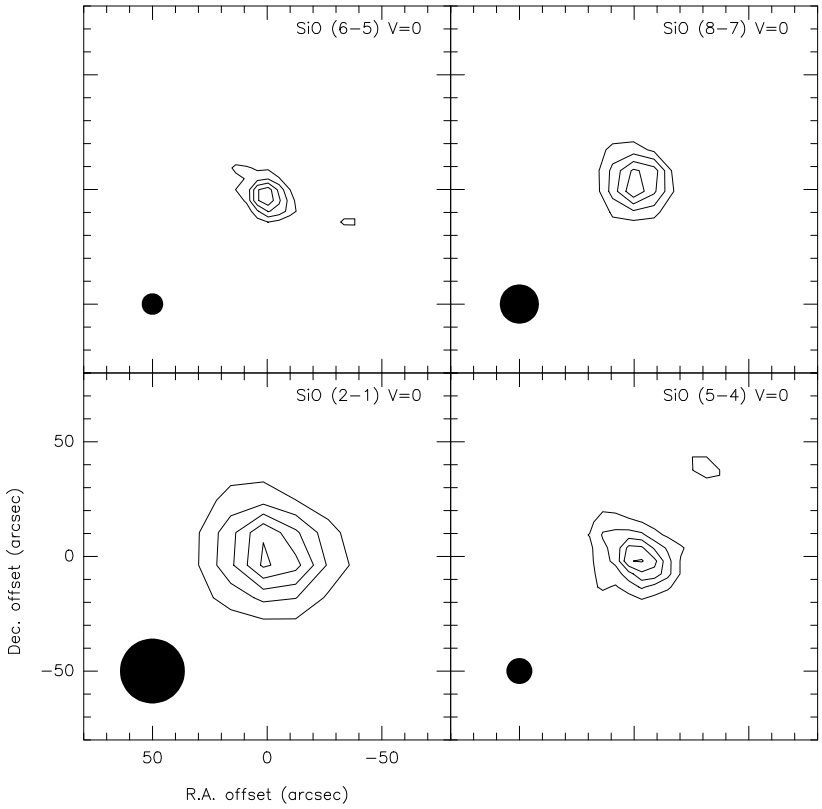

Figure 3.34 The W49A North images of four SiO transitions in the ground vibrational state integrated from -20 to $+30$ km s^{-1}. The SiO $J = 8 - 7$ integrated intensity map is shown in contours running from 15 to 45 K km s^{-1} in steps of 10 K km s^{-1}. The SiO $J = 6 - 5$ integrated intensity map is shown in contours running from 40 to 130 K km s^{-1} in steps of 30 K km s^{-1}. The SiO $J = 5 - 4$ integrated intensity map is shown in countours running from 20 to 140 K km s^{-1} in steps of 30 K km s^{-1}. The SiO $J = 5 - 4$ integrated intensity map is shown in contours running from 8 to 40 K km s^{-1} in steps of 8 K km s^{-1}. The beam sizes are shown in the bottom-left corner of each map.

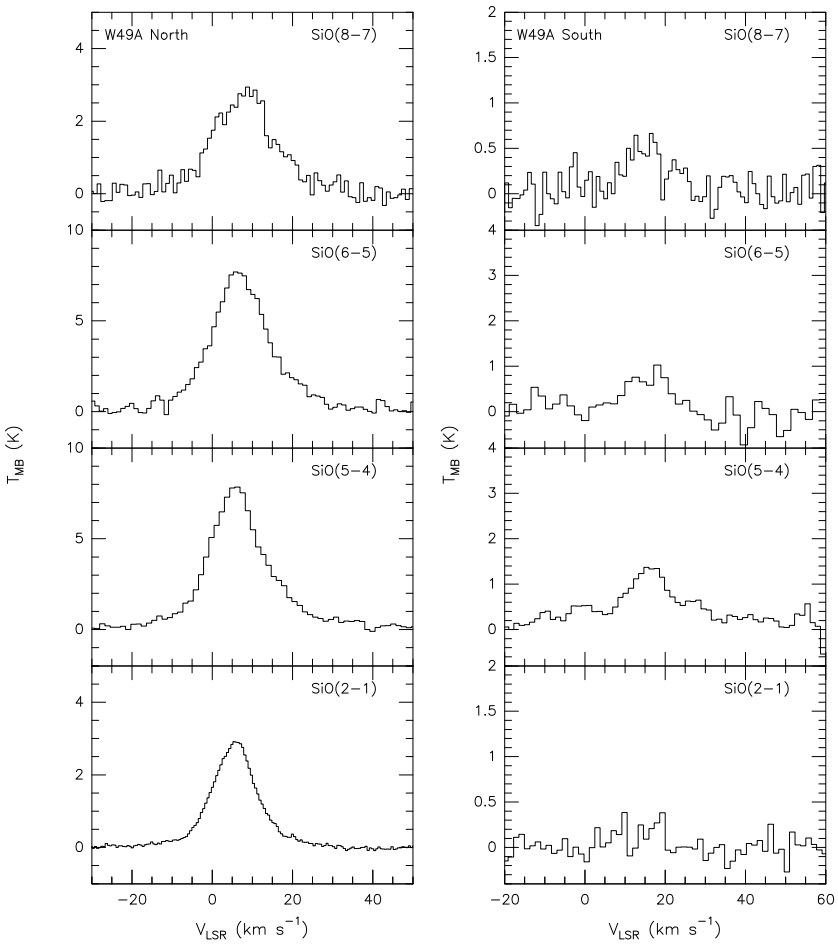

Figure 3.35 The spectra of the four SiO transitions in ground vibrational state in W49A North and South.

Table 3.6. The SiO measurements in W49A

	W49A North			W49A South			W49A Southwest		
	$T_{\rm peak}$[a] (K)	$V_{\rm LSR}$ (km s^{-1})	ΔV[b] (km s^{-1})	$T_{\rm peak}$[a] (K)	$V_{\rm LSR}$ (km s^{-1})	ΔV[b] (km s^{-1})	$T_{\rm peak}$[a] (K)	$V_{\rm LSR}$ (km s^{-1})	ΔV[b] (km s^{-1})
SiO $(8-7)$	2.9±0.2	8.8	14.8	0.6±0.2[c]	16.7	10.2	···	···	···
SiO $(6-5)$	7.7±0.3	5.8	15.1	1.0±0.3[c]	18.0	12.9	···	···	···
SiO $(5-4)$	7.8±0.1	6.3	15.5	1.4±0.2	15.8	14.1	< 0.2	···	···
SiO $(2-1)$	2.9±0.1	5.4	12.1	0.4±0.1[c]	14.0	13.4	0.2±0.1	11.4	···

[a]All transitions are in the ground vibrational state, and temperatures shown here are corrected to the mean beam temperature unit.

[b]Line widths are measured in FWHM.

[c]3σ detection

H_2S

The W49A image of the H_2S $1_{1,0} - 1_{0,1}$ emission shows a very similar distribution to the emission from the dense gas tracers such as HCO^+, HCN, and HNC. All three main components of W49A are seen in the H_2S image (Fig 3.36), and most of the clumps can be identified with UC H II regions. The H_2S $3_{1,2} - 3_{0,3}$ image of W49A North is shown in Figure 3.37, where the H_2S $3_{1,2} - 3_{0,3}$ emission is concentrated on source G2 with a FWHM size of $\sim 14'' \times 13''$, and extends to source K. This distribution is similar to the HCN $J = 8 - 7$ and HCO^+ $J = 10 - 9$ images. The measurements of H_2S are summarized in Table 3.7.

In W49A North (Fig. 3.39), the $V_{\rm LSR}$ of the H_2S $1_{1,0} - 1_{0,1}$ emission peak is 0.6 km s^{-1}, but another peak at ~ 4 km s^{-1} is also seen. The feature at ~ 16 km s^{-1} is due to the Perseus Arm absorption, and the Sagittarius Arm absorption features are also seen at ~ 40 km s^{-1} and ~ 60 km s^{-1} (Fig. 3.40). In the H_2S $3_{1,2} - 3_{0,3}$ line, three emission peaks appear at ~ 6 km s^{-1}, 10 km s^{-1}, and 12 km s^{-1}. The FWHM line widths for both transitions in W49A North are $\sim 13 - 14$ km s^{-1}, similar to the SiO lines. In W49A South, the H_2S $1_{1,0} - 1_{0,1}$ emission is relatively weak, and there is no detection for the $3_{1,2} - 3_{0,3}$ transition. However, W49A Southwest has a similar H_2S peak temperature but a smaller line width (~ 4 km s^{-1}) compared with the H_2S line in W49A South. The spectrum comparison of H_2S and SiO toward W49A North is shown in Figure 3.40, and it indicates that there is no close relation between the line profiles of SiO and H_2S.

The PV diagrams of the H_2S $1_{1,0} - 1_{0,1}$ line in W49A are shown in Figure 3.41. The second emission peak near W49A North at $\sim 17 - 19$ km s^{-1} is due to the Perseus Arm absorption. Besides, the moment maps shown in Figure 3.38 are similar to those of ^{13}CO, $C^{18}O$, HCN, HCO^+, and HCN.

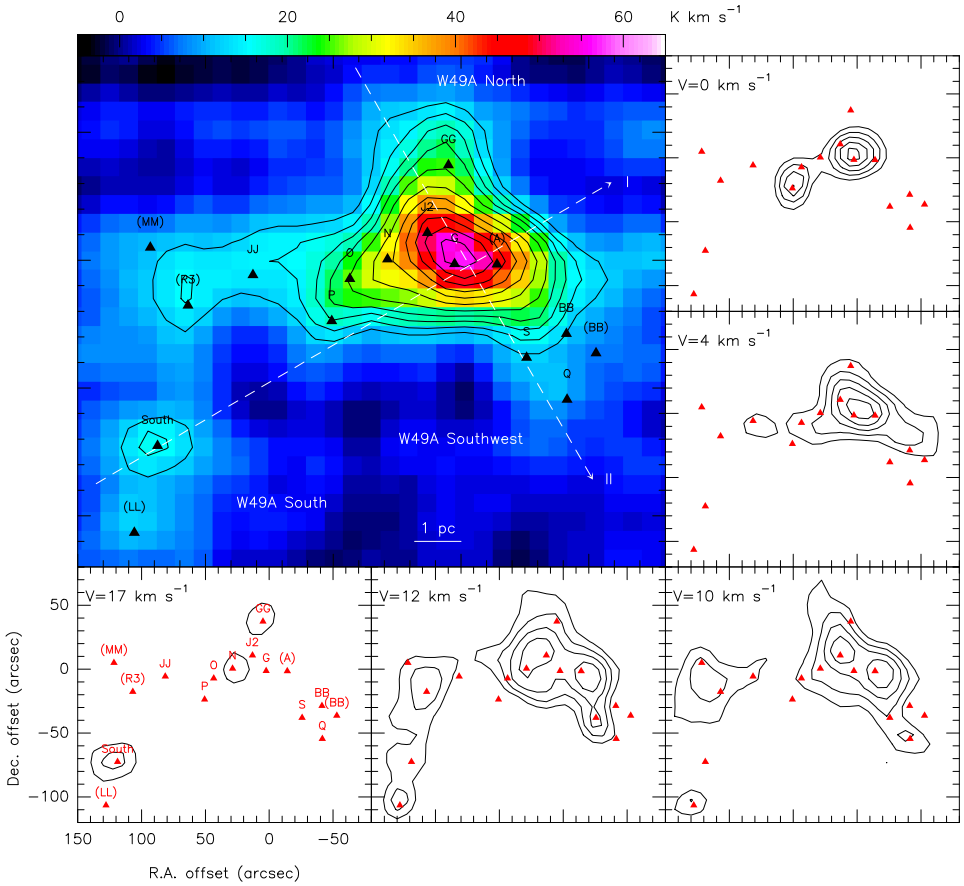

Figure 3.36 The smoothed (two Gaussian beams) H_2S integrated intensity image and selected velocity channel maps of W49A. The upper-left panel is the H_2S $1_{1,0} - 1_{0,1}$ image ($\theta_{\rm HPBW} = 14\farcs6$) and contours run from 12 to 21 K km s^{-1} in steps of 3 K km s^{-1} and the subsequent contours run from 25 to 60 K km s^{-1} in steps of 5 K km s^{-1} for clarity. One σ noise is 1.5 K km s^{-1} in the H_2S integrated intensity map. The rest panels are the five selected velocity channel maps of H_2S in contours running from 1 to 3 K km s^{-1} in steps of 0.4 K km s^{-1} (5 σ level). The two white dashed lines correspond to the two PV cuts shown in Figure 3.41.

Table 3.7. The H_2S measurement in W49A

	W49A North			W49A South			W49A Southwest		
	T_{peak}[a] (K)	V_{LSR} (km s^{-1})	ΔV[b] (km s^{-1})	T_{peak}[a] (K)	V_{LSR} (km s^{-1})	ΔV[b] (km s^{-1})	T_{peak}[a] (K)	V_{LSR} (km s^{-1})	ΔV[b] (km s^{-1})
H_2S ($3_{1,2} - 3_{0,3}$)	3.9±0.2	5.8	13.6	< 0.3	...	...	...	...	...
H_2S ($1_{1,0} - 1_{0,1}$)	3.3±0.1	0.6	13.2	2.0±0.3	16.1	8.3	2.0±0.4	8.6	3.5

[a]Temperatures shown here are corrected to the mean beam temperature unit.

[b]Line widths are measured in FWHM.

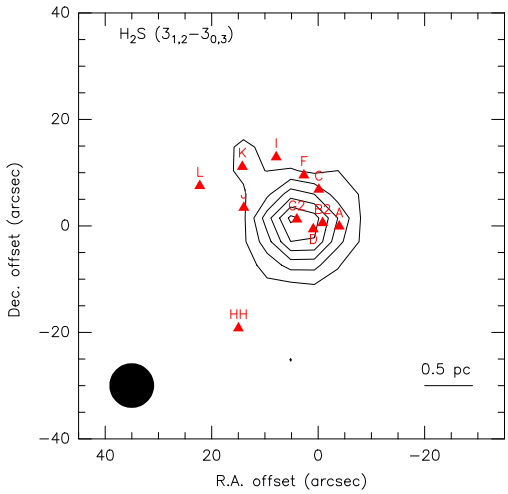

Figure 3.37 The integrated H_2S $3_{1,2} - 3_{0,3}$ intensity (from 0 to 20 km s^{-1}) image of W49A North with a beam size of 8.″4. Contours run from 30 to 180 K km s^{-1} in steps of 30 K km s^{-1} (4 σ level).

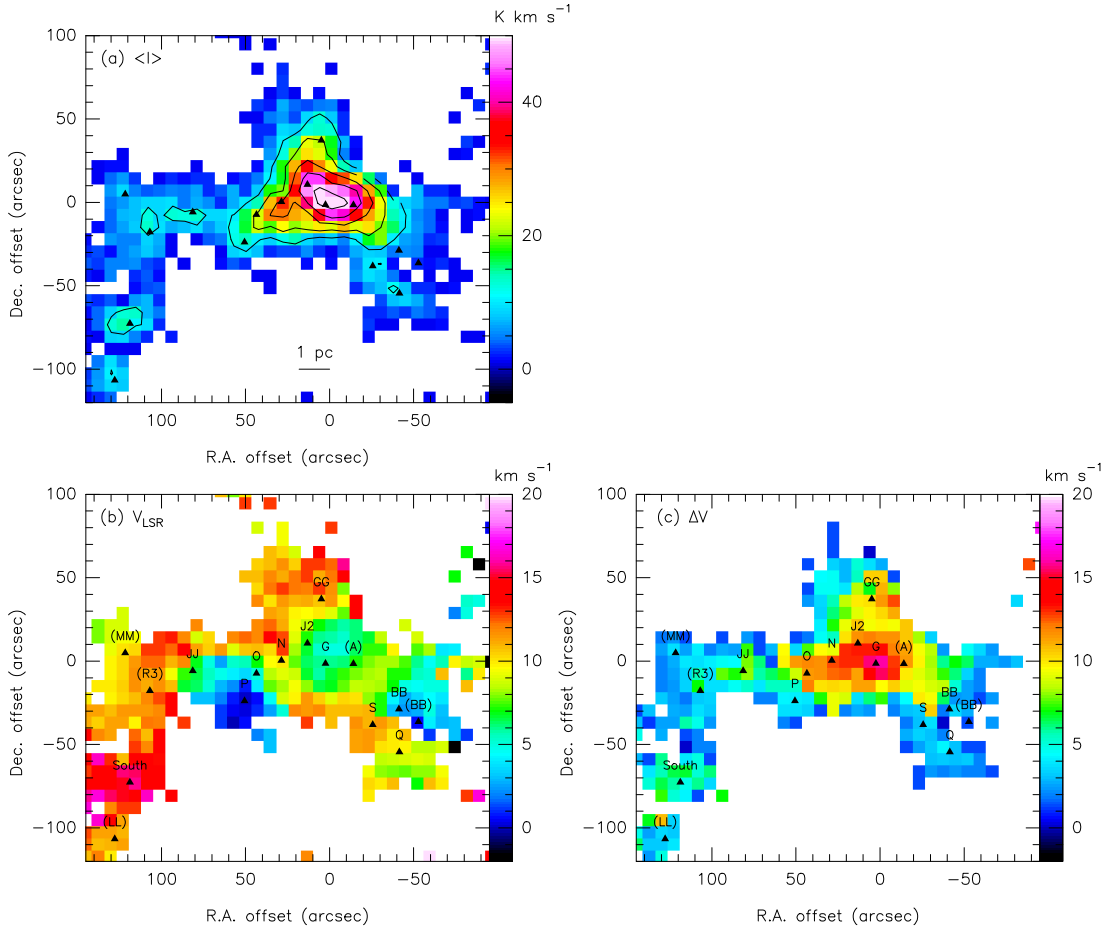

Figure 3.38 The H_2S $1_{1,0} - 1_{0,1}$ moment maps in W49A. (a) The mean intensity map is plotted in contours from 10 to 50 K km s^{-1} in steps of 10 K km s^{-1}. (b) The second moment of H_2S $1_{1,0} - 1_{0,1}$ shows the velocity distribution in W49A. (c) The third moment of H_2S $1_{1,0} - 1_{0,1}$ shows the line width distribution in W49A. The pixels whose temperatures are below 1 K are blanked.

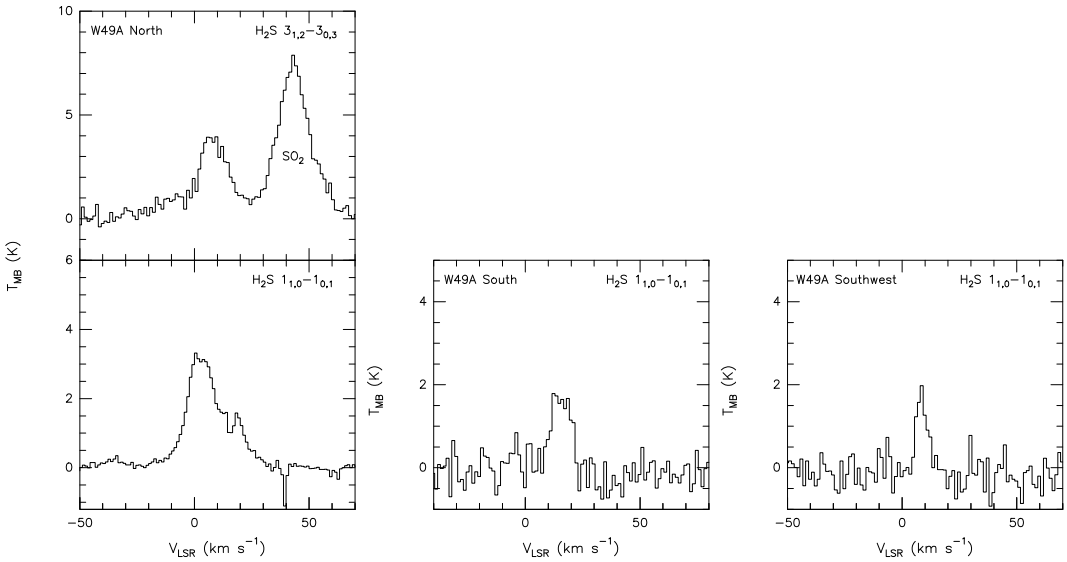

Figure 3.39 The H_2S spectra in W49A. The panel from left to right shows the H_2S $3_{1,2} - 3_{0,3}$ and $1_{1,0} - 1_{0,1}$ spectra in W49A North, South, and Southwest, respectively.

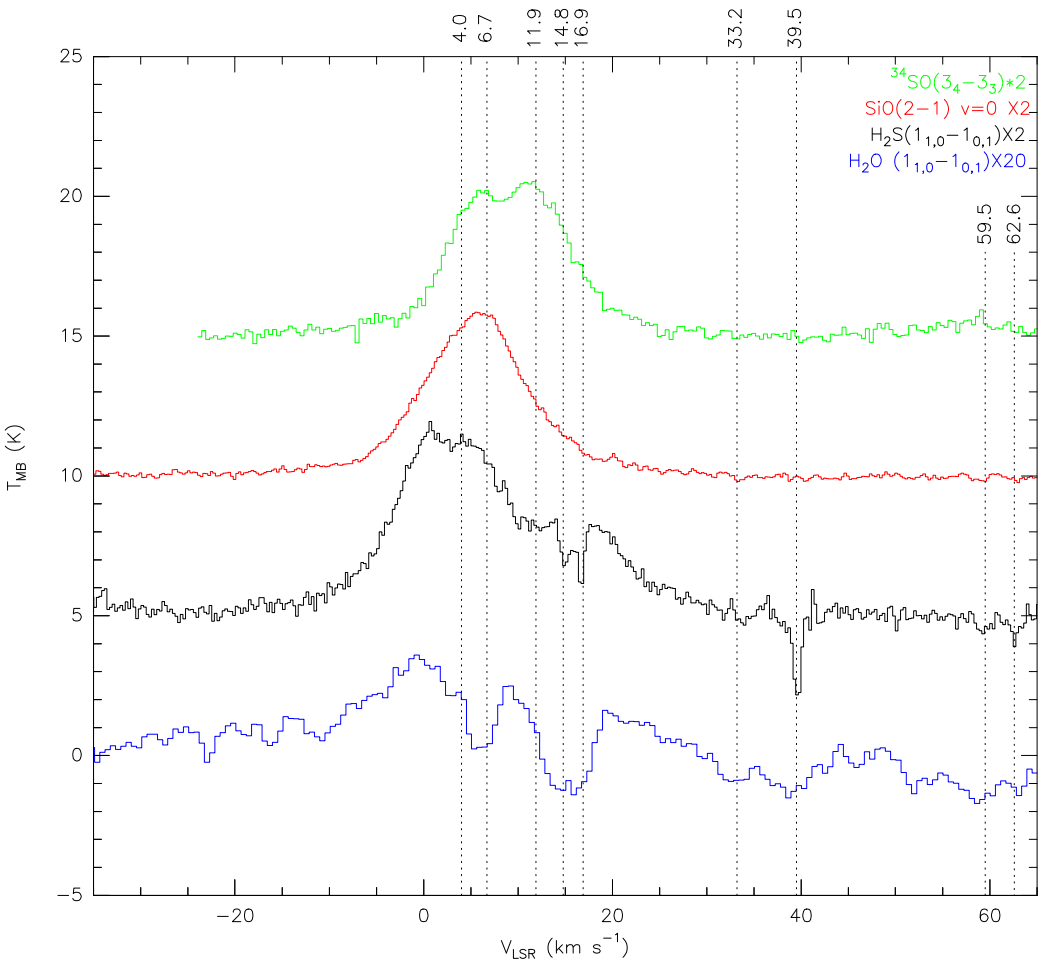

Figure 3.40 The spectrum comparison of H_2S, SO, SiO, and H_2O in W49A North. For clarity, the line profiles have been shifted.

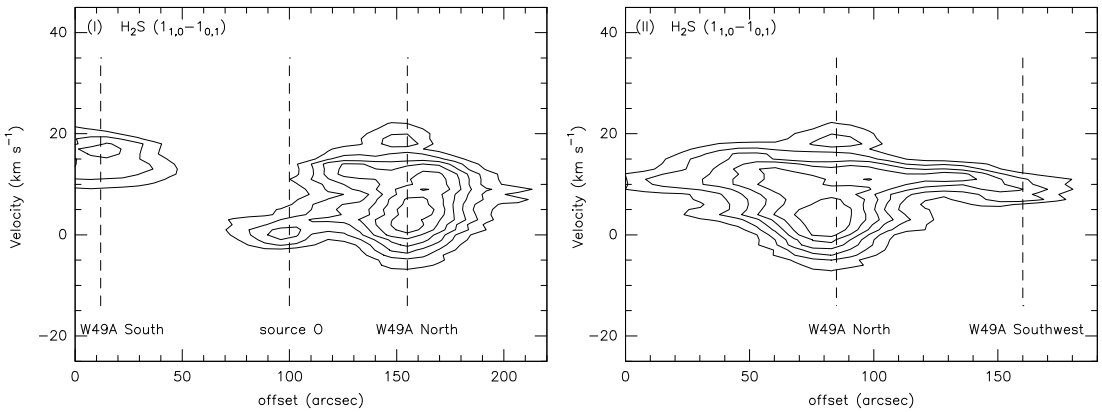

Figure 3.41 The PV diagrams of H_2S $1_{1,0} - 1_{0,1}$ in W49A. The positions of Cut I and II are shown in Figure 3.36. The contours run from 0.5 to 2.5 K in steps of 0.4 K.

3.2 Dust continuum emission

The LABOCA 870 μm dust continuum emission in Figure 3.42 shows a good correspondence to the images from the dense gas tracers such as HCN, HCO^+, and HCN, where the three main components of W49A are seen in the 870 μm map. The total dust mass can be estimated using Eq. B.32 (see Appendix B for details)

$$M_{\rm dust} = \frac{D^2 \Omega_{\rm s}}{\kappa_\nu} \left\{ -\ln\left[1 - \frac{S_\nu}{(B_\nu(T_{\rm d}) - B_\nu(T_{\rm bg}))\Omega_{\rm s}} \right] \right\}^{-1}, \tag{3.3}$$

where D the distance to W49A (11.4 kpc), $\Omega_{\rm s}$ the source solid angle, and κ_ν is the dust absorption coefficient. The dust absorption coefficient is frequency dependent

$$\kappa_\nu = 4.1 \times 10^{-3} \left(\frac{\nu}{226 \text{ GHz}} \right)^\beta \text{ cm}^2 \text{ g}^{-1}, \tag{3.4}$$

and we adopt $\beta = 2$ (Krügel 2008; Buckley & Ward-Thompson 1996) and $\kappa_\nu = 4.7 \times 10^{-3}$ cm^2 g^{-1}. In addition, the H_2 column density can be derived by using the dust opacity (Eq. B.34)

$$N_{\rm H_2} = \frac{\tau_\nu}{\mu m_{\rm p} \kappa_\nu}, \tag{3.5}$$

where $\mu = 2.33$ is the mean molecular weight per H_2, and $m_{\rm p}$ is the proton mass of 1.67×10^{-24} g.

In W49A, dense clumps are probably warm ($\gtrsim$ 50 K), but diffuse gas can be as cold as $\sim$ 20 K (Buckley & Ward-Thompson 1996; Sievers et al. 1991). Therefore, the dust mass estimate with the dust temperatures of 20 K and 50 K in the whole region is likely to be overestimated and underestimated, respectively. The total gas mass in the W49A North region ($\sim$ 40 pc^2) is $\sim 4 - 11 \times 10^5$ M$_\odot$, assuming a gas-to-dust mass ratio of 100. The gas mass of W49A North estimated by adopting the ^{13}CO excitation temperature (see §4.1) is similar to the dust mass estimate calculated in a dust temperature of 50 K. However, it is probably underestimated since most of the diffuse gas without a reliable excitation temperature estimate is filtered out (Fig. 3.42). Buckley & Ward-Thompson (1996) adopted κ_ν of 9×10^{-3} cm^2 g^{-1}, and a dust temperature of 17 K in a larger area ($\sim$ 60 pc^2) of W49A North in the JCMT observations, and they derived a total gas mass in W49A North of 4.9×10^5 M$_\odot$ with a gas-to-dust ratio of 100.

W49A South and W49A Southwest has a total gas mass ($T_{\rm d}$ = 50 K) of $\sim 8 \times 10^4$ M$_\odot$ and $\sim 4 \times 10^4$ M$_\odot$, respectively. Buckley & Ward-Thompson (1996) estimated the mass of W49A South and Southwest of $\sim 7 \times 10^3$ M$_\odot$ and $\sim 4 \times 10^3$ M$_\odot$, respectively, in a smaller region ($\sim$ 5 pc^2) with a dust temperature of $\sim$ 50 K, and their derived mass probably only represents the clump mass. In the end, the total gas mass of W49A has an order of 10^6 M$_\odot$, which is consistent with the virial mass of 10^6 M$_\odot$ derived by Simon et al. (2001), and in the same order of the mass estimated by Buckley & Ward-Thompson (1996) of $\sim 5 \times 10^5$ M$_\odot$.

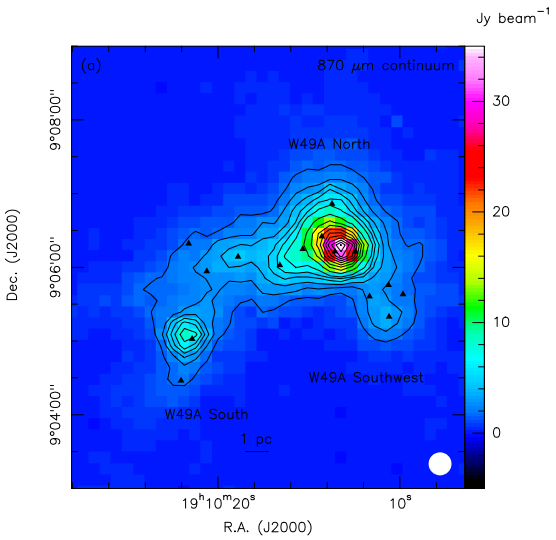

Figure 3.42 The 870 μm continuum emission image of W49A. The black contours run from 1 to 5 Jy beam^{-1} in steps of 1 Jy beam^{-1} (7 σ level) and the subsequent contours run from 6 to 30 Jy beam^{-1} in steps of 3 Jy beam^{-1}. The beam size is marked in the bottom-right corner of the image.

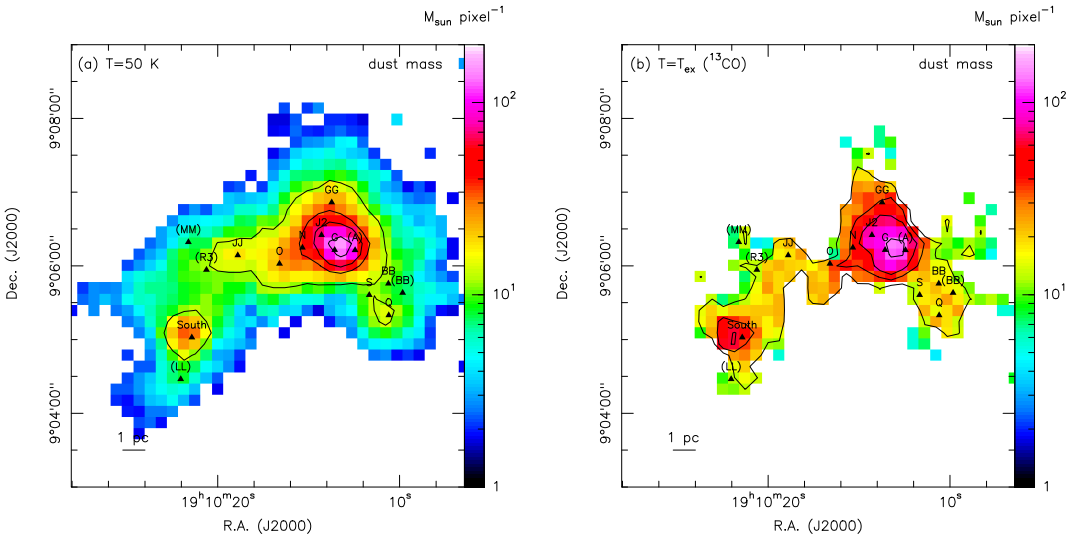

Figure 3.43 (a) The dust mass estimate in W49A by adopting a dust temperature of 50 K and κ_ν of 4.7×10^{-3} cm^2 g^{-1}. (b) The dust mass estimate in W49A by adopting the ^{13}CO excitation temperatures as dust temperatures (see §4.1) and the $\kappa_\nu = 4.7 \times 10^{-3}$ cm^2 g^{-1}. The contours denote dust optical depths of 0.01, 0.03, 0.05, and 0.1. All pixels with intensities below 3 σ are blanked.

Table 3.8. The dust mass estimate of W49A

Source	Size (pc^2)	$S_{870\mu m}$ (Jy)	L_{FIR}[a] ($L_\odot$)	T_{ex}[b] (K)	M_{dust}(25 K)[b] ($M_\odot$)	M_{dust}(50 K)[b] ($M_\odot$)	$M_{dust}(T_{ex})$[b] ($M_\odot$)
W49A North	40.3	483.0	6.8×10^6	∼58	1.1×10^4	4.4×10^3	4.3×10^3
W49A South	16.5	60.1	2.9×10^6	∼39	1.9×10^3	7.9×10^2	1.2×10^3
W49A Southwest	12.9	31.5	2.1×10^6	∼40	8.6×10^2	3.6×10^2	4.7×10^2

[a]The FIR luminosity and dust temperature values are taken from Buckley & Ward-Thompson (1996).

[b]The dust mass is estimated by applying dust temperatures of 25 K, 50 K, and the ^{13}CO $J = 2-1$ excitation temperatures derived from the ^{13}CO/C^{18}O $J = 2-1$ ratio (Table 4.1).

4

RADEX Modeling of W49A

To begin with, the density and temperature of W49A will be estimated in LTE. Then the RADEX modeling results for ^{13}CO and C^{18}O will be presented in §4.2.1. In addition, the RADEX modeling results of the abundance ratios among HCN, HCO$^+$, and HNC will be presented in §4.2.2. In the end, the modeling results of the density and temperature in W49A will be presented in §4.2.3.

4.1 Estimations of the temperature and the density

The excitation temperature and column density are important parameters to characterize molecular clouds, but their estimates can be tricky calculations. Without elaborate radiative transfer, the molecular excitation temperature and column density can be estimated easily under some assumptions. We use the method below together with the ^{13}CO and C^{18}O $J = 2 - 1$ data to derive the molecular excitation temperature and column density in W49A.

In the LTE assumption, where the excitation temperature equals the kinetic temperture ($T_{\rm k} = T_{\rm ex}$), and the Rayleigh-Jeans approxmation ($h\nu/kT \ll 1$), the brightness temperature can be derived from

$$T_{\rm b} = T_{\rm bg} e^{-\tau_\nu} + T_{\rm ex}(1 - e^{-\tau_\nu}), \tag{4.1}$$

where τ_ν is the optical depth at a specific frequency, and $T_{\rm bg}$ is the background temperature. Given the similar excitation parameters of ^{13}CO $J = 2 - 1$ and C^{18}O $J = 2 - 1$, it is reasonable to assume their excitation temperatures are equal. The relation between the optical depths and the brightness temperatures of ^{13}CO and C^{18}O $J = 2 - 1$ is then

$$\frac{T_{\rm b}(^{13}{\rm CO})}{T_{\rm b}({\rm C}^{18}{\rm O})} \approx \frac{1 - e^{-\tau(^{13}{\rm CO})}}{1 - e^{-\tau({\rm C}^{18}{\rm O})}}, \tag{4.2}$$

where we neglect the background radiation. We can solve Eq. 4.2 by assuming the optical depth ratio is approximated by the isotope abundance ratio of ^{13}C and ^{18}O. We adopted ^{13}C/^{12}C of 46 and ^{18}O/^{16}O of 510 (Wilson & Rood 1994; Langer & Penzias 1990) for W49A (8.1 kpc to the Galactic

Table 4.1. The estimates of the optical depth, excitation temperature, and column density in W49A

Source	$\tau(^{13}CO)^a$	$T_{ex}{}^a$ (K)	$N(C^{18}O)^a$ (cm^{-2})	$N(H_2)^b$ (cm^{-2})	$M_{dust}{}^c$ ($M_\odot$)
source G	3.83	57.9	1.7×10^{17}	4.4×10^{23}	103.4
source N	1.98	46.0	5.0×10^{16}	1.3×10^{23}	47.5
source O	1.47	47.6	3.4×10^{16}	8.7×10^{22}	26.6
W49A South	2.09	38.7	2.9×10^{16}	7.4×10^{22}	31.8
source S	1.91	42.3	2.1×10^{16}	5.4×10^{22}	13.0
source Q	1.50	37.5	1.7×10^{16}	4.3×10^{22}	14.6
source JJ	0.59	58.3	2.4×10^{16}	6.2×10^{22}	18.8

[a]The values are calculated in the resolution of twice the pixel size ($5\farcs6 \times 5\farcs6$).

[b]The H_2 column density is estimated by assuming the ^{12}CO to $C^{18}O$ abundance ratio of 510 and the ^{12}CO to H_2 abundance ratio of 2×10^{-4}.

[c]The mass is estimated using the LABOCA image (Fig. 3.42) with a dust temperature of 50 K, and is calculated in the resolution of twice the pixel size ($9\farcs1 \times 9\farcs1$).

center) which gives an optical depth ratio of 11 between ^{13}CO $J = 2-1$ and $C^{18}O$ $J = 2-1$. The temperature ratio between ^{13}CO $J = 2-1$ and $C^{18}O$ $J = 2-1$ (Fig. 4.1 a) ranges from 1 to 11, which implies $\tau_{^{13}CO}$ of $0.1-11$ (Fig. 4.1 b), assuming a beam filling factor of unity. Then, the excitation temperature of ^{13}CO and $C^{18}O$ $J = 2-1$ can be estimated via

$$T_{ex} = E_u \left[\ln\left(1 + \frac{E_u(1 - e^{-\tau(^{13}CO)})}{T_{MB}(^{13}CO)} \right) \right]^{-1}, \tag{4.3}$$

where E_u is the energy level of the upper state, and is 15.9 K for the ^{13}CO $J = 2-1$ transition. As seen from Figure 4.1 c, the excitation temperature ranges from ~ 20 K in the low-density gas to $40-60$ K in dense clumps. Using Eqs. B.22 and B.28 (see Appendix B), the total $C^{18}O$ column density can be derived from

$$N(C^{18}O) \simeq 1.19 \times 10^{13}\ (T_{ex} + 0.88)\ e^{\frac{E_u}{T_{ex}}} \int T_{MB} dV\ \mathrm{cm}^{-2}, \tag{4.4}$$

where E_u is 15.8 K for the $C^{18}O$ $J = 2-1$ transition. The estimates of excitation temperature and the $C^{18}O$ $J = 2-1$ column density are shown in Figure 4.1, and the results toward selected clumps are summarized in Table 4.1. Most clumps have excitation temperatures of $40-60$ K which means $T_{ex}/T_{bg} \gg 1$ and generally warm environments in these clumps. Therefore, the assumpsion to neglect the background radiation term in Eq. 4.2 is justified. The $C^{18}O$ column densities for the selected clumps are estimated to be $2-20 \times 10^{16}$ cm^{-2}, which implies H_2 column densities of $4-40 \times 10^{22}$ cm^{-2} assuming a ^{12}CO abundance of 2×10^{-4} (e.g., Lacy et al. 1994). The average H_2 column density in the whole W49A region is 5.7×10^{22} cm^{-2} in an area of about 64 pc^2, and the

average number density is estimated to be $\sim 2 \times 10^3$ cm^{-3}. Assuming the clumps in W49A have the same size as the beam size of ^{13}CO and C^{18}O $J = 2 - 1$ ($11\farcs2$), the number density of the clumps is $2 \times 10^4 - 2 \times 10^5$ cm^{-3}. The average mass of W49A is $\approx 6.8 \times 10^4$ M$_\odot$, which is of the same order as the previous mass estimate of $\sim 10^5$ M$_\odot$ (Simon et al. 2001; Buckley & Ward-Thompson 1996; Mufson & Liszt 1977). However, only the region with a good signal-to-noise ratio is taken into account for the density estimate. Thus, the average mass of 6.8×10^4 M$_\odot$ in a relative small area should be treated as a lower limit regarded to the whole W49A region.

In the ^{13}CO $J = 2 - 1$ optical depth image (Fig. 4.1 b), the most opaque region is the region near sources G and A in W49A North ($\tau_{^{13}\mathrm{CO}} \sim 4 - 5$), which has an H_2 column density of $\sim 4 \times 10^{23}$ cm^{-2}. As for W49A South and W49A Southwest (source S and Q), the H_2 column densities are about one order smaller than the density in the region near source G.

4.2 RADEX Modeling

4.2.1 ^{13}CO and C^{18}O

In the dense regions of molecular clouds, the density and the temperature are usually evaluated by assuming a Local Thermodynamic Equilibrium (LTE) condition, where the excitation temperature equals the kinetic temperature. In diffuse gas, however, the LTE assumption does not hold properly, and a non-LTE calculation is needed to estimate the excitation temperature and optical depth. The critical density of CO $J = 2 - 1$ (Table 1.1) is 7.1×10^3 cm^{-3} which is smaller than the density of the clumps in W49A, i.e., $2 \times 10^4 - 2 \times 10^5$ cm^{-3}, but higher than the average density of diffuse gas (2×10^3 cm^{-3}). Therefore, a non-LTE program (RADEX) was used to investigate whether the LTE calculation has a large discrepancy in W49A.

RADEX (van der Tak et al. 2007) is a non-LTE radiative transfer program which calculates the excitation temperature and the emission intensity from a homogeneous medium. RADEX uses the molecular data including energy levels, Einstein A coefficients, and collisional coefficients from the Leiden Atomic and Molecular Database (LAMDA; Schöier et al. 2005). The optical depth effects are also treated with the escape probability (β) approximation in the one-dimensional case with three different geometries, i.e., the large velocity gradient (LVG) approximation of expanding envelopes, a homogeneous slab, and a uniform sphere. The mean intensity can then be calculated via

$$J_\nu = S_\nu(1 - \beta), \tag{4.5}$$

where S_ν is the source function, the ratio of the emission and absorption coefficients. There are some limitations of the RADEX program one should be aware of, e.g., the dust and free-free continuous opacity have not been taken into account to the escape probability approximation, and the negative optical depth in maser phenomenon as well (van der Tak et al. 2007). In addition, RADEX cannot treat temperatures higher than 500 K.

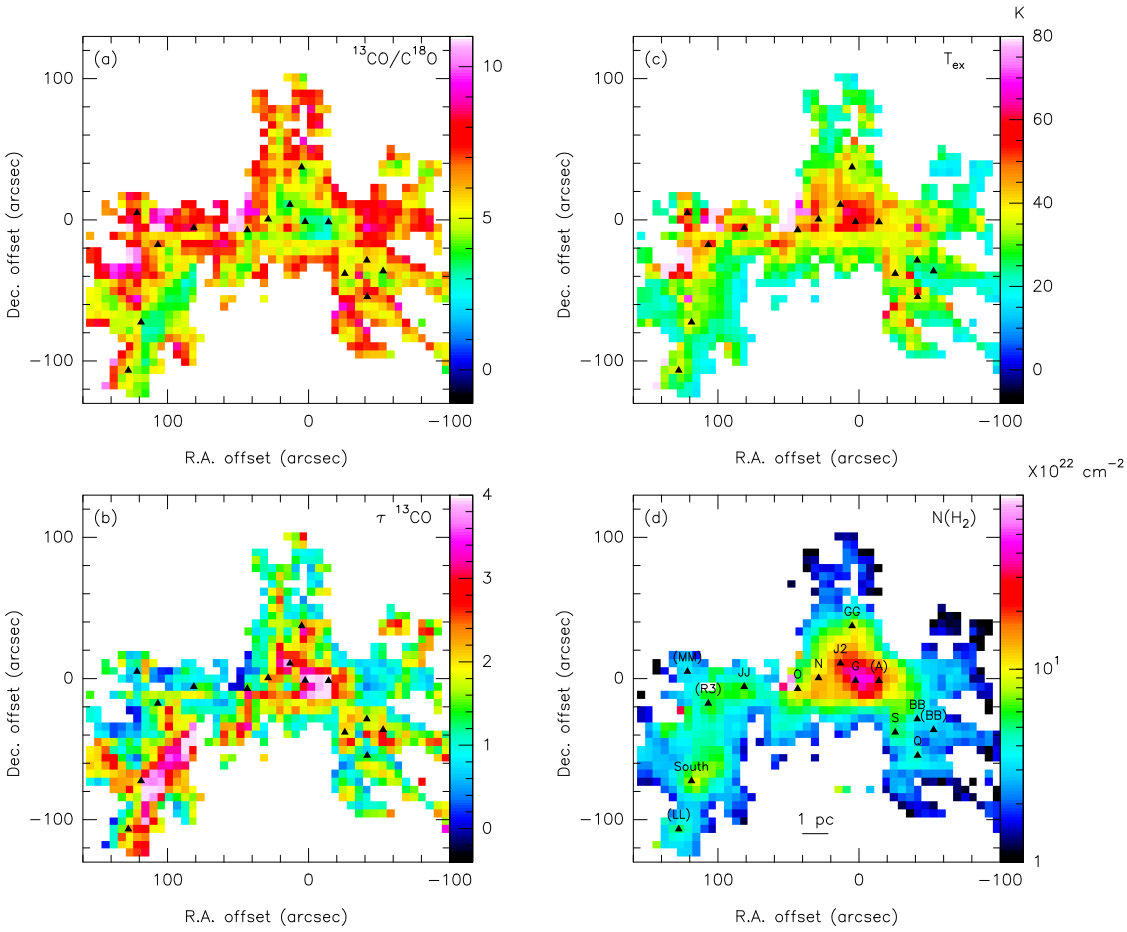

Figure 4.1 (a) The peak temperature ratio map between ^{13}CO $J = 2 - 1$ and C^{18}O $J = 2 - 1$. Pixels with the C^{18}O $J = 2 - 1$ temperatures below 1.5 K (3 σ level) or with the ^{13}CO $J = 2 - 1$ temperatures below 6 K (3 σ) are blanked. (b) The optical depth map of ^{13}CO $J = 2 - 1$. (c) The ^{13}CO and C^{18}O $J = 2 - 1$ excitation temperature map in W49A. (d) The H_2 column density map of W49A assuming a ^{12}CO abundance of 2×10^{-4} (e.g., Lacy et al. 1994).

The uniform sphere geometry was chosen for the RADEX modeling in W49A where the escape probability in a homogeneous medium is

$$\beta_{\rm sphere} = \frac{1.5}{\tau}\left[1 - \frac{2}{\tau^2} + \left(\frac{2}{\tau} + \frac{2}{\tau^2}\right)e^{-\tau}\right]. \quad (4.6)$$

Besides, only H_2 was chosen as a collision partner, and 2.73 K was adopted as the background temperature. The input parameters are kinetic temperatures and H_2 number densities. The model was iterated with a kinetic temperature ranging from 10 to 210 K, and an H_2 number density ranging from 10^4 to 10^8 cm^{-3}. Due to the shell structure in W49A, most spectra show two-component line profiles, and each component has an FWHM line width of $7-8$ km s^{-1} for ^{13}CO and C^{18}O $J = 2-1$. Therefore, the FWHM line widths (ΔV) of ^{13}CO and C^{18}O $J = 2 - 1$ were fixed at 7.5 km s^{-1}, and the column density ratio between C^{18}O and ^{13}CO was fixed at an abundance ratio of (46/510) in the RADEX modeling. The main output parameter is the molecular line radiation temperature ($T_{\rm R}$), and the line intensity is calculated as $\sqrt{\pi}/(2\sqrt{\ln 2})T_{\rm R}\Delta V$ in the RADEX program, where the factor converts the adopted rectangular line profile into a Gaussian profile with an FWHM of ΔV. The RADEX modeling results are shown in Figures 4.2 and 4.3.

The RADEX modeling results shown in Figure 4.2 indicate that most of gas has a C^{18}O column density ranging from 1×10^{16} to 8×10^{16} cm^{-2}, which is consistent with the LTE calculation for the selected clumps (Table 4.1) and the average C^{18}O column density of 2.2×10^{16} cm^{-2}. In addition, the kinetic temperatures of $20 - 80$ K are also consistent with the calculated excitation temperatures in W49A (Fig. 4.1 and Table 4.1). However, the H_2 number density is difficult to pinpoint in this model. The counterclockwise increase of the density in Figures 4.2 and 4.3 is because the upper states of ^{13}CO and C^{18}O are populated in the dense gas which leads to a decrease of the line intensity of ^{13}CO and C^{18}O in the $J = 2 - 1$ transition. Besides, the large spread of the ^{13}CO and C^{18}O intensities shown in Figure 4.3 is probably because many two-component lines from the shell structure are included, while only the peak temperature from one component is taken into account in Figure 4.2. In short, this RADEX modeling agrees with the previous LTE calculation of ^{13}CO and C^{18}O for both column densities and excitation temperatures.

4.2.2 The abundance ratios among HCN, HCO$^+$, and HNC

HCN, HCO$^+$, and HNC are similar dense gas tracers (see §3 and Table 1.1) whose emission, in many conditions, is optically thick. Their ^{13}C isotopologues, H^{13}CN, H^{13}CO$^+$, and HN^{13}C, are thus useful because of their optically thin emission. Since the tight correlations among these molecules are observed (Figs. 4.4 and 4.5), it is thus reasonable to assume fixed relative abundance ratios among HCN, HCO$^+$, and HNC on a large scale and a fixed isotope ratio of ^{12}C/^{13}C (~ 46). Therefore, we can determine the abundance ratio among these three molecules by correlating their line intensities or brightness temperatures. Hence, another RADEX modeling was carried out for this purpose with the same uniform sphere geometry as for the CO isotopologue modeling.

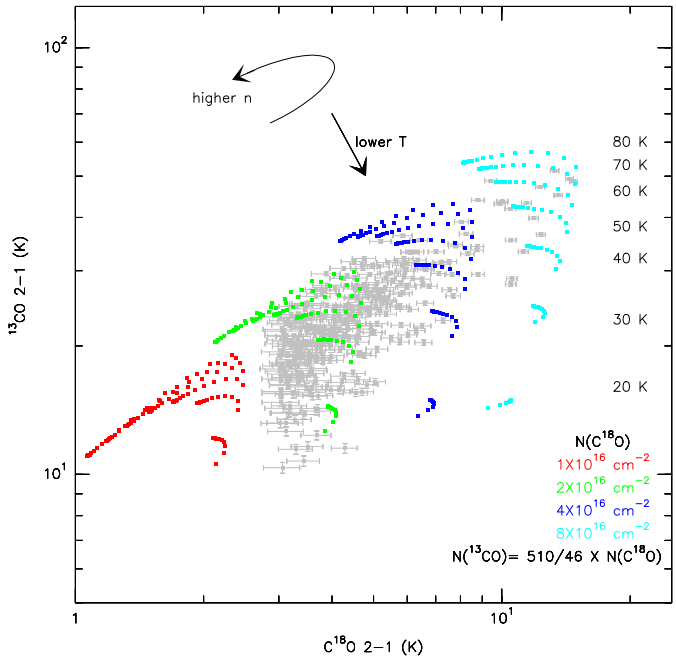

Figure 4.2 The RADEX modeling results for ^{13}CO and C^{18}O. The line widths were fixed to 7.5 km s^{-1} for both ^{13}CO and C^{18}O $J = 2 - 1$, and the C^{18}O to ^{13}CO column density ratio is adopted the abundance ratio of (46/510). The color points are the RADEX results, and the grey points are the peak temperatures of ^{13}CO and C^{18}O $J = 2 - 1$ from the observations. The four colors correspond to the different column densities of ^{13}CO and C^{18}O as the input parameters. The output results are plotted in a temperature range of $20 - 80$ K, and in a density range of $10^4 - 10^7$ cm^{-3}, where the lower ^{13}CO intensity tends to a have lower temperature, and the number density increases counterclockwise as denoted. All points with the C^{18}O $J = 2-1$ temperatures below 3 σ are blanked.

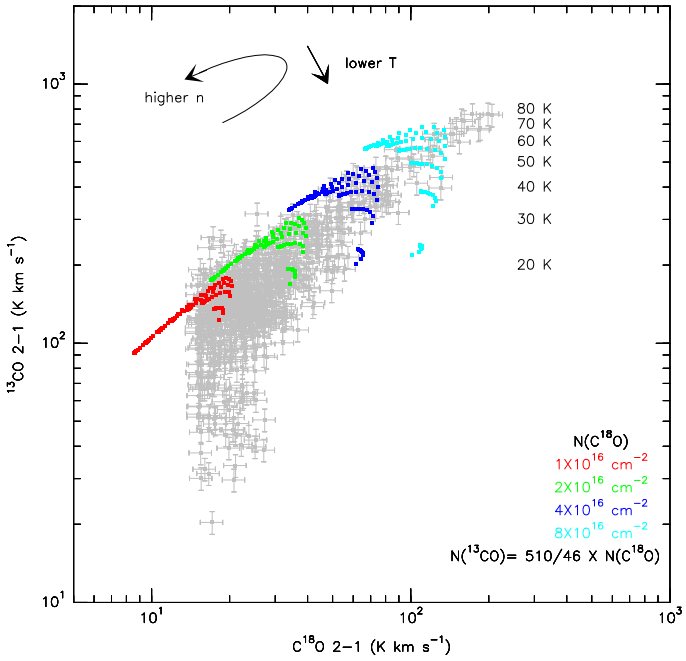

Figure 4.3 The same RADEX modeling as in Figure 4.2 but is shown in integrated intensities. All points with the $C^{18}O$ $J = 2 - 1$ intensities below 3 σ are blanked.

The model was calculated with an input kinetic temperature ranging from 10 to 210 K, and an H_2 number density ranging from 10^4 to 10^8 cm^{-3}. Since the two-component line profiles have similar FWHM line widths of $7 - 8$ km s^{-1} for each component, the line widths in the RADEX modeling for HCN, HCO^+, HNC, and their ^{13}C isotopologues were fixed at 7.5 km s^{-1}. Therefore, the brightness temperatures of HCN, HCO^+, and HNC were calculated in RADEX with the H_2 densities and kinetic temperatures in the range mentioned above. The abundance ratios among these three molecules is a free parameter which needs to be determined in the modeling. Besides, the comparison with the data is done mainly by eye for peak temperatures to avoid the confusion of integrated intensities that might include two components. Because the ^{13}C isotopologic and high-J lines of HCN, HCO^+, and HNC are only obtained toward W49A North, South, and Southwest (sources S and Q), the comparison between models and the data has only been done in these three sources. The selected RADEX modeling results are shown in this chapter, and the rest of the results are shown in Appendix 3, where the models were iterated with different abundance ratios. The best modeling results are selected by eye according to their less discrepancy compared to the data in both ^{12}C and ^{13}C isotopologues and in different transitions.

In Figures 4.6–4.7 and C.1–C.3, all RADEX modeling results show a turnover trend where the $H^{13}CN$ and $H^{13}CO^+$ intensities decrease altogether (clockwise). The turnover points appear at high densities ($\geq 10^5$ cm^{-3} for $J = 1 - 0$; $\geq 10^6$ cm^{-3} for $J = 3 - 2$ and $J = 4 - 3$), and are not sensitive to kinetic temperatures. The decrease of the $H^{13}CN$ and $H^{13}CO^+$ radiation temperatures

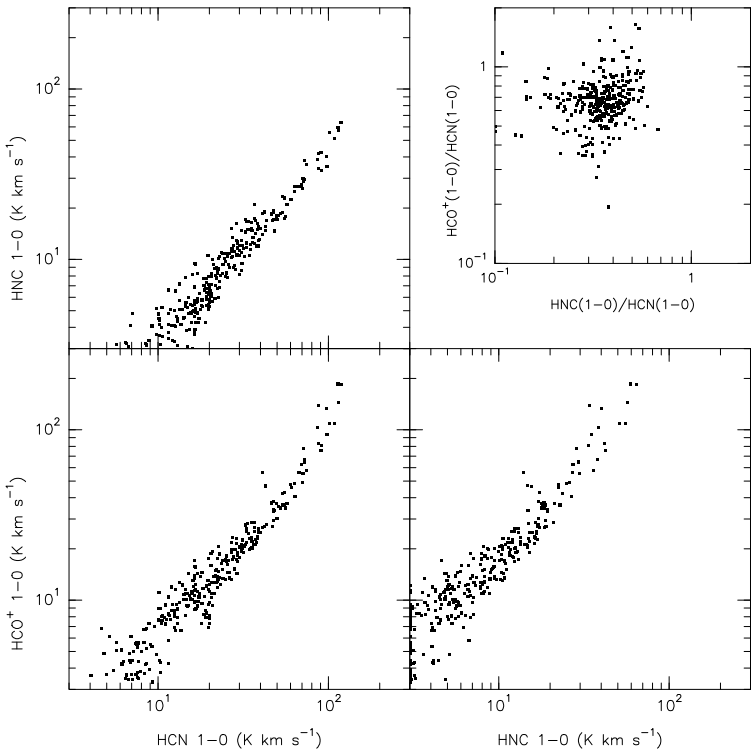

Figure 4.4 The correlations between the HCO^+, HCN, and HNC $J = 1-0$ line intensities. Each data point represents one pixel of the integrated intensity map. Upper-right panel shows the correlation between the HNC/HCN and HCO^+/HCN ratios.

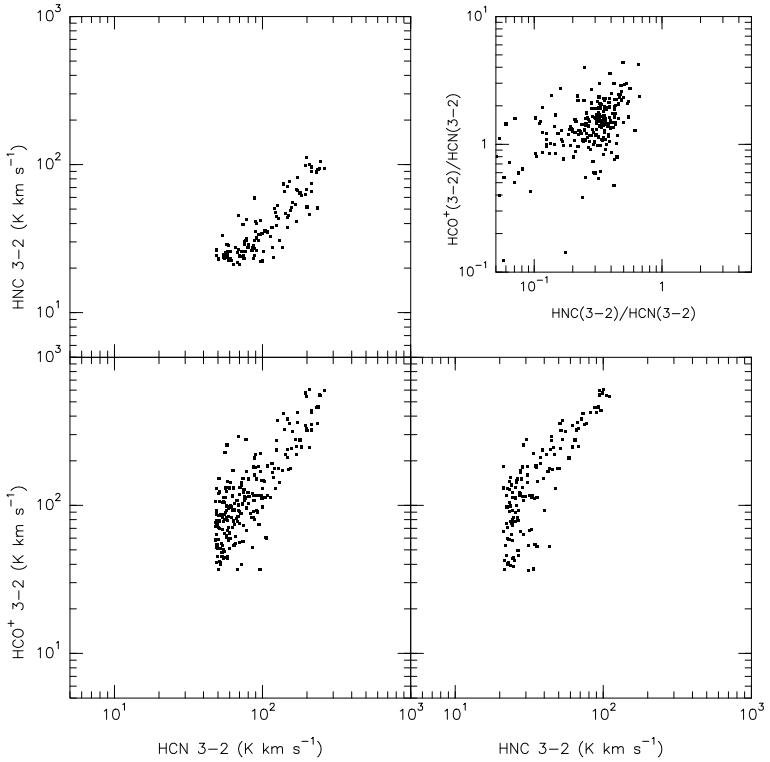

Figure 4.5 The correlations between the HCO^+, HCN, and HNC $J = 3-2$ line intensities. Each data point represents one pixel of the integrated intensity map. Upper-right panel shows the correlation between the HNC/HCN and HCO^+/HCN ratios.

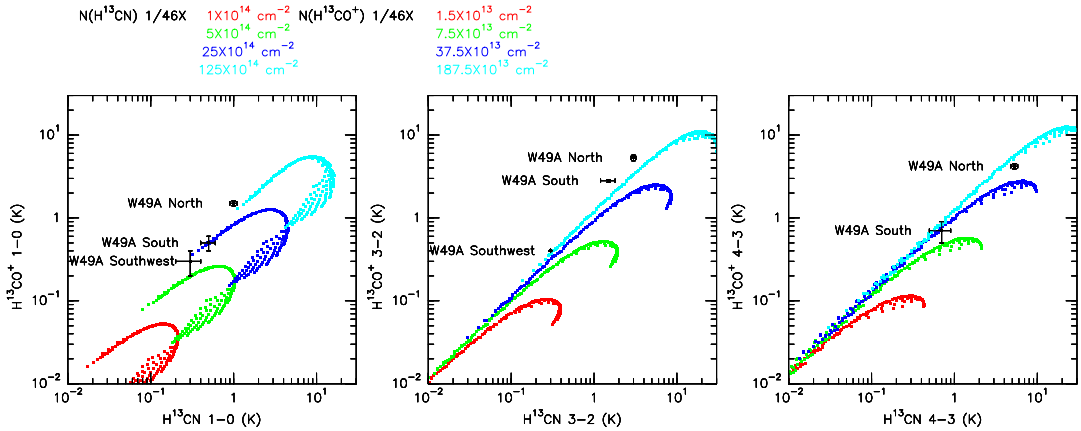

Figure 4.6 The RADEX modeling for the peak temperature correlations between $H^{13}CN$ and $H^{13}CO^+$ in W49A North, South, and Southwest. The four different colors are the RADEX results for different column densities plotted in an H_2 density range of $10^4 - 10^7$ cm^{-3} and a temperature range of $20 - 150$ K. The relative column density ratio between $H^{13}CN$ and $H^{13}CO^+$ is fixed at $20 : 3$. The data points of W49A North, South, and Southwest are denoted.

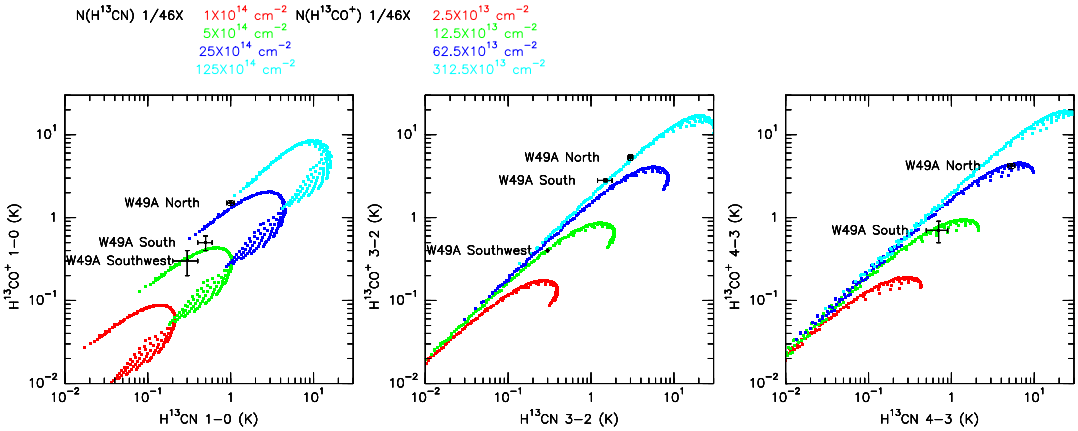

Figure 4.7 The similar modeling as in Figure 4.6 with a different $H^{13}CN/H^{13}CO^+$ column density ratio of 4 : 1.

can be explained by the underpopulated lower-J transitions in a dense region. The Two best RADEX models compared with the data are shown in Figures 4.6 and 4.7, where the $H^{13}CN$ column density is about $4-7$ times larger than that of $H^{13}CO^+$. The peak temperatures of $H^{13}CN$ and $H^{13}CO^+$ are relatively high in the $J = 3-2$ transition, probably due to a smaller beam size of $\sim 9''$ compared with that of the $J = 1-0$ transition ($\sim 28''$) and the $J = 4-3$ transition ($\sim 17''$). Additionally, because of beam dilution, the actual brightness temperatures might be higher, and the column densities derived here are likely lower limits. Hence, W49A North has an $H^{13}CO^+$ column density of $\gtrsim 1.4 \times 10^{13}$ cm^{-2}, and W49A South and Southwest have an $H^{13}CO^+$ column density of $\gtrsim 2.7 \times 10^{12}$ cm^{-2}. Similar results can be concluded from the correlations between the ratios of $H^{13}CN$ and $H^{13}CO^+$ in different transitions (Figs. 4.8–4.9 and C.4–C.6). However, in Figure 4.9, the $H^{13}CN/H^{13}CO^+ J = 4-3$ ratios for W49A North and South are only half of the RADEX modeling value, and it is likely due to the filling factor effect that a larger beam size in the $J = 4-3$ transition smears out the concentrated HCO^+ and $H^{13}CO^+$ emission, and in turn decreases the HCO^+/HCN and $H^{13}CO^+/H^{13}CN$ peak temperature ratios.

Figure 4.10 shows the RADEX modeling results for the HCN and HCO^+ high-J transitions. These models with an HCN/HCO^+ abundance ratio of $\sim 4-7$ (Figs. 4.10 and C.9–C.10) are well consistent with the data of W49A North and South, and are also consistent with the ^{13}C isotopologue RADEX modeling results shown above. However, it seems that the brightness temperature of HCO^+ $J = 10-9$ in W49A North is enhanced compared with the model by a factor of ~ 2.

The RADEX modeling results for the low-J transitions of HCN, HCO^+, and HNC are shown in Figures 4.11 and C.11–C.14. A similar turnover trend at a higher density ($\geq 10^5$ cm^{-3}) is also seen. The modeling results with a similar HCN/HCO^+ abundance ratio of $\sim 4-7$ are consistent with the data in the $J = 3-2$ and $J = 4-3$ transitions. In the $J = 1-0$ transition, however, there is a clear deviation between the RADEX model results and the data whose HCO^+ $J = 1-0$ brightness temperatures are above 7 K. Since this strong HCO^+ $J = 1-0$ emission comes from

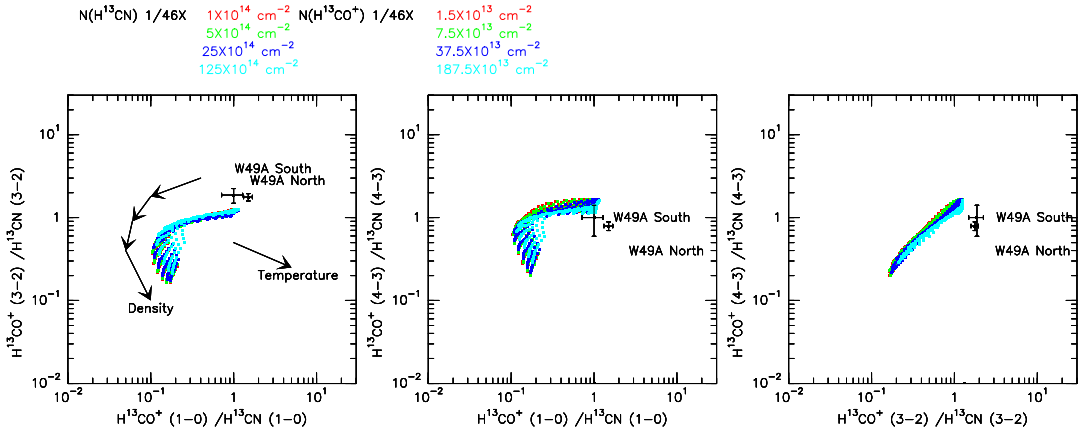

Figure 4.8 The same RADEX modeling as in Figure 4.6. The four different colors are the RADEX results for different column densities plotted in an H_2 density range of $10^4 - 10^7$ cm^{-3} and a temperature range of $20 - 150$ K. The relative column density ratio between $H^{13}CN$ and $H^{13}CO^+$ is fixed at $20:3$. The data points of W49A North, South, and Southwest are denoted.

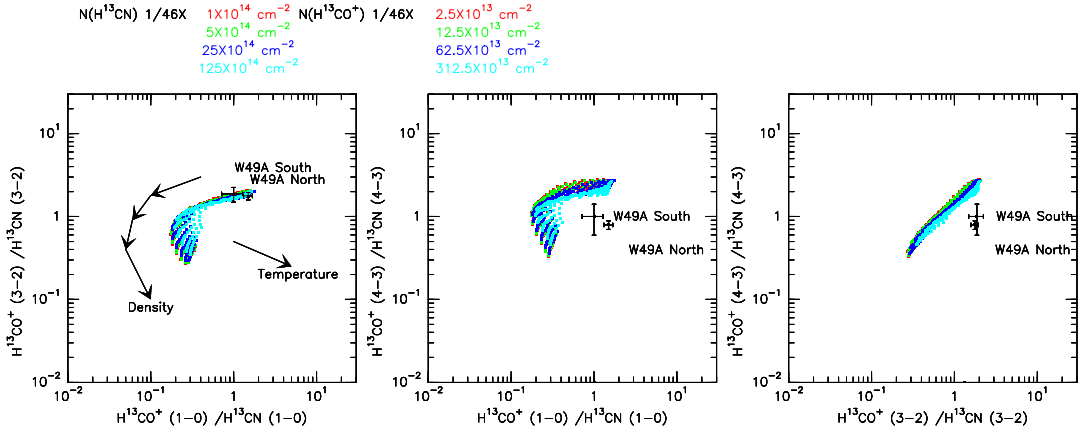

Figure 4.9 The same RADEX modeling as in Figure 4.7. The four different colors are the RADEX results for different column densities plotted in an H_2 density range of $10^4 - 10^7$ cm^{-3} and a temperature range of $20 - 150$ K. The relative column density ratio between $H^{13}CN$ and $H^{13}CO^+$ is fixed at $4:1$. The data points of W49A North, South, and Southwest are denoted.

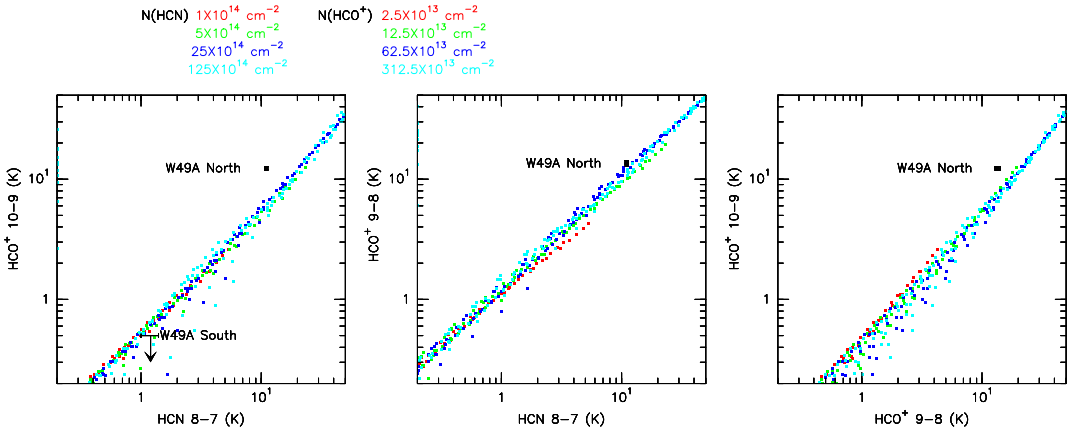

Figure 4.10 The RADEX modeling for the brightness temperature correlation between the high-J HCN and HCO^+ transitions. The four different colors are the RADEX results for different column densities plotted in an H_2 density range of $10^4 - 10^7$ cm^{-3} and a temperature range of $20 - 150$ K. The relative column density ratio between HCN and HCO^+ is fixed at 4 : 1. The data points of W49A North are denoted.

W49A North (around source G), this deviation indicates that the HCO^+ $J = 1 - 0$ emission is also enhanced in this region.

In short, an HCN/HCO^+ abundance ratio of $\sim 4 - 7$ is estimated from the RADEX modelings toward W49A North, South, and Southwest, and the result from the same model is also consistent with the data from the selected clumps shown in Figure 4.12. In Figure 4.12, the correlations of the HCO^+/HCN and HNC/HCN ratios for the selected clumps suggest an abundance ratio among HCN, HCO^+ and HNC of 20:5:8, where HCN is the most abundant molecule among these three molecules, and HCO^+ and HNC probably have similar abundance in W49A. However, the HCN/HNC abundance ratio is less certain in these models due to the lack of the collisional coefficients for HNC, and the HCN collisional coefficients were adopted for HNC. Besides, the abundance ratio does not reflect the line intensity or brightness ratio among these three molecules. The estimated column density and abundance of HCN, HCO^+, and HNC are summarized in Table 4.2. The average HCN abundance $X(\mathrm{HCN}) = \mathrm{N(HCN)/N(H_2)}$ in W49A is about $2 - 9 \times 10^{-9}$, and about 1×10^{-9} and $1 - 4 \times 10^{-9}$ for HCO^+ and HNC, respectively. The HCO^+ abundance is consistent with the value of about 10^{-9} derived by Welch et al. (1987).

4.2.3 H_2 density and kinetic temperature distribution

In order to constrain the molecular gas density and temperature in W49A, the RADEX modeling of CO isotopologues (i.e., ^{13}CO and C^{18}O) and dense gas tracers (i.e., HCO^+) was combined to disentangle the degeneracy between density and temperature. Because of the difference in the critical densities between the HCO^+ $J = 1 - 0$ (2.4×10^5 cm^{-3}) and $J = 3 - 2$ transitions (2.3×10^6 cm^{-3}),

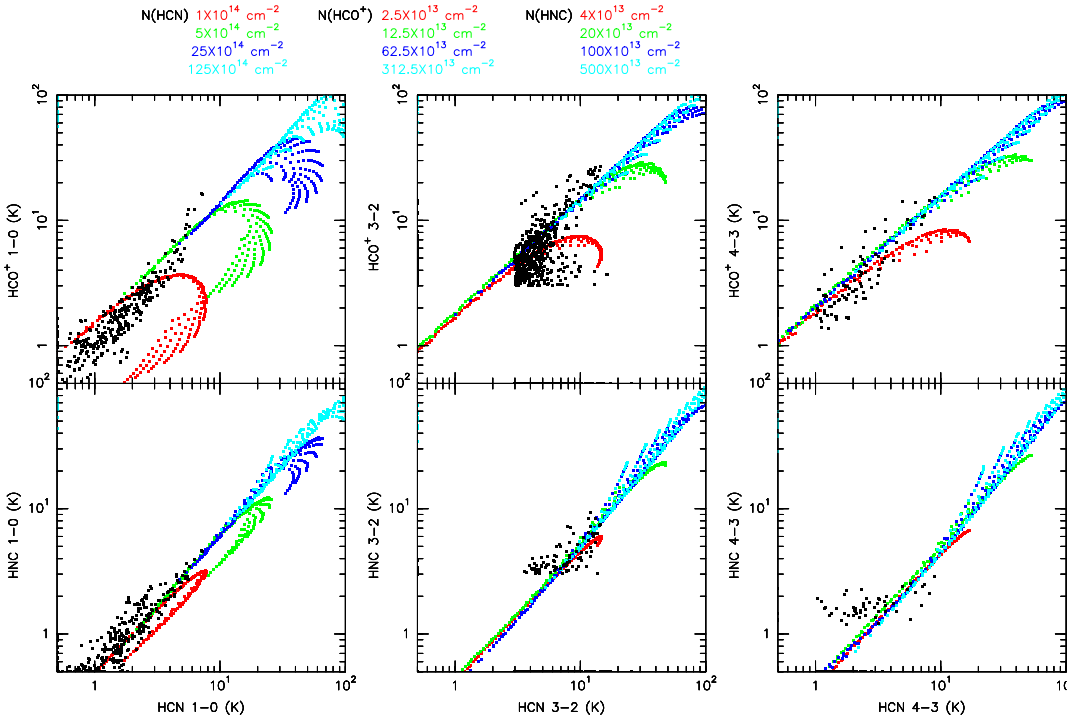

Figure 4.11 The RADEX modeling results of HCN, HCO^+, and HNC. The line widths were fixed at 7 km s^{-1} for all lines. The four different colors are the RADEX results for different column densities plotted in an H_2 density range of $10^4 - 10^7$ cm^{-3} and a temperature range of $20 - 150$ K. The relative column density ratio among HCN, HCO^+, and HNC is fixed at $10 : 2.5 : 4$. The black dots are the peak temperatures. All points with intensities below 3 σ are blanked.

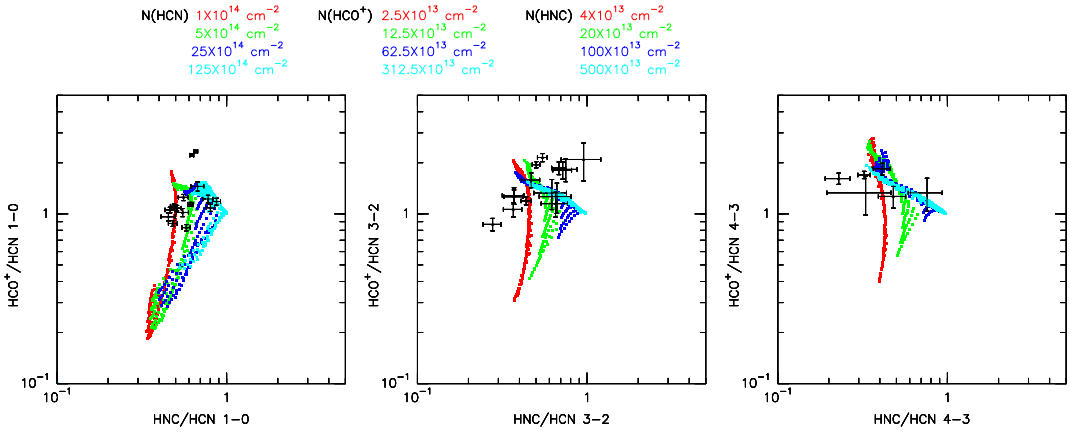

Figure 4.12 The same RADEX modeling results as shown in Figure 4.11, but shown in the intensity ratio correlation among HCN, HCO^+, and HNC. The four different colors are the RADEX results for different column densities plotted in an H_2 density range of $10^4 - 10^7$ cm^{-3} and a temperature range of $20 - 150$ K. The relative column density ratio among HCN, HCO^+, and HNC is fixed at $10 : 2.5 : 4$. The data points for the selected clumps in W49A are marked.

Table 4.2. The column density and abundance estimates for HCN, HCO^+, and HNC in W49A

	$N(H_2)$[a] (10^{22} cm^{-2})	N(HCN) (10^{14} cm^{-2})	X(HCN) (10^{-9})	$N(HCO^+)$ (10^{14} cm^{-2})	$X(HCO^+)$ (10^{-9})	N(HNC) (10^{14} cm^{-2})	X(HNC) (10^{-9})
W49A North[b]	43.5	$\gtrsim 25.0$	$\gtrsim 5.7$	$\gtrsim 6.3$	$\gtrsim 1.4$	$\gtrsim 10.0$	$\gtrsim 2.3$
W49A South	7.4	$\gtrsim 5.0$	$\gtrsim 6.8$	$\gtrsim 1.3$	$\gtrsim 1.8$	$\gtrsim 2.0$	$\gtrsim 2.7$
W49A Southwest	4.9[c]	$\gtrsim 5.0$	$\gtrsim 10.2$	$\gtrsim 1.3$	$\gtrsim 2.0$	$\gtrsim 2.0$	$\gtrsim 4.1$
W49A average	5.7	$\sim 1.0 - 5.0$	$\sim 1.8 - 8.8$	$\sim 0.3 - 1.3$	$\sim 0.5 - 2.3$	$\sim 0.4 - 2.0$	$\sim 0.7 - 3.5$

[a]The H_2 density results are taken from Table 4.1.

[b]The central position of W49A North is the region close to source G.

[c]Data are averaged over sources S and Q.

their intensity ratios are thus more sensitive to density. On the other hand, although the intensity ratios between ^{13}CO $J = 2-1$ and C^{18}O $J = 2-1$ depend on density, the ^{13}CO $J = 2-1$ emission is less optically thin, and can also highly depend on temperature. Hence, these four emission lines are chosen to be modeled with RADEX. The same geometry was used in this modeling, and the line widths of ^{13}CO $J = 2-1$, C^{18}O $J = 2-1$, HCO$^+$ $J = 1-0$, and HCO$^+$ $J = 3-2$ were fixed at 7.5 km s^{-1}. Three models have three different HCO$^+$ column densities of 2.5×10^{13} cm^{-2}, 1.25×10^{14} cm^{-2}, and 6.25×10^{14} cm^{-2} as fixed input parameters based on Table 4.2. Densities in a range of $10^4 - 10^7$ cm^{-3} and temperatures in a range of $20 - 220$ K are the free input parameters. In addition, each model of a fixed HCO$^+$ column density will be executed for four different C^{18}O column densities of 2×10^{16} cm^{-2}, 3×10^{16} cm^{-2}, 6×10^{16} cm^{-2}, and 8×10^{16} cm^{-2}. The ^{13}CO/C^{18}O abundance was fixed at the ^{13}C/^{18}O isotope ratio of (510/46). In the end, total 3×4 combinations of the HCO$^+$ and C^{18}O column densities are modeled. The modeling results are compared with the data where the HCO$^+$ $J = 3-2$ data are smoothed to the same resolution of the HCO$^+$ $J = 1-0$ data ($28''$). The results are shown in Figures 4.13–4.15.

In Figure 4.13 (a), where the input HCO$^+$ and C^{18}O column density is 2.5×10^{13} cm^{-2} and 2×10^{16} cm^{-2}, respectively, most of gas has a density of $10^5 - 10^6$ cm^{-3} and a kinetic temperature of $20 - 80$ K. This density is similar to the value of $6 \times 10^4 - 5 \times 10^5$ cm^{-3} derived from the H_2CO absorption by Dickel & Goss (1990). Some clumps in W49A South and the eastern region (near source JJ) have densities up to few times 10^6 cm^{-3}. The RADEX modeling results for the three main clumps and the whole W49A region are summarized in Table 4.3. The temperatures from the modeling results for the three main clumps are $\sim 10-18$ K lower than the ^{13}CO $J = 2-1$ excitation temperatures due largely to different beam sizes.

Since W49A South and Southwest (sources S and Q) probably have higher HCO$^+$ column densities, e.g., the model shown in Figure 4.14, the densities of both sources can be as high as 10^7 cm^{-3}. In a similar way, W49A North also shows a high HCO$^+$ column density, and the models shown in Figure 4.15 (b)–(d) indicate W49A North has a density of $\gtrsim 10^6$ cm^{-3}, which is consistent with the density value of $2 - 6 \times 10^6$ cm^{-3} derived from the CS observation (Serabyn, Guesten, & Schulz 1993).

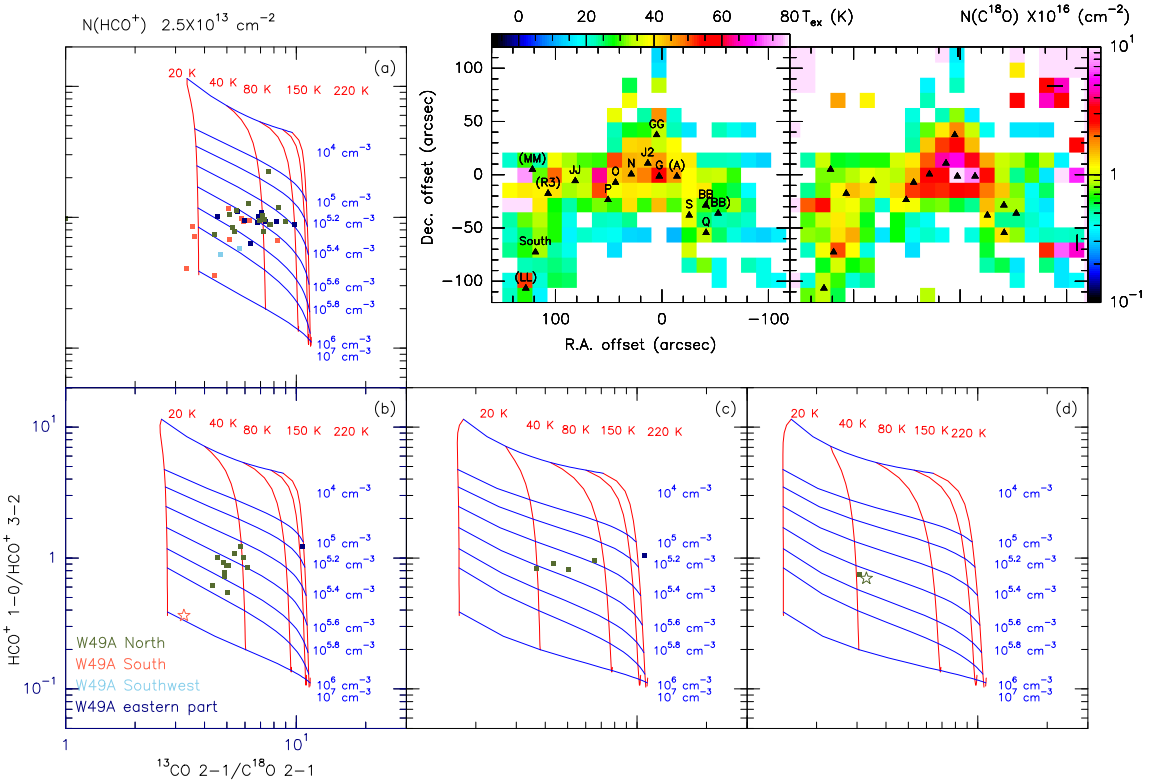

Figure 4.13 The RADEX modeling results of the ^{13}CO, C^{18}O, and HCO$^+$ peak temperature ratios in W49A. The column density of HCO$^+$ was fixed at 1×10^{13} cm^{-1}. The excitation temperature and column density of C^{18}O are shown in the upper right images (smoothed to 28″). The C^{18}O to ^{13}CO column density ratio is fixed to the abundance ratio (compared to ^{12}CO) of 46/510. (a) The modeling input C^{18}O column density N(C^{18}O) is 2×10^{16} cm^{-2}, and the data with a C^{18}O density less than 2×10^{16} cm^{-2} are plotted. (b) The input N(C^{18}O) is 3×10^{16} cm^{-2}, and the data with a C^{18}O density ranging from 2×10^{16} to 4×10^{16} cm^{-2} are plotted. (c) The input N(C^{18}O) is 6×10^{16} cm^{-2}, and the data with the C^{18}O density ranging from 4.0×10^{16} to 8.0×10^{16} cm^{-2} are plotted. (d) The input N(C^{18}O) is 8×10^{16} cm^{-2}, and the data with the C^{18}O density greater than 8×10^{16} cm^{-2} are plotted. The green, red, light blue, and dark blue points represent the pixels in the W49A North, South, Southwest, and eastern regions, respectively. The red star represents W49A South, and the green star represents source G.

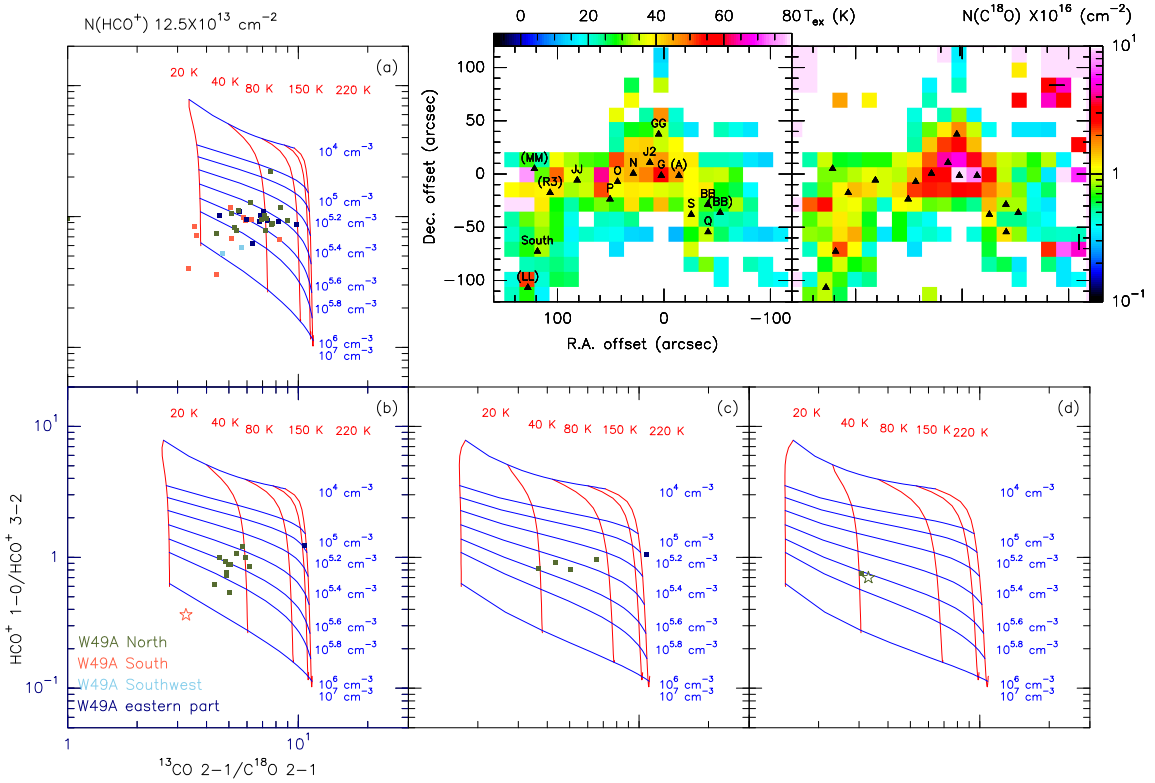

Figure 4.14 The same modeling as in Figure 4.13 with a different HCO^+ column density of 1.25×10^{14} cm^{-1}.

Table 4.3. The RADEX modeling results of W49A

Source	T_{ex} [a] (K)	T_{RADEX} [b] (K)	n_{RADEX} [b] (cm^{-3})
W49A North	57.9	~ 40	$\sim 10^6 - 10^7$
W49A South	38.7	~ 25	$\gtrsim 10^7$
W49A Southwest[c]	39.9	~ 30	$\sim 10^6$
W49A average	$\sim 20 - 60$	$\sim 20 - 80$	$\sim 10^5 - 10^7$

[a]The excitation temperature results are taken from Table 4.1 with a resolution of $\sim 18''$.

[b]The RADEX modeling results are taken from Figures 4.13 to 4.15 with a resolution of $\sim 28''$.

[c]Data are averaged over sources S and Q.

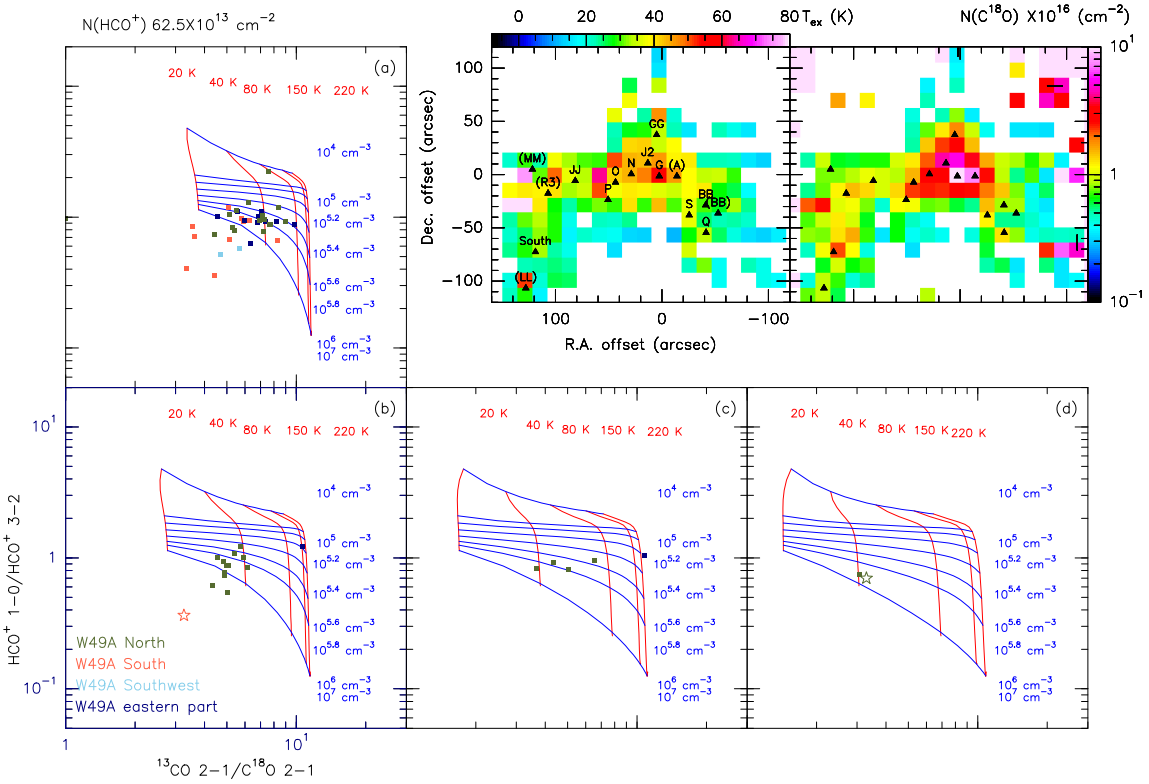

Figure 4.15 The same modeling as in Figure 4.13 with a different HCO^+ column density of 6.25×10^{14} cm^{-1}.

5

W49A Discussion

This chapter is divided by five parts. The shell structure and large-scale gas ejection in W49A will be discussed in §5.1 and §5.2. The characteristics of the UC H II regions in W49A will be discussed in §5.3. The discussion of the HCO^+/HCN and HNC/HCN ratios will be given in §5.4. In the end, the X-ray and SiO emission in W49A will be discussed in §5.5.

5.1 Expanding shells in W49A

A recent study of the mid-infrared (MIR, 5-40 μm) dust bubbles from the Galactic Legacy Infrared Mid-Plane Survey Extraordinaire (GLIMPSE; Benjamin et al. 2003) shows that, given the position coincidence with known HII regions, many MIR bubbles are produced by hot young stars, and are likely driven by expanding HII shells (Churchwell et al. 2006; Watson et al. 2008), which in turn may trigger star formation in the surrounding area. However, a similar structure in W49A has not been investigated yet, and as we shall see in this section, the shell structure plays a key role in star formation of W49A.

Figure 5.1 shows the evidence for shell structures in W49A in the 4.5 μm and 8.0 μm images from the GLIMPSE archive obtained with the Spitzer Infrared Array Camera (IRAC; Fazio et al. 2004). The 4.5 μm band, which contains pure rotational transition emission from H_2, mainly traces the distribution of warm H_2. The 8.0 μm band, which includes two aromatic infrared features at 7.7 μm and 8.6 μm, is believed to be contributed by polycyclic aromatic hydrocarbon (PAH) molecules primarily excited by UV radiation. The angular resolutions of IRAC range from $\sim 1\farcs5$ at 3.6 μm to $\sim 1\farcs9$ at 8.0 μm. In two other IRAC bands (3.6 μm and 5.8 μm), however, the same structure can be also clearly seen (Fig. 5.2). The shells were first identified by eye and then investigated in the molecular data cube. Two MIR shells have been identified (Fig. 5.1) with long axes of $55'' - 58''$ and short axes of $28'' - 35''$, which implies an average radius of $\sim 2 - 3$ pc. The average thickness

[1]The results of §5.1 and §5.2 have been submitted to A&A. W49A: A starburst triggered by expanding shells, Peng, T.-C.; Wyrowski, F.; van der Tak, F.; Menten, K. M.; Walmsley, M.

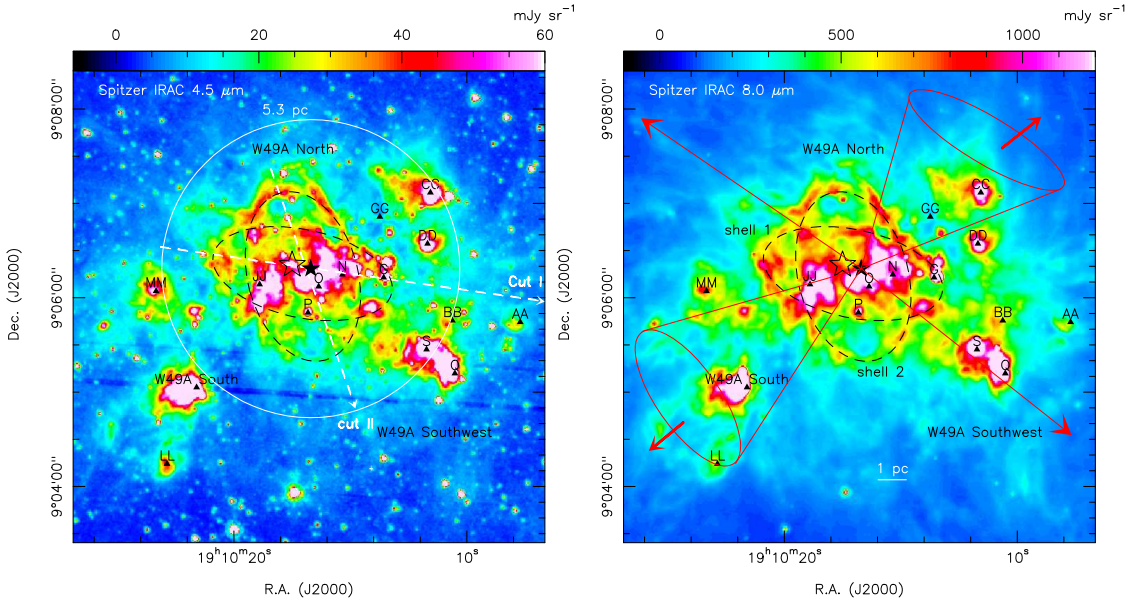

Figure 5.1 The Spitzer-GLIMPSE IRAC 4.5 μm (left) and 8.0 μm (right) images of W49A. Black triangles denote the UC HII regions observed by De Pree, Mehringer, & Goss (1997). The black dotted-lines are the suggestive expanding shells, and the black filled-star represents the center of an averaged expanding shell and the gas ejections (see text). The larger unfilled black star represents the embedded cluster center inferred by Alves & Homeier (2003). The white circle in the left image indicates the largest radius (5.3 pc) used in the circular PV diagram, and two white dashed-lines represent the linear PV cuts. Red lines and arrows in the right image indicate the direction of gas ejections.

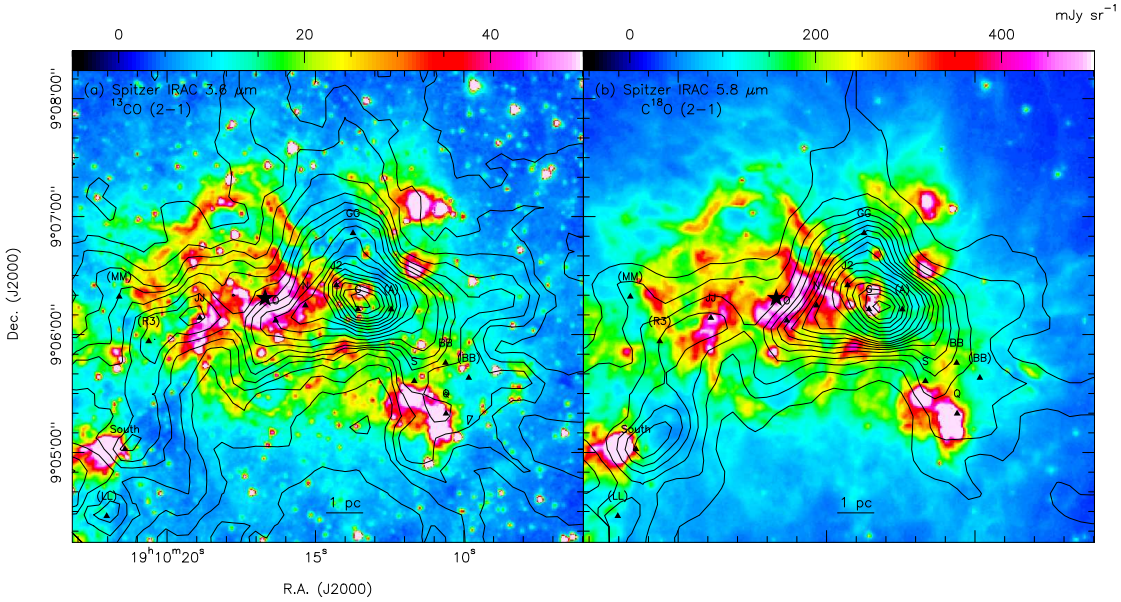

Figure 5.2 (a) The Spitzer IRAC 3.6 μm image overlaid with the ^{13}CO $J = 2 - 1$ contours running from 30 to 210 K km s^{-1} in steps of 30 K km s^{-1} and subsequent contours running from 250 to 750 K km s^{-1} in steps of 50 K km s^{-1}. (b) The Spitzer IRAC 5.8 μm image overlaid with the C^{18}O $J = 2 - 1$ contours from 9 to 66 K km s^{-1} in steps of 6 K km s^{-1} and subsequent contours running from 75 to 180 K km s^{-1} in steps of 15 K km s^{-1}. The radio sources in the region are marked.

of the MIR shells is estimated to be $7\farcs5 \pm 1\farcs9$ (0.4±0.1 pc) by fitting Gaussian profiles to the shells. These two MIR shells lie in the east-west and north-south direction, and have a similar size and elliptical shape. In addition, they seem to share a same geometry center.

However, it is difficult to identify any similar shell struture in the channel maps of the ^{13}CO and C^{18}O $J = 2 - 1$ lines (see Fig. 5.4). PV diagrams are thus applied to investigate this shell structure, and are used to examine whether a shell is an expanding ring/bubble also in the molecular line data. The linear PV diagrams of ^{13}CO $J = 2 - 1$ and C^{18}O $J = 2 - 1$ are shown in Figure 5.3, corresponding to the east-west cut (Cut I) and the north-south cut (Cut II) in Figure 5.1, where the two MIR shells are revealed in the PV diagrams. In addition, the clumps are located along the shells which indicates a connection between them. In order to estimate the mass and kinematic properties of the multi-shell structure, we applied a circular PV diagram which azimuthally averages the velocity in a given radius from a center. The center was chosen to have the largest velocity difference between the peaks in the C^{18}O $J = 2 - 1$ spectra, and was found to be close to the UC HII regions O and N. Besides, the circular PV diagram (Fig. 5.5) shows a clear half ellipse signature which implies an expanding motion centered on a common origin. Therefore, it seems likely that those two MIR shells share a common expansion center with an average inner radius of $\approx$ 2.9 pc assuming 10% uncertainty and an expanding velocity of $\sim$ 5 km s^{-1}. It is unlikely

that the shells are actually molecular rings (Beaumont & Williams 2009) because two-component spectra are seen toward the center of the shells probing the front and back of the shells. The linear PV diagrams of different molecular lines through the shells are shown in Figures A.2–A.14.

In the LTE assumption, we can estimate the H_2 density of the expanding shells from the $^{13}CO/C^{18}O$ $J = 2 - 1$ ratio, assuming their optical depth ratio is the same as the abundance ratio. We adopted $^{12}C/^{13}C$ of 46 and $^{16}O/^{18}O$ of 510 (Wilson & Rood 1994; Langer & Penzias 1990) for W49A (8.1 kpc to the Galactic center, Gwinn, Moran, & Reid 1992). The excitation temperature of the averaged shell is estimated to be about 25 K. The averaged H_2 column density of the shell is $\approx 8.5 \times 10^{22}$ cm^{-2}, excluding the contribution from source G, e.g., consider the shell density only within a radius of 40″. The temperature and density of the average shell are shown in Figure 5.6. Assuming a 10% uncertainty, we calculate an H_2 density, $n(H_2)$, of $\approx 6.7 \pm 2.1 \times 10^3$ cm^{-3} in a spherical structure with a filling factor of 1, and a ^{12}CO abundance of 2×10^{-4} (e.g., Lacy et al. 1994). The mass of the averaged shell ($M_{\rm sh}$) can also be estimated as $1.9 \pm 0.7 \times 10^4$ M$_\odot$. Then the kinetic energy ($\frac{1}{2}M_{\rm sh}V_{\rm sh}^2$) and momentum ($M_{\rm sh}V_{\rm sh}$) can be computed to be $4.6 \pm 3.0 \times 10^{48}$ erg and $9.3 \pm 4.0 \times 10^4$ M$_\odot$ km s^{-1}, respectively, assuming a 20% uncertainty in the expansion speed measurement.

5.1.1 Molecular spectra toward the shell expansion center

Figure 5.7 shows the Spitzer pseudo-color image overlaid with the ^{13}CO $J = 2 - 1$ emission peaking at the region near source G. The MIR shells structure is clearly seen in the east of source G. The reason that this shell structure is not obvious in the ^{13}CO $J = 2 - 1$ and $C^{18}O$ $J = 2 - 1$ integrated images and their channel maps (Figs. 3.5 and 3.6) is probably due to the small expansion velocity (~ 5 km s^{-1}) which makes it difficult to distinguish the expanding shells from the ambient gas.

The spectra toward the suggestive shell expansion center are shown in Figures 5.8 and 5.9. The shell expansion has an initial $V_{\rm LSR}$ at ~ 8 km s^{-1} with an expansion velocity of ~ 5 km s^{-1}. The absorption features at $14 - 19$ km s^{-1} are due to the absorption by the Perseus Arm (see §3.1). The absorption features at ~ 6 km s^{-1} are probably due to self-absorption associated with the whole W49A North cloud, since these features are seen throughout W49A North, e.g., the PV diagrams of HCN, HCO^+, and ^{12}CO in §3 and the H_2O spectrum from the SWAS (Figs. 5.8 and 5.9). In Figure 5.9, the 6 km s^{-1} absorption features are more obvious in the HCO^+ spectra than in the HCN spectra, which indicates that the HCO^+ emission suffers more from self-absorption than the HCN emission does. Figure 5.8 also shows that the blueshifted shell component seen in the ^{12}CO $J = 3 - 2$ and ^{13}CO $J = 2 - 1$ spectra is self-absorbed, and the line wings of the redshifted shell component are absorbed by the Perseus Arm. In addition, the $C^{18}O$ $J = 2 - 1$ spectra show weak absorption at these two velocities (~ 6 km s^{-1} and $14 - 19$ km s^{-1}).

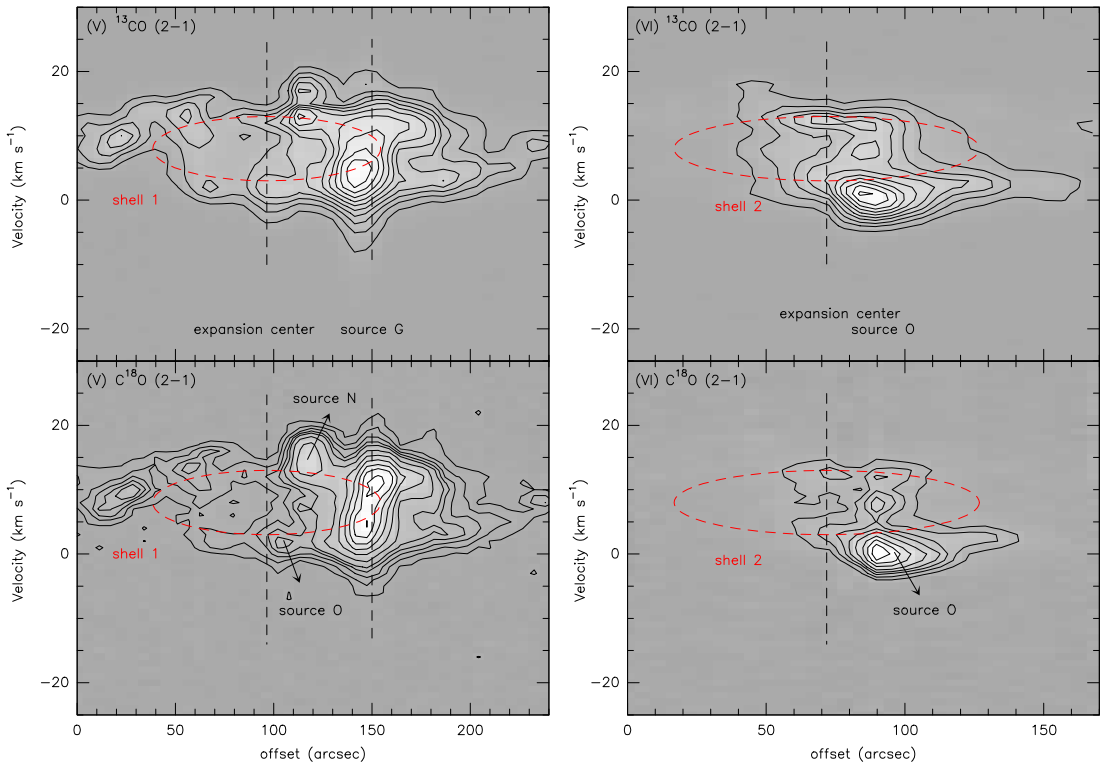

Figure 5.3 The PV diagrams of the ^{13}CO and C^{18}O $J = 2 - 1$ emission in the molecular shell shown in Figure 5.1. (V) The ^{13}CO $J = 2 - 1$ contours run from 4 to 44 K in steps of 4 K, and the C^{18}O $J = 2 - 1$ contours run from 0.5 to 2.5 K in steps of 0.5 K, and the subsequent contours are from 3.5 to 11 K in steps of 1.5 K. (VI) The ^{13}CO $J = 2 - 1$ contours run from 3 to 31 K in steps of 4 K, and the C^{18}O $J = 2 - 1$ contours run from 0.8 to 2.3 K in steps of 0.5 K, and the subsequent contours run from 3 to 6 K in steps of 1 K. The red dashed ellipses correspond to the MIR shells seen in Figure 5.1 with an expansion speed of 5 km $^{-1}$. The shell expansion center and sources O and N are indicated in the diagrams, and the circular PV diagrams for different molecules are shown in Figures A.14 and A.15.

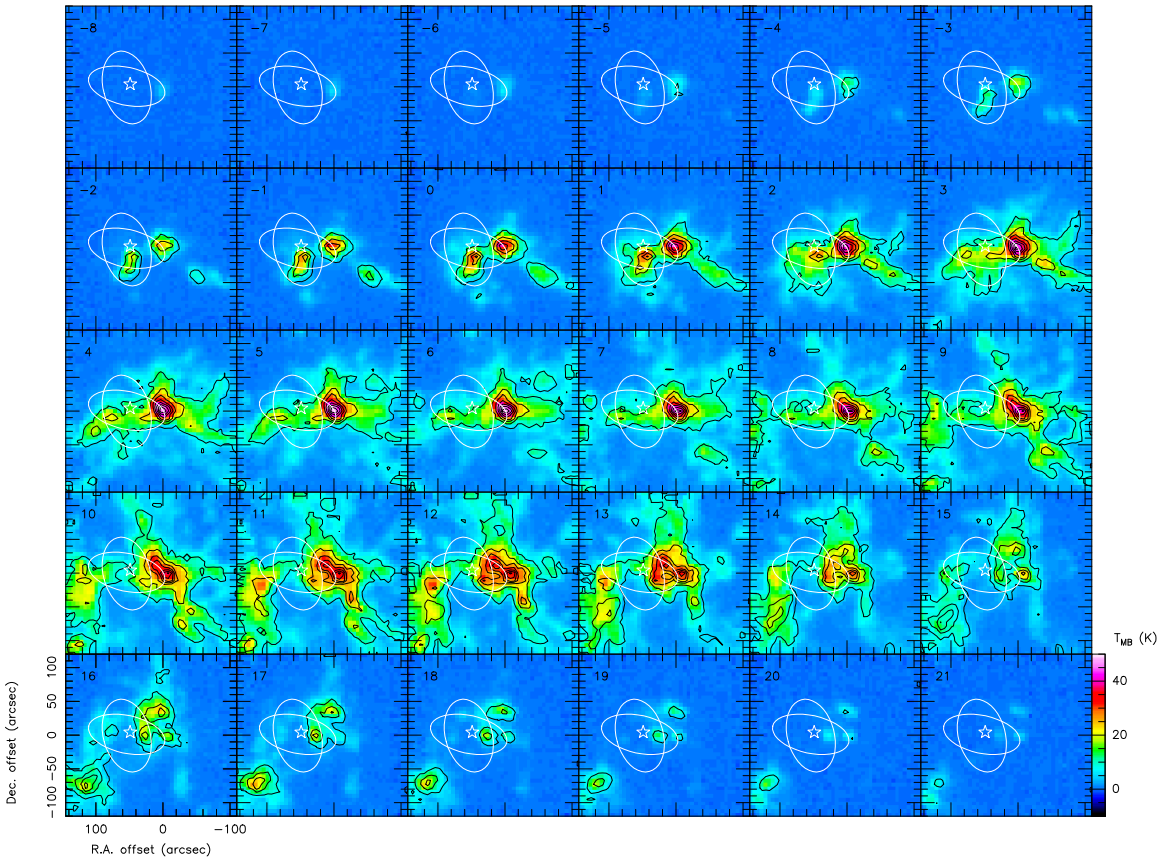

Figure 5.4 The channel maps of ^{13}CO $J = 2-1$ overlaid with the C^{18}O $J = 2-1$ emission in black contours with a resolution of $11''$. The contours are plotted from 1 to 15 K in steps of 2 K. The white ellipses represent two suggestive shells, and the white star marks the shell expansion center. The $(0'', 0'')$ position is located at the region around source G.

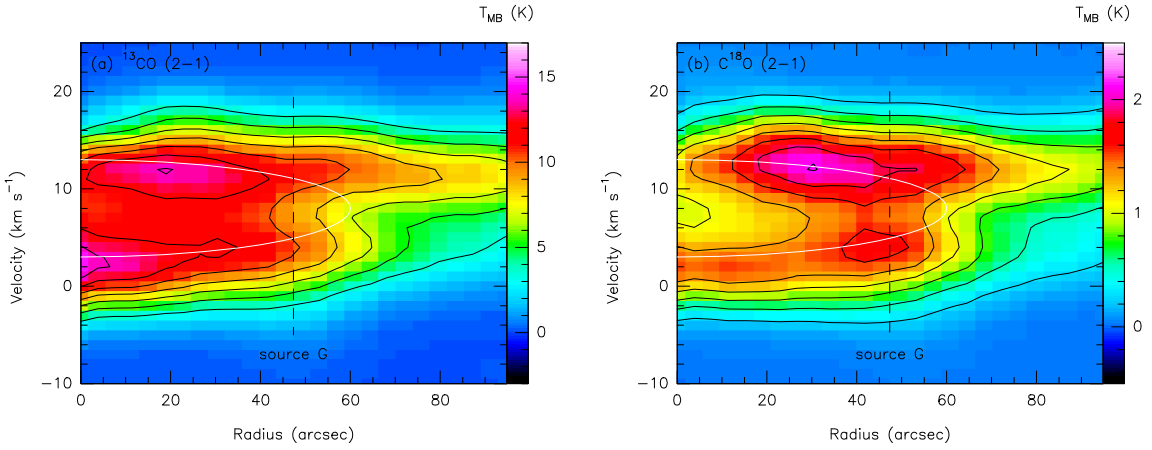

Figure 5.5 The circular PV diagrams of the ^{13}CO and C^{18}O $J = 2-1$ emission in the molecular shell shown in Figure 5.1. The white ellipses represent an averaged expanding shell with an expansion speed of 5 km $^{-1}$ centered at ~ 8 km s^{-1}.

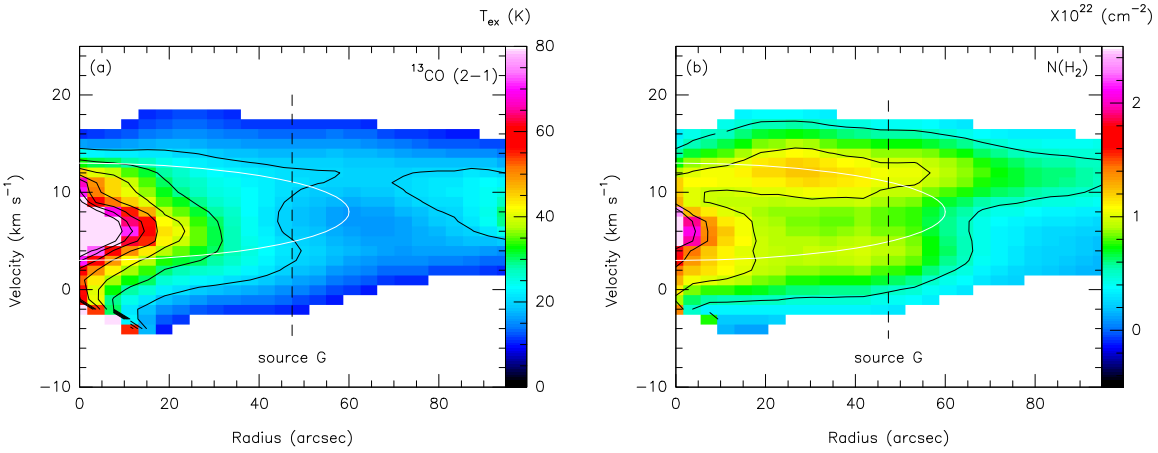

Figure 5.6 The circular PV diagrams of the excitation temperature and H_2 density. (a) The black contours denote temperatures running from 20 to 80 K in steps of 10 K. (b) The black contours denote H_2 column densities of 0.5×10^{22} cm^{-2}, 1.0×10^{22} cm^{-2}, and 1.5×10^{22} cm^{-2}. The white ellipses represent an averaged expanding shell with an expansion speed of 5 km $^{-1}$ centered at ~ 8 km s^{-1}.

5.1.2 Mid-infrared emission of the shells

In Figure 5.10, two intensity cuts for all four IRAC bands show clear peaks corresponding to the expanding shells. Both shells show counterparts in all bands at the same position. Only shell 2 in Cut a has an offset of about 3″ between the 3.8/4.5 μm and 5.8/8.0 μm emission. The reason for this offset is not clear. At the angular resolution of the IRAC range (from $\sim 1\farcs5$ at 3.6 μm to $\sim 1\farcs9$ at 8.0 μm), this offset is barely resolved. Besides, both shells show relatively large widths of $\sim 12''$ in Cut a, and smaller widths of $\sim 3''$ in Cut b compared with the average shell width of $\sim 7.5''$. This large difference in shell widths is also not clear, but is likely due to projection effects.

Figure 5.11 shows a similar figure as Figure 5.10 but in the color-color diagrams of [3.6]–[4.5] μm and [4.5]–[5.8] μm. It is clear that the [4.5]–[5.8] color decreases in both shells except for shell 1 in Cut a. The smaller [4.5]–[5.8] color means that the 5.8 μm emission decreases inside the shells, or the 4.5 μm emission is enhanced. On the other hand, the [3.6]–[4.5] color seems to increase in both shells 1 and 2. Therefore, the anti-correlation between two colors indicates that the 4.5 μm emission, which contains a pure rotational transition (S9) of H_2 at 4.69 μm, is enhanced. Since the (S9) line requires the excitation of the $J = 11$ rotational state, which is ~ 10000 K above the ground, the enhanced 4.5 μm emission provides evidence for extra heating in the shell structure of W49A. Furthermore, the color-color diagram shown in Figure 5.12 also reveals three tendencies (a−c). Trend a has a roughly constant [3.6]–[4.5] colors with [4.5]–[5.8] colors ranging from 0 to 4, and trend b has an anti-correlation between the [3.6]–[4.5] and the [4.5]–[5.8] colors. However, trend c, which is only shown in the region around source G, has roughly constant [4.5]–[5.8] colors with [3.6]–[4.5] colors ranging from 1 to 3. Trend c indicates enhanced 4.5 μm emission, and this

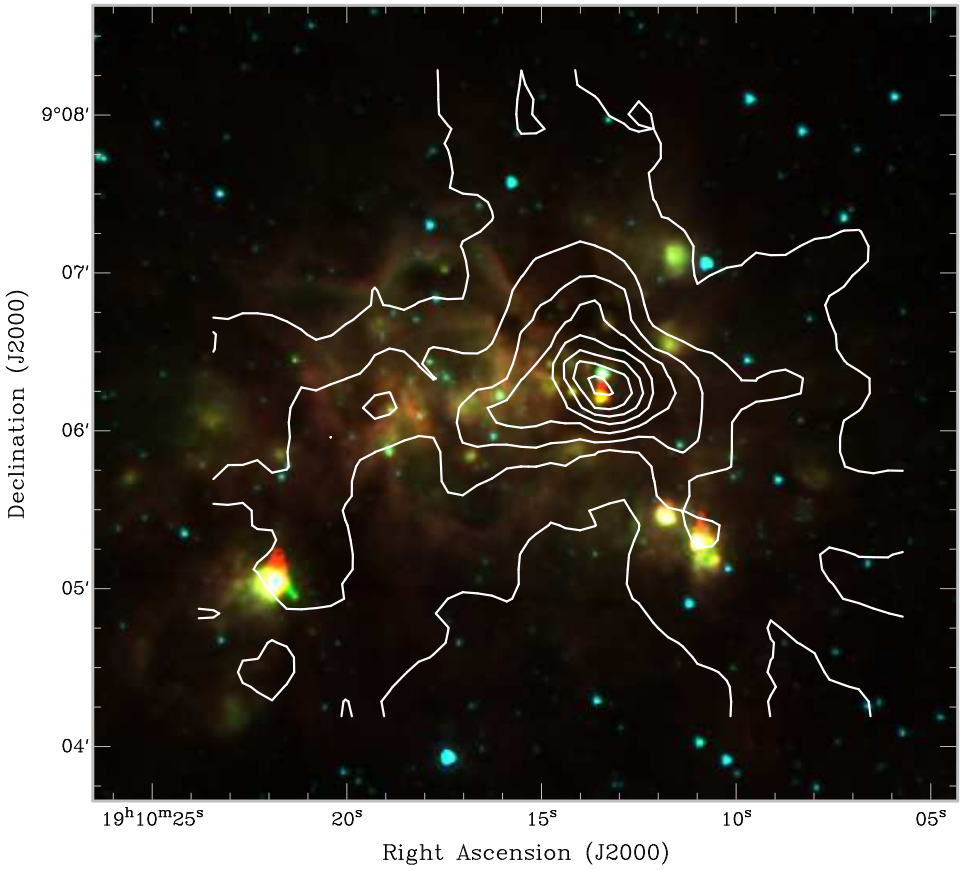

Figure 5.7 The Spitzer pseudo-color image of W49A. Red, green, and blue color represents the IRAC 3.6 μm, 4.5 μm, and 8.0 μm image, respectively. The white contours represent the ^{13}CO $J = 2 - 1$ emission (11.″2) from 50 to 750 K km s^{-1} in steps of 100 K km s^{-1}.The ^{13}CO emission peak is located at the region near source G (1 parsec=18.″1).

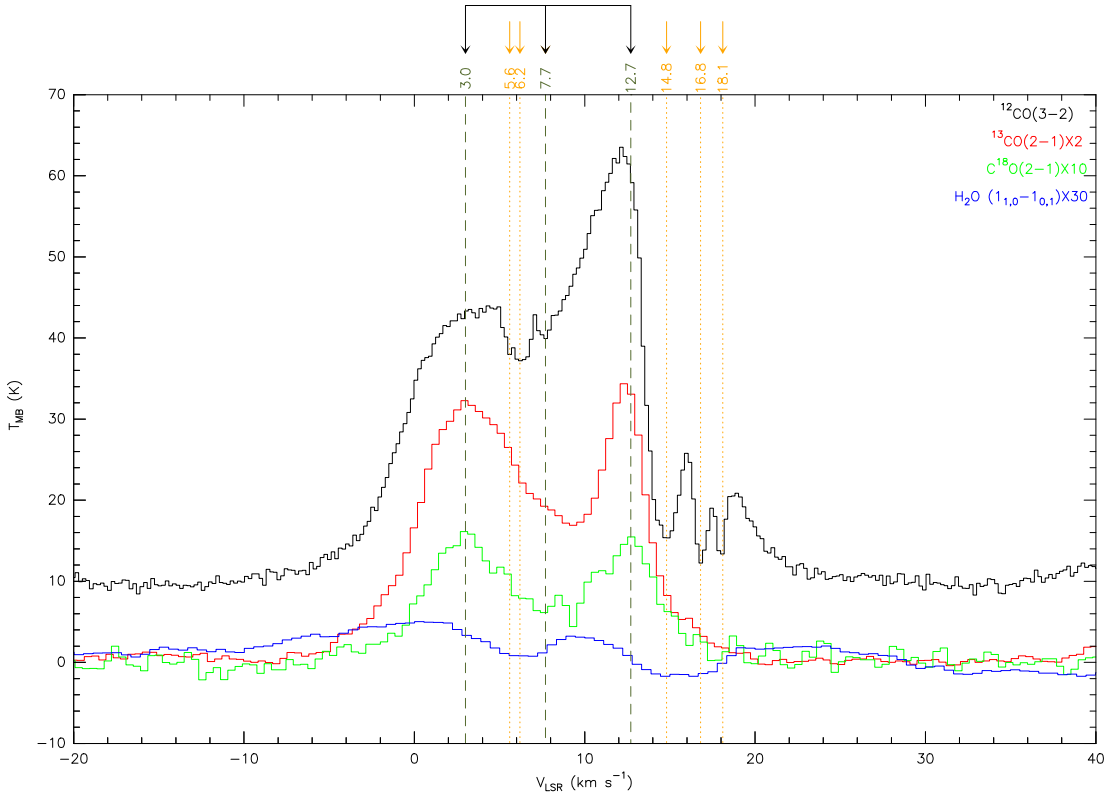

Figure 5.8 The ^{12}CO $J = 3-2$, ^{13}CO $J = 2-1$, C^{18}O $J = 2-1$, and H_2O $1_{1,0} - 1_{0,1}$ spectra in the suggestive shell expansion center. The expanding shell and the central cloud emission are indicated in olive dashed-lines, and the absorption lines are indicated in orange dotted-lines. For clarity, the line profiles have been shifted.

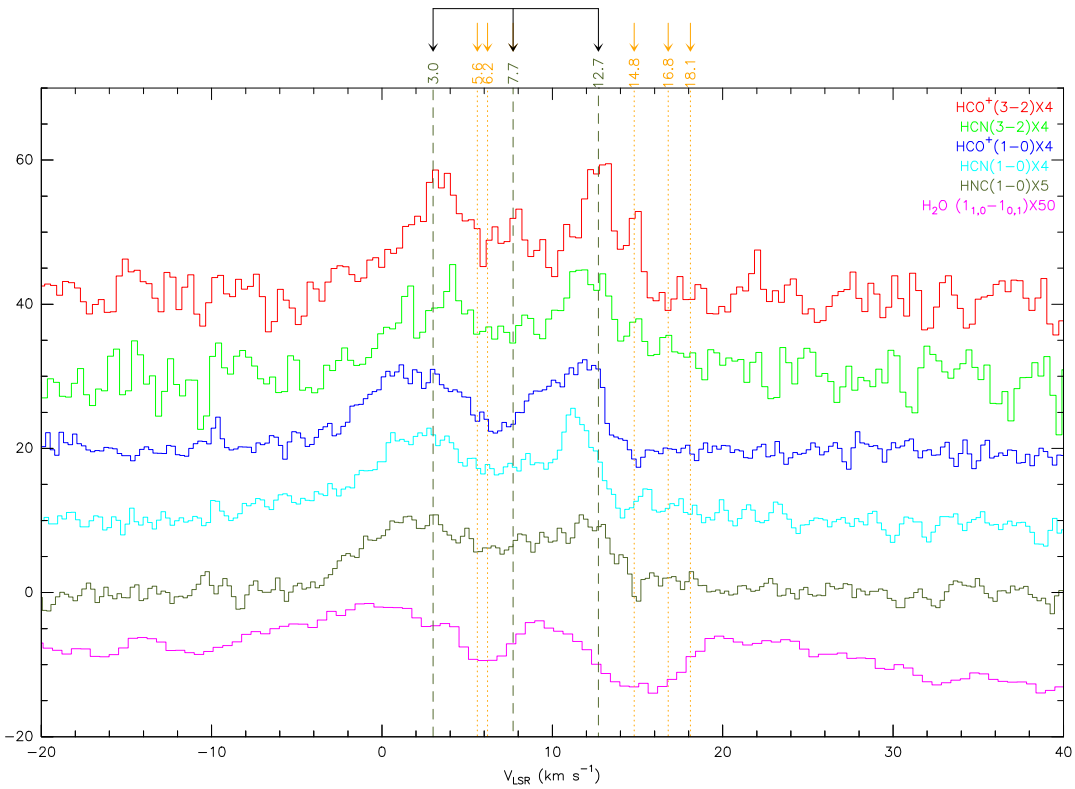

Figure 5.9 The HCO^+, HCN, HNC, and H_2O spectra in the suggestive shell expansion center. The expanding shell and the central cloud emission are indicated in olive dashed-lines, and the absorption lines are indicated in orange dotted-lines. For clarity, the line profiles have been shifted.

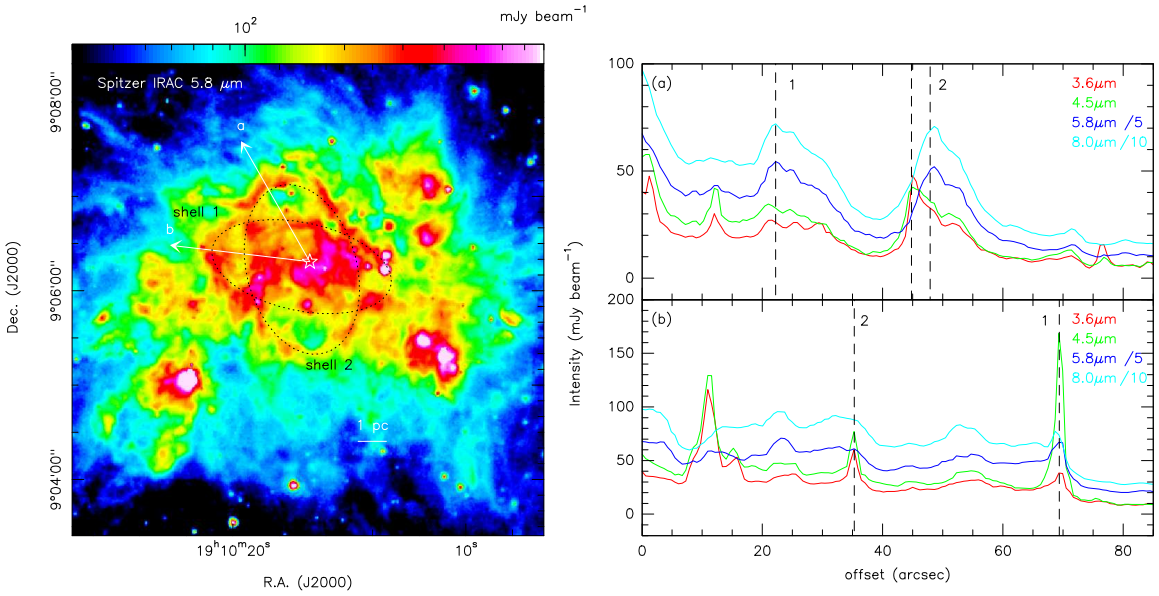

Figure 5.10 Left image shows the Spitzer IRAC 5.8 μm image. Right panel shows two intensity strips corresponding to the two cuts in the left image. Shells 1 and 2 are marked in black dotted-ellipses, and the white star represents the suggestive shell expansion center.

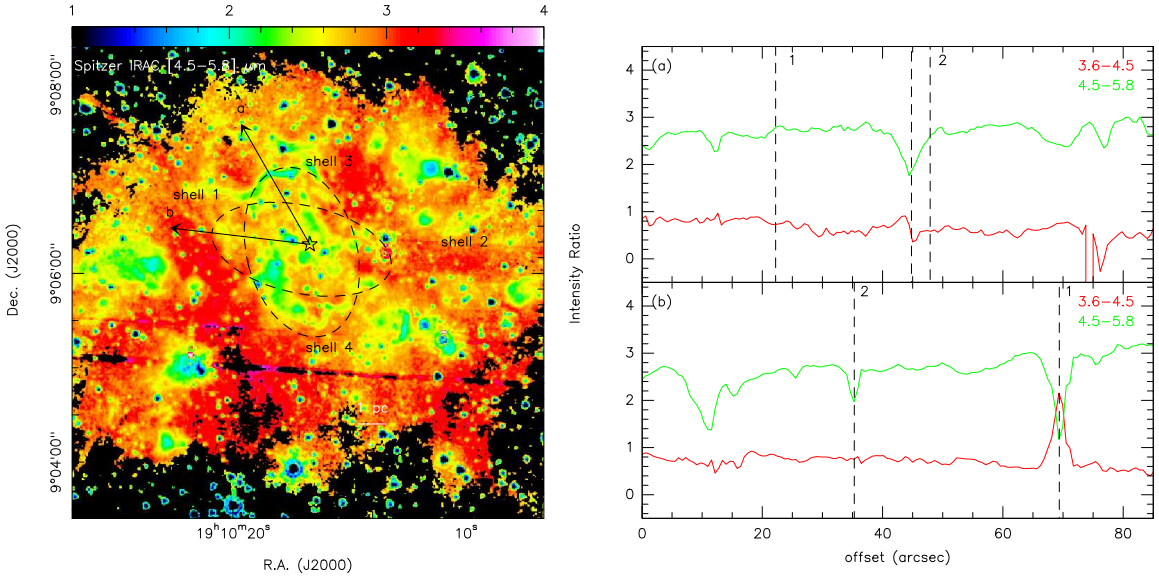

Figure 5.11 Left image shows the Spitzer IRAC [4.5]–[5.8] color-color image. Right panel shows two intensity ratio strips corresponding to the two cuts in the left image. The suggestive shells are marked, and the black star represents the suggestive shell expansion center.

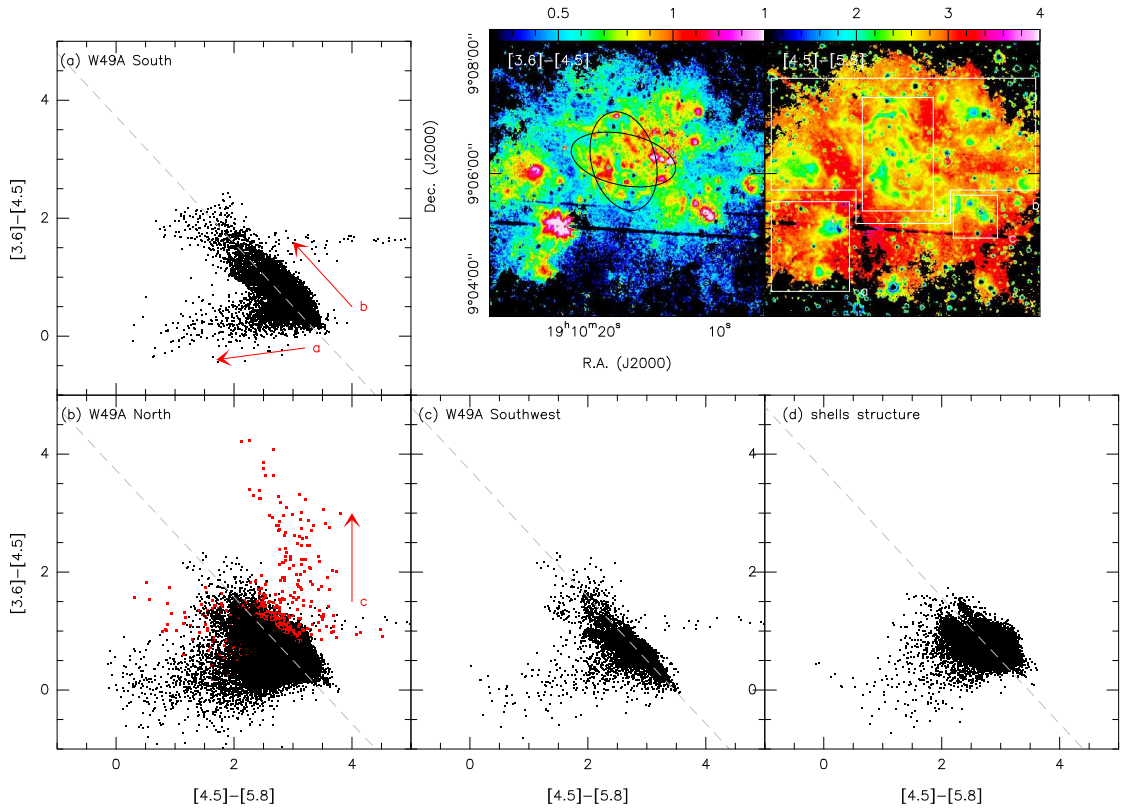

Figure 5.12 The IRAC color-color ([4.5]–[5.8] verse [3.6]–[4.5]) diagrams of W49A. The two color-color images are shown in the upper-right corner. (a)-(d) The color-color diagrams in W49A North, South, Southwest, and the central part of the shells structure. Three main trends (a, b, and c) of the data are indicated in red arrows. The red squares represent the data in the source G region.

enhancement is clear seen in W49A South, Southwest, and the shell structure. Trend a is the result from very red sources deeply embedded inside the cloud, where some sources even have [3.6]–[4.5] color values smaller than unity. However, trend c is probably similar to trend b but shows even strong enhancement of the 4.5 μm emission due to local shock activities, e.g., outflows associated with the H_2O masers.

5.1.3 The driving mechanism of the expanding shells

The reason for the elliptical shape of the two shells is not clear, but it is probably due to the different expansion velocities in two axes, or due to a more complicated explosion. In the interstellar bubble model of Weaver et al. (1977), where the expanding shells are driven by winds, the age of an average expanding shell in W49A can be estimated as $3.4 \pm 0.4 \times 10^5$ yr from the shell radius and the expansion speed ($t = \frac{3}{5}\frac{R_{\rm sh}}{V_{\rm sh}}$). Here, the radius of the shell depends on the mass-loss rate $\dot{M}$ of the

driving source (Weaver et al. 1977)

$$R_{\rm sh}(t) = 28.1 \left(\frac{\dot{E}}{10^{36}\ {\rm erg\ s^{-1}}}\right)^{1/5} \left(\frac{\mu\ n_0}{1\ {\rm cm^{-3}}}\right)^{-1/5} \left(\frac{t}{10^6\ {\rm yr}}\right)^{3/5} {\rm pc}, \tag{5.1}$$

where $\dot{E}$ is the mechanical luminosity ($\dot{E} = \frac{1}{2}\dot{M}_w V_w^2$), and n_0 is the ambient H density. We derived an average H_2 density of $\sim 2 \times 10^3$ cm^{-3} in W49A by using the ^{13}CO/C^{18}O $J = 2 - 1$ ratio mentioned above, and we adopted n_0 of 4×10^3 cm^{-3} here (see §4.1), and a stellar wind velocity V_w of 2000 km s^{-1}. Therefore, a constant mass-loss rate of $\sim 1.2 \times 10^{-6}$ M$_\odot$ yr^{-1} is needed to sustain a wind-driven bubble in a size of ~ 4.4 pc, which corresponds to an O star. In addition, $\sim 20\%$ of the wind energy is channeled into the kinetic energy of the swept-up shell (Weaver et al. 1977), which means a total energy of $\approx 3.4 \times 10^{48}$ erg is provided by winds during the expansion. This energy agrees with the averaged shell kinetic energy of $4.6 \pm 3.0 \times 10^{48}$ erg. However, because of the elliptical shape of the two shells, their expansion might not follow the interstellar bubble model discussed above. Therefore, a reasonable upper-limit of the shell age ($t \leq \frac{R_{\rm sh}}{V_{\rm sh}}$) is estimated as $5.7 \pm 1.3 \times 10^5$ yr, assuming a monotonic decreasing expansion velocity or a constant velocity. Hence, the age of these expanding shells is likely about $3 - 7 \times 10^5$ yr.

On the other hand, the high radiation pressure in HII regions can also provide enough energy to drive an expanding shell (e.g., Krumholz & Matzner 2009). Homeier & Alves (2005) estimate a cluster mass of $\sim 1 \times 10^4$ M$_\odot$ around sources O and N by summing 54 stars with masses greater than 20 M$_\odot$ within 2.5 pc, which means this cluster probably hosts $\sim 30 - 50$ O6 stars with an ionization luminosity $Q \sim 1 \times 10^{51}$ s^{-1} (Vacca, Garmany, & Shull 1996), which in turn corresponds to a luminosity of $L = 8 \times 10^{40}$ erg s^{-1}. The luminosity ($L = P_{\rm sh}c/t$) needed for energy-driven shells can be estimated to $\sim 8 \times 10^{39}$ erg s^{-1}, assuming no photon leaking. Therefore, no matter whether the expanding shells are momentum-driven by winds or energy-driven by radiation pressure, only a few massive stars can account for the driving energy instead of the whole cluster. A recent model of W49A by Murray, Quataert, & Thompson (2010) demonstrated that the radiation pressure from a new born cluster forms a bubble, then disrupts the whole cloud eventually. In their one-dimensional model, the outward force is dominated by protostellar jets during the first 3×10^5 yr. Radiation pressure dominates thereafter until the first supernova explode. However, it is not clear how those jets can drive the shell in W49A. Furthermore, leaking photons might also reduce the radiation force on the shell. Nevertheless, the shell structure we see in W49A is hardly explained by radiation pressure alone, and might involve more complicated factors. Additionally, since most of the embedded sources seen by Homeier & Alves (2005) are probably the stars formed after shell fragmentation, it is likely that the multi-shell structure has a common origin at the beginning, which is close to the embedded cluster center indicated by Homeier & Alves (2005), and triggers the star formation later when the shells expand.

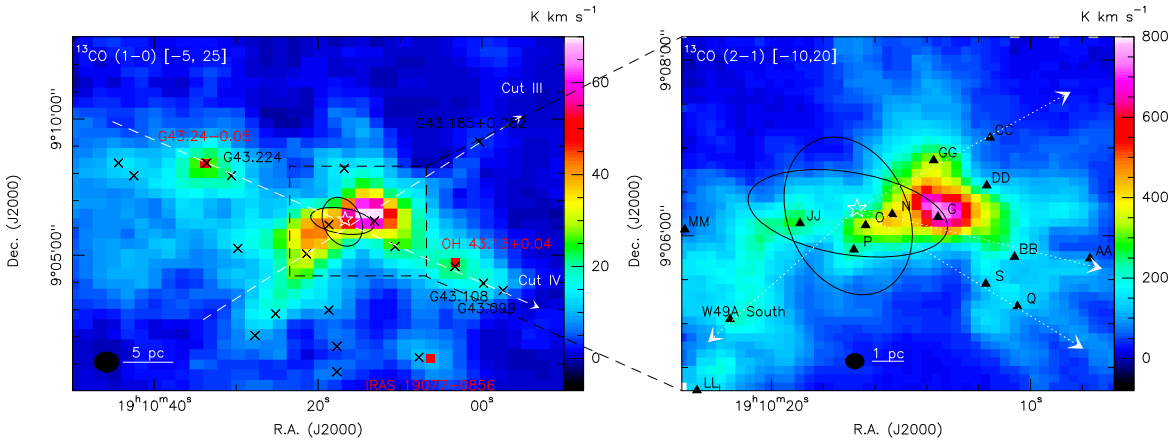

Figure 5.13 Left panel shows the large-scale GRS ^{13}CO $J = 1 - 0$ emission of the W49 complex, and the right panel shows the ^{13}CO $J = 1 - 0$ emission from the IRAM 30m telescope in the local area of W49A. The MIR shell structure is indicated with black ellipses. The white-dashed lines represent two linear PV cuts shown in Figure 5.14. The white dotted-lines represent the suggestive alignments or ejections of molecular gas. Black crosses denote the 850 μm dust continuum sources from Matthews et al. (2009). Black triangles denote the UC HII regions from De Pree, Mehringer, & Goss (1997).

5.1.4 Fragmentation of the shell

According to Whitworth et al. (1994), an expanding shell begins to fragment at $t_{\rm fragment} \sim (G\rho_o\mathcal{M})^{-1/2}$, depending on the ambient density ρ_0 and the shell Mach number $\mathcal{M}$, and the time scale for fragmentation, $t_{\rm fragment}$, is shorter than the time scale needed for the shells to become dominated by self-gravity, $t_{\rm gravity} \sim (G\rho_{\rm sh})^{-1/2}$. The value of $t_{\rm fragment}$ is estimated to be $\approx 3.7 \times 10^5$ yr, with a sound speed $C_{\rm H_2}$ of 0.35 km s^{-1}, and a Mach number of about 14 inside the shell. The time-scale for the shell in W49A to fragment into clumps and further collapse to form new stars is within $\sim 1 \times 10^5$ yr, which roughly corresponds to the massive star forming time-scale (Zinnecker & Yorke 2007). The clumps formed after fragmentation are well-separated as shown in Figure 5.3, and the two velocity components at ~ 4 km s^{-1} and ~ 12 km s^{-1} toward source G should be treated as two clumps on the line-of-sight.

5.2 Large-scale gas ejections

A recent paper by Matthews et al. (2009) reveals the distribution of dust clumps in the large-scale environment of the W49 complex, including one UC HII region G43.24 − 0.05 (Kurtz, Churchwell, & Wood 1994) and one hydroxyl maser source OH 43.13 + 0.04 (Becker, White, & Proctor 1992). Many dust clumps are aligned toward the region near sources O and N, which is close to the center of the expanding shells (Fig. 5.13). Furthermore, the PV diagrams obtained from the Galactic Ring

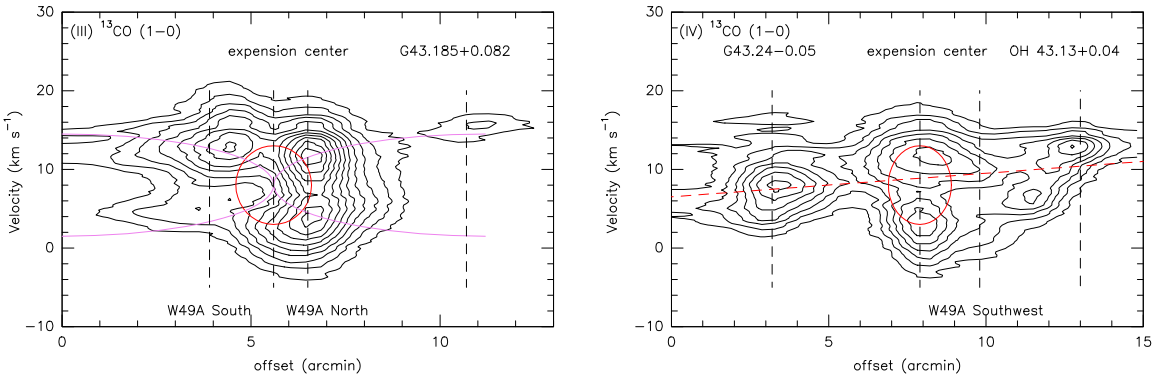

Figure 5.14 (III)-(IV) The SE-NW and NE-SW PV diagrams corresponding to Cut III and IV in Figure 5.13.A shell of a radius size about 4 pc is indicated in red circles. The violet lines represents the double-cone shape gas ejections, and the red dashed-line represents the direction of the bipolar gas ejection. The ^{13}CO $J = 1 - 0$ contours run from 0.4 to 4.8 K in steps of 0.4 K.

Survey (GRS; Jackson et al. 2006) ^{13}CO $J = 1-0$ emission apparently show a corresponding outflow structure. For example, the PV diagram of Cut IV shown in Figure 5.14 indicates a bipolar outflow between G43.24−0.05 and OH 43.13+0.04 where expanding shells are located in the center. The dust clump alignment and the symmetric PV diagram is unlikely a coincidence. Besides, other evidence comes from the alignment of UC HII regions (Fig. 5.13) toward the shell expansion center, and the ^{13}CO $J = 2 - 1$ filaments also have an obvious radial geometry coming from the shell expansion center, although those filaments might be related to W49A North or source G. Still further evidence for the gas ejections comes from the large-scale gas distribution of the W49 complex in the NE-SW axis, where no obvious gas accumulation have been seen but highly aligned dust clumps, and in the NW-SE direction that widely-distributed molecular gas and UC HII regions present together with a double-cone structure shown in Figure 5.13. The two-axis morphology mimicking the shape of a butterfly is also similar to the H_2 fingers seen in the Orion BN/KL region (Allen & Burton 1993).

We can estimate the energy of the gas ejections by assuming that they happened at the same time when the shells start to expand (i.e., 5.7×10^5 yr as an upper-limit), and by adopting the clump mass estimated by Matthews et al. (2009). In the northeastern ejection, G43.24–0.05 and submillimeter source G43.224–0.038 have a total projected kinetic energy of $1.3 \pm 0.6 \times 10^{50}$ erg; in the southwestern ejection, W49A Southwest, OH 43.13+0.04, submillimeter sources G43.108+0.044 and G43.099–0.050 have a total projected kinetic energy of $1.1 \pm 0.3 \times 10^{50}$ erg, assuming 20% uncertainty in their mass measurements. The kinetic energy estimates are summarized in Table 5.1. The ejection for both directions is roughly equal and has a total projected energy of $2.4 \pm 0.7 \times 10^{50}$ erg. Only if the ejection age was seven times larger than the age of expanding shells, the kinetic energy for both events would be similar. Whether the gas ejection happened earlier or not, the total energy released by the shells expansion and gas ejection has a magnitude of 10^{50} erg. It is worth noting that G43.24–0.05 is located at a similar distance ($11.7^{+0.8}_{-0.7}$ kpc; Watson et al. 2003) as

Table 5.1. The kinetic energy estimates of gas ejections

Source	D^{a} (pc)	M^{b} ($M_\odot$)	V^{c} (km s^{-1})	$E_{\rm kin}$ ($\times 10^{49}$ erg)
G43.224–0.038	12.6	2.6×10^3	21.7 ± 4.9	1.2 ± 0.6
G43.24–0.05	15.6	1.6×10^4	26.8 ± 6.0	11.4 ± 5.6
W49A Southwest	6.2	3.5×10^4	10.7 ± 2.4	4.0 ± 2.0
OH43.13+0.04	12.2	8.0×10^3	21.0 ± 4.7	3.5 ± 1.7
G43.108+0.044	15.9	1.9×10^3	27.4 ± 6.1	1.4 ± 0.7
G43.009+0.050	18.0	2.0×10^3	31.0 ± 6.9	1.9 ± 0.9

[a]The distance to the shell expansion center without a projection correction.

[b]The gas mass of clumps are adopted from Matthews et al. (2009).

[c]The ejection velocity of clumps assuming a constant ejection velocity in 5.7×10^5 yr.

W49A, and probably hosts a newly born star producing the UC HII region. In addition, it is likely that the nearby source G43.224–0.038 is related to G43.24–0.05. The nature of the OH maser source OH43.13+0.04 is not clear, since it is not associated with any Infrared Astronomical Satellite (IRAS) source (Becker, White, & Proctor 1992). However, OH43.13+0.04 is unlikely an OH/IR foreground star because of its extended morphology in the ^{13}CO $J = 1 - 0$ image (Fig. 5.13), and is possibly associated with an HII region. Furthermore, the nature of the submm sources G43.108+0.044 and G43.009+0.050 is also unknown, and more investigations are needed.

The magnetic field measurement by Brogan & Troland (2001) shows a gradient in the line-of-sight component of the magnetic field, $B_{\rm los}$, in the NE-SW direction crossing the expansion center, where a very weak $B_{\rm los}$ is derived from the 7 km s^{-1} HI component. For a radially increasing magnetic field, a very weak $B_{\rm los}$ should be indeed expected in the shell expansion center ($V_{\rm LSR} \sim 7-8$ km s^{-1}). The fact that $B_{\rm los}$ increases in the northeastern and southwestern directions is probably related to the bipolar outflow in the NE-SW direction. In addition, another strong $B_{\rm los}$ peak in the northwestern direction at 4 km s^{-1} probably relates to the NW-SE gas ejection with a double-cone shape. However, it is not clear what event can possibly cause a large-scale gas ejection with a kinetic energy of $\sim 10^{50}$ erg. A supernova explosion is unlikely in our case since such an explosion would destroy the whole cloud at once with a kinetic energy of $\sim 10^{51}$ erg. A stellar merger of two 30 $M_\odot$ stars can release a kinetic energy as high as $\sim 2 \times 10^{50}$ erg (Bally & Zinnecker 2005), however, there is no evidence, and it might be in principle impossible to find conclusive evidence for such an event. It is also not clear whether stellar collisions can cause gas ejections on the scale observed here. Thus, the question about the driving source should be tackled by examining the region around the shell expansion center in detail.

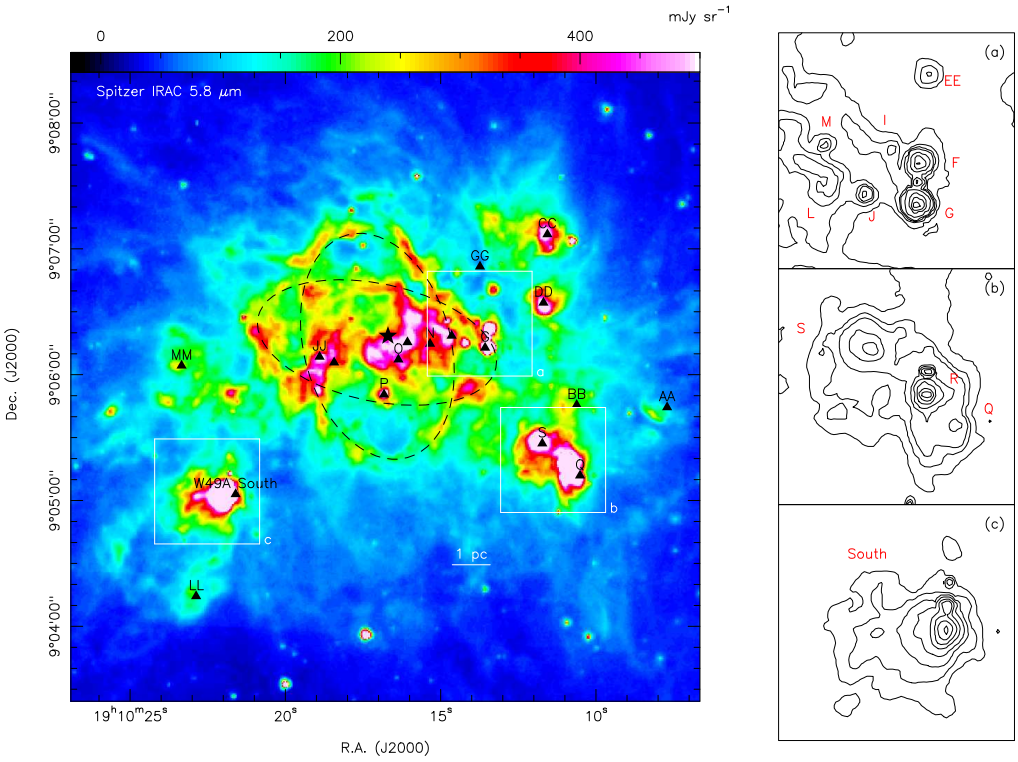

Figure 5.15 Spitzer IRAC 5.8 μm image of W49A. The shells structures are indicated in black dashed ellipses. Right panel shows a close-up view for the W49A North central part, W49A Southwest, and South, respectively. (a) The contours represent 0.2, 0.3, 0.4, 0.5, 0.8, 1.6, 3.2, 6.4, and 12.8 mJy sr^{-1} and the corresponding UC H II regions are denoted. (b) The contours represent 0.2, 0.3, 0.4, 0.8, 1.6, 3.2, 6.4, and 12.8 mJy sr^{-1} and the radio sources S, R, and Q are denoted. (c) The contours represent 0.2, 0.3, 0.5, 1.0, 2.5, 5.0, 10.0, and 20.0 mJy sr^{-1}.

5.3 UC H II regions in W49A

Source G

The UC H II source G is the densest region (Figs. 5.15 and 5.16) in W49A and has a mid-IR (12-20 μm) luminosity of $\sim 2 \times 10^5$ L$_\odot$ (Smith et al. 2000). It consists of five subcomponents or about five O5.5−O6 stars (De Pree, Mehringer, & Goss 1997) within a size of $\sim 7'' \times 6''$ in the 3.6 cm continuum emission. The H_2 column density of 4.4×10^{23} cm^{-2} derived for source G (see §4.1) is consistent with the value of 5×10^{23} cm^{-2} estimated by the interstellar extinction from the X-ray data (Tsujimoto et al. 2006). The gas mass for a larger area around source G ($\theta_{\rm HPBW} \sim 18''$) is estimated to be $\sim 1 \times 10^5$ M$_\odot$ (see Table 4.1) assuming a gas-to-dust mass ratio of 100, and is roughly one-fourth of the total gas mass of W49A North. The RADEX modeling results (see §4.2) also show a very high H_2 density of $\sim 10^6$ cm^{-3} for the region around source G ($\theta_{\rm HPBW} \sim 28''$).

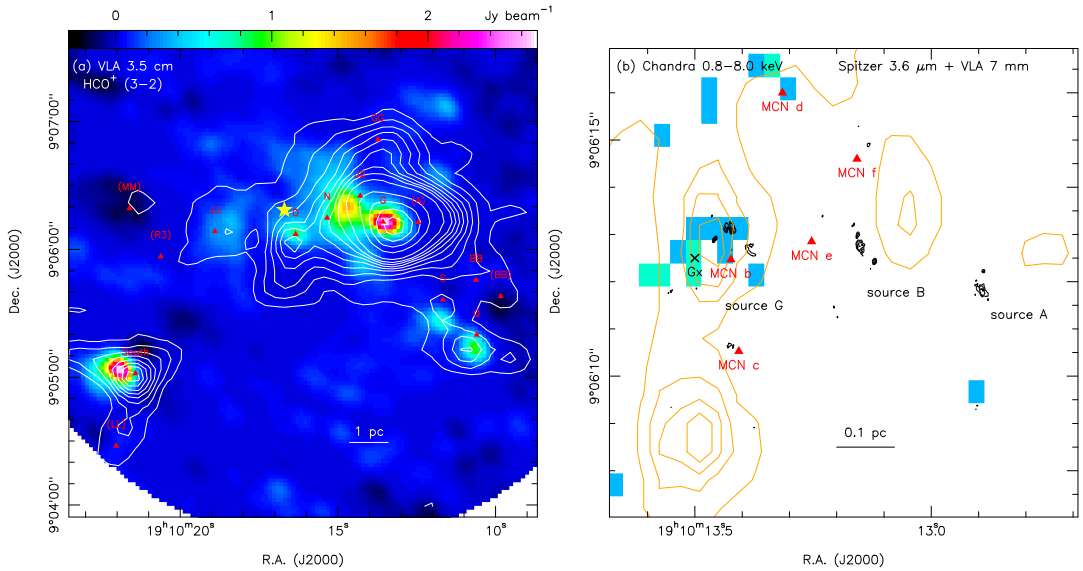

Figure 5.16 (a) The VLA 3.5 cm continuum emission overlaid with the HCO^+ $J = 3 - 2$ emission in white contours running from 160 to 480 K km s^{-1} in steps of 80 K km s^{-1}. The yellow star represents the center of the expanding shells. (b) The close-up image in the region near sources G, B, and A. The green color represents the Chandra ASIC detection of 3 X-ray photons, and blue represents 2 counts in a period of 96.6 ks. The orange contours denote the IRAC 3.6 μm emission running from 10 to 60 mJy sr^{-1} in steps of 10 mJy sr^{-1}. The red triangles represent the CH_3CN emission of hot cores (Wilner et al. 2001) and the black cross represents the X-ray source G_x (Tsujimoto et al. 2006).

Additionally, source G is associated with strong H_2O masers (see e.g., McGrath, Goss, & De Pree 2004; Gwinn, Moran, & Reid 1992) with a total maser velocity range up to $\sim$ 700 km s^{-1}.

The derived kinetic temperature for source G is about 58 K (Table 4.1), and is also close to the RADEX result of about 50 K (Figs. 4.13–4.15 d). However, the detections of the high-J HCN and HCO^+ lines and even vibrationally excited transitions of HCN and HNC (see §3) suggest a high excitation (e.g., 1000 K) in this region provided either by a high temperature (collisionally excited) or by IR pumping (radiatively excited). On the other hand, since source G is located in one shell, and was formed likely due to shell fragmentation, it is possible that the region around source G is part of a PDR heated externally by FUV photons from OB stars close to the shell expansion center.

Strong hard X-ray (0.8 – 8.0 keV) emission has been detected around source G (Tsujimoto et al. 2006) with a X-ray luminosity (3.0 – 8.0 keV) of $\sim 3 \times 10^{33}$ erg s^{-1} within $\sim 5''$, which is clearly shown in Figure 5.16. Tsujimoto et al. (2006) discussed three possible mechanisms for this extended X-ray emission: interacting winds from massive stars, a wind-blown bubble interacting with cold gas, or the emission is mainly due to an ensemble of unresolved point sources. However, no conclusive answer was given in their paper.

Because of the shell structure in W49A, the two-component spectra seen toward the region around source G are actually two distinct clumps on the line-of-sight. This is also supported by the CH_3CN observations (Wilner et al. 2001): Most of the hot molecular cores traced by the CH_3CN emission has $V_{\rm LSR}$ of ~ 4 and ~ 12 km s^{-1} in this region. In Figure 5.17, the four Spitzer images overlaid with the HCN, HCO^+, HNC, and H_2S emission show that most emission peaks are located in the region around sources G and B. Our telescope beams for these observations cover both source G and source B (Fig. 5.17), which are associated with the CH_3CN hot cores MCN b/c and MCN e/f, respectively. MCN c has a $V_{\rm LSR}$ of 3.7 ± 2 km s^{-1}, and MCN f has a $V_{\rm LSR}$ of 10.6 ± 2 km s^{-1}, corresponding to the 4 km s^{-1} and 12 km s^{-1} components. However, two other hot cores, MCN b and e, have $V_{\rm LSR}$ of 0.9 ± 2 km s^{-1}and 7.6 ± 2 km s^{-1}, respectively, which both have velocity differences of ~ 3 km s^{-1}. It is possible that MCN b and e are the blueshifted counterparts of MCN c and f, whose CH_3CN emission is weaker. The feature of a stronger blueshifted component together with a weaker redshifted component indicates infall motion associated with source G and B. However, the intensity uncertainty in the paper of Wilner et al. (2001) is about 40%, and about 2 km s^{-1} for the velocity uncertainty. In contrast, the $V_{\rm LSR}$ of source G derived from the Gaussian fits of the H92α, H52α, and He92α lines is $\sim 9 - 10$ km s^{-1}, but with a poor velocity resolution of $\sim 4 - 20$ km s^{-1}. Therefore, more observations are needed to bridge the connection between these hot cores and UC H II regions.

W49A South

W49A South harbors a cometary UC H II region, and is associated with gas ejected from W49A (see §3.4). W49A South is detected in most of the molecular emission lines, and is also bright in Spitzer MIR images (Fig. 5.17). The IR and radio continuum images all show a similar morphology as the emission peaks in the western part of the clump with diffuse emission in the east (Smith et al. 2000; De Pree, Mehringer, & Goss 1997). The central part of W49A South has an H_2 column density of 7.7×10^{22} cm^{-2} and a kinetic temperature of about 40 K, which is close to the temperature of about 50 K from a cool dust component (Smith et al. 2000; Buckley & Ward-Thompson 1996). Besides, the warm dust component with a temperature of ~ 200 K is present (Smith et al. 2000; Buckley & Ward-Thompson 1996). The total gas mass in the W49A South region (~ 17 pc^2) is 7.9×10^4 M$_\odot$, assuming a gas-to-dust mass ratio of 100 and an average dust temperature of 50 K. The total mass is larger than the recalculated value of 4.4×10^4 M$_\odot$ from Buckley & Ward-Thompson (1996), by adopting κ_ν of 4.7×10^{-3} cm^2 g^{-1}. The discrepancy is due to the smaller area of ~ 5 pc^2 they used. Besides, the results from the RADEX modeling show a very high H_2 density in W49A South about 10^7 cm^{-3}, compared with $\sim 3 - 5 \times 10^4$ cm^{-3} estimated in LTE assuming a size of $0.5 - 1$ pc. This large discrepancy is because the $V_{\rm LSR}$ of ~ 16 km s^{-1} is located at the absorption feature of the Perseus Arm and probably due to self-absorption at ~ 16 km s^{-1}, which results in an underestimated brightness temperature of the HCO^+ $J = 1 - 0$ line. Therefore, most data in the W49A South region

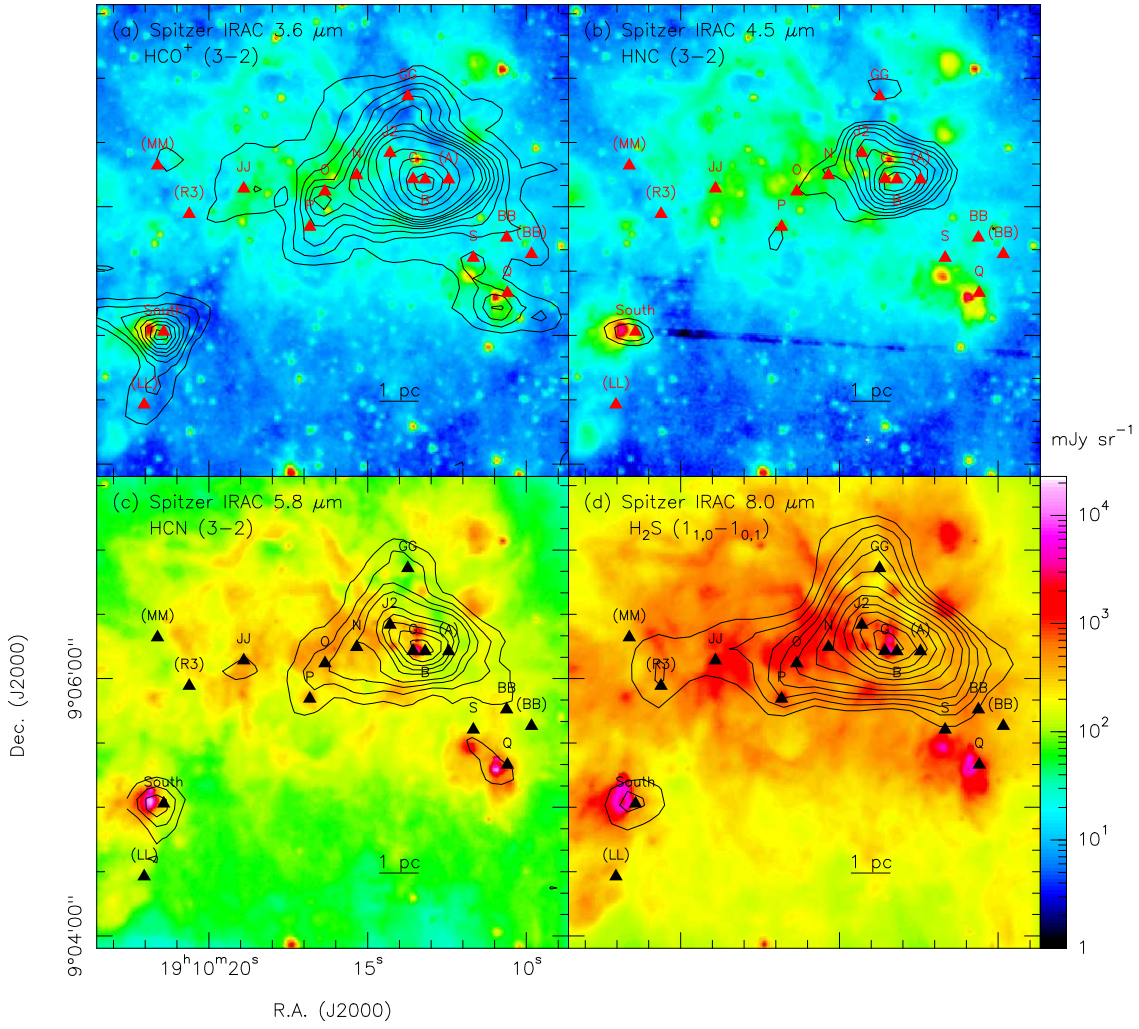

Figure 5.17 The Spitzer IRAC four bands image in 3.6 μm, 4.5 μm, 5.8 μm, and 8.0 μm overlaid with the HCO^+ $J = 3 - 2$, HNC $J = 3 - 2$, HCN $J = 3 - 2$, and H_2S $1_{1,0} - 1_{0,1}$ contours, respectively. The molecular emissions are plotted as the same contours as shown in Figures 3.11, 3.27, 3.19, and 3.36.

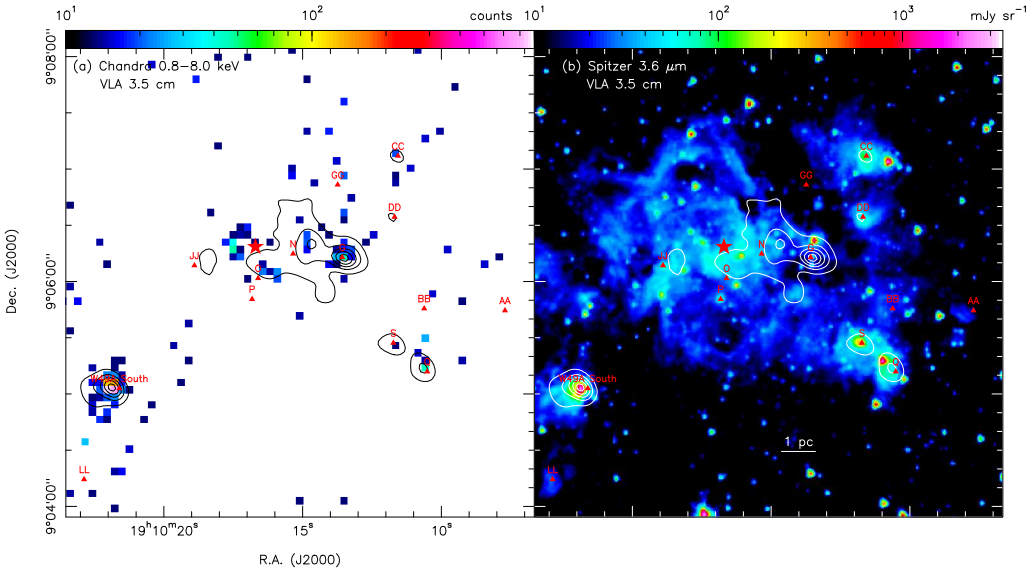

Figure 5.18 (a) The Chandra ASIC (0.5−8.0 keV) image overlaid with the VLA 3.5 cm continuum emission in black contours representing 10 % (30 σ), 30%, 50%, 70%, and 90% of the peak intensity (2.8 Jy beam^{-1}). (b) The IRAC 3.6 μm image overlaid the with VLA 3.5 cm continuum emission in white contours. The corresponding radio sources are marked. The red star represents the center of the expanding shells.

tend to show higher densities in the RADEX modeling results (Figs. 4.13−4.15).

It is worth noting that W49A South shows the strongest hard X-ray emission in W49A (Figure 5.18). Since an embedded cluster which contained about 10 O stars was suggested for W49A South (Alves & Homeier 2003), the strong X-ray emission might result from the interacting winds of young O stars or wind-blown bubbles interacting with cold gas (see Tsujimoto et al. 2006).

W49A Southwest

W49A Southwest consists of three UC H II regions, sources S, R, and Q. The distance between source R and source Q is $\sim 10''$, which is usually covered by one telescope beam in our observations. Source Q has stronger radio continuum emission (De Pree, Mehringer, & Goss 1997) and most of the molecular lines (e.g., HCN, HCO$^+$, HNC, ^{13}CO, and C^{18}O), than toward source R. However, source R is more prominent in MIR (Smith et al. 2000) and Spitzer IRAC images (Fig. 5.15) than source Q. This difference probably indicates that source R is more evolved than source Q, which is still very deeply embedded in gas and dust. Source S and source Q has a similar H_2 column density of 5.4×10^{22} cm^{-2} and 4.3×10^{22} cm^{-2}, respectively. The kinetic temperature is about 40 K for both sources which is consistent to the temperature of 48 K from the cool dust component estimated by Buckley & Ward-Thompson (1996), where the temperature of warm dust is about 240 K. The total mass in the W49A Southwest region (~ 13 pc^2) is 3.6×10^4 M$_\odot$ assuming a gas-to-dust mass

ratio of 100 and an average dust temperature of 50 K. The gas mass of source S and source Q is 1.3×10^3 $M_\odot$ and 1.5×10^3 $M_\odot$, respectively. The total mass in the W49A Southwest region is close to the recalculated value of 2.8×10^4 $M_\odot$ from Buckley & Ward-Thompson (1996), by adopting κ_ν of 4.7×10^{-3} cm^2 g^{-1} in an area of ~ 5 pc^2. The H_2 densities for sources S and Q are about 10^6 cm^{-3} from the RADEX modeling (Fig. 4.13), but with slightly lower temperatures of ~ 30 K. This relatively high H_2 density from the RADEX results is probably due to self-absorption in the HCO^+ $J = 1 - 0$ line at ~ 6 km s^{-1} discussed before, which decreases the HCO^+ $J = 1 - 0$ to $J = 3 - 2$ ratio. The estimated H_2 density calculated from the dust mass by assuming a size of $0.3 - 0.5$ pc is $\sim 4 - 6 \times 10^4$ cm^{-3} and $\sim 3 - 5 \times 10^4$ cm^{-3} for source S and source Q, respectively.

W49A Southwest is also part of the large-scale gas ejection, which means sources S and Q should have similar ages because of their short distance to each other. Our molecular line observations show that these two sources have similar characteristics in kinetic temperature, H_2 density, peak gas mass, and size, which support that they are in a similar evolutionary stage. However, the nature of source R is not clear. Besides, source R has a spectral energy distribution (SED) falling from 13 to 20, which probably indicates a lack of cooler dust or less absorption at shorter wavelengths (Smith et al. 2000).

5.4 The HCO^+/HCN and HNC/HCN ratios

This section will address the question whether the HCO^+/HCN and HNC/HCN ratios can be used to distinguish between PDRs and XDRs in W49A. The ratio images among these three molecules are shown in Figure 5.19.

The critical densities of HCN and HNC are almost identical and are over one order of magnitude larger than the HCO^+ critical density for the same transition (see Table 1.1). Table 5.2 shows the emission concentrations for HCN, HCO^+, and HNC by measuring the FWHM size of the peak intensities. The emission sizes of HCN are slightly larger than those of HCO^+, though the differences are equal to or less than a beam size. In addition, the emission sizes of HNC are smaller than the sizes of HCN in the $J = 1 - 0$ and $J = 4 - 3$ transitions.

HCO^+/HCN

Table 5.3 shows the HCO^+/HCN and HNC/HCN ratios for the selected clumps in W49A. Only source G has an HCO^+/HCN $J = 1 - 0$ ratio larger than unity, while the other sources have HCO^+/HCN $J = 1 - 0$ ratios ranging from 0.6 to 0.8 (Fig. 5.20). However, for the $J = 3 - 2$ and $J = 4 - 3$ transitions, most of the sources have HCO^+/HCN ratios above unity. The reason that most of the clumps have relatively small HCO^+/HCN $J = 1 - 0$ ratios is probably due to the larger beam size ($28''$) in the $J = 1 - 0$ transition (see Table 5.2), which dilutes the more concentrated HCO^+ emission. Additionally, the original maps were smoothed to lower resolutions to study the

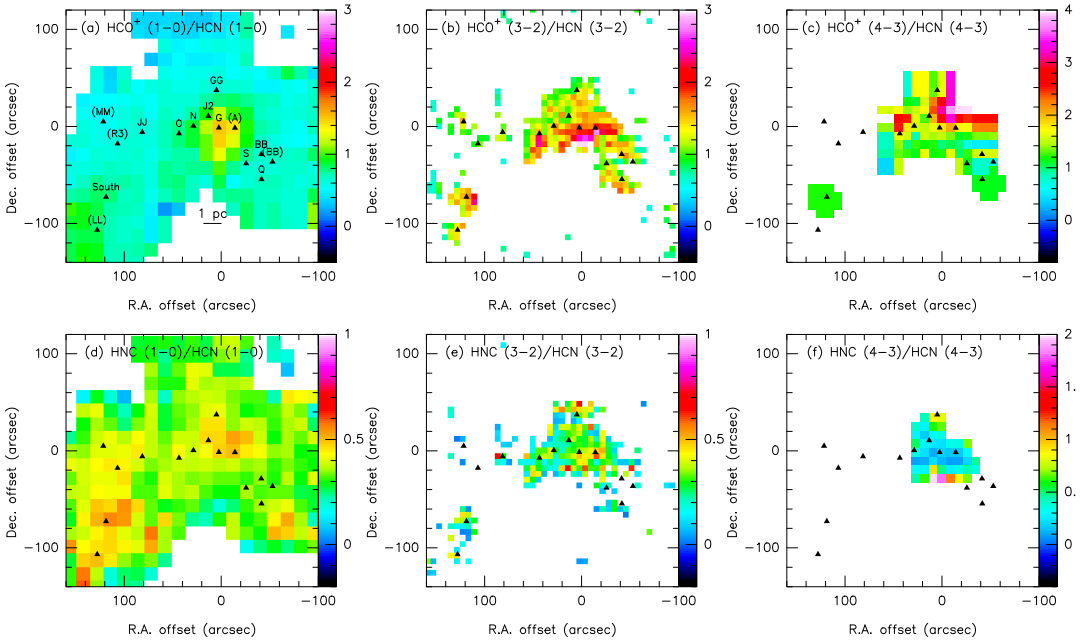

Figure 5.19 The HCO$^+$/HCN and HNC/HCN intensity ratio maps in W49A. The beam size of $J = 1 - 0$, $J = 3 - 2$, and $J = 4 - 3$ is $28''$, $12''$, and $17''$, respectively. All images are half-beam sampled and the pixels whose HCN intensity is below 3 σ are blanked. There is no data for W49A South and Southwest in the HNC $J = 4 - 3$ transition.

Table 5.2. The emission sizes of HCO$^+$, HCN, and HNC in W49A

Transition	HCO$^+$($''$)	HCN($''$)	HNC($''$)	$\theta_{\rm HPBW}$($''$)
$J = 1 - 0$	46.6	75.2	58.6	~ 28
$J = 3 - 2$	25.4	31.6	24.8	~ 9
$J = 4 - 3$	26.4	28.4	31.6	~ 17

[a]The emission sizes (in diameter) are estimated as the FWHM of the integrated intensity from the W49A North emission peak (near source G).

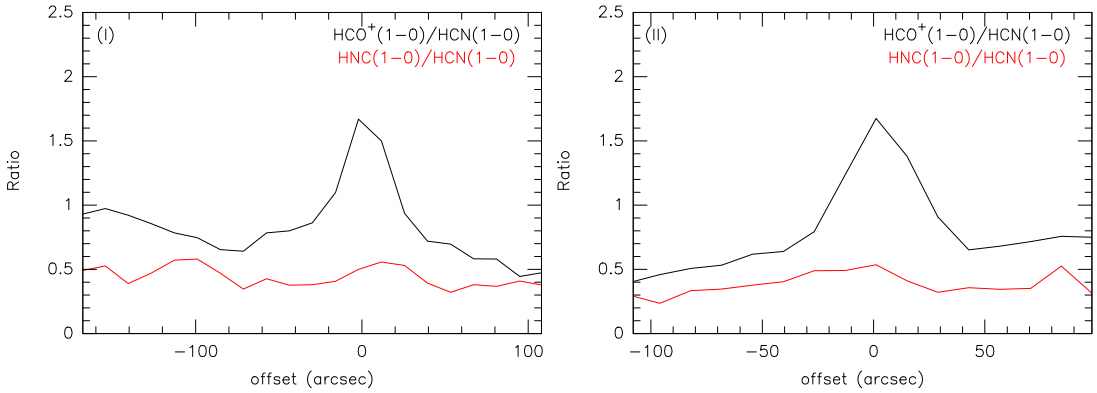

Figure 5.20 The position-ratio diagrams of two molecular line intensity ratios. The positions of the cuts are the same as in Figure 3.11. The black lines show the integrated intensity ratios between HCO^+ $J = 1 - 0$ and HCN $J = 1 - 0$, and the red lines show the ratios between HNC $J = 1 - 0$ and HCN $J = 1 - 0$. W49A North is located at the offset of $0''$.

Table 5.3. The HCO^+/HCN and HNC/HCN ratios for the selected clumps in W49A

Source	$\frac{HCO^+}{HCN}$ (1-0)	$\frac{HNC}{HCN}$ (1-0)	$\frac{HCO^+}{HCN}$ (3-2)	$\frac{HNC}{HCN}$ (3-2)	$\frac{HCO^+}{HCN}$ (4-3)	$\frac{HNC}{HCN}$ (4-3)
source G	1.52±0.02	0.48±0.01	2.28±0.07	0.39±0.01	1.89±0.06	0.19±0.01
source O	0.80±0.02	0.39±0.02	1.39±0.12	0.32±0.04	1.68±0.35	···
W49A South	0.79±0.05	0.56±0.04	1.87±0.17	0.35±0.04	1.21±0.18	···
source S	0.65±0.05	0.36±0.03	1.98±0.50	0.83±0.22	1.14±0.54	···
source Q	0.70±0.05	0.36±0.03	1.29±0.23	0.14±0.06	1.15±0.54	···
source JJ	0.64±0.04	0.46±0.03	1.21±0.37	0.25±0.11	···	···

[a]The intensity ratios are measured in beam sizes of $28''$, $9''$, and $17''$ for the $J = 1 - 0$, $J = 3 - 2$, and $J = 4 - 3$ transition, respectively.

effect of the observing region with different beam sizes. In Figure 5.21, the HCO^+/HCN $J = 1 - 0$ ratio decreases with an increasing beam size from the intensity peak. Moreover, because of a much smaller beam size in the $J = 3 - 2$ transition, the HCO^+/HCN $J = 3 - 2$ intensity ratio (Fig 5.22) reveals a prominent change in a smaller beam size, but still tends to decrease in a larger beam size. Noteworthily, the HCO^+/HCN $J = 3 - 2$ intensity ratio drops 0.5 (from 2.4 to 1.9) at a beam size of about $30''$, which indicates that probably most clumps could have higher HCO^+/HCN $J = 1 - 0$ intensity ratios given a smaller beam size. Therefore, because of the size differences between the HCO^+ and HCN emission, their intensity ratios can be confusing without an adequate spatial resolution. Besides, the HCO^+/HCN ratios in diffuse gas of W49A are generally below unity in the $J = 1 - 0$ transition. As for the $J = 3 - 2$ and $J = 4 - 3$ transitions, because of their low signal-to-noise ratios, the HCO^+/HCN ratios in the low-density gas are unavailable, but are likely smaller than unity.

Table 5.4 shows the ^{13}C isotopologue intensity ratios among these three molecules in W49A

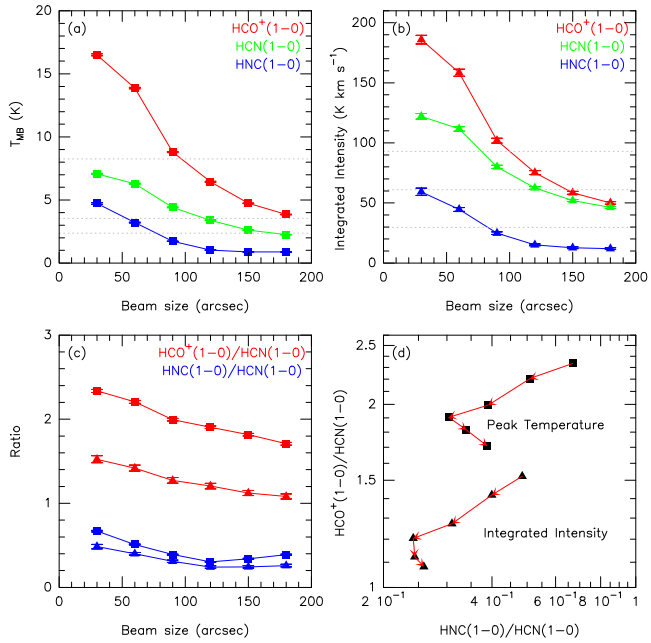

Figure 5.21 The peak temperature, integrated intensity, and the HCO$^+$/HCN and HNC/HCN ratios as a function of beam sizes are plotted in different panels. (a) The main beam temperatures of HCO$^+$, HCN, and HNC $J = 1 - 0$ change with beam sizes. (b) The integrated intensities of HCO$^+$, HCN, HNC $J = 1 - 0$ change with beam sizes. (c) The HCO$^+$/HCN and HNC/HCN ratios change with beam sizes where the filled rectangles denote the main beam temperature ratios and the filled triangles denote the integrated intensity ratios. (d) The correlation between the HNC/HCN and HCO$^+$/HCN ratios change with beam sizes.

North, South, and Southwest. The H^{13}CO$^+$/H^{13}CN $J = 3 - 2$ ratios for W49A North and South are especially high compared with the ratios in the $J = 1 - 0$ and $J = 4 - 3$ transitions, which indicates that the H^{13}CO$^+$ $J = 3 - 2$ emission is somehow enhanced in W49A North and South. This enhancement is also seen in the HCO$^+$/HCN $J = 3 - 2$ ratio of some clumps (Table 5.3), and it probably results from the beam size effect mentioned above.

According to the RADEX modeling results in §4.2, the column density ratio between HCN and HCO$^+$ is $\sim 4 - 7$, and the ratio between the HCN and HNC column density is $\sim 2 - 3$ in W49A. In most of the cases, the intensity ratios between HCO$^+$ and HCN can be above unity even though the HCO$^+$ column density is few times smaller than the HCN column density, which merely reflects the fact that HCO$^+$ has a smaller critical density than HCN does, e.g., 3 to 6 smaller at the transitions from $J = 2 - 1$ to $J = 7 - 6$ (see Fig. 1.4). In the interclump gas (e.g., $10^4 - 10^5$ cm^{-3}) of W49A, both HCO$^+$ and HCN are subthermal. Because HCN is more abundant than HCO$^+$, the emission of HCN is stronger than of HCO$^+$. However, in the clumps (e.g. $10^5 - 10^7$ cm^{-3}) of W49A, the clump density can be higher than the HCO$^+$ critical density but smaller than that of HCN. Therefore, the thermalized HCO$^+$ emission can be stronger than the subthermal HCN emission.

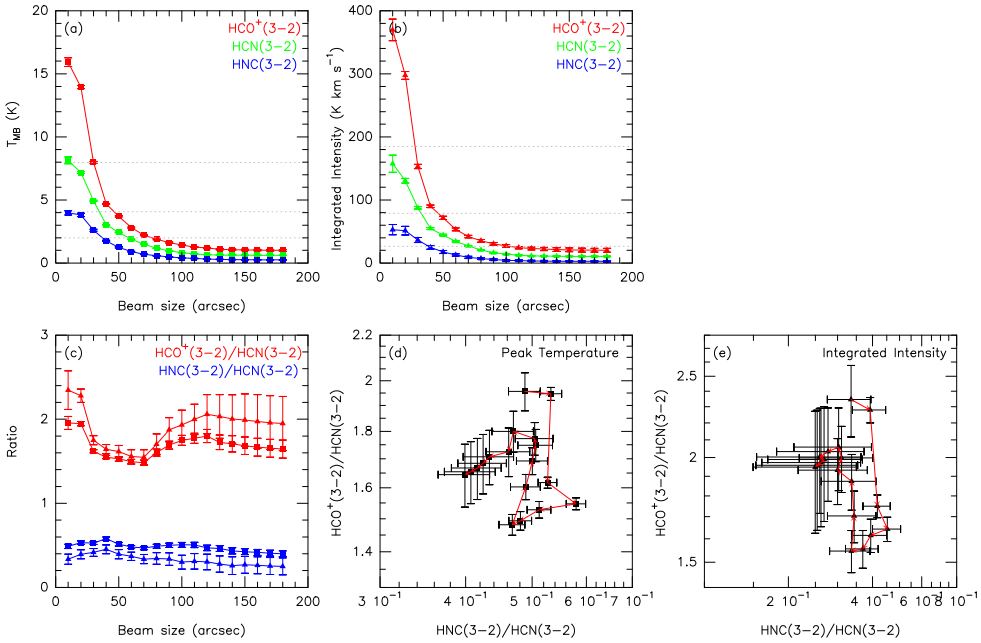

Figure 5.22 Same as Figure 5.22 but shown in the $J = 3 - 2$ transition.

In the paper of Meijerink, Spaans, & Israel (2007), they show the HCO^+/HCN $J = 1 - 0$ and $J = 4 - 3$ ratios decrease with an increasing H_2 density in dense PDRs (1 pc size) with an H_2 density of $10^4 - 10^{6.5}$ cm^{-3} and a UV radiation field of $10^2 - 10^5$ G_0, where $G_0 = 1$ is the local Galactic interstellar radiation field of 1.6×10^{-3} erg cm^{-2} s^{-1} (Habing flux). However, their PDR model results cannot explain our data in W49A. The high density XDR model from Meijerink, Spaans, & Israel (2007) can explain the high HCO^+/HCN ratio toward the clumps in W49A, but a high X-ray flux of $1.6 - 160$ erg s^{-1} cm^{-2} (integrate from 1 to 100 keV) is needed. For example, the X-ray luminosity ($3.0 - 8.0$ keV) of source G is 3×10^{33} erg s^{-1} in a size of 0.3 pc (Tsujimoto et al. 2006), which has an X-ray flux of 3.5×10^3 erg s^{-1} cm^{-2}. It is not clear if source G can have an integrated X-ray radiation field up to $1.6 - 160$ erg s^{-1} cm^{-2}. Therefore, no conclusive explanation for the HCO^+/HCN ratios in W49A is provided by their PDR and XDR models.

HNC/HCN

The intensity ratios between HNC and HCN in W49A are usually smaller than unity, and are slightly larger in clumps than in the interclump gas for the $J = 1 - 0$ and $J = 3 - 2$ transitions. However, in the $J = 4 - 3$ transition, the HNC/HCN ratio seems to decrease toward W49A North (Fig. 5.19). Figures 5.21 and 5.23 also show that the HNC/HCN ratio increases with a increasing beam size centered on W49A North, which indicates stronger extended HNC emission beyond the central part of W49A North in the interclump gas compared to HCN, e.g., HCN is more abundant than HNC in a warm cloud (Schilke et al. 1992). In most of the clumps, the HNC/HCN $J = 1 - 0$ ratios are

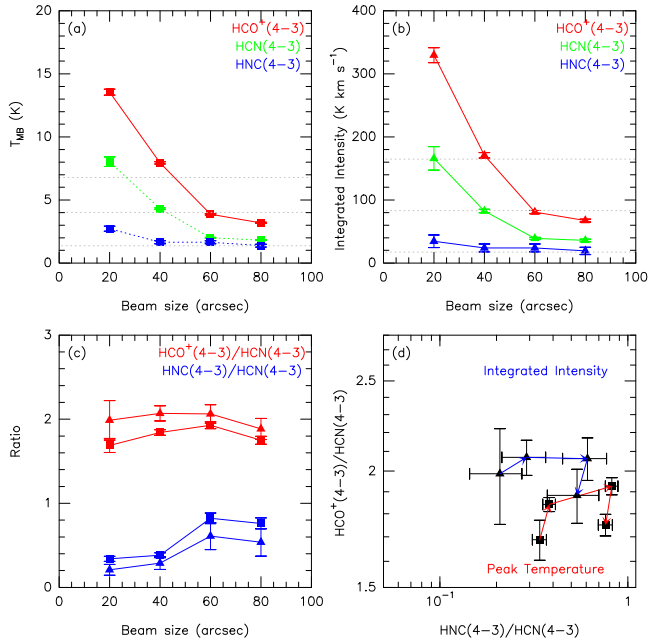

Figure 5.23 The similar figure as Figure 5.22 but shown in the $J = 4 - 3$ transition.

$\sim 0.4 - 0.6$ (Table 5.3), and the HNC/HCN $J = 3 - 2$ ratios are $\sim 0.3 - 0.4$ except for sources S (~ 0.8) and Q (~ 0.1). The large HNC/HCN ratio difference in these two sources is not clear. In addition, the HN^{13}C/H^{13}CN $J = 1 - 0$ and $J = 3 - 2$ ratios in W49A North and South are $\sim 0.2 - 0.3$. Due to the lack of the collisional coefficients for HNC, the HNC abundance derived from the RADEX modeling results is less certain (see §4.2). However, it seems likely that HNC is less abundant than HCN in W49A.

In the paper of Meijerink, Spaans, & Israel (2007), they show that the HNC/HCN $J = 1-0$ ratio in dense PDRs is around unity, which is also not consistent with our data. Besides, their XDR models predict a small HNC/HCN ratio value (< 1) in the low density ($10^4 - 10^5$ cm^{-3}) but high X-ray radiation (10–100 erg s^{-1} cm^{-2}) region. As mentioned before, it is not clear if any clumps in W49A can reach that high X-ray radiation. Therefore, the same models from Meijerink, Spaans, & Israel (2007) cannot explain the HNC/HCN ratios in W49A either.

Starburst galaxies and AGN-dominated galaxies

As mentioned in §1, it is important to clarify the origin of the high luminosity in (U)LIRGs, hence to study whether they mainly consist of starburst or AGN-dominated galaxies. Therefore, distinguishing these two kinds of galaxies is the key to understand (U)LIRGs and star formation in the external galaxies. One approach of this study is using the HCO$^+$/HCN and HNC/HCN ratios as a diagnostic to probe the radiation fields inside these two kinds of galaxies (e.g., Kohno 2005), where starbursts are dominated by PDRs while AGNs are powered by the central black holes whose strong

Table 5.4. The $H^{13}CO^+/H^{13}CN$ and $HN^{13}C/H^{13}CN$ ratios in W49A

Source	$\frac{H^{13}CO^+}{H^{13}CN}$ (1-0)	$\frac{HN^{13}C}{H^{13}CN}$ (1-0)	$\frac{H^{13}CO^+}{H^{13}CN}$ (3-2)	$\frac{HN^{13}C}{H^{13}CN}$ (3-2)	$\frac{H^{13}CO^+}{H^{13}CN}$ (4-3)	$\frac{HN^{13}C}{H^{13}CN}$ (4-3)
W49A North[b]	1.50±0.18	0.28±0.04	1.76±0.18	0.30±0.04	0.79±0.09	0.15±0.04
W49A South	1.00±0.28	0.24±0.08	1.87±0.38	···	1.00±0.40	···
W49A Southwest	1.00±0.47	···	···	···	···	···

[a]The intensity ratios are measured in beam sizes of $28''$, $9''$ and $17''$ for the $J = 1 - 0$, $J = 3 - 2$, and $J = 4 - 3$ transition, respectively.

[b]The region around source G

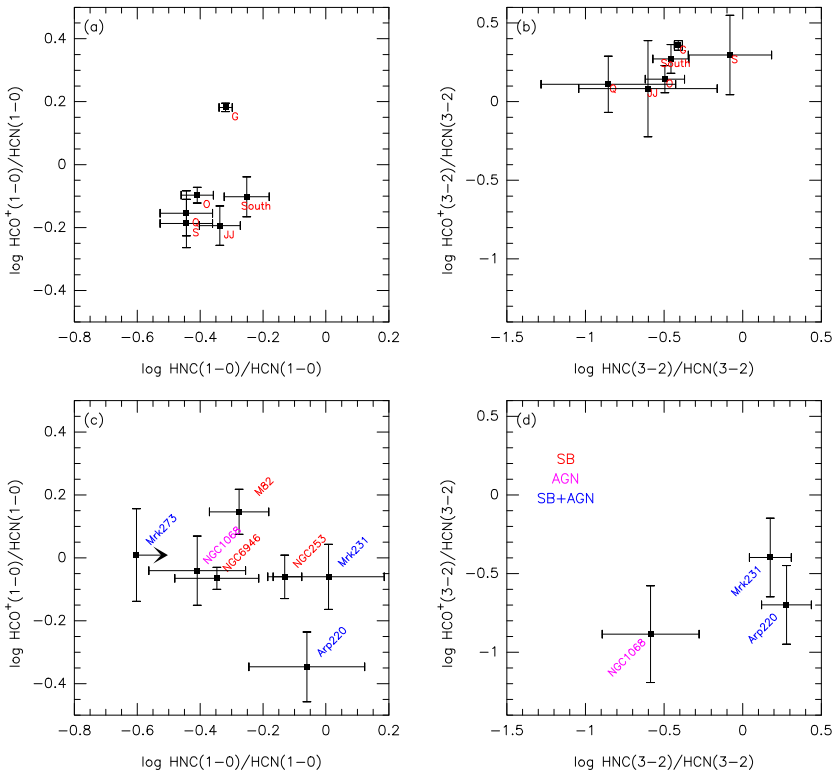

Figure 5.24 (a)-(b) The HCO$^+$/HCN and HNC/HCN ratio correlation in W49A. (b)-(c) The same comparison for external galaxies in three colors. Red points represent starburst galaxies, and magenta points represent the AGN-dominated galaxy NGC 6946. Blue points represent the galaxies involved both starburst and AGN.

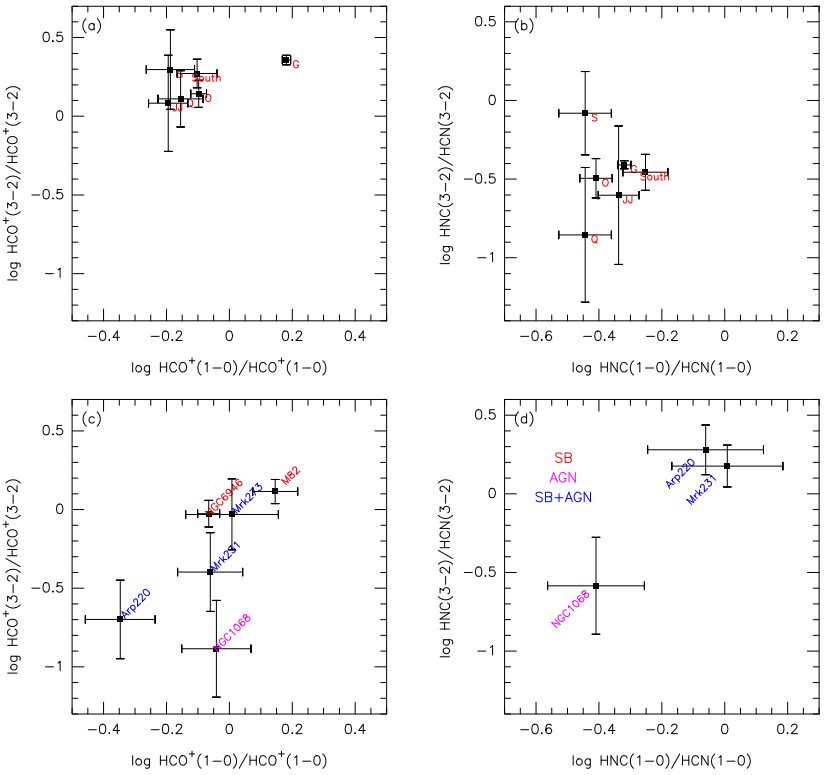

Figure 5.25 (a)-(b) The HCO^+/HCN $J = 1 - 0$ and $J = 3 - 2$ ratio correlation in W49A. (b)-(c) The HNC/HCN $J = 1 - 0$ and $J = 3 - 2$ ratio correlation in external galaxies. Red points represent starburst galaxies, and magenta points represent the AGN-dominated galaxy NGC 6946. Blue points represent the galaxies involved both starburst and AGN.

X-ray emission forms XDRs. According to the PDR and XDR models of Meijerink, Spaans, & Israel (2007) and Meijerink & Spaans (2005), for high density PDRs and XDRs (see discussion above), the HCO^+/HCN ratios tend to be larger than unity in PDRs, and the HNC/HCN ratios tend to be larger than unity in XDRs.

Table 5.5 and Figures 5.24–5.25 show the comparison of the HCO^+/HCN and HNC/HCN ratios between W49A and some selected galaxies. The HCO^+/HCN and HNC/HCN $J = 1 - 0$ ratios in Figure 5.24 clearly show that source G is similar to the starburst galaxy M82, and other clumps are similar to the starburst galaxies NGC 253 and NGC 6946. However, most of the clumps in W49A have relatively low HCO^+/HCN $J = 1 - 0$ ratios. Additionally, the HNC/HCN $J = 1 - 0$ ratios for the clumps in W49A and starburst galaxies are usually < 1. As for the $J = 3 - 2$ ratios (Fig. 5.24), there is a clear trend that most clumps in W49A have an HCO^+/HCN $J = 3 - 2$ ratio $\gtrsim 1$, and the galaxies involved both starburst and AGN have an HCO^+/HCN $J = 3 - 2$ ratio below unity. However, the AGN-dominated galaxy NGC 1068, which has relatively small HNC/HCN ratios compared with Arp 220 and Mrk 231, seems to contain a large amount of diffuse gas but with a strong X-ray radiation field according to the XDR models of Meijerink, Spaans, & Israel (2007).

In short, the clumps in W49A have different properties especially in the HCO^+/HCN $J = 3 - 2$ and HNC/HCN $J = 1 - 0$ and $J = 3 - 2$ ratios compared with those of AGN or partly AGN-dominated galaxies. Besides, source G has similar HCO^+/HCN and HNC/HCN $J = 1 - 0$ ratios as M82, which is expected for their similar starburst activities. However, another starburst NGC 253, which is more massive than M82 (see Martín, Martín-Pintado, & Viti 2009), is different from source G and M82 in the HCO^+/HCN ratios, but close to the value of the clumps in W49A with stronger HNC $J = 1 - 0$ emission. Thus, as a Galactic starburst template, W49A does show similar features to those starburst galaxies. However, in most of the cases, those galaxies are covered by one single dish beam which might include one strong XDR in AGN-dominated galaxies, or many PDRs in starburst galaxies, or both. Therefore, they will have different degrees of beam dilution, which result in different line intensity ratios. Furthermore, as mentioned above, the emission sizes for HCO^+ and HCN are not the same, which also add an uncertainty into the line ratio comparison. Besides, our RADEX modeling results indicate that the HCO^+/HCN ratios do not reflect the abundance ratios between these two molecules. Thus, caution must be taken for interpreting the line ratios without a sufficient angular resolution.

5.5 X-ray emission and shock tracers

In Figure 5.26, the hard X-ray emission (0.5–8.0 keV) from the Chandra X-ray telescope is spatially correlated to the UC H II regions in W49A, i.e., sources G, S, Q, O, and W49A South. It has been reported by Tsujimoto et al. (2006) that source G has an X-ray luminosity (3.0–8.0 keV) of $\sim 3 \times 10^{33}$ erg s^{-1} and a plasma temperature of ~ 7 keV within 0.3 pc. As mentioned before, W49A South has the strongest extended hard X-ray emission in W49A. Besides, the strong X-ray emission around source O seems to be related to the shell expansion center. Table 5.6 and Figures 5.27–5.28 show the measurements of the hard X-ray emission, SiO $J = 2 - 1$, H_2S $1_{1,0} - 1_{0,1}$, and HNC $J = 1 - 0$ emission in W49A, where the contribution from individual velocity components has been also taken into account. SiO, whose abundance is 100 times larger than the upper limits observed in dark clouds, is believed to be enhanced in high temperature or shock regions where SiO is released from grain surfaces (Ziurys, Snell, & Dickman 1989). Besides, H_2S is also believed to be enhanced for a similar reason as SiO (Minh, Ziurys, Irvine, & McGonagle 1991; Minh, Irvine, McGonagle, & Ziurys 1990). Therefore, the comparison between these two molecular emission together with the X-ray emission can help to disentangle the origin of the hard X-ray emission and the enhancement of SiO and H_2S.

Figures 5.27 and 5.28 show that the hard X-ray emission has no clear correlation with the dust mass. But some clumps show anti-correlation between the X-ray emission and the dust mass and other molecular emission (Fig. 5.28). In addition, the correlation between the HNC and H_2S emission is clear. However, SiO has no clear intensity correlation to the hard X-ray emission in W49A, but shows a similar trend with the dust mass (Fig. 5.28).

Table 5.5. The HCO^+/HCN and HNC/HCN ratios for the selected clumps in W49A

Source	D (Mpc)	$L_{\rm FIR}$ (log $L_\odot$)	$\frac{HCO^+}{HCN}$ (1-0)	$\frac{HNC}{HCN}$ (1-0)	$\frac{HCO^+}{HCN}$ (3-2)	$\frac{HNC}{HCN}$ (3-2)	$\frac{HCO^+}{HCN}$ (4-3)	$\frac{HNC}{HCN}$ (4-3)	Class	References
source G	0.0114	6.8	1.52±0.02	0.48±0.01	2.28±0.07	0.39±0.01	1.89±0.06	0.19±0.01		This work
W49A South	0.0114	6.5	0.79±0.05	0.56±0.04	1.87±0.17	0.35±0.04	1.21±0.18	···		This work
NGC 253	3.3	10.5	0.87±0.06	0.74±0.04	···	···	1.24±0.29	···	SB	[1]
M82	3.4	10.7	1.40±0.10	0.53±0.05	1.30±0.10	···	3.64±0.78	···	SB	[2]
NGC 6946	5.5	10.1	0.86±0.03	0.45±0.06	0.94±0.08	···	···	···	SB	[3]
NGC 1068	16.7	11.2	0.91±0.10	0.39±0.06	0.13±0.04	0.26±0.08	0.27±0.05	0.19±0.03	AGN	[4]
Arp 220	74.7	12.0	0.45±0.05	0.87±0.16	0.20±0.05	1.90±0.30	0.18±0.05	···	SB+AGN	[5]
Mrk 273	152.2	12.0	1.02±0.15	< 0.25	0.93±0.21	···	···	···	SB+AGN	[6]
Mrk 231	170.3	12.4	0.87±0.09	1.02±0.18	0.40±0.10	1.50±0.20	···	···	SB+AGN	[7]

References. — (1) Knudsen et al. (2007); (2) Krips et al. (2008); Baan et al. (2008); Seaquist & Frayer (2000); Nguyen et al. (1992);(3) Krips et al. (2008); Baan et al. (2008); Nguyen et al. (1992);(4) Pérez-Beaupuits et al. (2009); Baan et al. (2008);(5) Greve, Papadopoulos, Gao, & Radford (2009); Krips et al. (2008); Aalto, Spaans, Wiedner, Hüttemeister (2007); Graciá-Carpio, García-Burillo, Planesas, & Colina (2006); (6) Graciá-Carpio et al. (2008); Aalto, Polatidis, Hüttemeister, & Curran (2002);(7) Juneau et al. (2009); Krips et al. (2008); Aalto, Spaans, Wiedner, Hüttemeister (2007)

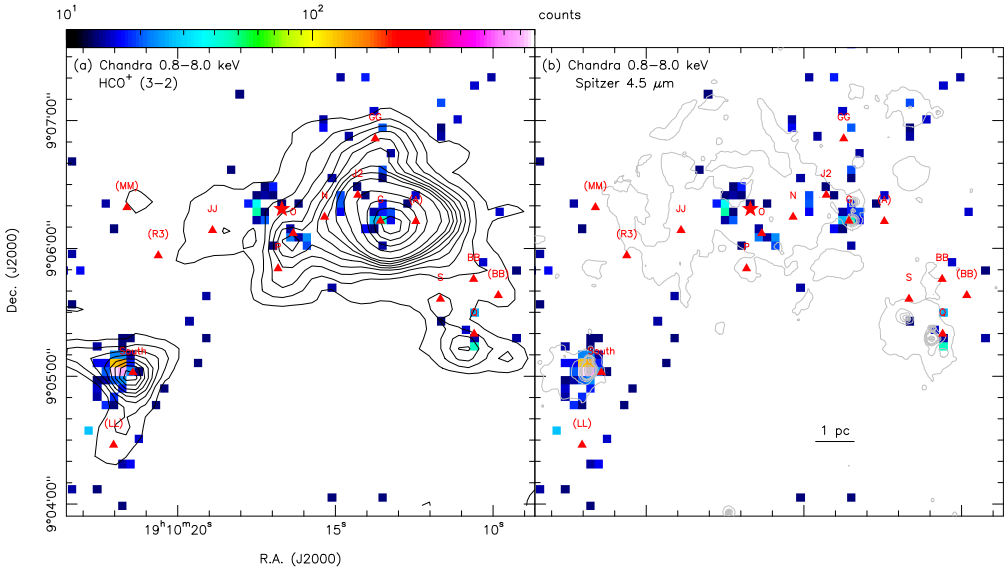

Figure 5.26 (a) The Chandra ASIC (0.5–8.0 keV) image overlaid with the HCO^+ $J = 3-2$ emission in white contours running from 160 to 480 K km s^{-1} in steps of 80 K km s^{-1}. (b) The Chandra ASIC (0.5–8.0 keV) image overlaid with the IRAC 4.5 μm emission in green contours representing 40 mJy sr^{-1}, 80 mJy sr^{-1}, 160 mJy sr^{-1}, 320 mJy sr^{-1}, and running from 800 to 4000 mJy sr^{-1} in steps of 800 mJy sr^{-1}. The corresponding radio sources are marked. The red star represents the center of the expanding shells.

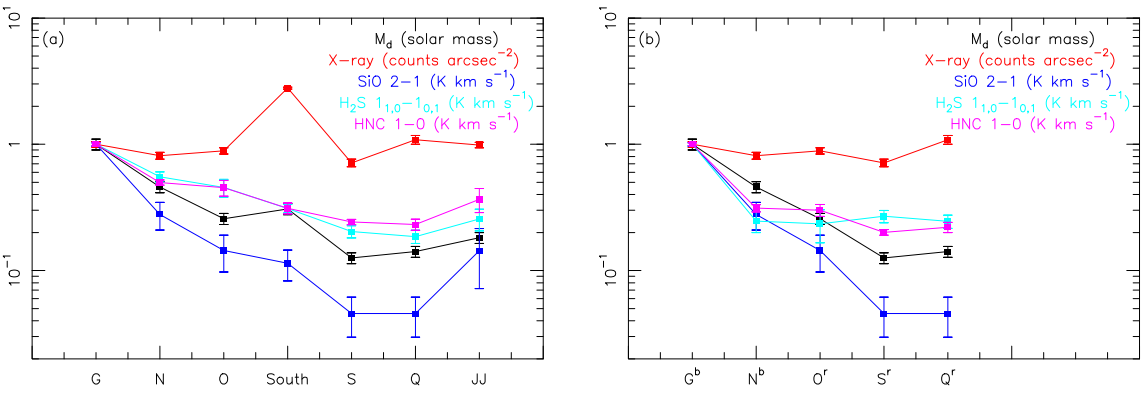

Figure 5.27 The plot of the dust mass, X-ray emission, and the intensities of SiO $J = 2-1$, H_2S $1_{1,0} - 1_{0,1}$, and HNC $J = 1-0$ for the selected clumps in W49A. (a) The plot is shown in the integrated intensity of both blue- and redshifted components (e.g., ~ 4 km s^{-1} and ~ 12 km s^{-1} for source G). (b) The plot is shown in the integrated intensity of the same component (the blueshifted component of sources G and N, and the redshifted component of sources O, S, and Q). W49A South and source JJ are not shown here because their H_2S emission is only detected in the redshifted components, while the SiO emission has 2 σ detection toward the blueshifted component. All intensities are normalized with respect to the intensities of source G.

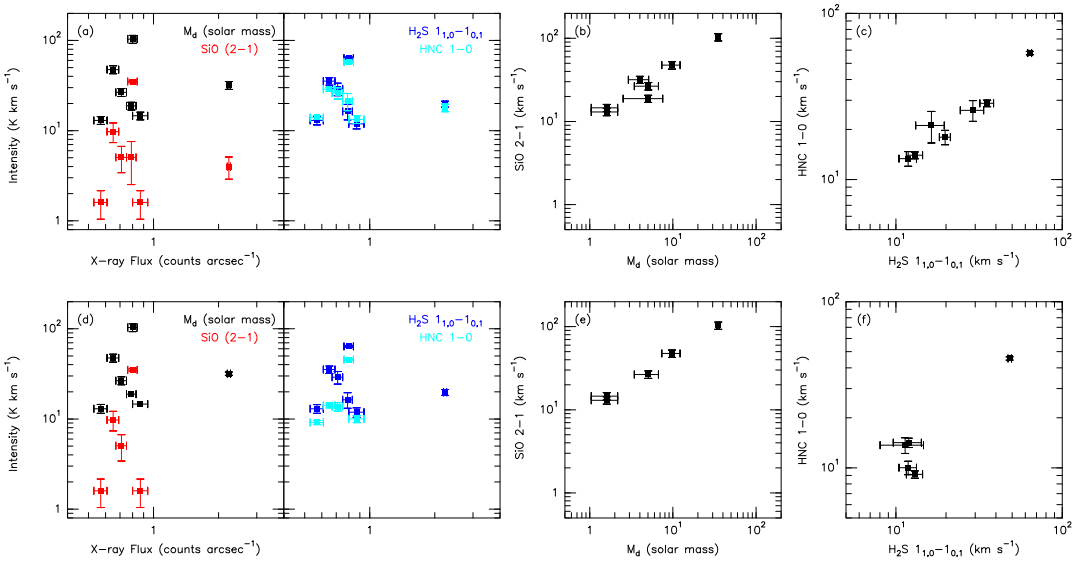

Figure 5.28 The plot of the dust mass, X-ray emission, and the intensities of SiO $J = 2 - 1$, H_2S $1_{1,0} - 1_{0,1}$, and HNC $J = 1 - 0$ for the selected clumps in W49A as Figure 5.27.

The hard X-ray emission in massive star forming regions, as mentioned in §5.2, might be generated by interacting winds of young O stars or by wind-blown bubbles interacting with cold gas (see Tsujimoto et al. 2006), and both mechanisms are associated with stellar winds from young stars. Additionally, a correlation between the SiO and Fe 6.4 keV emissions has been reported in the Galactic center, and suggested that strong shocks are probably responsible for the grain destruction that produce abundant gas phase SiO and also generate the hard X-ray emission which excites the Fe line (Martín-Pintado et al. 2000). On the other hand, Greaves, Ohishi, & Nyman (1996) suggested that shocks are not needed to produce moderate SiO abundances of 10^{-10} according to the SiO absorption in the clouds of the Galactic spiral arms. In W49A, the fact that no clear correlation between hard X-ray and SiO emission was found indicates that probably the enhanced SiO emission is not mainly due to the shock/outflow activities. However, the relatively broad SiO line width (~ 14 km s^{-1}) compared to the line widths of HCN or HCO^+ (~ 8 km s^{-1} for a single component) shows a clear shock/outflow feature in source G, where the strong H_2O masers are located. Since most of the clumps in W49A have similar kinetic temperatures of $\sim 40 - 60$ K, the enhancement of SiO emission especially in source G is unlikely due to the temperature, but due mainly to the high density of source G or a difference in strength of the shocks. Furthermore, the especially strong hard X-ray emission seen in W49A South is puzzling. If young massive stars, either produce wind-blown bubbles or generate stellar winds interacting with each other, are responsible for the X-ray emission, then it is not clear why W49A Southwest, with a similar amount of embedded O stars (Alves & Homeier 2003), does not show strong X-ray emission. One likely explanation is that the embedded cluster in W49A South is more compact or contains more massive stars. For instance, Homeier &

Alves (2005) show that W49A South contains four massive star with an inferred gas mass up to 100 $M_{\odot}$, and three of them are probably due to multiplicity.

H_2S, as shown in §3.1, has a similar emission distribution as those of HCN, HCO^+, HNC. Therefore, the emission correlation between H_2S $1_{1,0} - 1_{0,1}$ and HNC $J = 1 - 0$ indicates that they both come from the dense ($n \gtrsim 10^5$ cm^{-3}) and warm ($\sim 40 - 60$ K) clumps. In that sense, the enhanced H_2S abundance is not necessary the results of shock/outflow activities but is likely due to the high temperature gas-phase chemistry.

Although the XDR models of Meijerink, Spaans, & Israel (2007) and Meijerink & Spaans (2005) showed enhanced HNC emission in XDRs, we do not find any tight correlation between the hard X-ray and HNC emission. This is probably because the X-ray emission in W49A is not strong enough ($\ll 1.6 - 160$ erg s^{-1} cm^{-2}), and the radiation field is still dominated by FUV photons which form PDRs.

Table 5.6. The comparison of the X-ray, SiO, H_2S, and HNC emission in W49A

Source	T_{ex}[a] (K)	$N(H_2)$[b] (cm^{-2})	M_{dust}[c] ($M_\odot$)	X-ray (counts $arcsec^{-2}$)	SiO $(2-1)$[d] (K km s^{-1})	H_2S $(1_{1,0}-1_{0,1})$[d] (K km s^{-1})	HNC $(1-0)$[d] (K km s^{-1})
source G	57.9	4.4×10^{23}	103.4	0.80±0.04	35.09±1.21	63.82±1.60	57.66±1.38
	...	...	...	...	35.09±1.21	48.34±1.15	45.49±1.04
	...	...	...	...	...	15.48±1.11	12.17±0.91
source N	46.0	1.3×10^{23}	47.5	0.65±0.04	9.75±2.40	35.31±3.33	28.72±1.33
	...	...	...	...	9.75±2.40	11.92±2.28	14.18±0.92
	...	...	...	...	...	23.39±2.43	14.54±0.96
source O	47.6	8.7×10^{22}	26.6	0.71±0.04	5.05±1.63	29.05±4.65	26.10±3.70
	...	...	...	...	...	17.71±3.25	12.42±1.24
	...	...	...	...	5.05±1.63	11.34±3.32	13.68±1.47
W49A South	38.7	7.4×10^{22}	31.8	2.23±0.04	4.00±1.10	19.75±1.51	17.96±1.78
	...	...	...	...	4.00±1.10	...	5.69±1.33
	...	...	...	...	...	19.75±1.51	12.27±1.19
source S	42.3	5.4×10^{22}	13.0	0.57±0.04	1.60±0.56	13.00±1.45	13.99±0.67
	...	...	...	...	...	...	4.86±0.49
	...	...	...	...	1.60±0.56	13.00±1.45	9.13±0.46
source Q	37.5	4.3×10^{22}	14.6	0.87±0.07	1.60±0.56	11.86±1.42	13.36±1.35
	...	...	...	...	...	...	3.34±0.99
	...	...	...	...	1.60±0.56	11.86±1.42	10.02±0.93
source JJ	58.3	6.2×10^{22}	18.8	0.79±0.04	5.04±2.52	16.34±3.18	21.15±4.55
	...	...	...	...	5.04±2.52	...	3.99±2.90
	...	...	...	...	...	16.34±3.18	17.16±3.51

[a]The value in a pixel size of $5\farcs6\times5\farcs6$.

[b]The H_2 column density is estimated by assuming a ^{12}CO to $C^{18}O$ abundance ratio of 510 and a ^{12}CO to H_2 abundance ratio of 2×10^{-4}.

[c]The mass is estimated using the LABOCA image (Fig. 3.42) with a dust temperature of 50 K. The pixel size is $9\farcs1\times9\farcs1$.

[d]The first value shows the total integrated intensity, and the subsequent values show the intensities from the blue- and redshifted components. Source JJ and W49A Southwest (including both sources S and Q) have 2 σ detection in SiO $J=2-1$.

6

W49A Conclusions

As outlined in §1, I want to answer several questions in the study of W49A, which will be given as follows.

The evidence of expanding shells in W49A is shown in the MIR and molecular emission, and the dense clumps lie peripherally along the shells. Therefore, the expanding shells in W49A provide a natural explanation of the observed molecular line profiles, and triggered massive star formation in just $\sim 10^5$ yr. The expanding shells are likely to have a common origin close to source O with an expansion speed of ~ 5 km s^{-1} and an age of $\sim 3 - 7 \times 10^5$ years. However, there is no decisive evidence for the driving mechanism of this shell expansion. The average mass of the expanding shells is $\sim 2 \times 10^4$ M$_\odot$ with a kinetic energy of $\sim 10^{49}$ erg which is probably powered by a few very massive stars in the center, and the expanding shells are either driven by strong winds or by the radiation pressure. In addition, evidences for the gas ejections have been presented in the large-scale GRS ^{13}CO $J = 1 - 0$ data. Both ejections seem to share the same center as the expanding shells with a total energy of few times 10^{50} erg. The main driving mechanism for the gas ejections is unclear, but is likely related to the coeval or probably later shell expansion, which triggers a starburst in W49A. The property of the central source driving the expanding shells and gas ejections needs more investigation.

In the RADEX modeling, it is clear that the column density ratios among HCO$^+$, HCN, and HNC do not directly reflect the line intensity ratios. Therefore, caution must be taken when interpreting those ratios. Besides, since the spatial distributions of the emission from HCO$^+$, HCN, and HNC are not the same, different telescope beam sizes will result in different intensity ratios among those molecules. Therefore, the beam filling effect is critical in the use of the HCO$^+$/HCN and HNC/HCN ratios, especially for the study in external galaxies. Furthermore, the HCO$^+$/HCN and HNC/HCN ratios in W49A do not agree well with the existing PDR/XRD models, but do show a similarity to the starburst galaxies M82 and NGC 253, which in turn confirms the nature of W49A as a Galactic mini-starburst. Therefore, the study in the starburst template W49A is helpful to

bridge the gap of massive star formation in out Galaxy and in external galaxies.

In the end, there is no clear correlation between the hard X-ray and SiO emissions in W49A, which means that the strong X-ray emission is not directly related to the shock region traced by the SiO emission. Besides, the mechanism for the strong hard X-ray emission seen in W49A South is not clear, and can result from interacting winds of young O stars or wind-blown bubbles interacting with cold gas. However, both mechanisms are associated with massive stars, which probably indicates a few very massive stars or a compact cluster are embedded in W49A South.

Part II

Large-Scale Mappings of highly excited CO in Orion Molecular Cloud 1

7

Observations toward OMC-1

7.1 APEX Observations

Observations of the ^{13}CO and C^{18}O $J = 3 - 2$ lines were carried out using the APEX telescope in 2007 November on Llano de Chajnantor in Chile. The double-sideband heterodyne receiver APEX-2a (Risacher et al. 2006) was used to obtain large maps ($\sim 300'' \times 350''$) toward OMC-1 with the OTF mode. The APEX-2a receiver had a system temperature of 60 K, and the typical system noise was from 100 to 200 K. The ($0''$, $0''$) position was chosen at Orion BN ($\alpha = 05^{\rm h}35^{\rm m}14\overset{\rm s}{.}117$, $\delta = -05°22'22\overset{''}{.}9$, J2000.0). The position switching mode was used for all spectra in an emission-free reference position at the offset ($-500''$, $0''$), and the Fast Fourier Transform Spectrometer backend (FFTS; Klein et al. 2006) was used and configured to a bandwidth of 1000 MHz and a resolution of $\sim$ 0.1 km s^{-1}. The spectra were corrected to the main-beam temperature scale with $T_{MB} = T_A^*/\eta_{MB}$. For APEX at 352 GHz, the main-beam efficiency, η_{MB}, is 0.73 (Güsten et al. 2006).

During the early CHAMP$^+$ (Kasemann et al. 2006) observations with the APEX telescope from 2007 to 2008, the new 2×7 elements heterodyne array in the 450 μm and 350 μm atmospheric windows was tested toward OMC-1. The ^{12}CO $J = 6 - 5$ and $J = 7 - 6$ lines were observed simultaneously, and the ^{13}CO $J = 8 - 7$ and C^{18}O $J = 6 - 5$ lines were observed simultaneously for the same area later. The MPIfR Array Correlator Spectrometer (MACS) was first used as the backend for non-central pixels, and has been replaced by the FFTS backend afterwards. The resolution of MACS and FFTS was $\sim$ 0.42 km s^{-1} and $\sim$ 0.05 km s^{-1}, respectively. The OTF mapping was used to obtain large-scale images with a reference position at the offset ($-500''$, $0''$). For CHAMP$^+$ at 661 GHz and 890 GHz, $\eta_{\rm MB}$ is 0.47 and 0.44, respectively. The APEX observation parameters toward OMC-1 are summarized in Table 7.1.

The pointing of the APEX telescope during the APEX-2a observations was carried out every hour with the observations toward R Lepus in the line-pointing mode using the ^{12}CO $J = 3 - 2$ line. The pointing accuracy is better than $2''$. In the CHAMP$^+$ observations, *o* Ceti was used as a

Table 7.1. The APEX observation parameters for the OMC-1 mapping

Line	Frequency (GHz)	$\theta_{\rm HPBW}$ ($''$)	$\eta_{\rm MB}$	Receiver	$T_{\rm sys}$ (K)[a]
^{13}CO $(3-2)$	330.59	17.9	0.75	APEX2a	220
C^{18}O$(3-2)$	329.33	18.0	0.75	APEX2a	220
C^{18}O $(6-5)$	658.55	9.0	0.47	CHAMP$^+$	1800
^{12}CO $(6-5)$	691.47	8.6	0.47	CHAMP$^+$	1600
^{12}CO $(7-6)$	691.47	8.6	0.47	CHAMP$^+$	3900
^{13}CO $(8-7)$	881.27	6.7	0.47	CHAMP$^+$	3650

[a]System temperatures are averaged from the data.

line-pointing source in the ^{12}CO $J=6-5$ line. Since pointing shifts in the 2007 data were found after the initial observations, the simultaneous observations with the similar setup of ^{12}CO $J=7-6$ and ^{13}CO $J=6-5$ were re-observed toward the Orion BN/KL region in 2008 summer. However, because the subsequent shifts of the pointing in the subscan of one OTF scan were seen in the 2008 observations. The corrections of the pointing were carried out in two steps. The Methyl Cyanide CH_3CN line at 661 GHz, arising from a compact region centered at the Orion Hot Core, was first corrected according to its first OTF subscan, which had a correct pointing. The pointing-corrected images of CH_3OH $J=11_{1,10}-10_{0,10}$, $^{13}CH_3OH$ $J=14_{1,13}-13_{0,12}$, $(CH_3)_2O$ $J=21_{5,16}-20_{4,17}$, CH_3CN $J=36_9-35_9$, and SO_2 $J=37_{1,37}-36_{0,36}$ (see Fig. 8.14) have the positions of emission peaks consistent with Beuther et al. (2005). Secondly, the pointing-corrected ^{12}CO $J=7-6$ image observed in 2008 was used to correct the ^{12}CO $J=6-5$ and ^{12}CO $J=7-6$ data in 2007 with the compact line wing emission integrated from -50 to -30 km s^{-1} in the Orion BN/KL region. In the end, the pointing accuracy was estimated to be $\sim 2''-4''$ after the pointing correction mentioned above, and the calibration error is estimated to be about 10%. All data were reduced using the standard procedures in the GILDAS package.

8

OMC-1 Results

8.1 Large-scale characteristics of OMC-1

In this section, the general characteristics of OMC-1 will be described, and the results for the individual sources will be given in the following sections. The positions of four sources in OMC-1 are listed in Table 8.1. The large-scale ^{12}CO $J = 6 - 5$ and $J = 7 - 6$ images of OMC-1 are shown in Figure 8.1, and the ^{13}CO $J = 8 - 7$ and C^{18}O $J = 6 - 5$ images are shown in Figure 8.2. The measurements of CO isotopologues are summarized in Table 8.2.

Figure 8.1 shows the ^{12}CO $J = 6 - 5$ and $J = 7 - 6$ integrated intensity maps in an area of $\sim 8' \times 6'$ and in a range of radial velocities from -25 km s^{-1} to $+30$ km s^{-1}. Both rotational transitions show a remarkable correspondence. These observations for the first time resolve the ^{12}CO $J = 6-5$ and $J = 7-6$ emission from the OMC-1 region, and also reveal that the PDR surrounding the Trapezium cluster has a very sharp and surprisingly well-defined "rectangle" morphology. This morphology confirms that PDR is a pronounced edge of an H II blister nearly tangential to the line of sight, and forms a "rectangle" structure surrounding the Trapezium cluster. This "rectangle" structure is seen in all our CO isotopologue (i.e., ^{12}CO, ^{13}CO, and C^{18}O) maps.

Figure 8.1 reveals that the warm and dense gas peaking mostly in four objects: Orion BN/KL, Orion South, the Orion Bar, and the Orion East region. The peak main beam temperatures ($T_{\rm MB}$) of ^{12}CO $J = 7 - 6$ and $J = 6 - 5$ are $\gtrsim 160$ K toward these objects. The FWHM line widths of ^{12}CO $J = 6 - 5$ and $J = 7 - 6$ in the Orion Bar and in Orion East are ~ 4 km s^{-1}. The FWHM line widths are ~ 6 km s^{-1} in Orion South, and generally > 25 km s^{-1} in the BN/KL region, due to outflow activities (see Zapata et al. 2005, 2006, 2009, 2010). Furthermore, clear line wings toward Orion BN/KL and South are observed, and extremely extended line wings up to ± 100 km s^{-1} are seen in the Orion BN/KL region. All measurements are in good agreement with the results from Schmid-Burgk et al. (1989), Graf et al. (1990), Wilson et al. (2001), Kawamura et al. (2002), and Marrone et al. (2004).

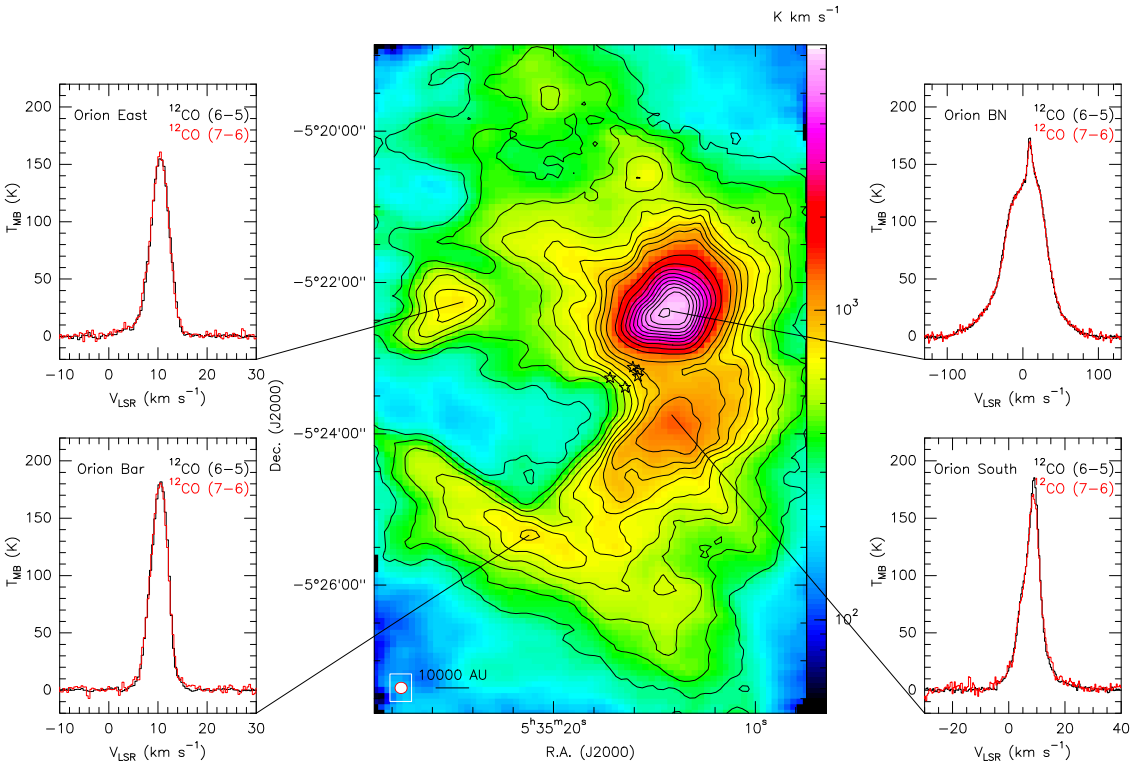

Figure 8.1 The OMC-1 ^{12}CO $J = 6 - 5$ integrated intensity $[-25, +30]$ km s^{-1} image overlaid with the $J = 7 - 6$ contours running from 300 to 1000 K km s^{-1} in steps of 100 K km s^{-1}, and the subsequent contours are plotted from 1200 to 7000 K km s^{-1} in steps of 600 K km s^{-1}. The ^{12}CO $J = 6 - 5$ (black) and ^{12}CO $J = 7 - 6$ (red) spectra are shown for Orion BN, Orion South, Orion Bar, and Orion East. The black stars mark the five Trapezium stars (θ^1 Ori A, B, C, D, and E). Both images are smoothed by two Gaussian beams, and the original beam sizes are shown at the bottom left of the image for ^{12}CO $J = 6-5$ and $J = 7-6$ in red ($9\farcs6$) and white ($8\farcs2$), respectively.

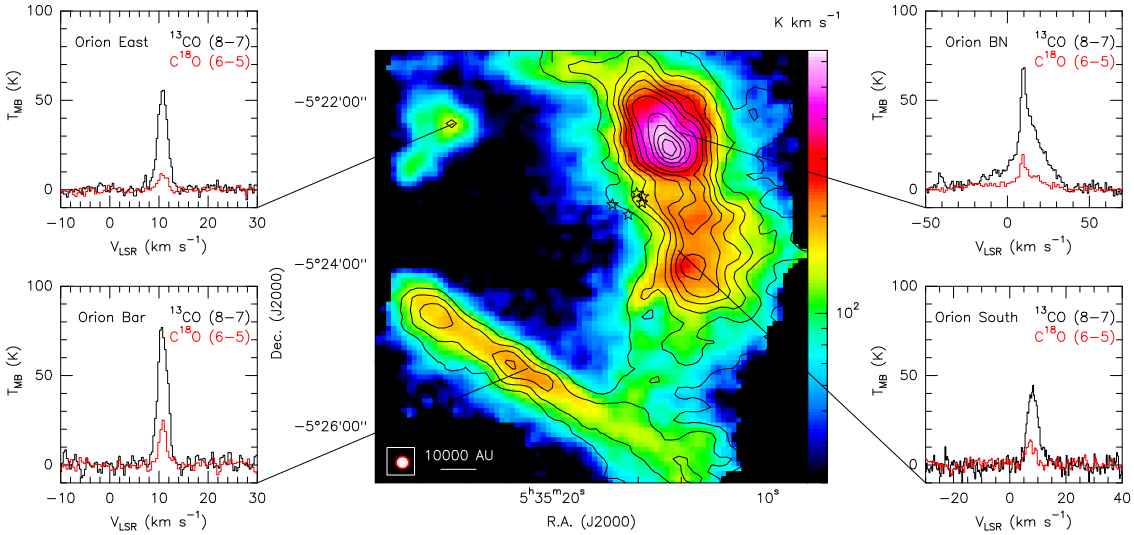

Figure 8.2 The OMC-1 ^{13}CO $J = 8 - 7$ integrated intensity [+5, +15] km s^{-1} image overlaid with the C^{18}O $J = 6 - 5$ [+4, +12] contours running from 15 to 65 K km s^{-1} in steps of 10 K km s^{-1}, and the subsequent contours are plotted from 80 to 200 K km s^{-1}in steps of 30 K km s^{-1}. The ^{13}CO $J = 8 - 7$ (black) and C^{18}O $J = 6 - 5$ (red) spectra are shown for Orion BN, Orion South, Orion Bar, and Orion East at the same positions as in Figure 8.1. The black stars mark the five Trapezium stars (θ^1 Ori A, B, C, D, and E). Both images are smoothed by two Gaussian beams, and the original beam sizes are shown at the bottom left of the image for ^{13}CO $J = 8 - 7$ and C^{18}O $J = 6 - 5$ in red (7.″5) and white (10.″1), respectively.

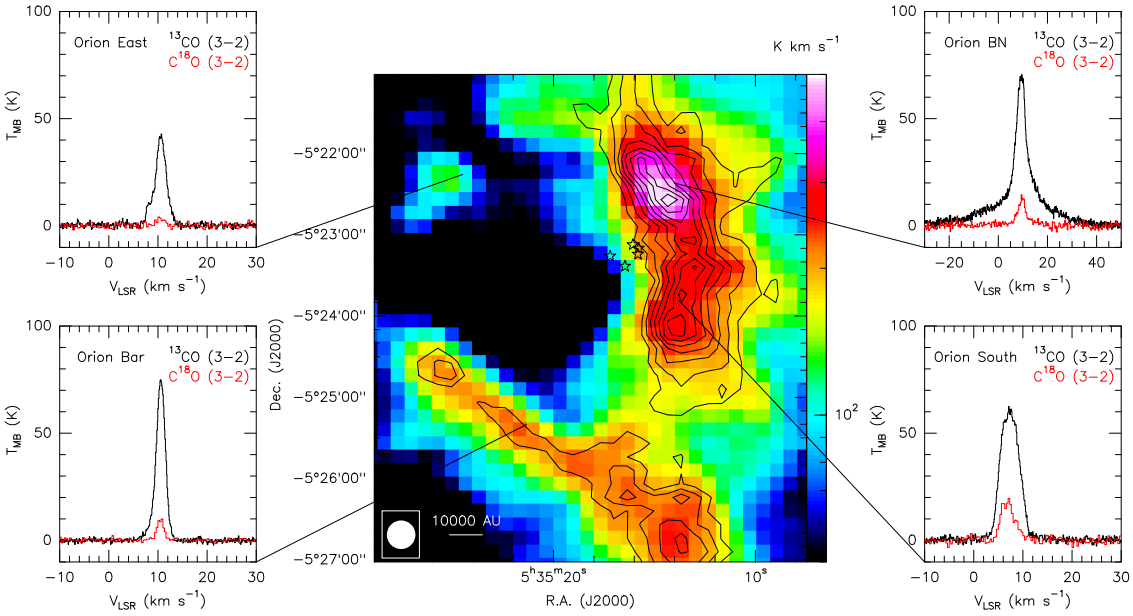

Figure 8.3 The OMC-1 ^{13}CO $J = 3 - 2$ integrated intensity [+5, +15] km s^{-1} image overlaid with the C^{18}O $J = 3 - 2$ [+4, +12] contours running from 24 to 80 K km s^{-1} in steps of 8 K km s^{-1}. The ^{13}CO $J = 3 - 2$ (black) and C^{18}O $J = 3 - 2$ (red) spectra are shown for Orion BN, Orion South, Orion Bar, and Orion East at the same positions as in Figure 8.1. The black stars mark the five Trapezium stars (θ^1 Ori A, B, C, D, and E). The beam size of 21.″1 is shown at the bottom left of the image.

Figure 8.2 shows the ^{13}CO $J = 8 - 7$ and C^{18}O $J = 6 - 5$ integrated intensity maps in a similar area of the ^{12}CO map but in a smaller range of radial velocities (between +5 to +15 km s^{-1} for ^{13}COand +4 to +12 km s^{-1} for C^{18}O). Both maps also show good correspondence, but the integrated emission from the C^{18}O $J = 6 - 5$ line is fainter than the ^{13}CO $J = 8 - 7$ line. These two isotopologues have fainter and less broader emission compared with the one of the ^{12}CO emission, which is expected for optically thin lines. The Orion Bar is well resolved in both lines and also shows a sharp shape. The line widths of the ^{13}CO $J = 8 - 7$ and C^{18}O $J = 6 - 5$ lines toward all four objects are narrow, even in the outflow zones, i.e., Orion BN/KL and South. The ^{13}CO $J = 3 - 2$ and C^{18}O $J = 3 - 2$ integrated intensity maps are shown in Figure 8.3 which was made in a similar area as the ^{12}CO map, and in a range of radial velocities equal to the ^{13}CO $J = 8 - 7$ line and the C^{18}O $J = 6 - 5$ line. The C^{18}O $J = 3 - 2$ line is only present where the ^{13}CO $J = 3 - 2$ line is stronger. The ^{13}CO and C^{18}O line profiles of these rotational transitions toward the Orion BN/KL and South regions are very broad, and show well-defined wings. The emission in the southwestern part of the Bar is especially strong in the lower J transition for both isotopologues.

Table 8.1. The positions of the selected sources in OMC-1

Source	R.A. (J2000)	Dec. (J2000)	offset ($''$)
Orion BN	$05^h35^m14\overset{s}{.}117$	$-05°22'22\overset{''}{.}9$	$(-1, -1)$
Orion South[a]	$05^h35^m14\overset{s}{.}273$	$-05°23'50\overset{''}{.}4$	$(+2, -89)$
Orion Bar[b]	$05^h35^m21\overset{s}{.}178$	$-05°25'15\overset{''}{.}8$	$(+105, -174)$
Orion East	$05^h35^m24\overset{s}{.}627$	$-05°22'17\overset{''}{.}5$	$(+156, +4)$

[a]Corresponding to Clump B in the Orion South region (see §8.3).

[b]Corresponding to the central clump in the Orion Bar region (see §8.4).

8.1.1 Velocity Structure

Velocity channel maps of the ^{12}CO $J = 6 - 5$ and $J = 7 - 6$ emission are shown in Figure 8.4. These reveal the well resolved and complex structure of OMC-1 at ambient velocities as well as high radial velocities. The outflows, located mainly in the Orion BN/KL and Orion South regions, and toward the north of Orion BN/KL, are also clearly seen in these images. These differences are distinct between the outflows emanating from the BN/KL and the Orion South regions. The outflows associated with the former region are poorly collimated and display a very broad radial velocity range, while the outflows in Orion South are very collimated and have different orientations (see §8.3).

In addition, the Orion Bar also shows some filaments crossing the Dark Bay connected to the northern cloud, e.g., $V_{\rm LSR}$= 10 − 12 km s^{-1} channels in Figure 8.4. However, no clear north-south velocity gradients across OMC-1 are observed. Figure 8.5 shows the moment images of ^{12}CO $J = 6 - 5$ and $J = 7 - 6$ where some large-scale filaments can be seen. In addition, the explosive outflow in the Orion BN/KL region shows large $V_{\rm LSR}$ difference in the first moment map, where the blueshifted emission lies in the northwest and redshifted emission in the southeast.

8.1.2 Line Ratios

The maps showing the line ratios between different ^{12}CO lines and isotopologic lines are shown in Figures 8.6–8.10. Figure 8.6 shows the ratio between ^{12}CO $J = 6 - 5$ and $J = 7 - 6$ at three different radial velocities of 5 km s^{-1}, 10 km s^{-1}, and 15 km s^{-1}. The three panels show clear gradients across the integrated line emission. It is interesting to note that at the cloud velocity of 10 km s^{-1}, there are large positive gradients located very close to the position of the Trapezium stars. Those gradients are likely produced by those massive stars that heat the molecular cloud. The ratio gradients at high velocities are maybe produced by shock heating of the outflows located in the Orion BN/KL and South regions. A similar gradient is also seen in the Orion Bar which goes in perpendicular direction to the Trapezium stars with the warmer gas in the central zone (Fig.

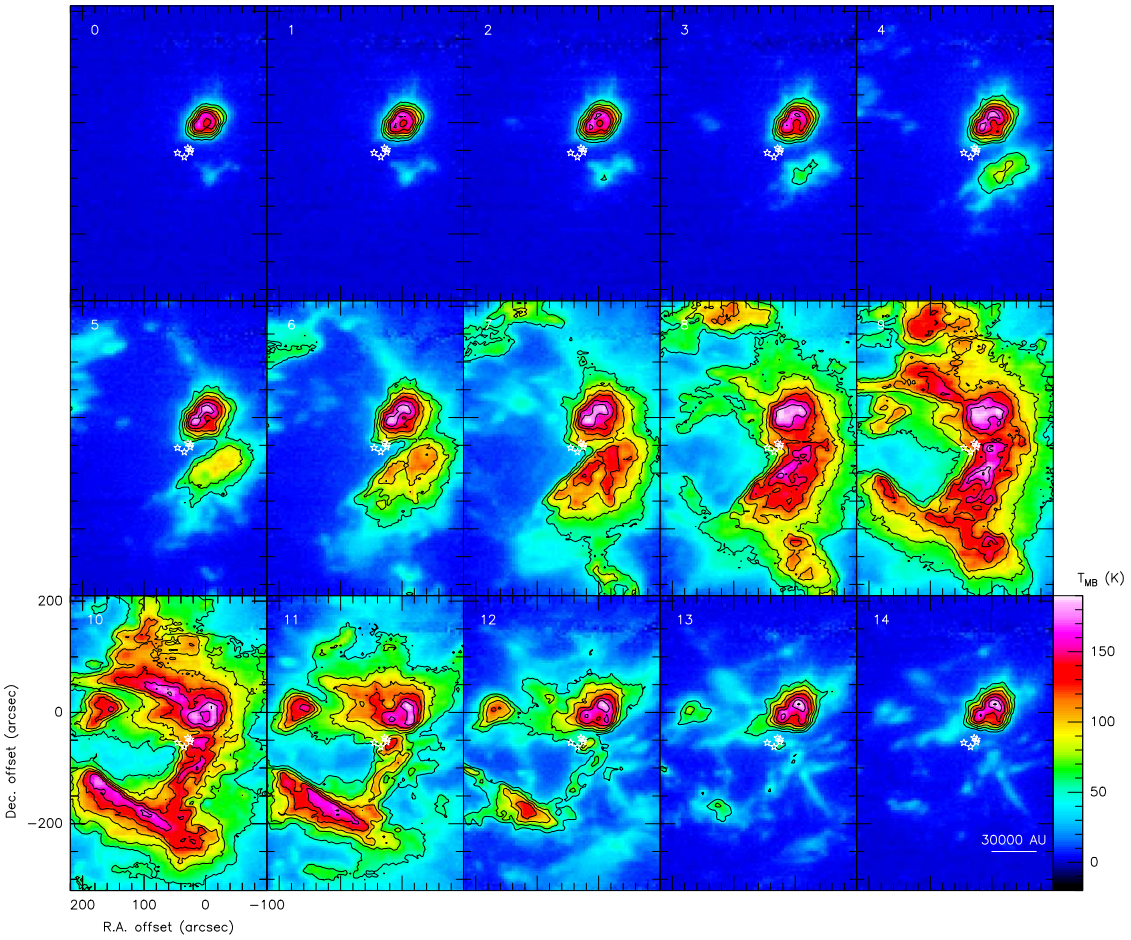

Figure 8.4 Velocity channel maps of the ^{12}CO $J = 6 - 5$ line with the $J = 7 - 6$ contours in OMC-1. The contours are running from 50 to 200 K in steps of 25 K. The white stars mark the five Trapezium stars (θ^1 Ori A, B, C, D, and E) in each map.

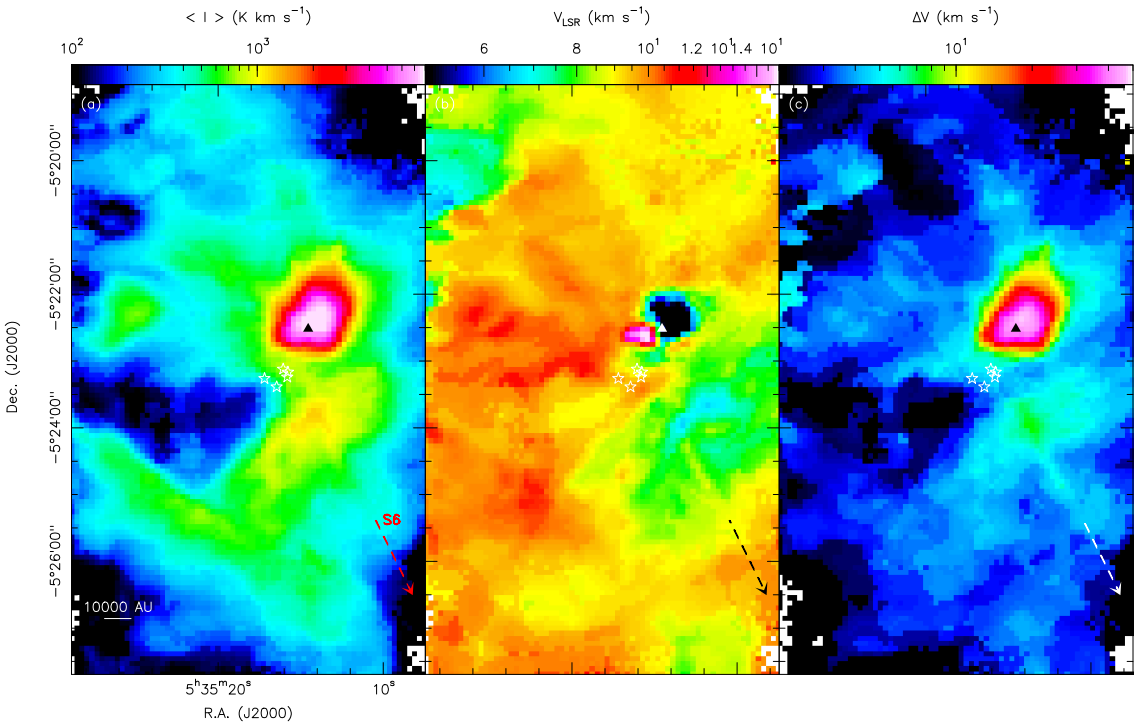

Figure 8.5 Moment maps of the ^{12}CO $J = 6 - 5$ line. The temperatures below 25 K are blanked. The outflow Ori-S6 in the Orion South is marked. The triangle denotes the Orion Hot Core, and the white stars mark the five Trapezium stars (θ^1 Ori A, B, C, D, and E) in each map.

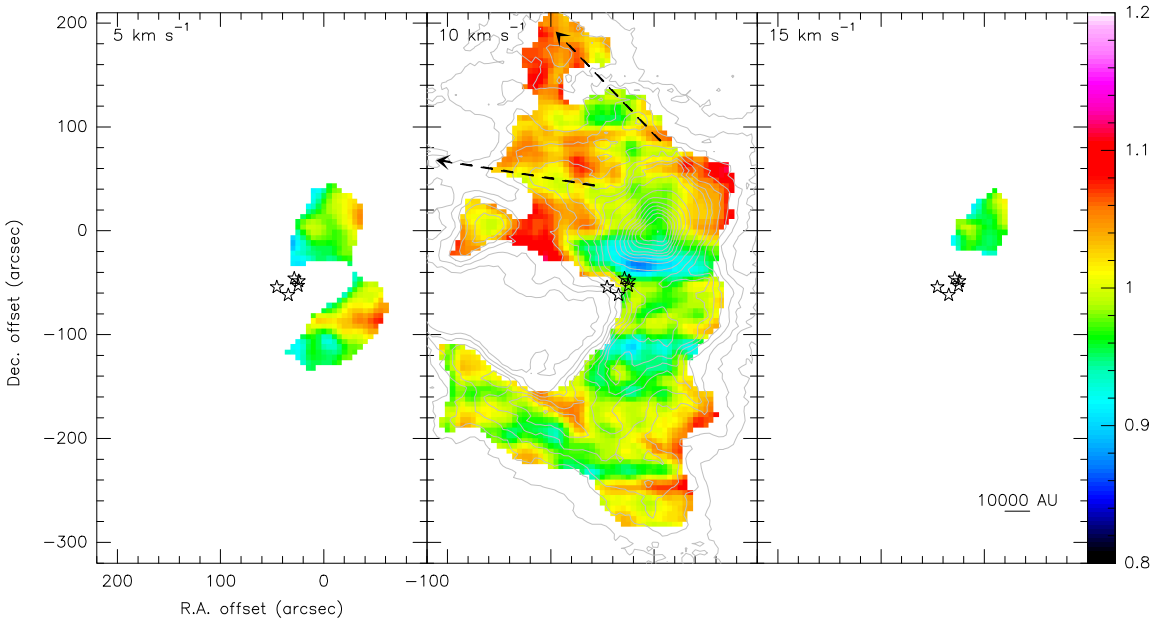

Figure 8.6 The OMC-1 velocity channel maps (5, 10, and 15 km s^{-1}) of the ^{12}CO $J = 6 - 5$ to $J = 7 - 6$ integrated intensity ratio ($\theta_{\rm HPBW} = 10''$). The 10 km s^{-1} image is overlaid with the ^{12}CO $J = 6 - 5$ contours as shown in Figure 8.1.

8.7 at $V_{\rm LSR}$=11 km s^{-1}). However, some patches with higher $T(^{12}{\rm CO}\ J = 6 - 5)$ are seen inside the Bar or behind the ionization front. Some horizontal and vertical strips, artifacts from the OTF mapping, are also seen in the Orion Bar and South regions. These can affect the intensity ratio by $\sim 14\%$ given the calibration errors of 10% for both ^{12}CO $J = 6 - 5$ and $J = 7 - 6$. However, some structures seen in the ^{12}CO $J = 6 - 5$ to $J = 7 - 6$ ratio maps, e.g., the dashed-lines in Figure 8.6, are unlikely due to the calibration error or scanning strips during the observation, and seem to be footprints of filemants of outflows. In Figure 8.7, the channel maps of the ^{12}CO $J = 6 - 5$ to $J = 7 - 6$ ratio show an interesting feature that at $V_{\rm LSR} = 11 - 12$ km s^{-1} the ^{12}CO $J = 6 - 5$ to $J = 7 - 6$ ratio is particularly low in the edge close to the Orion BN/KL, South, and Bar regions. Moreover, the ^{12}CO $J = 6 - 5$ to $J = 7 - 6$ ratio is also low in the Orion South PDR region shown in Figure 8.7 at $5 - 7$ km s^{-1}, which indicates that the luminous ^{12}CO $J = 7 - 6$ line is excited by the Trapezium stars.

In the ratio maps of ^{13}CO to C^{18}O $J = 3 - 2$ shown in Figures 8.8 and 8.9, an elongated and dense ridge in the north-south direction is clearly detected. A similar elongated dense ridge is also seen in the ^{13}CO $J = 8 - 7$ to C^{18}O $J = 6 - 5$ ratio map, and is more clearly seen in the peak temperature ratio image (Fig. 8.9). In the C^{18}O $J = 3 - 2$ to $J = 6 - 5$ ratio images, the Orion BN/KL, the Orion Bar, and Orion East shows low ratios (< 1), which indicates a higher excitation in those regions.

The spatial distribution of high optical depth regions at different velocities is shown in

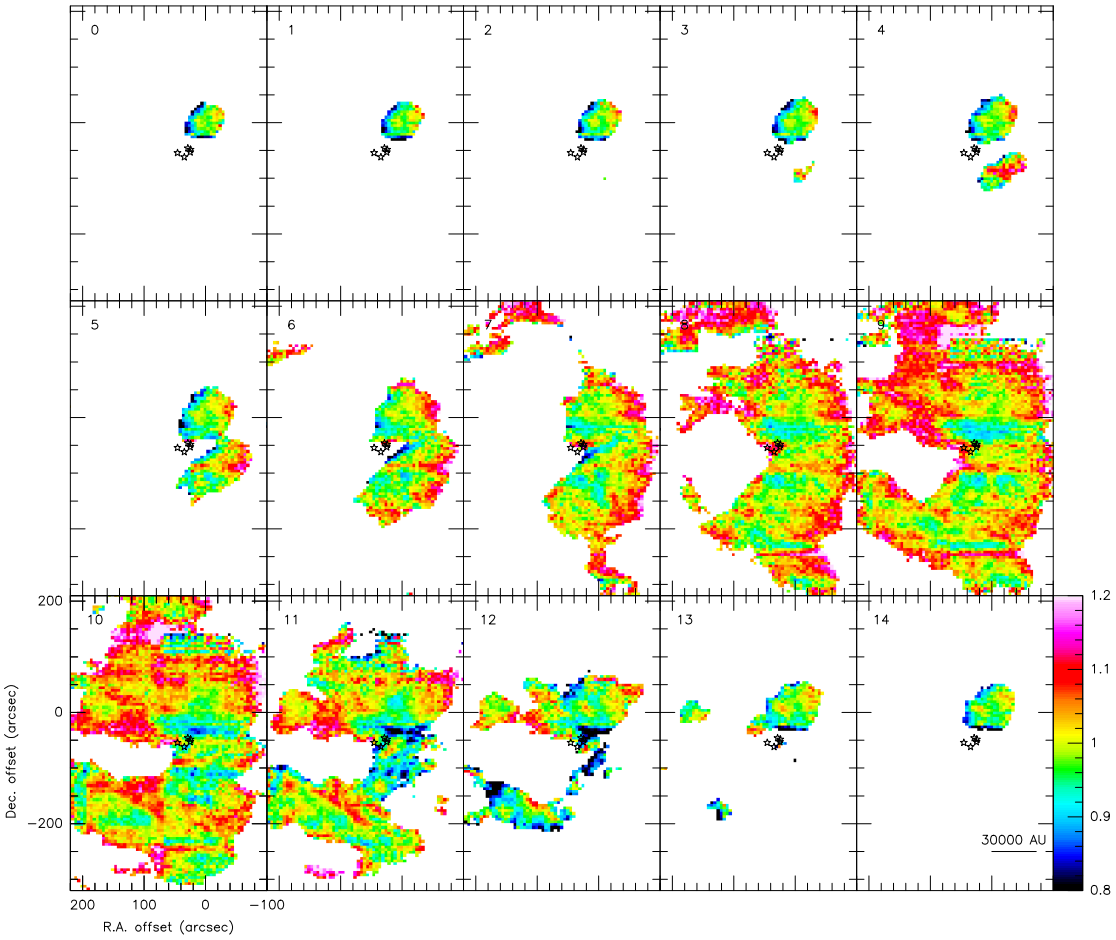

Figure 8.7 The velocity channel maps of the ^{12}CO $J = 6 - 5$ line in OMC-1. The contours are running from 50 to 200 K in steps of 25 K. The black stars mark the five Trapezium stars (θ^1 Ori A, B, C, D, and E) in each map.

Table 8.2. The measurements of the CO isotopologues in the selected sources of OMC-1

Line	Orion BN			Orion South			Orion Bar			Orion East		
	$T_{\rm peak}$[a] (K)	$V_{\rm LSR}$ (km s^{-1})	ΔV[b] (km s^{-1})	$T_{\rm peak}$[a] (K)	$V_{\rm LSR}$ (km s^{-1})	ΔV[b] (km s^{-1})	$T_{\rm peak}$[a] (K)	$V_{\rm LSR}$ (km s^{-1})	ΔV[b] (km s^{-1})	$T_{\rm peak}$[a] (K)	$V_{\rm LSR}$ (km s^{-1})	ΔV[b] (km s^{-1})
^{13}CO (8 − 7)	63.8±2.3	10.3	9.0	41.0±3.6	8.1	4.9	75.9±3.3	10.7	2.7	55.7±2.5	10.6	2.3
^{12}CO (7 − 6)	168.5±2.2	9.8	55.5	165.6±2.0	8.7	6.9	179.9±2.6	10.5	4.0	156.2±3.1	10.5	4.0
^{12}CO (6 − 5)	164.6±1.6	9.5	53.3	187.5±1.4	9.1	6.4	180.9±0.9	10.4	3.8	156.7±1.2	10.4	4.7
C^{18}O (6 − 5)	19.0±1.3	10.0	5.8	10.2±1.9	7.6	4.4	23.9±2.2	10.9	1.8	8.2±1.3	10.4	2.2
^{13}CO (3 − 2)	68.7±0.5	9.6	5.6	62.1±1.1	7.3	4.5	90.1±1.1	10.8	2.4	41.6±1.1	10.6	2.3
C^{18}O (3 − 2)	12.4±0.7	10.2	3.0	19.8±1.6	7.0	3.3	13.4±1.0	10.8	1.7	3.9±1.0	10.4	2.3

[a]Temperatures shown here are corrected to the main beam temperature unit.

[b]Line widths are measured in FWHM.

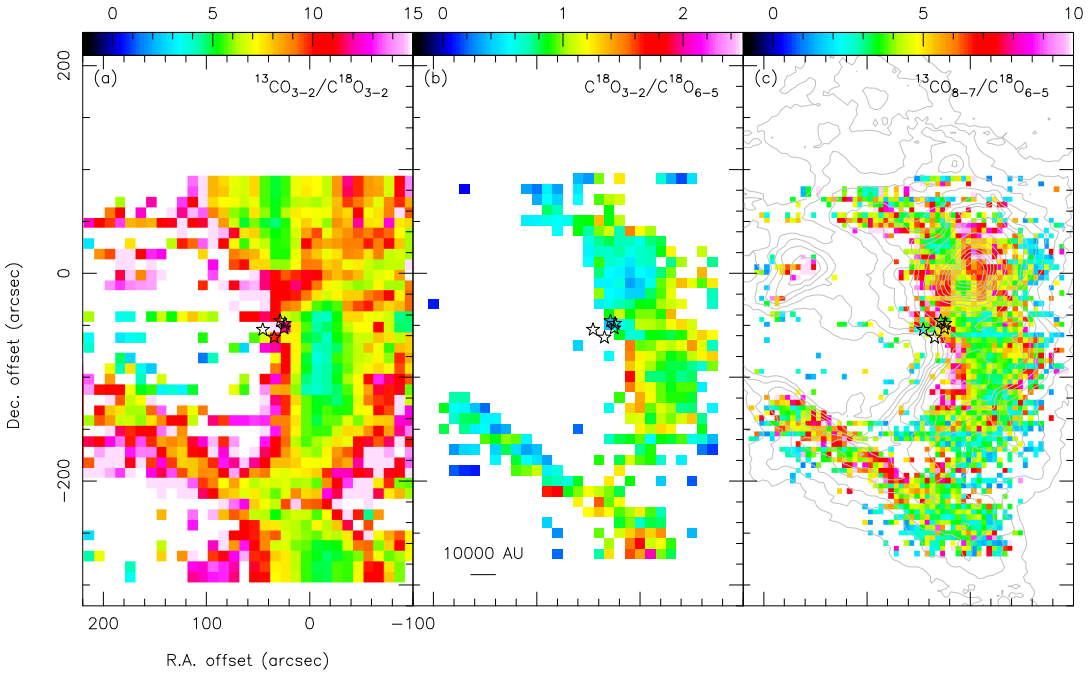

Figure 8.8 (a) The OMC-1 ^{13}CO $J = 3-2$ to C^{18}O $J = 3-2$ integrated intensity ratio map ($\theta_{\rm HPBW} = 20''$). (b) The C^{18}O $J = 3-2$ to $J = 6-5$ integrated intensity ratio map ($\theta_{\rm HPBW} = 20''$). (c) The ^{13}CO $J = 8-7$ to C^{18}O $J = 6-5$ integrated intensity ratio map ($\theta_{\rm HPBW} = 10''$).

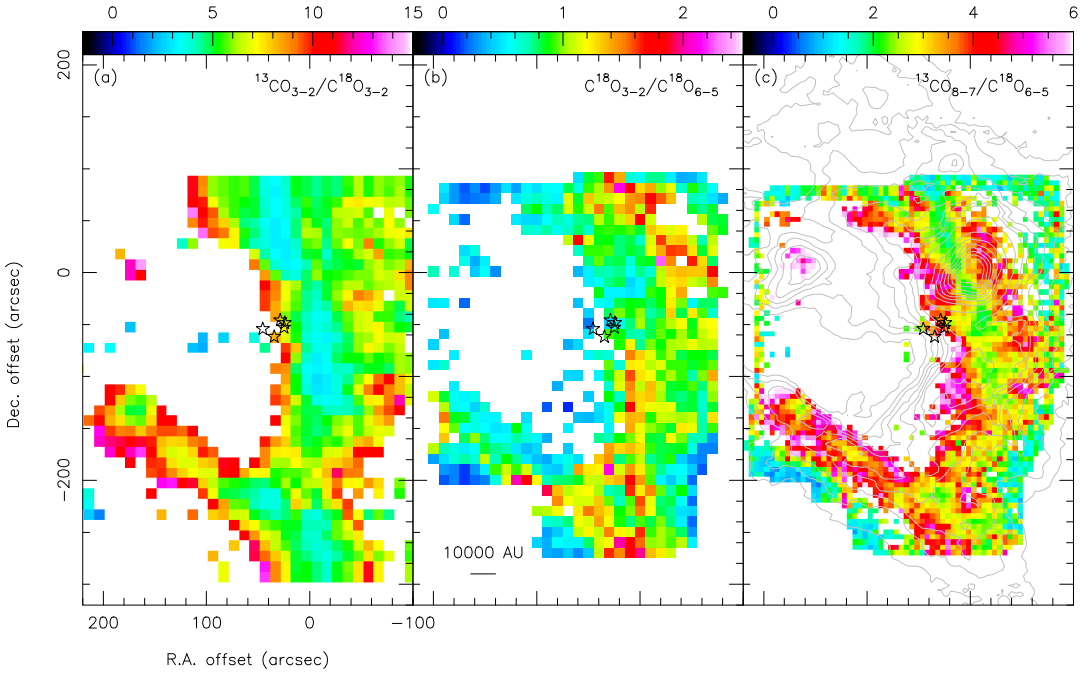

Figure 8.9 (a) The OMC-1 ^{13}CO $J = 3-2$ to C^{18}O $J = 3-2$ peak temperature ratio map ($\theta_{\rm HPBW} = 20''$). (b) The C^{18}O $J = 3-2$ to $J = 6-5$ integrated intensity ratio map ($\theta_{\rm HPBW} = 20''$). (c) The ^{13}CO $J = 8-7$ to C^{18}O $J = 6-5$ integrated intensity ratio map ($\theta_{\rm HPBW} = 10''$).

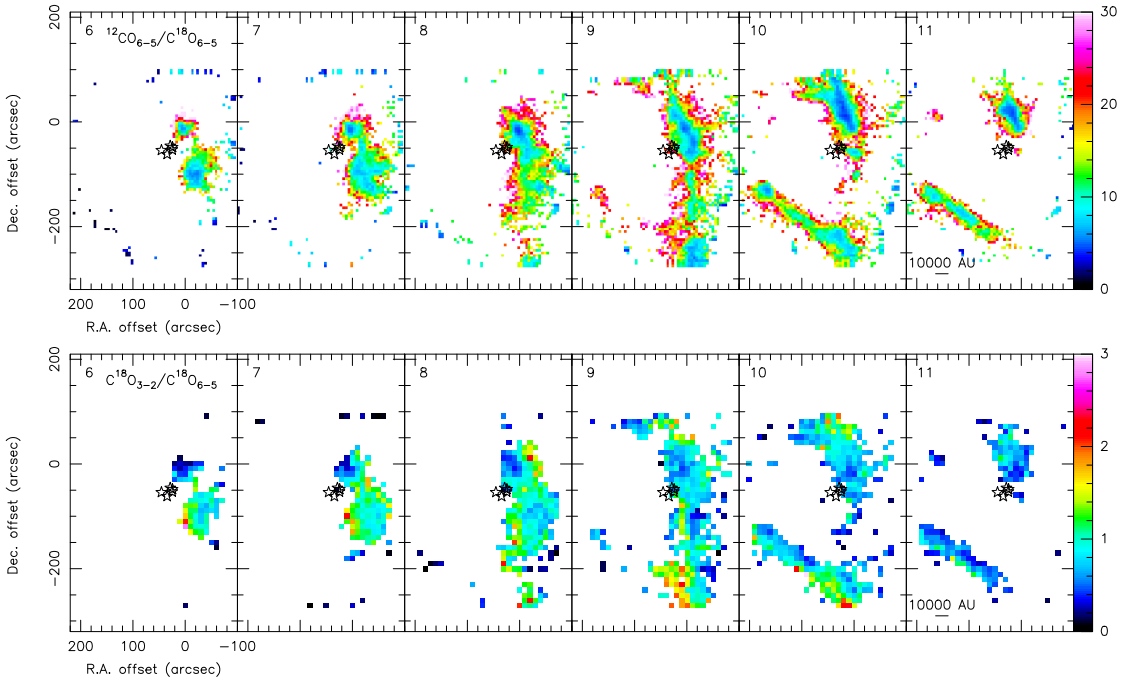

Figure 8.10 The lower panel is the $C^{18}O$ $J = 3 - 2$ to $J = 6 - 5$ ratio channel maps ($\theta_{\rm HPBW} = 20''$) at different velocities from 6 to 11 km s^{-1} in OMC-1. The upper panel is the corresponding ^{12}CO $J = 6 - 5$ to $C^{18}O$ $J = 6 - 5$ ratio channel maps ($\theta_{\rm HPBW} = 10''$). The edge cut and empty area are due to different image sizes and blanking values. Orion BN is located at the offset (0″, 0″), and the five Trapezium stars are marked in each map.

the ^{12}CO to $C^{18}O$ $J = 6 - 5$ ratio image (Fig. 8.10). The dense ridge is clearly seen in the 9 km s^{-1} channel in Figure 8.10, and the Orion Bar is seen mainly in the 10–11 km s^{-1} channels. The dense ridge extends from the north of Orion BN/KL to the western clump of the Orion Bar, and is consistent to the dust emission imaged by Lis et al. (1998). This high optical depth ridge is similar to the filamentary structure observed in the NH_3 emission (Wiseman & Ho 1998, 1996), but has some morphological differences in the north of the Orion BN/KL region. In addition, the $C^{18}O$ $J = 3 - 2$ to $J = 6 - 5$ ratio channel maps in Figure 8.10 comfirm that some relatively high temperature regions are located in the Orion BN/KL region and the surface of the Orion Bar close to the ionization front.

8.2 Orion BN/KL

Emission morphology

A shell-like structure is seen in the ^{12}CO $J = 6 - 5$ and $J = 7 - 6$ images of the Orion BN/KL region (from 0 to 10 km s^{-1} in Fig. 8.12), and is probably partly due to the high optical depth in the cloud

Table 8.3. The positions of the selected sources in the Orion BN/KL region

Source	R.A. (J2000)	Dec. (J2000)	offset ($''$)
Orion BN	$05^h35^m14\overset{s}{.}117$	$-05°22'22\overset{''}{.}9$	$(-1, -1)$
Orion Hot Core[a]	$05^h35^m14\overset{s}{.}580$	$-05°22'31\overset{''}{.}0$	$(+6, -10)$
Orion Compact Ridge[a]	$05^h35^m14\overset{s}{.}200$	$-05°25'41\overset{''}{.}0$	$(+1, -20)$
Explosion center[b]	$05^h35^m14\overset{s}{.}370$	$-05°22'27\overset{''}{.}9$	$(+3, -6)$

[a]Friedel & Snyder (2008).

[b]Zapata et al. (2009).

center which leads to self-absorption. The line profiles of ^{12}CO $J = 6 - 5$ and $J = 7 - 6$ show very broad line wings extending from about -100 to 100 km s^{-1} as shown in Figure 8.11, and highly asymmetric line profiles are seen both in Orion BN and the Hot Core. The peak temperatures of ^{12}CO $J = 6-5$ and $J = 7-6$ in Orion BN, the Hot Core and Compact Ridge range from 160 to 170 K, where BN has higher temperature in the ^{12}CO $J = 6-5$ transition, and the Compact Ridge has higher temperature in the ^{12}CO $J = 7 - 6$ transition instead. The Orion Hot Core has roughly the same temperatures in both transitions (Fig. 8.11). The CO isotopologue measurements for these three sources are summarized in Table 8.4, and their ratios are listed in Table 8.5.

The integrated intensity map of the ^{13}CO $J = 8 - 7$ emission (Fig. 8.13) shows that the emission peak is around the Hot Core, and the C^{18}O $J = 6 - 5$ emission is peaked between the Hot Core and the Compact Ridge. Both ^{13}CO $J = 8 - 7$ and C^{18}O $J = 6 - 5$ show elongated structure at $\sim$ 10 km s^{-1} in the NW-SE direction, which is similar to the dust continuum emission (e.g. Plambeck et al. 1995; Wright, Sandell, Wilner, & Plambeck 1992). The channel maps of the line ratios shown in Figure 8.15 reveal that both Hot Core and Compact Ridge lie along the large-scale dense ridge seen in the ^{12}CO $J = 6-5$ to C^{18}O $J = 6-5$ ratio maps, but the high excitation region is concentrated around the Hot Core, which is also seen in the C^{18}O $J = 3 - 2$ to C^{18}O $J = 6 - 5$ ratio maps. The high optical depth ridge is also evident in the ^{13}CO to C^{18}O ratio maps (Fig. 8.16), and the velocity gradient is obvious in the NW-SE direction along the dense ridge.

Figure 8.14 shows the peak temperature maps for various molecules in the Orion BN/KL region, where the emission of ^{13}CO $J = 8 - 7$, $J = 6 - 5$, and C^{18}O $J = 6 - 5$ all peak around the Compact Ridge at 8 km s^{-1}. The oxygen-bearing molecules, such as Methanol (CH_3OH) and Dimethyl Ether ($(CH_3)_2O$), are believed to be abundant near the Compact Ridge. On the other hand, the nitrogen-bearing species are thought to be more abundant in the Hot Core. In our data, the emission peaks of CH_3OH $11_{1,10} - 10_{0,10}$, $^{13}CH_3OH$ $14_{1,13} - 13_{0,12}$, and $(CH_3)_2O$ $21_{5,16} - 20_{4,17}$ are all strongly related to the Compact Ridge (at $\sim$ 8 km s^{-1}). The emissions peaks of Methyl Cyanide CH_3CN $36_9 - 35_9$ and SO_2 $37_{1,37} - 36_{0,36}$ seem to be associated with the Hot Core (at $\sim$ $5 - 6$ km s^{-1}), and have similar positions in the SMA observation by Beuther et al. (2005). The

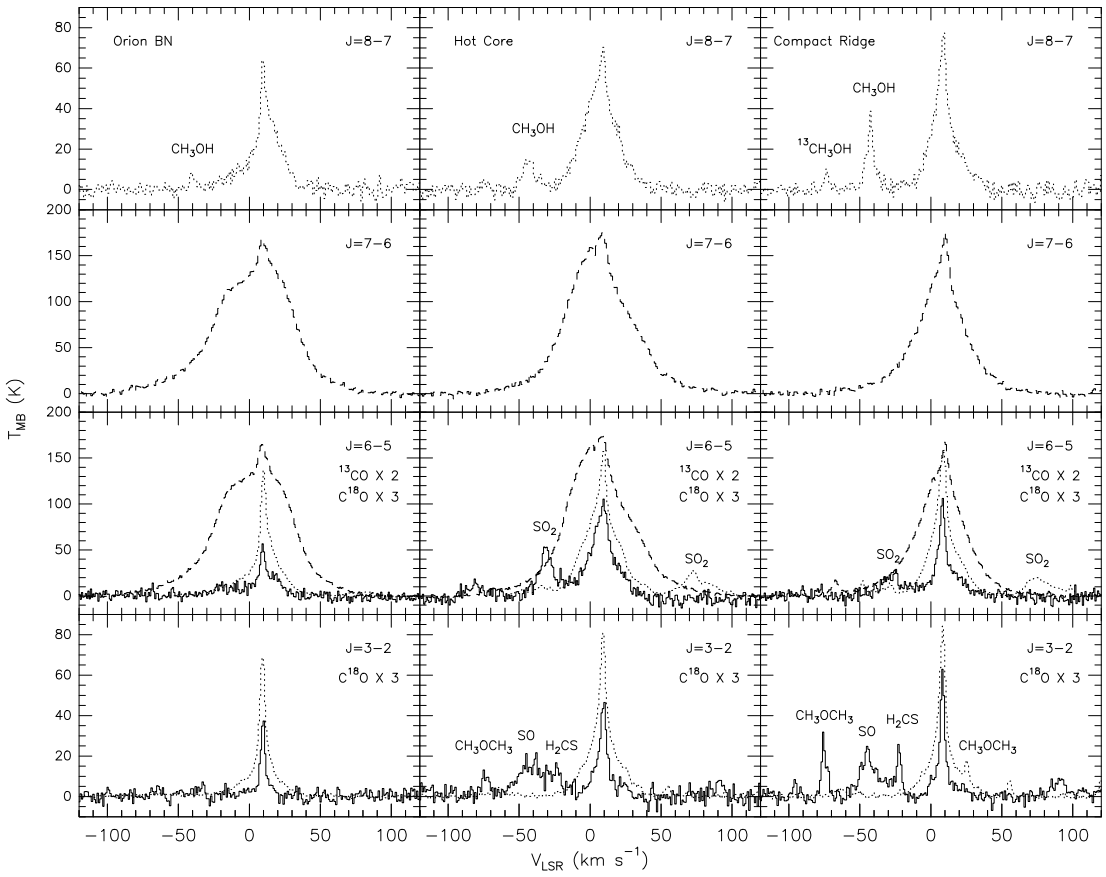

Figure 8.11 The Spectra of different CO isotopologic transitions in the Orion BN/KL region. ^{12}CO is shown in dashed-lines, ^{13}CO in dotted-lines, and C^{18}O in solid lines. The CH_3OH $13_{3,10} - 12_{2,11}$ A line at 881.4 GHz and the $^{13}CH_3OH$ $13_{1,13} - 120, 12$ A line at 881.5 GHz are seen together with the spectra of ^{13}CO $J = 8-7$. The SO_2 $36_{1,35} - 35_{2,34}$ line at 658.6 GHz and the SO_2 $22_{7,15} - 35_{6,16}$ line at 660.9 GHz are seen together with the spectra of C^{18}O $J = 6 - 5$ and ^{13}CO $J = 6 - 5$, respectively. The SO $2_1 - 1_0$ line at 329.4 GHz is seen together with the C^{18}O $J = 3 - 2$ spectra. The CH_3OCH_3 $17_{2,16} - 161, 15$ EE line at 343.8 GHz and the H_2CS $10_{2,8} - 9_{2,7}$ line at 343.8 GHz are seen in the image band of the C^{18}O $J = 3 - 2$ spectra. The CH_3OCH_3 $19_{0,19} - 18_{1,18}$ EE line at 342.6 GHz is seen in the image band of the ^{13}CO $J = 3 - 2$ spectra.

.

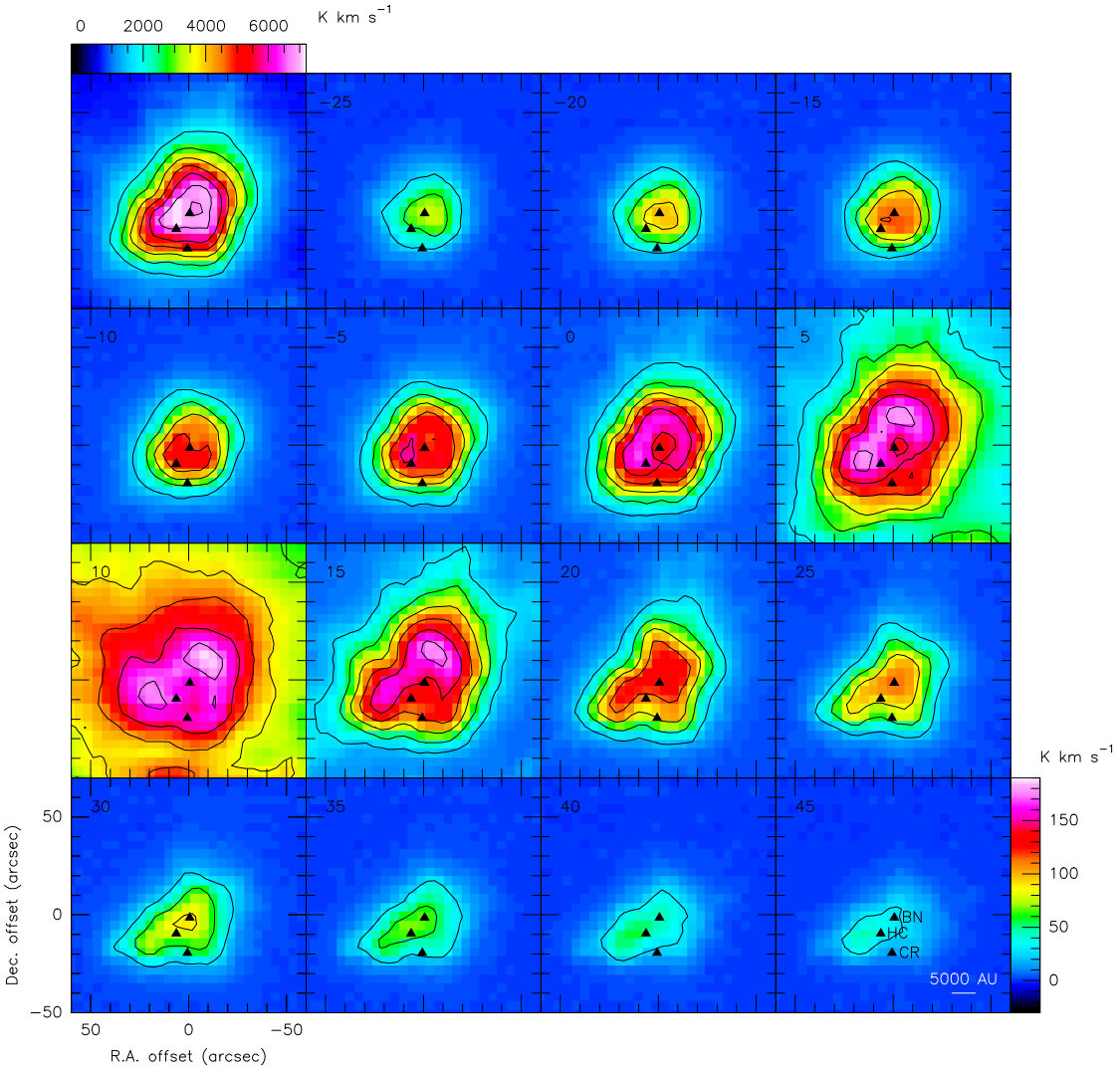

Figure 8.12 The ^{12}CO $J = 6-5$ (color image) and the $J = 7-6$ (contours) velocity channel maps in the Orion BN/KL region. The top-left panel is the ^{12}CO $J = 6-5$ integrated intensity $[-25, +30]$ km s^{-1} image overlaid with the ^{12}CO $J = 7-6$ contours running from 2000 to 7000 K km s^{-1} in steps of 1000 K km s^{-1}. The other eight panels show the ^{12}CO $J = 7-6$ contours plotted from 30 to 180 K km s^{-1} in steps of 30 K km s^{-1} overlaid with the ^{12}CO $J = 6-5$ velocity channel maps from -25 to $+45$ km s^{-1}. Orion BN, the Hot Core (HC), and Compact Ridge (CR) are represented in filled triangles shown in the bottom-right panel.

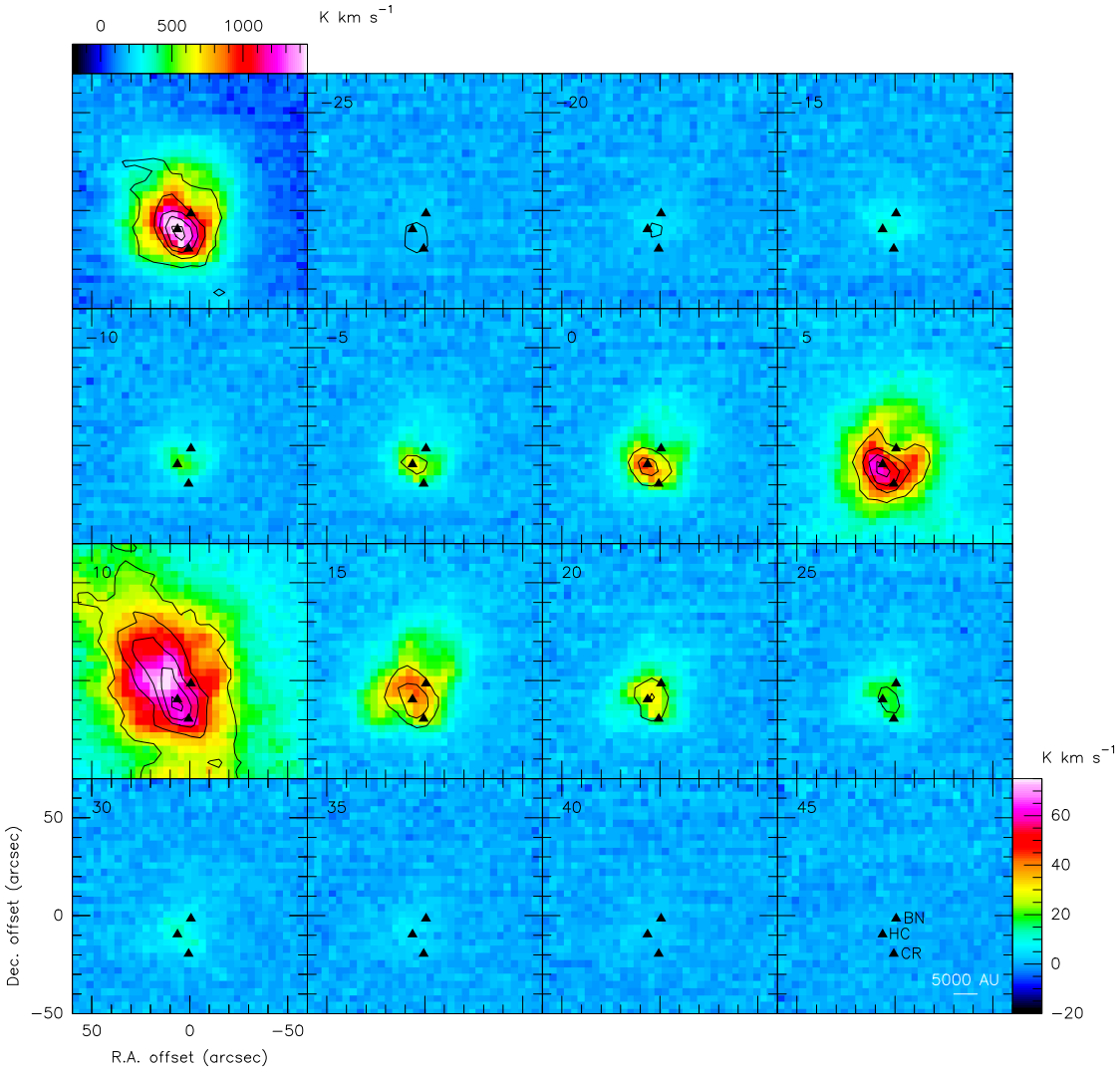

Figure 8.13 The ^{13}CO $J = 8 - 7$ (color image) and the C^{18}O $J = 6 - 5$ (contours) velocity channel maps in the Orion BN/KL region. The top-left panel is the ^{13}CO $J = 8 - 7$ integrated intensity $[-10, +30]$ km s^{-1} image overlaid with the C^{18}O $J = 6 - 5$ $[-5, +25]$ km s^{-1} contours running from 100 to 500 K km s^{-1} in steps of 100 K km s^{-1}. The other eight panels show the C^{18}O $J = 6 - 5$ contours plotted in steps of 6 K km s^{-1} from 6 to 30 K km s^{-1} with the ^{13}CO $J = 8 - 7$ velocity channel maps from -25 to $+45$ km s^{-1}. Orion BN, the Hot Core (HC) and Compact Ridge (CR) are represented in filled triangles shown in the bottom-right panel.

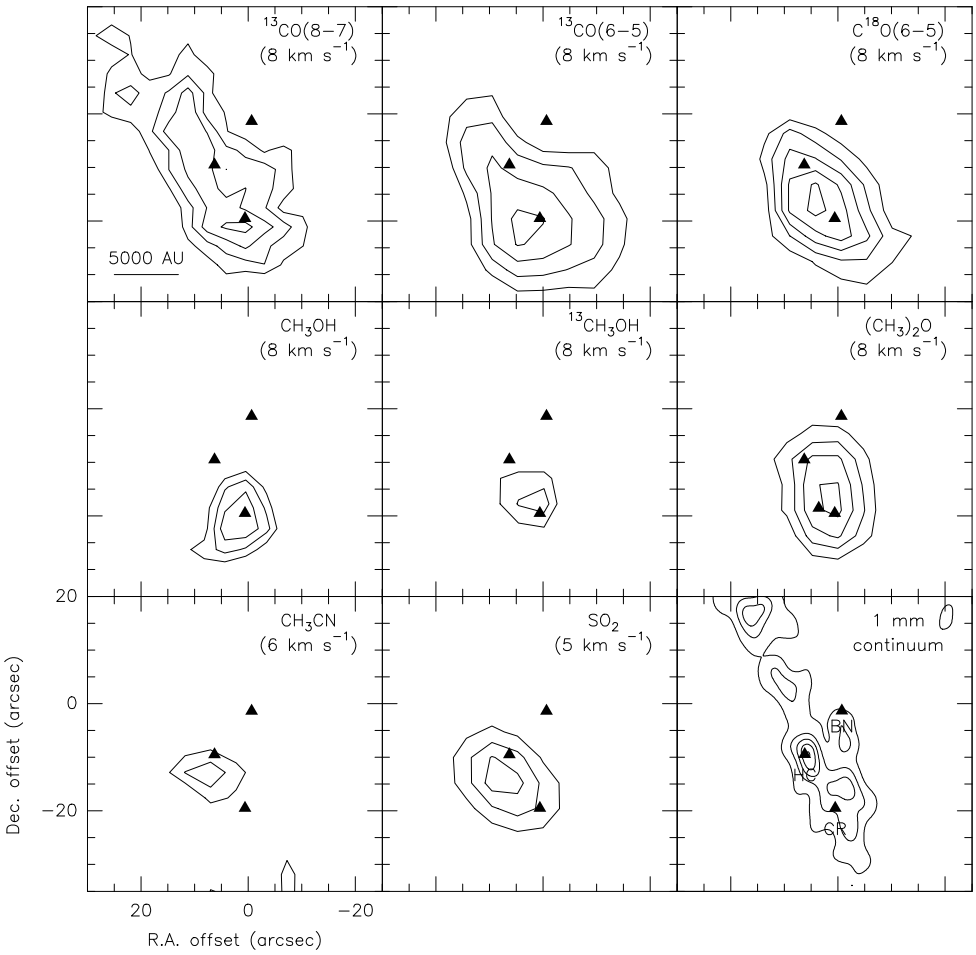

Figure 8.14 Various molecular emission in the Orion BN/KL region. For clarity, four contours denote the intensity from 60 to 75 K km s^{-1} in steps of 5 K km s^{-1} in the ^{13}CO $J = 8 - 7$ and $J = 6 - 5$ maps. For C^{18}O $J = 6 - 5$, contours are plotted from 20 to 36 K km s^{-1} in steps of 4 K km s^{-1}. The contours of CH_3OH $11_{1,10} - 10_{0,10}$ emission are running from 22 to 30 K km s^{-1} in steps of 4 K km s^{-1} (3 σ level). The contours of $^{13}CH_3OH$ $14_{1,13} - 13_{0,12}$ emission represent 3.0 K km s^{-1} and 4.2 K km s^{-1} (7 σ level). The contours of CH_3OCH_3 $21_{5,16} - 20_{4,17}$ emission are plotted from 4 to 10 K km s^{-1} in steps of 2 K km s^{-1} (6 σ level). The contours of CH_3CN $36_9 - 35_9$ emission represent 0.9 K km s^{-1} and 1.5 K km s^{-1} (5 σ level). The contours of SO_2 $37_{1,37} - 36_{0,36}$ emission are plotted from 6 to 18 K km s^{-1} in steps of 4 K km s^{-1} (13 σ level). The bottom-right panel shows the SMA 1 mm continuum emission (Zapata, private communications) in contours running from 0.2 to 2 Jy beam^{-1} in steps of 0.4 Jy beam^{-1}. Orion BN (0″, 0″), the Hot Core (HC), and Compact Ridge (CR) are marked in filled triangles.

SO_2 $37_{1,37} - 36_{0,36}$ emission is also consistent with the data from Beuther et al. (2005), where the SO_2 emission appears both in the Hot Core and Compact Ridge, and the emission seems to extend between the Hot Core and Compact Ridge. However, the paper by Friedel & Snyder (2008) shows a much more complicated distribution of O-bearing and N-bearing species in the Orion BN/KL region, and the emission from large O-bearing molecule $(CH_3)_2O$ actually originates from the region near IRc5 and IRc6, located at about $4''$ and $14''$ to the north of the Compact Ridge, respectively. This is also seen in our data (Fig. 8.14) that the $(CH_3)_2O$ emission peak has an offset of few arcsecond from the Compact Ridge, and is close to IRc5 and IRc6. Friedel & Snyder (2008) also show that the lack of CH_3OH emission in the Compact Ridge is because most of the flux from the extended emission was resolved out by the CARMA.

Kinematics

The compact and warm structures toward the Orion BN/KL region traced by the ^{12}CO $J = 6 - 5$ and $J = 7 - 6$ lines are part of the enigmatic molecular outflow that seems to be produced by a violent explosion during the disruption of a massive young stellar system (Zapata et al. 2009). These observations reveal some faint filamentary structures toward the northern blueshifted components of the "outflow", e.g., at $V_{\rm LSR}$=5 km s^{-1} in Figure 8.4, which are very likely associated with the ^{12}CO fingers reported by Zapata et al. (2009).

In Figure 8.17, the shell structure surrounding Orion BN is shown in the $3 - 7$ and $13 - 17$ km s^{-1} images. In the higher velocity ranges, i.e., $17 - 70$ and $-70 - 3$ km s^{-1}, the redshifted ^{12}CO emission moves toward the H_2 emission Peak 2, and the blueshifted emission moves toward the H_2 emission Peak 1, the peak position of vibrationally excited molecular hydrogen emission (Beckwith et al. 1978). At very high velocities up to $\pm$100 km s^{-1}, the ^{12}CO outflows are clearly associated with the H_2 emission Peak 1 and 2 (Fig. 8.18), which was shown in Figure 8.5. This very high velocity outflow has been observed in different ^{12}CO transitions before (see Rodríguez-Franco, Martín-Pintado, & Wilson 1999; Schulz et al. 1995), and the morphology of the high velocity ^{12}CO $J = 6 - 5$ emission is similar to the result obtained by Rodríguez-Franco, Martín-Pintado, & Wilson (1999), where the high speed bullets seem to be associated with the H_2 emission Peak 1 and 2. This high-velocity CO emission might represent the postshock gas in the cooling zone. However, the upper limit of the H_2 outflows radial velocity is $\sim 34 - 40$ km s^{-1} (Nissen et al. 2007), which is only half of the velocity of the high speed CO bullets. Another noteworthy similarity between the H II fingers and CO outflows is that the wide-angle distribution in the northwestern part is presented both in the H_2 observations and our data. In addition, the red- and blueshifted line wings of ^{13}CO $J = 8 - 7$, $J = 6 - 5$, and C^{18}O $J = 6 - 5$ emission peaks (Fig. 8.19) have no obvious offset, and peak around the region between Orion BN and the Hot Core, which is close to the center of the explosive outflow reported by Zapata et al. (2009).

In the PV diagrams of Orion BN/KL (Fig. 8.20), a clear shell structure is seen in Cut I,

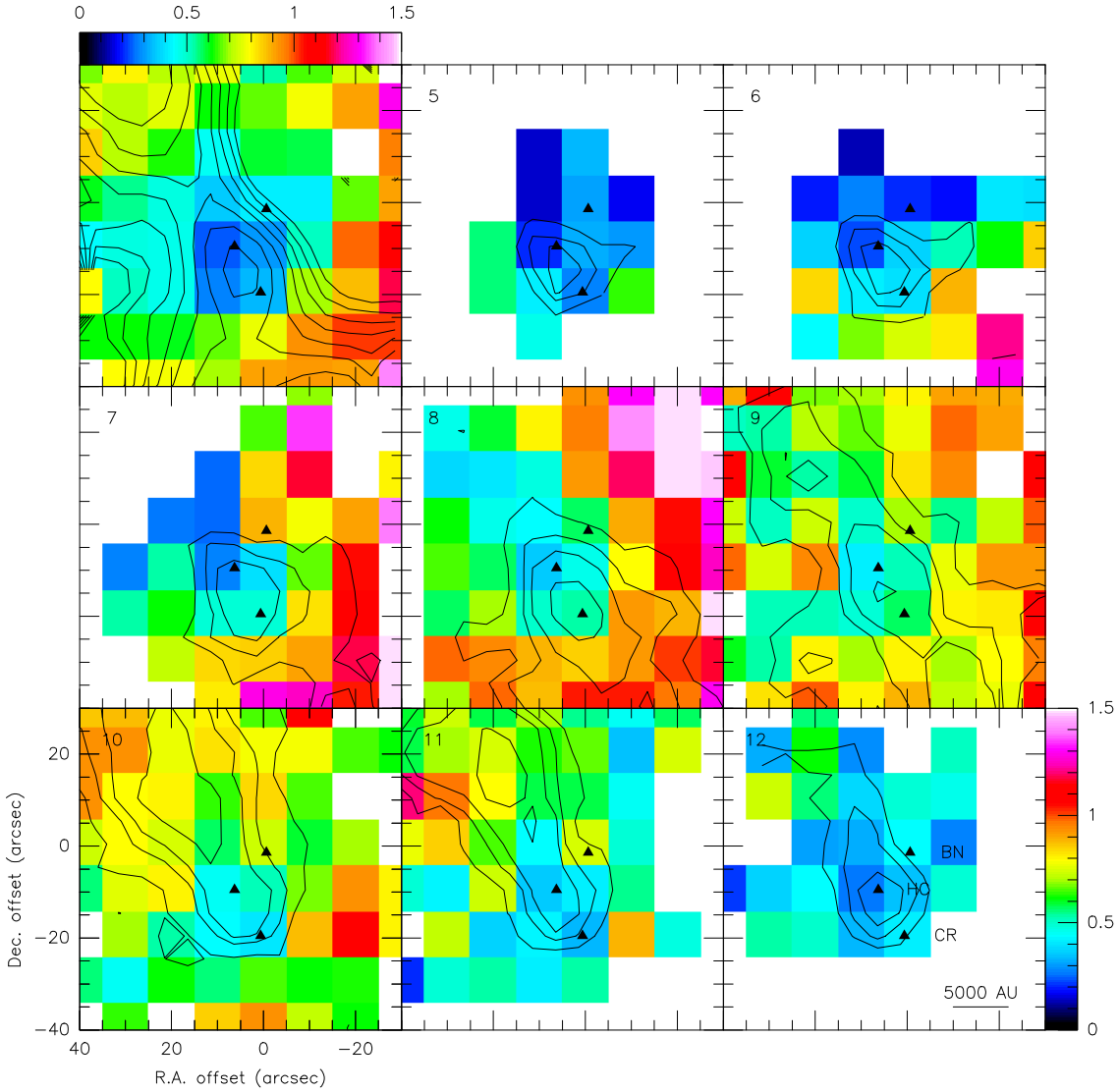

Figure 8.15 The top-left panel shows the $C^{18}O$ $J = 3 - 2$ to $C^{18}O$ $J = 6 - 5$ integrated intensity ratio (color image) overlaid with the ^{12}CO $J = 6 - 5$ to $C^{18}O$ $J = 6 - 5$ integrated intensity ratio in contours running from 20 to 50 in steps of 5, where the lowest value (< 5) is located between the Orion Hot Core and Compact Ridge. The rest eight panels show the $C^{18}O$ $J = 3 - 2$ to $C^{18}O$ $J = 6 - 5$ emission ratio in the different velocity from 5 to 12 km s^{-1} overlaid with the ^{12}CO $J = 6 - 5$ to $C^{18}O$ $J = 6 - 5$ ratio contours in ratio values of 13, 9, 7, and 5. The empty area is due to the blanking value of 2 K km s^{-1} for $C^{18}O$ $J = 6 - 5$.

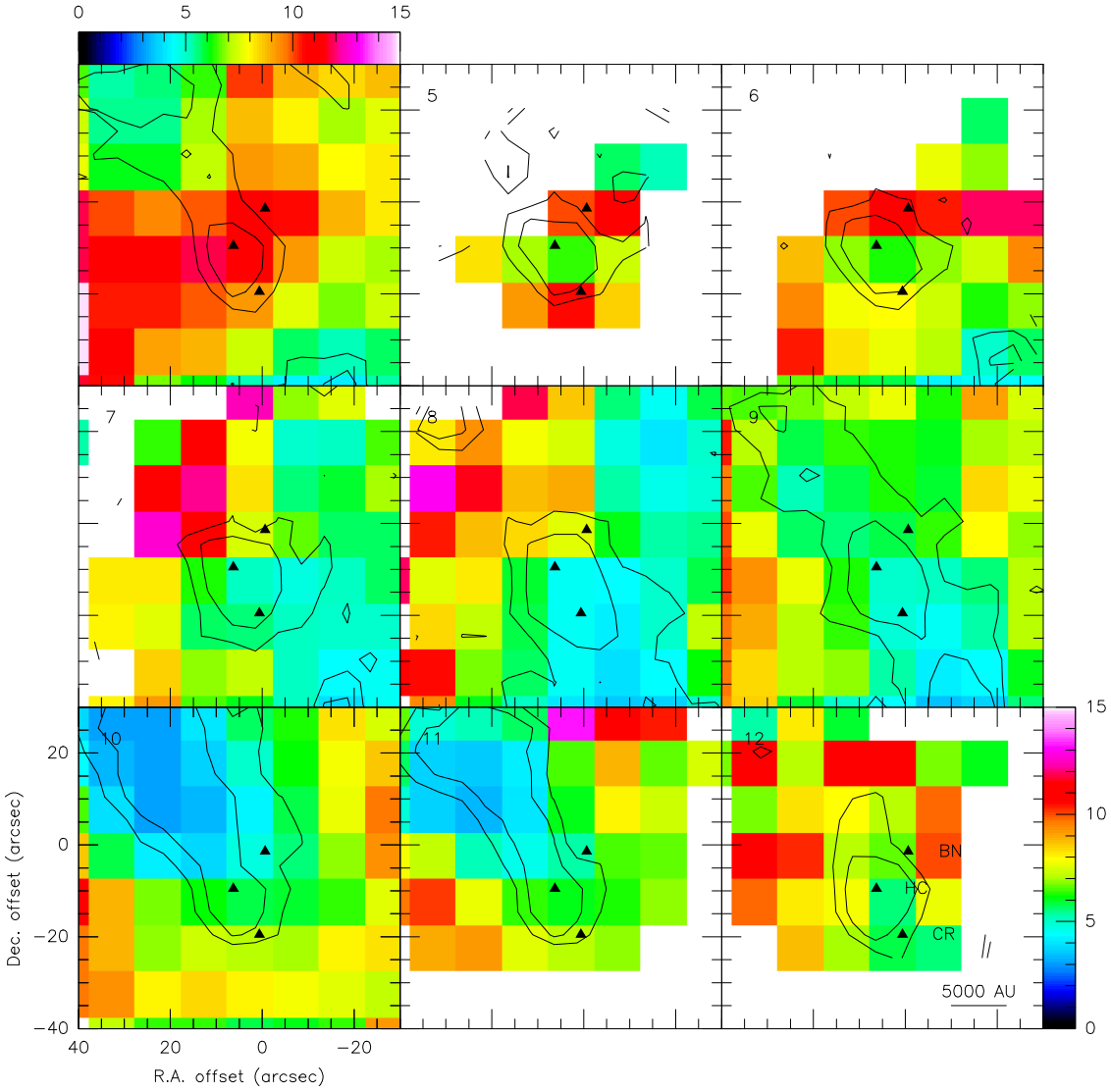

Figure 8.16 The ^{13}CO to C^{18}O ratio channel maps in the Orion BN/KL region. The top-left panel shows the ^{13}CO $J = 3 - 2$ to C^{18}O $J = 3 - 2$ integrated intensity ratio (color image) overlaid with the ^{13}CO $J = 6 - 5$ to C^{18}O $J = 6 - 5$ ratio (contours) in values of 4 (inner contour) and 5 (outer contour). The rest eight panels show the ^{13}CO to C^{18}O $J = 3 - 2$ ratio (color image) in different velocities from 5 to 12 km s^{-1} overlaid with the $J = 6 - 5$ ratio (contours) in values of 3 (inner contour) and 4 (outer contour). The empty area is due the blanking value of 1.5 K km s^{-1} for C^{18}O $J = 3 - 2$.

Table 8.4. The CO isotopologue measurements in the Orion BN/KL region

Line	Orion BN			Hot Core			Compact Ridge		
	$T_{\rm peak}$[a] (K)	$V_{\rm LSR}$ (km s^{-1})	ΔV[b] (km s^{-1})	$T_{\rm peak}$[a] (K)	$V_{\rm LSR}$ (km s^{-1})	ΔV[b] (km s^{-1})	$T_{\rm peak}$[a] (K)	$V_{\rm LSR}$ (km s^{-1})	ΔV[b] (km s^{-1})
^{13}CO (8 − 7)	63.8±2.3	10.3	9.0	70.2±2.4	9.3	18.9	76.0±2.8	8.8	11.0
^{12}CO (7 − 6)	168.5±2.2	9.8	55.5	175.1±2.2	9.4	44.6	175.6±2.0	9.8	25.0
^{12}CO (6 − 5)	164.6±1.6	9.5	53.3	174.5±1.6	9.5	43.2	167.6±0.9	9.8	25.4
^{13}CO (6 − 5)	69.5±0.3	10.2	7.0	80.6±0.4	9.5	15.0	78.7±0.4	8.7	10.0
C^{18}O (6 − 5)	19.0±1.3	10.0	5.8	35.3±2.5	9.5	12.4	35.7±1.6	8.4	4.9
^{13}CO (3 − 2)	68.7±0.5	9.6	5.6	80.7±0.7	9.3	7.6	84.2±0.5	8.4	6.3
C^{18}O (3 − 2)	12.4±0.7	10.2	3.0	15.5±1.0	9.7	6.0	20.9±0.7	8.2	3.7

[a]Temperatures shown here are corrected to the main beam temperature unit.

[b]Line widths are measured in FWHM.

Table 8.5. The CO isotopologue line ratios in the Orion BN/KL region

Ratio	Orion BN	Hot Core	Compact Ridge	$\theta_{\rm HPBW}$
$^{12}CO_{6-5}/^{12}CO_{7-6}$	1.03±0.03	1.05±0.03	1.01±0.03	10″
$^{13}CO_{8-7}/C^{18}O_{6-5}$	3.46±0.36	2.12±0.15	2.03±0.13	10″
$^{13}CO_{3-2}/^{13}CO_{8-7}$	1.07±0.05	1.12±0.05	1.08±0.04	21″
$C^{18}O_{3-2}/C^{18}O_{6-5}$	0.74±0.09	0.45±0.04	0.54±0.04	21″
$^{13}CO_{6-5}/C^{18}O_{6-5}$	3.66±0.33	2.37±0.19	2.25±0.12	10″
$^{13}CO_{3-2}/C^{18}O_{3-2}$	5.55±0.51	5.22±0.51	4.59±0.25	21″

[a]Line ratios are derived using the peak temperatures smoothed to the same resolution.

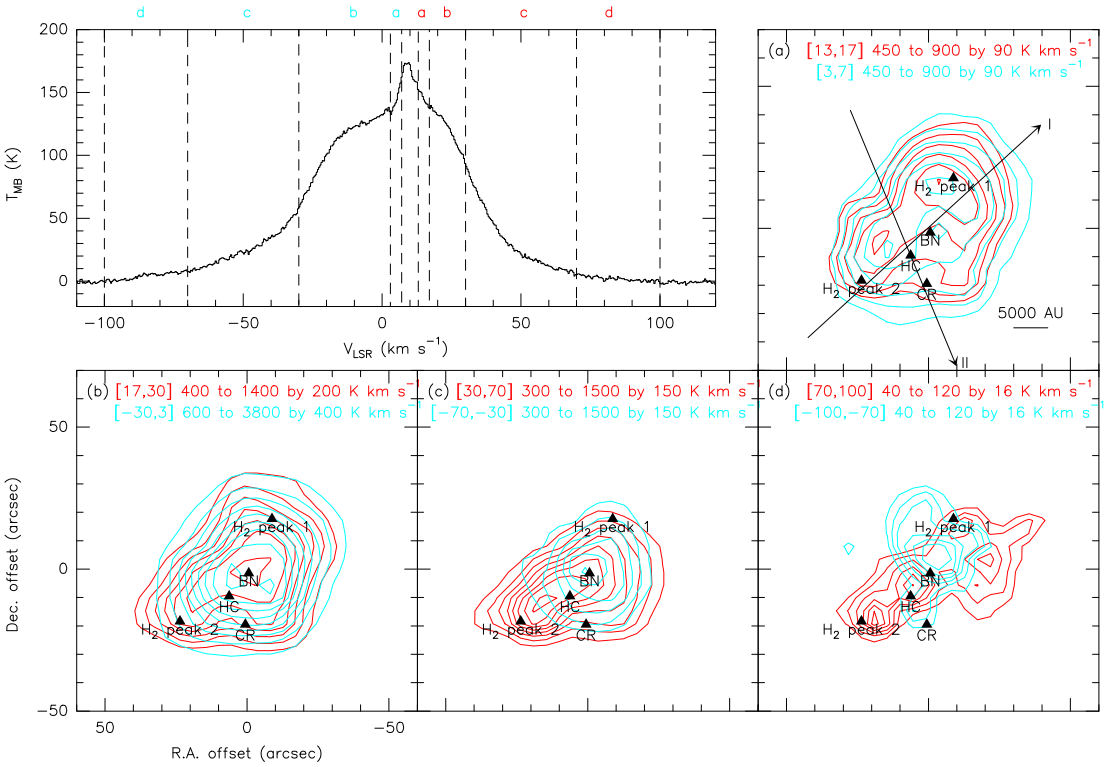

Figure 8.17 The velocity structures of ^{12}CO $J = 6-5$ in the Orion BN/KL region. Upper left panel shows the ^{12}CO $J = 6-5$ spectra of Orion BN, and the dashed-lines separate different red- and blueshifted emissions into five steps corresponding to the right and bottom panels. One σ noise is 3, 4, 10, and 8 K km s^{-1} for panel a, b, c, and d, respectively. The two solid lines in panel (a) correspond to the PV diagrams shown in Figure 8.20. The contour values and velocity ranges are shown in each map. Orion BN, the Hot Core (HC), Compact Ridge (CR) together with the H_2 emission Peak 1 and 2 (Sugai et al. 1994) are marked in filled triangles.

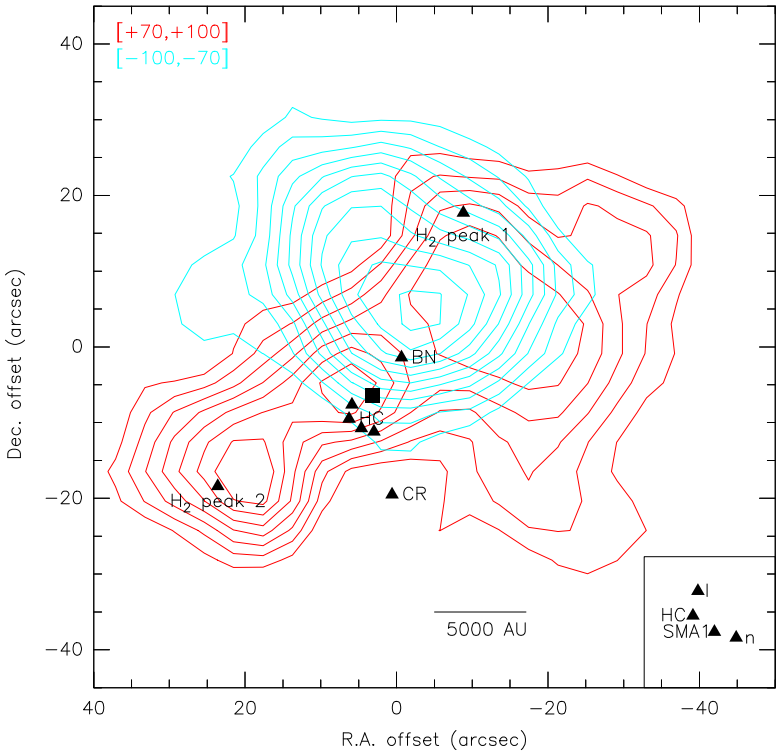

Figure 8.18 Zoomed image of the high velocity emission in the ^{12}CO $J = 7 - 6$ transition. This image was smoothed by two Gaussian beams (16.″4), and the red contours are running from 30 to 90 K km s^{-1} in steps of 10 K km s^{-1}(2 σ level). The blue contours are running from 30 to 130 K km s^{-1} in steps of 10 K km s^{-1} (2 σ level). The radio source I, the Hot Core (HC), SMA 1 and source n are represented in black triangles, and their relative positions are indicated in the bottom right panel. The black square represents the origin of the explosive outflows (Zapata et al. 2009).

where Orion BN and the Hot Core are enclosed within the shell. However, it is unlikely that the shell structure is merely caused by self-absorption, where both red- and blueshifted emissions show similar structures. Besides, the PV diagram of Cut II (Fig. 8.20) indicates a twist motion close to the Hot Core which is probably related to the shell structure seen in Cut I. A detailed discussion will be given in §10.1.

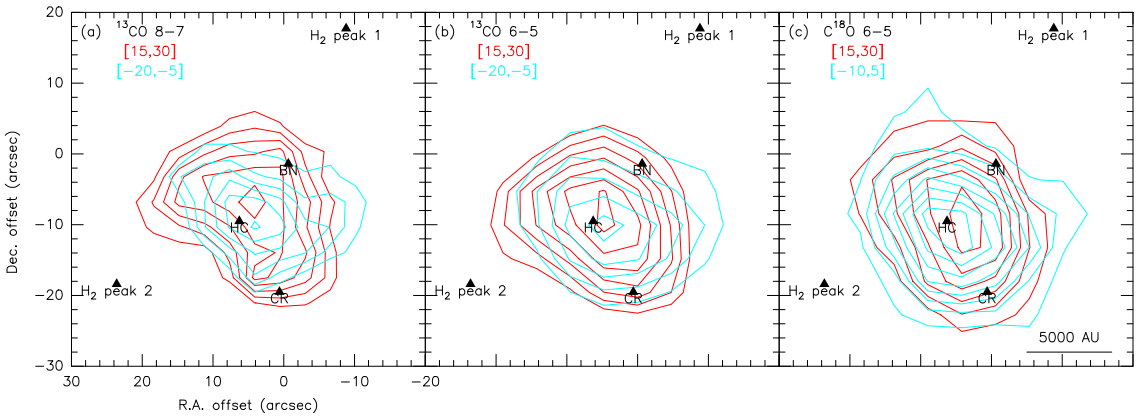

Figure 8.19 (a) The ^{13}CO $J = 8-7$ integrated intensity map for the red- and blueshifted components with 1 σ noise of 10 and 11 K km s^{-1}, respectively. The red contours are plotted in step of 40 K km s^{-1} from 200 to 400 K km s^{-1}, and the blue contours are plotted in step of 30 K km s^{-1} from 120 to 300 K km s^{-1} with a beam size of 7.″5. (b) The ^{13}CO $J = 6-5$ integrated intensity map for the red- and blueshifted components with 1 σ noise of 4 and 5 K km s^{-1}, respectively. The red contours are plotted in step of 30 K km s^{-1} from 200 to 380 K km s^{-1}, and blue contours are plotted in step of 30 K km s^{-1} from 80 to 200 K km s^{-1} with a beam size of 10.″0. (c) The C^{18}O $J = 6-5$ integrated intensity map for the red- and blueshifted components with 1 σ noise of 5 and 6 K km s^{-1}, respectively. The red contours are plotted in step of 20 K km s^{-1} from 40 to 160 K km s^{-1}, and the blue contours are plotted in step of 20 K km s^{-1} from 40 to 190 K km s^{-1} with a beam size of 10.″1. Orion BN, the Hot Core (HC), Compact Ridge (CR) together with the H$_2$ emission Peak 1 and 2 (Sugai et al. 1994) are marked in filled triangles in each map.

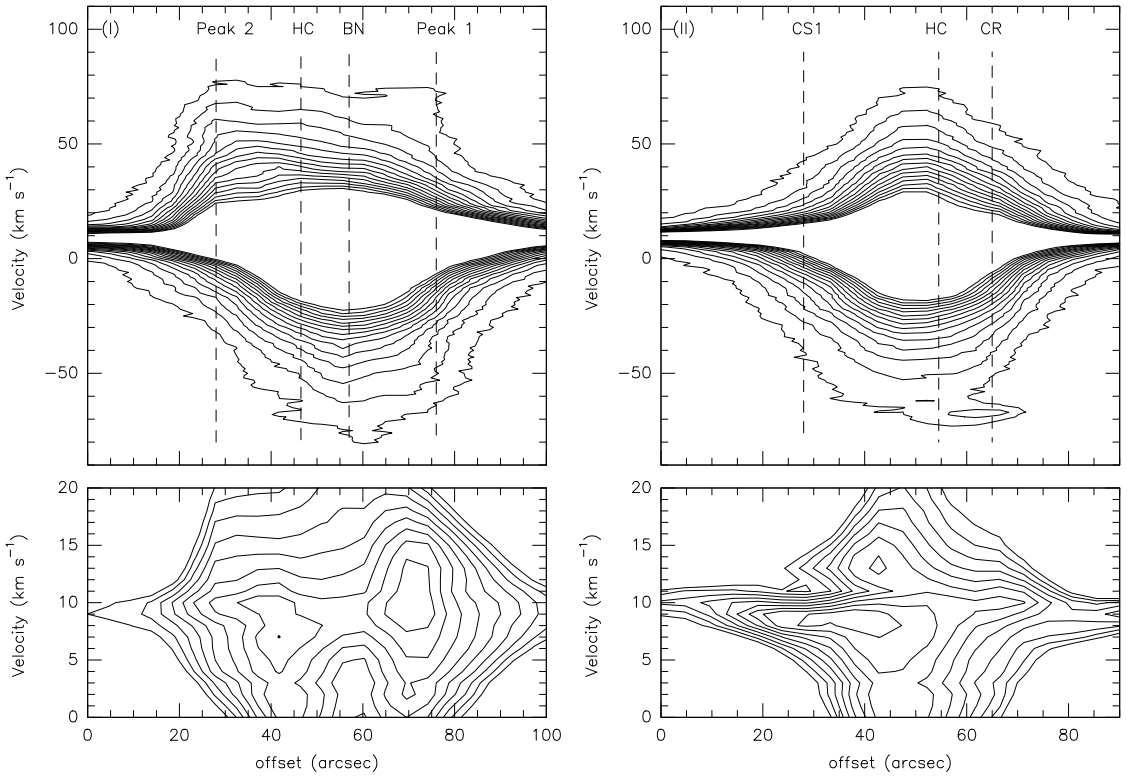

Figure 8.20 Two PV slices of ^{12}CO $J = 6 - 5$ in the Orion BN/KL region corresponding to the cuts in Figure 8.17. (I) The SE-NW slice shows the outflows are associated with the H_2 emission Peak 1 and 2. (II) The NE-SW slice shows a shell structure surrounds the Hot Core and Compact Ridge regions.

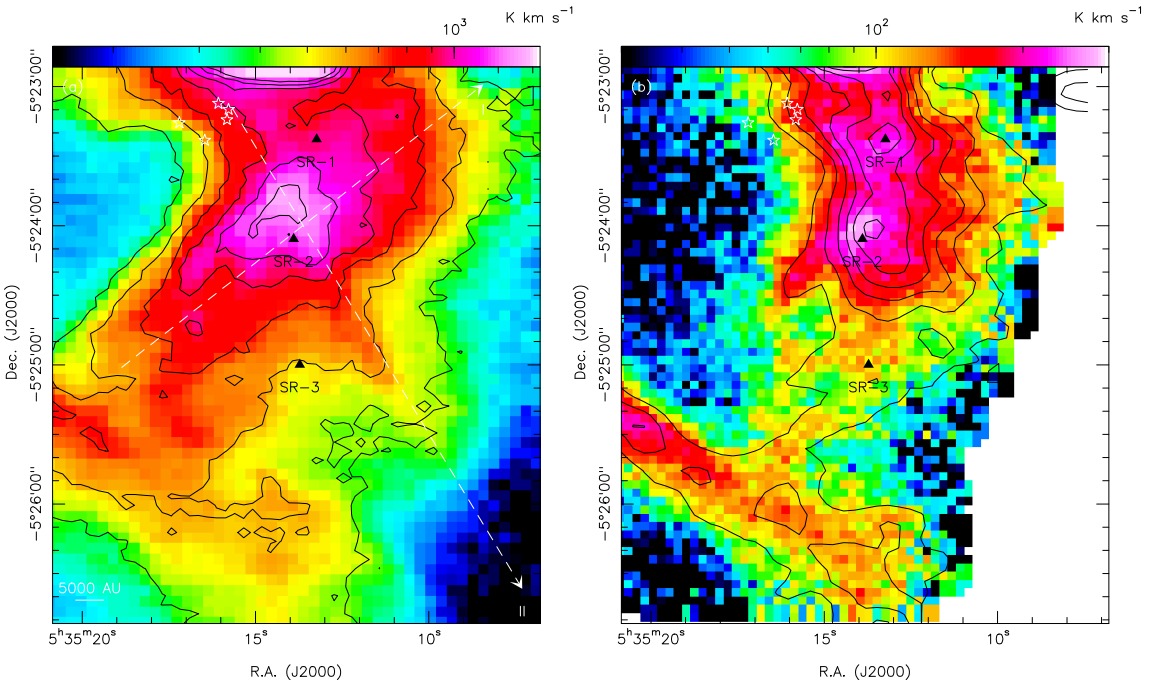

Figure 8.21 Zoomed images of the Orion South region in the mid-J CO isotopologic emission shown in Figures 8.1 and 8.2. Left image shows the ^{12}CO $J = 6 - 5$ $[-25, +30]$ km s^{-1} emission overlaid with the ^{12}CO $J = 7 - 6$ contours running from 400 to 1600 K km s^{-1} in steps of 200 K km s^{-1}. Two dashed-lines represent the PV cuts shown in Figure 8.25. The right image shows the ^{13}CO $J = 8 - 7$ $[+3, +15]$ km s^{-1} image overlaid with the C^{18}O $J = 6 - 5$ $[+4, +12]$ km s^{-1} contours running from 20 to 90 K km s^{-1} in steps of 10 K km s^{-1}. The Orion South Ridge 1, 2, and 3 are marked in filled triangles in both maps.

8.3 Orion South

Emission morphology

The Orion South or OMC-1S region has roughly the same size as the Orion BN/KL cloud ($\sim 2' \times 2'$) but only a bolometric luminosity of $\sim 10^4$ L$_\odot$, which is an order smaller than the luminosity of the Orion BN/KL region (Mezger, Zylka, & Wink 1990). Orion South also hosts several outflows, e.g., the outflow Ori-S6, associated with star forming activities. Figure 8.22 shows clearly extended outflows and filaments, especially the famous outflow Ori-S6 extending to the southwest, which was first discovered by Schmid-Burgk et al. (1990). There are at least three outflows (WO-1, WO-2, and WO-3) seen in the western part of Orion South (Fig. 8.22). The redshifted component of the ^{12}CO $J = 6 - 5$ and $J = 7 - 6$ lines reveals several sources (sources A to F in Fig. 8.22) which are deeply embedded. Measurements of CO isotopologic lines are summarized in Tables 8.6 and 8.7, and their ratios are listed in Table 8.8.

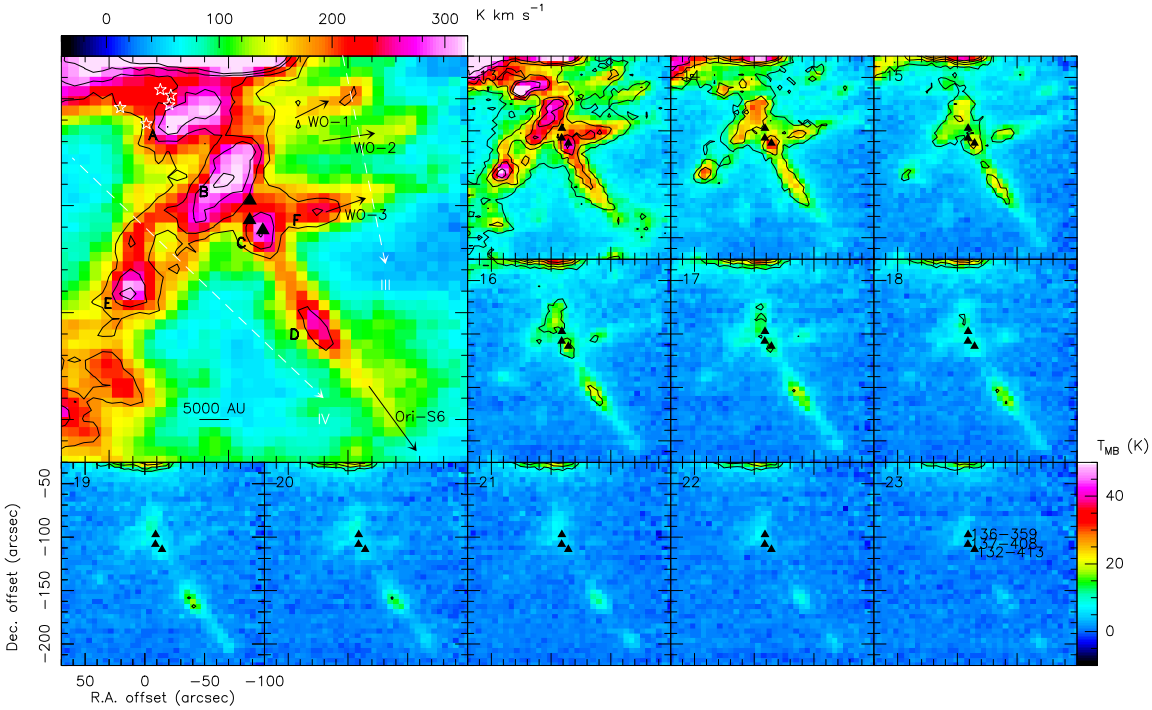

Figure 8.22 The ^{12}CO $J = 6 - 5$ velocity channel maps in Orion South with the ^{12}CO $J = 7 - 6$ contours. Upper-left map shows the integrated intensity $[+11, +25]$ image of ^{12}CO $J = 6-5$ overlaid with the $J = 7-6$ contours plotted in steps of 60 K km s^{-1} from 200 to 380 K km s^{-1}. Two dashed-lines correspond to the PV diagrams shown in Figure 8.26. For the channel map from 12 to 22 km s^{-1}, the contours are plotted from 15 to 50 K in steps of 10 K. Source 137-408, 136-359 and 132-413 are marked in filled triangles in each map.

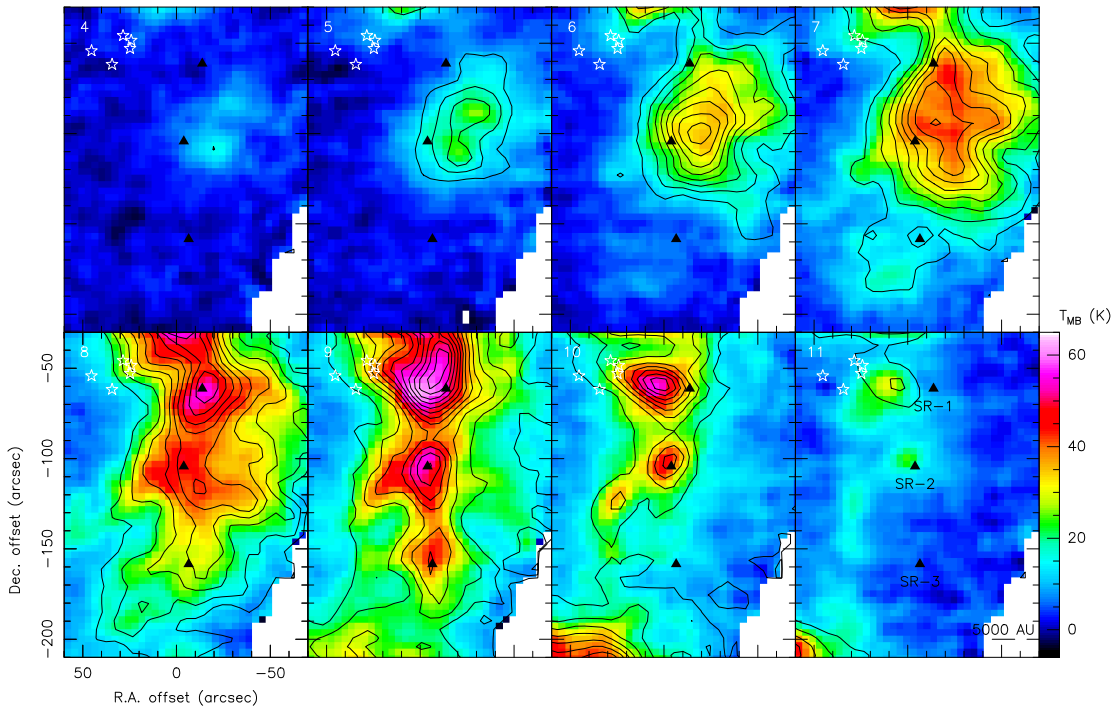

Figure 8.23 The ^{13}CO $J = 8 - 7$ velocity channel maps of Orion South with the C^{18}O $J = 6 - 5$ contours. Both images were smoothed by two Gaussian beams (15″ for ^{13}CO $J = 8 - 7$, and 20″ for C^{18}O $J = 6 - 5$). The contours are running from 3 to 15 K in steps of 2 K. The Orion South Ridge 1, 2, and 3 are marked in filled triangles.

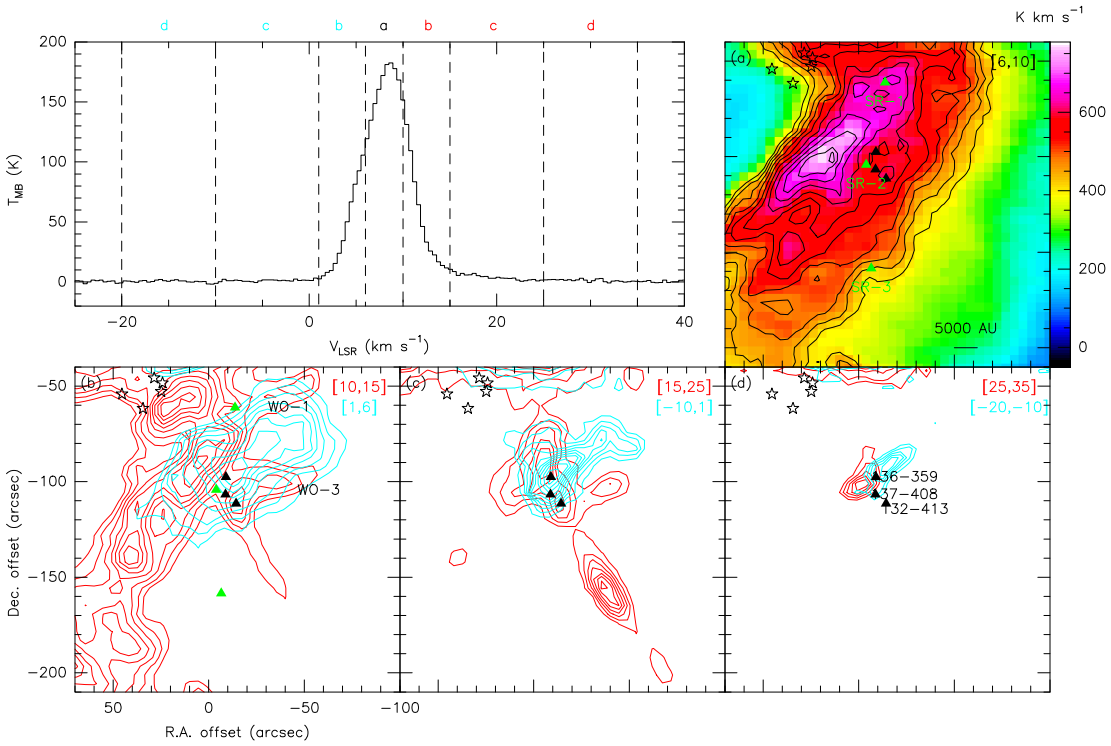

Figure 8.24 The velocity structures of ^{12}CO $J = 6 - 5$ in the Orion South region. Upper-left panel shows the ^{12}CO $J = 6 - 5$ spectrum from the emission peak $(+20'', -100'')$ and the dashed lines separate different red- and blueshifted integrated emissions into four steps corresponding to the maps shown in the right and bottom panels. (a) The ^{12}CO $J = 6 - 5$ integrated intensity map with ^{12}CO $J = 7 - 6$ contours running from 400 to 800 K km s^{-1} in steps of 40 K km s^{-1}. (b) The contours are plotted from 210 to 540 K km s^{-1} in steps of 30 K km s^{-1}. (c) The red contours are from 40 to 130 K km s^{-1} in steps of 15 K km s^{-1}, and the blue contours are plotted from 40 to 190 K km s^{-1} in steps of 15 K km s^{-1}. (d) The contours are plotted from 24 to 48 K km s^{-1} in steps of 6 K km s^{-1}. Sources 137-408, 136-359 and 132-413 are marked in black triangles in each map, and the Orion South Ridge 1, 2, and 3 are marked in green triangles.

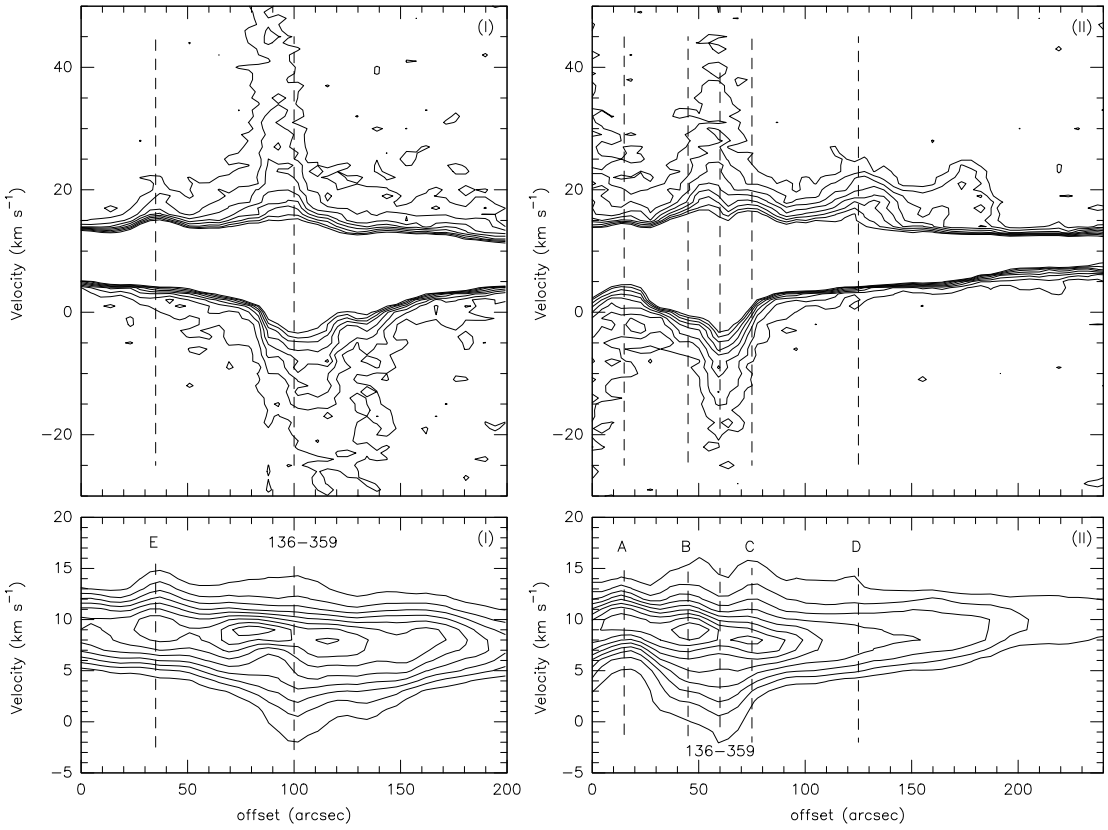

Figure 8.25 The PV diagrams of Cut I and II in Orion South (Fig. 8.21). (I) The SE-NW slice in the upper panel shows the bipolar outflows associated with source 136-359. The zoomed central part is shown in the lower panel where the outflow from source 136-359 seems to be associated with two emission peaks. (II) The NE-SW slice which is almost perpendicular to the Slice I cuts through several clumps in the Orion South region. Upper panel shows the outflow associated with source 136-359. The elongated structure to the southwest is the low-velocity outflow Ori-S6.

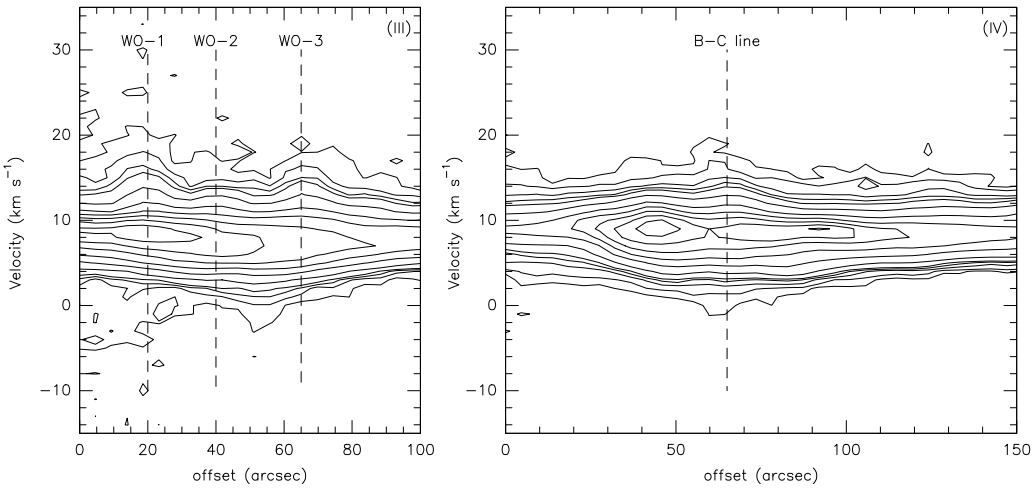

Figure 8.26 The PV diagrams of Cuts III and IV in Orion South (Fig. 8.21). (III) Three outflows WO-1, WO-2, and WO-3 can be seen, and the contours are running from 2% to 8% in steps of 2% of the peak temperature (130 K), and the subsequent contours are running from 15% to 90% in steps of 15% of the peak temperature. (IV) The PV diagram through the straight shape of Orion South. The contours represent 1.5% and from 2.5% to 8.5% in steps of 2% of the peak temperature (170 K), and the subsequent contours are running from 15% to 90% in steps of 15% of the peak temperature. The B-C line is the line linking sources B and C.

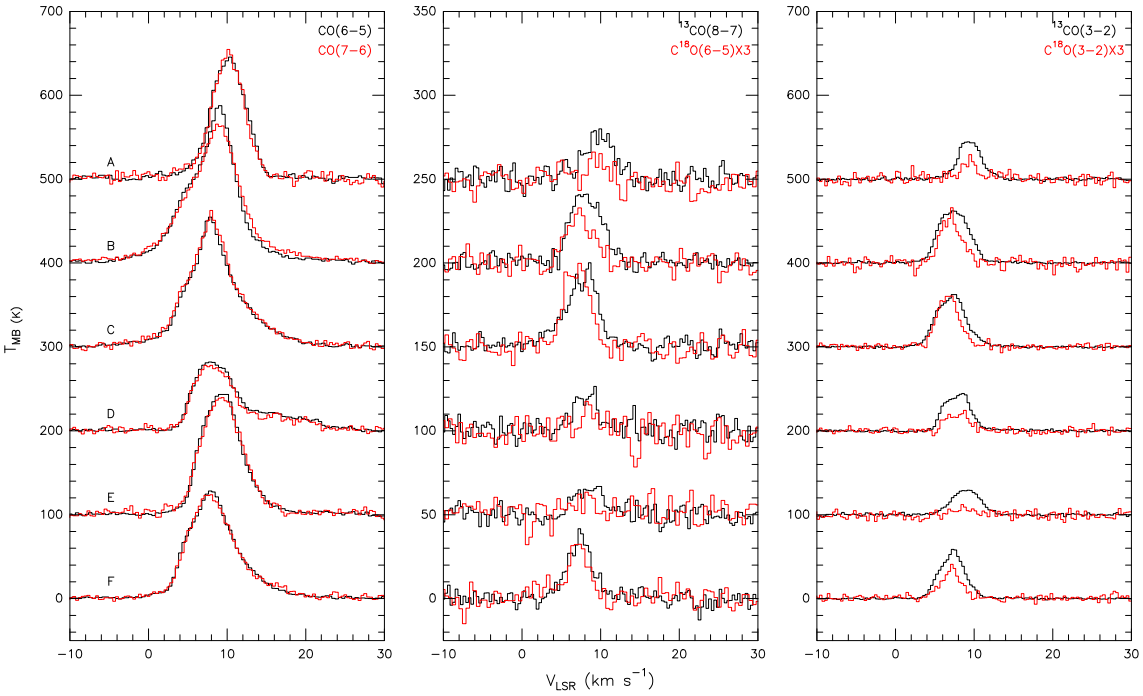

Figure 8.27 The selected spectra of ^{12}CO, ^{13}CO, and C^{18}O in the Orion South region. The positions of these sources are marked in the Figure 8.22.

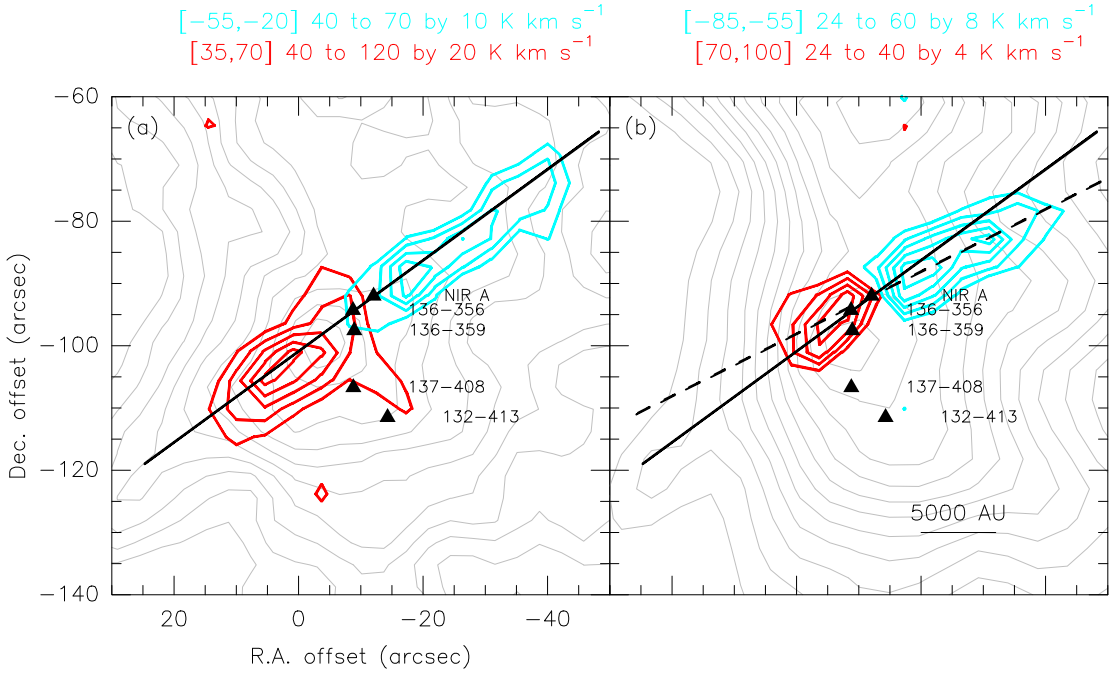

Figure 8.28 The collimated outflow in the Orion South region. (a) The high-speed ^{12}CO $J = 6 - 5$ outflow from the red and blue wings with a similar noise of 7 K km s^{-1}. The grey contours denote the smoothed ^{13}CO $J = 8 - 7$ [−10, +30] km s^{-1} emission running from 180 to 300 K km s^{-1} in steps of 15 K km s^{-1}. (b) The very high speed ^{12}CO $J = 6 - 5$ outflow is shown in red and blue contours with a similar noise of 7 K km s^{-1}. The grey contours denote the smoothed C^{18}O $J = 6 - 5$ [+4, +12] km s^{-1} emission running from 40 to 80 K km s^{-1} in steps of 5 K km s^{-1}. The solid line represents the P.A. of $\sim -54°$, and the dashed-line represents the P.A. of $\sim -63°$.

In Figure 8.21, the sharp shape of the ^{12}CO emission facing the Trapezium stars is clearly seen. The ^{13}CO and C^{18}O emission (Fig. 8.21) shows a different morphology as ^{12}CO : the north-south ridge is more prominent with the ^{13}CO and C^{18}O emission peaking at three positions, i.e., the Orion South Ridge (SR) 1, 2, and 3. This is more clear in the velocity channel maps shown in Figure 8.23 ($V_{\rm LSR}$=8 − 10 km s^{-1}). In addition, SR-1 has more extended emission shown in the ^{13}CO and C^{18}O images (Figs. 8.21 and 8.23).

Kinematics

The collimated outflows detected in the Orion South region are well correlated in position and orientation (Figs. 8.24 and 8.28) with the cluster of ^{12}CO and SiO outflows mapped by Zapata et al. (2005, 2006, 2010) using the Submillimeter Array (SMA). They are part of the large-scale HH objects mapped at optical and infrared wavelengths that also emanate from this region (Bally et al. 2000; Smith et al. 2004; Henney et al. 2007). The highly collimated outflow around source C observed both in the ^{12}CO $J = 6-5$ and $J = 7-6$ emission can be clearly seen in the PV diagrams shown in Figure 8.25. In the PV Cut I, the collimated outflow is evident in the SW-NE direction. The red- and blueshifted wings from the ^{12}CO line show high speed components with a velocity up to almost ±100 km s^{-1}. The position angle (P.A.) of the high speed outflow is $\sim -54°$ (Fig. 8.28), but slightly different from the very high speed outflow with a P.A. of $\sim -63°$, where the very high speed red- and blueshifted bullets are closer to each other. The density can be estimated using Eqs. B.22 and B.28 (see Appendix B) for the very high speed bullets from the ^{12}CO $J = 6-5$ emission by assuming the optically thin emission at high velocities, and the excitation temperature is close to the dust temperature of 80 K (Zapata et al. 2005) in LTE:

$$N(^{12}\mathrm{CO}) \simeq 1.2 \times 10^{12}\ f\ (T_{\rm ex} + 0.92)\ e^{\frac{E_{\rm u}}{T_{\rm ex}}} \int T_{\rm MB} dV\ \mathrm{cm}^{-2}, \tag{8.1}$$

where $E_{\rm u}$ is the energy level of the upper state (116.2 K for the ^{12}CO $J = 6-5$ transition), and f is the filling factor. The filling factor was calculated by comparing the outflow size in the ^{12}CO $J = 2-1$ interferometry data with that of the ^{12}CO $J = 6-5$ emission. Therefore, the mass of the outflows can be estimated by adopting the isotope abundance ratio [CO]/[H$_2$] of 8×10^{-5} in OMC-1 (Wilson & Matteucci 1992). The derived parameters of this outflow are summarized in Table 8.9.

The total mass ($M_{\rm outflow}$) of the very high speed is $\sim 0.6-1.3$ M$_\odot$, which is a lower limit calculated from the optically thin ^{12}CO emission in high velocities. The total energy ($E_{\rm outflow} = \frac{1}{2} M_{\rm outflow} V^2_{\rm outflow}$) of this outflow is about $3.7-8.6 \times 10^{46}$ erg, which is comparable to the explosive outflow in Orion BN/KL ($\sim 10^{47}$ erg). The dynamical age ($t_{\rm outflow}$) of the ^{12}CO outflow is estimated to be $\sim$ 500 yr for the blueshifted bullet (with a length of about 33″), and $\sim$ 800 yr for the redshifted bullet (with a length of about 20″), without a projection correction. This age estimate is consistent with the result of 600 yr derived by Zapata et al. (2005). Besides, the total mechanical luminosity ($L_{\rm mech} = E_{\rm outflow} t_{\rm outflow}$) is $\sim 400-1000$ L$_\odot$, which is much larger than the bolometric luminosity

Table 8.6. The measurements of the ^{12}CO peak temperatures in the Orion South region

Source		^{12}CO (7-6)			^{12}CO (6-5)		
	offset position[a] ($''$)	$T_{\rm peak}$[b] (K)	$V_{\rm LSR}$ (km s^{-1})	ΔV[c] (km s^{-1})	$T_{\rm peak}$[b] (K)	$V_{\rm LSR}$ (km s^{-1})	ΔV[c] (km s^{-1})
A	$(+23, -62)$	154.5±4.4	10.2	4.7	145.5±1.9	10.4	5.1
B	$(+2, -89)$	165.6±2.0	8.7	6.9	187.5±1.4	9.1	6.4
C	$(-14, -113)$	162.7±2.9	8.0	6.2	154.7±1.2	7.9	5.9
D	$(-36, -156)$	77.9±3.1	7.3	6.2	82.0±1.3	7.9	6.4
E	$(+41, -141)$	139.5±3.5	9.4	6.2	143.4±1.3	9.1	5.9
F	$(-37, -102)$	123.8±2.8	8.0	6.5	128.2±1.1	7.9	6.8

[a]The offset positions are corresponding to the position of Orion BN.

[b]Temperatures shown here are corrected to the main beam temperature unit.

[c]Line widths are measured in FWHM.

Table 8.7. The CO isotopologue measurements of the selected sources in the Orion South region

Source	^{13}CO (8 − 7)		C^{18}O (6 − 5)		^{13}CO (3 − 2)		C^{18}O (3 − 2)	
	$T_{\rm peak}$[a] (K)	$V_{\rm LSR}$ (km s^{-1})	$T_{\rm peak}$[a] (K)	$V_{\rm LSR}$ (km s^{-1})	$T_{\rm peak}$[a] (K)	$V_{\rm LSR}$ (km s^{-1})	$T_{\rm peak}$[a] (K)	$V_{\rm LSR}$ (km s^{-1})
A	28.5±4.5	9.1	3.8±2.1	9.4	44.4±1.6	9.3	8.3±1.7	9.7
B	41.0±3.6	8.1	10.2±1.9	7.6	62.1±1.1	7.3	19.8±1.6	7.0
C	45.1±3.9	8.8	15.9±1.6	7.6	62.4±1.1	7.3	20.1±0.9	7.0
D	21.1±5.0	8.8	5.5±2.2	8.4	44.5±1.3	8.6	6.6±0.9	8.3
E	16.1±4.1	9.5	4.1±2.1	8.5	29.2±1.4	9.3	2.8±1.1	8.3
F	40.1±3.8	7.5	10.6±1.8	9.4	58.7±1.0	7.3	12.2±0.9	7.0

[a]Temperatures shown here are corrected to the main beam temperature unit.

[b]Line widths are measured in FWHM.

Table 8.8. The CO isotopologue line ratios in the Orion South region

Source	^{12}CO $\frac{6-5}{7-6}$	$\frac{^{13}\mathrm{CO}\ 8-7}{\mathrm{C}^{18}\mathrm{O}\ 6-5}$	^{13}CO $\frac{3-2}{8-7}$	C^{18}O $\frac{3-2}{6-5}$	$\frac{^{13}\mathrm{CO}\ 3-2}{\mathrm{C}^{18}\mathrm{O}\ 3-2}$
A	0.97±0.03	7.44±3.63	1.49±0.14	0.89±0.21	5.33±1.12
B	1.17±0.03	3.37±0.59	1.39±0.10	1.24±0.19	3.13±0.25
C	1.01±0.03	2.87±0.40	1.28±0.09	1.37±0.20	3.10±0.14
D	1.12±0.06	3.02±1.09	2.01±0.32	0.99±0.36	6.72±0.96
E	1.06±0.03	3.84±1.77	1.54±0.25	0.44±0.25	10.43±3.95
F	1.09±0.04	3.53±0.74	1.54±0.14	0.93±0.14	4.82±0.37

[a]Line ratios are derived using the peak temperatures smoothed to the same resolution.

Table 8.9. The Orion South well-collimated outflow parameters

Component	f[a] (%)	M_{outflow} ($\mathrm{M}_\odot$)	Momentum[b] ($\mathrm{M}_\odot$ km s^{-1})	Energy[b] (10^{46} erg)	L_{mech}[b] ($\mathrm{L}_\odot$)
B $[-85, -55]$	0.9	$0.5 - 1.1$	$39 - 92$	$3.1 - 7.2$	$311 - 733$
R $[+70, +100]$	3.1	$0.1 - 0.2$	$8 - 18$	$0.6 - 1.4$	$107 - 245$
B $[-80, -26]$[b]	1.0	$1.6 - 2.3$	$128 - 186$	$10.1 - 14.8$	$1025 - 1494$
R $[+22, +82]$[b]	1.5	$2.2 - 3.5$	$178 - 277$	$14.2 - 22.0$	$1260 - 1957$

[a]Filling factor is estimated by comparing the emission size with the SMA ^{12}CO $J = 2 - 1$ emission from Zapata et al. (2005).

[b]The energy, momentum, and mechanical luminosity are calculated by adopting a maximum velocity of 80 km s^{-1}.

[c]To compare with the results of Zapata et al. (2005).

Table 8.10. The positions of the three clumps in the Orion Bar region

Source	R.A. (J2000)	Dec. (J2000)	offsets ($''$)[a]
Central clump	$05^h35^m21\overset{s}{.}162$	$-05°25'22\overset{''}{.}5$	$(+105, -180)$
Eastern clump	$05^h35^m25\overset{s}{.}325$	$-05°24'36\overset{''}{.}3$	$(+167, -135)$
Western clump	$05^h35^m14\overset{s}{.}582$	$-05°26'24\overset{''}{.}5$	$(+6, -243)$

[a]The offset positions are corresponding to the position of Orion BN.

of the possible powering source 136-359 (8 $L_\odot$) (Zapata et al. 2005).

We used a larger range of the velocity in the calculation in order to compare our results with that of Zapata et al. (2005), and our derived physical parameters are much larger, e.g. 5–8 times larger in the outflow mass. Over a large range of velocity, the ^{12}CO emission can become less optically thin. However, this effect might only result in an underestimated outflow mass. Thus, the reason for the mass overestimate is probably because the emission from the ambient cloud is included, especially in the outflow regions such as Orion South and Orion BN/KL. Therefore, the integrated intensities in higher velocities, i.e., from -55 to -85 km s^{-1} for blueshifted component and from $+70$ to $+100$ km s^{-1} for redshifted component, are more reliable for the outflow mass estimate, which gives a total outflow mass of ~ 1 $M_\odot$.

The position angle of this collimated outflows derived from the SMA observations (Zapata et al. 2005) is $-73°$, which is smaller than the position angle derived from the ^{12}CO $J = 6 - 5$ emission of $\sim -54°$. The difference in both position angles is probably due to a bigger beam size from the single dish observations, which makes the position angle estimate less accurate.

8.4 Orion Bar

One of the best studied photon-dominated regions (PDRs), the Orion Bar, is believed to be the edge-on transition region between the neutral H_2 cloud and the H II region ionized by the O type star θ^1 Ori C, located at $\sim 2'$ in the northwest. A number of investigations at different wavelengths show a clear stratified structure of the Orion Bar where the $H^+/H^0/H_2$ transition is predicted by the PDR model (see Hollenbach & Tielens 1997). However, part of the Orion Bar seems to be connected with the Orion South region, as can be seen from the ^{12}CO $J = 6 - 5$ blueshifted line wing emission in Figures 8.29 and 8.30, where the ^{12}CO emission has an almost rectangular shape between the Bar and Orion South. In addition, the redshifted line wing of ^{12}CO $J = 6 - 5$ shows more clumpy but less widespread emission features. In the ^{13}CO $J = 8 - 7$ and C^{18}O $J = 6 - 5$ emission, there are three dense clumps inside the Orion Bar (Fig. 8.32 and Table 8.10), which can be also seen in the $J = 3 - 2$ emission. The central clump is probably the closest part of the Bar to θ^1 Ori C ($\sim 140''$), and has the strongest $T_{\rm MB}$ up tp ~ 180 K of the ^{12}CO $J = 7 - 6$ and $J = 6 - 5$

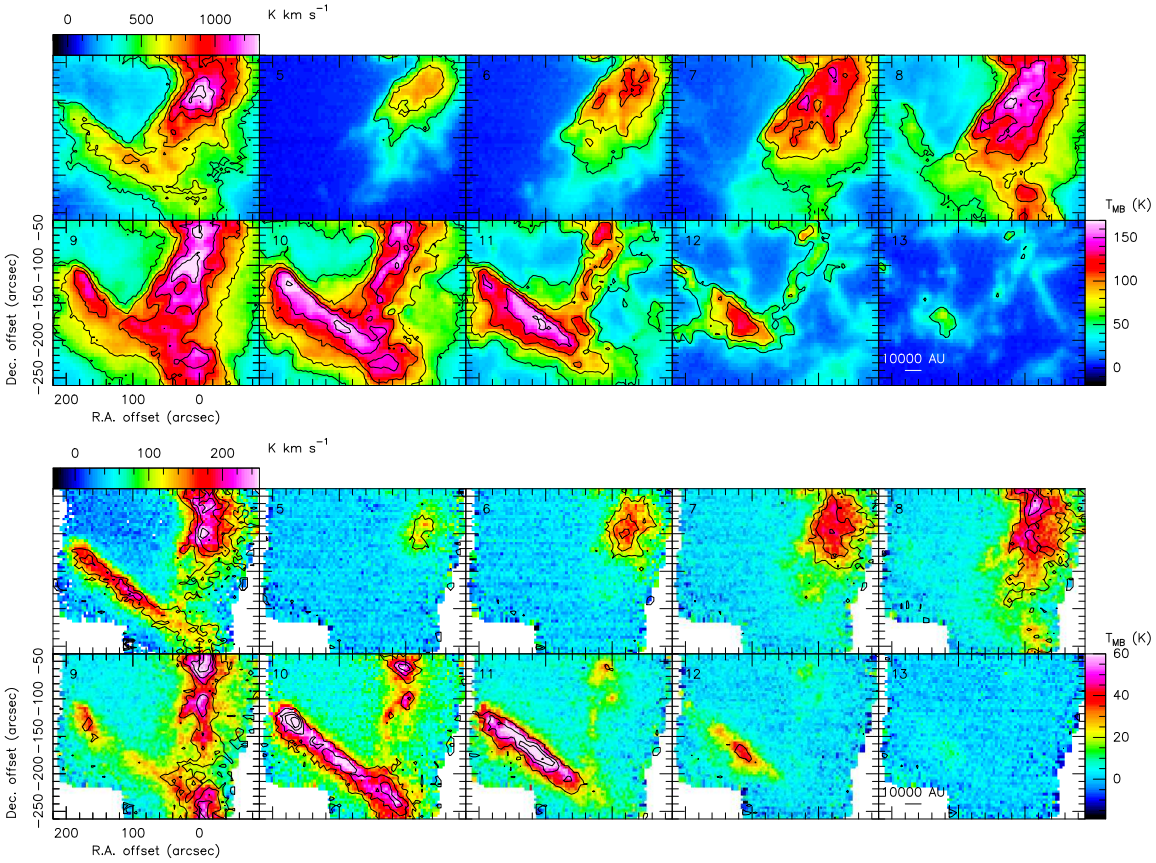

Figure 8.29 Upper panel: The ^{12}CO $J = 6 - 5$ velocity channel maps in the Orion South and Bar regions overlaid with the ^{12}CO $J = 7 - 6$ contours. Upper-left map shows the ^{12}CO $J = 6 - 5$ [−25, +30] km s^{-1} image overlaid with the $J = 7 - 6$ contours running from 400 to 140 K km s^{-1}in steps of 200 K km s^{-1}. The contours in the rest velocity channel maps are running from 50 to 170 K in steps of 30 K. Lower panel: The ^{13}CO $J = 8 - 7$ velocity channel maps in the Orion South and Bar regions overlaid with the C^{18}O $J = 6 - 5$ contours. Upper-left map shows the ^{13}CO $J = 6 - 5$ [−5, +15] km s^{-1} image overlaid with the C^{18}O $J = 6 - 5$ contours running from 25 to 85 K km s^{-1}in steps of 15 K km s^{-1}. The contours in the rest velocity channel maps are running from 6 to 24 K in steps of 6 K.

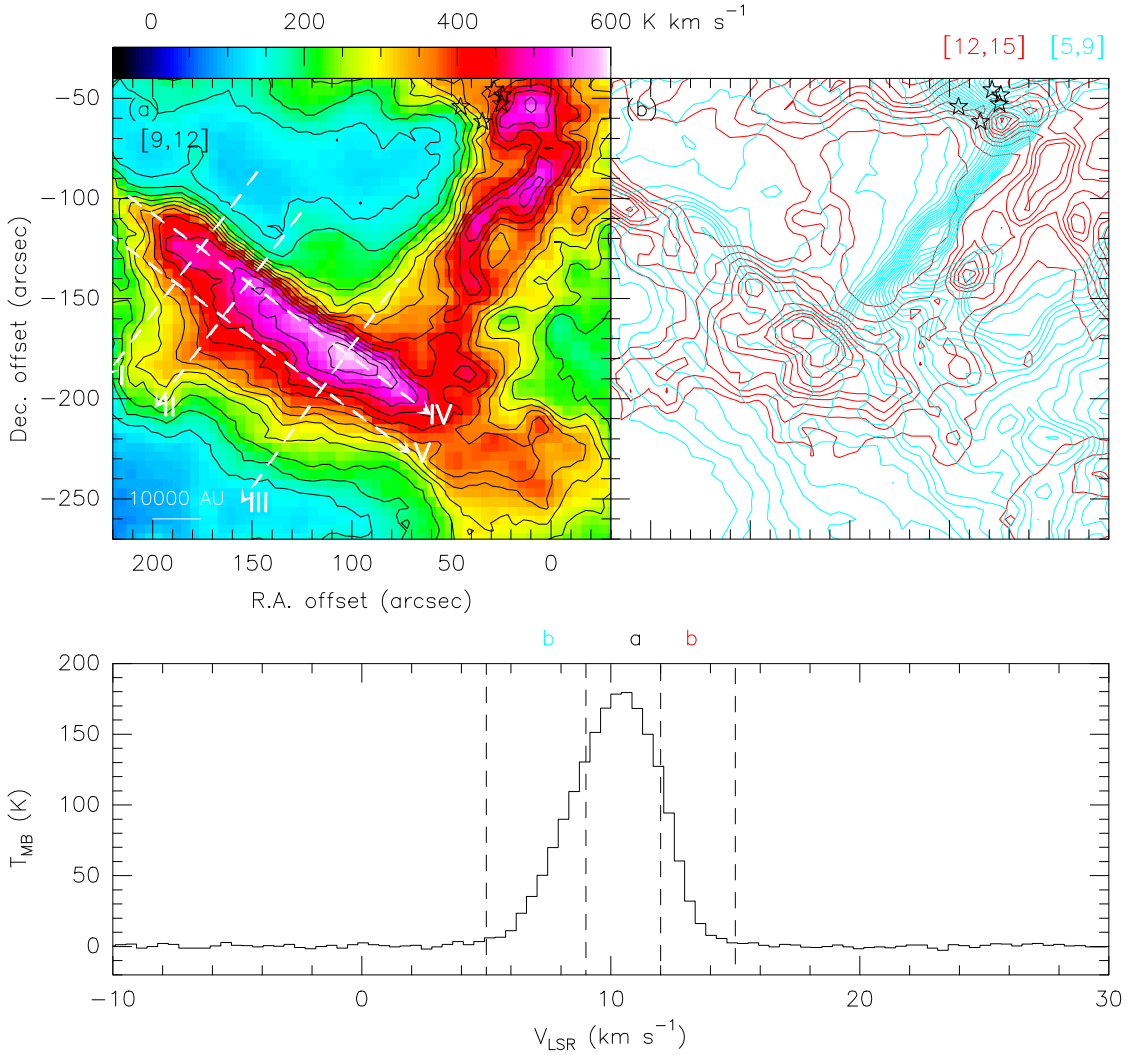

Figure 8.30 The velocity structure in the Orion Bar region. Upper panel shows the different velocity intervals corresponding to the spectrum shown in the lower panel.(a) The image of ^{12}CO $J = 6 - 5$ [+9, +12] km s^{-1} emission overlaid with the ^{12}CO $J = 7 - 6$ contours plotted in steps of 40 K km s^{-1} from 140 to 600 K km s^{-1}. (b) The red- and blueshifted line wings of ^{12}CO $J = 6 - 5$ in the Orion Bar. The red contours are plotted in steps of 20 K km s^{-1} from 40 to 240 K km s^{-1}, and the blue contours are plotted from 80 to 500 K km s^{-1} in steps of 20 K km s^{-1}.

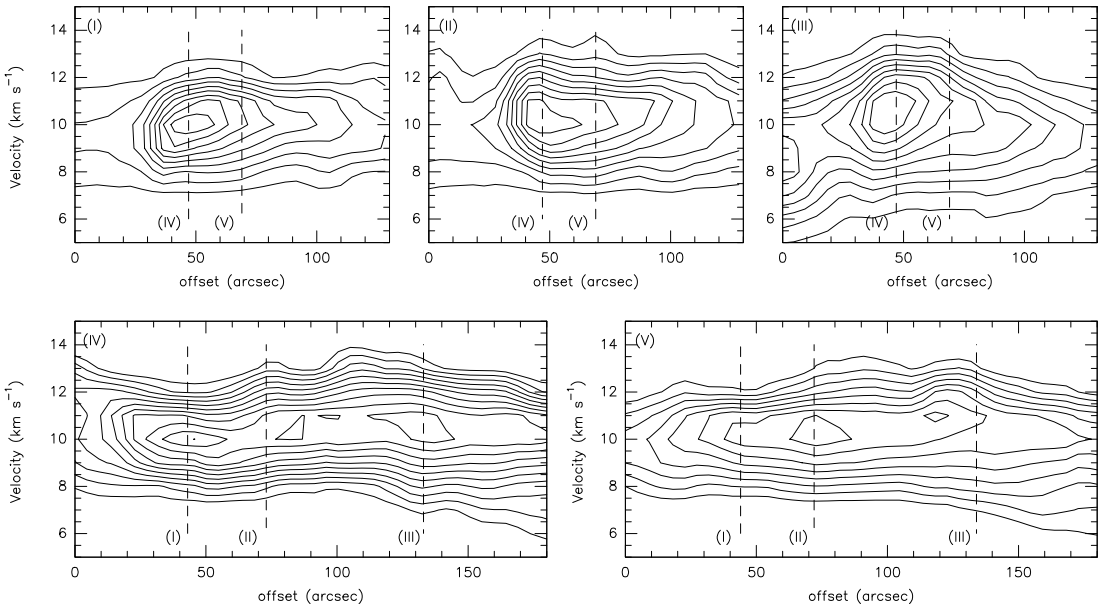

Figure 8.31 Five position-velocity slices in the Orion Bar region. Upper panels are the perpendicular cuts through the Orion Bar ionization front, where the panel I and III are corresponding to the eastern clump and central clumps in Figure 8.32, respectively. Lower panels are the parallel cuts inside the Orion Bar, and the positions of Cut I, II, and III are also marked.

lines. Table 8.11 lists the observation results of the three selected clumps in the Orion Bar. The ^{12}CO $J = 6 - 5$ and $J = 7 - 6$ FWHM line widths are ~ 4 km s^{-1}, and the line widths of the ^{13}CO and C^{18}O lines are ~ 2 km s^{-1} for the three clumps. All CO isotopologic lines show narrow line widths, which indicate no obvious outflow activities in the Bar. The $V_{\rm LSR}$ of isotopologic CO lines is slightly different among these three clumps (Table 8.11). The CO isotopologue measurements are summarized in Table 8.11, and the spectra are shown in Figure 8.34. The CO isotopologue ratios are listed in Table 8.12.

The stratified structure of the Orion Bar is shown in Figure 8.32, where the recombination emission from ionized carbon is located between the 3.6 cm free-free continuum emission and our CO isotopologue emission. The morphology of the Orion Bar ^{13}CO $J = 8 - 7$ and C^{18}O $J = 6 - 5$ emission agrees with each other, so does the emission of ^{13}CO and C^{18}O $J = 3 - 2$. However, a slightly different position between the low-J and mid-J CO isotopologue emission is found in the Bar (Fig. 8.33), where the mid-J CO isotopologue lines are closer to the ionization front. As shown in Figure 8.33, the positions of ^{12}CO $J = 7 - 6$ and $J = 6 - 5$ peak temperatures offset from the positions of the ^{13}CO and C^{18}O $J = 3 - 2$ emission. It has been reported by Lis, Schilke, & Keene (1997) that the position of ^{13}CO $J = 6 - 5$ emission is $\sim 10''$ closer to the ionization front than the position of the ^{13}CO $J = 2 - 1$ emission. It is likely that the emission offset is due to different beam sizes which lead to different emission peaks in the Bar since the low-J CO isotopologue lines

trace more diffuse gas compared with the highly excited mid-J CO lines (see Table 1.1). Besides, the physical widths of the Bar in different CO isotopologue lines shown in Figure 8.36 also indicate that the ^{13}CO $J = 8 - 7$ and C^{18}O $J = 6 - 5$ lines tend to have smaller widths compared with the ^{12}CO lines and the low-J ^{13}CO and C^{18}O lines. Furthermore, the emission superposition map in Figure 8.33 is consistent with the result of Lis & Schilke (2003) that the H^{13}CN emission from the dense clumps coincides with the ^{13}CO $J = 3 - 2$ emission peaks. In Figure 8.35, the position-intensity diagram of CO isotopologic lines through θ^1 Ori C are shown together with the 3.6 cm free-free emission and the C91α emission from Wyrowski et al. (1997). Noteworthily, the C91α emission in the three slices all show a two-component feature that the C91α emission (counted from the ionization front) first drops when the ^{12}CO emission raises, and then again local maxima when the ^{13}CO and C^{18}O lines become brighter. Moreover, the offsets between the two C91α emission components are about $10'' - 15''$, and the following emission local minimums are coincident with the CO isotopologue line emission peaks. In addition, the PV diagrams of the perpendicular cuts through the Orion Bar (Fig. 8.36) also show similar features mentioned above. The anti-correlation between the atomic carbon C91α recombination line and CO isotopologic lines indicates the fact that most of the carbon is locked in CO molecules inside the cloud.

8.5 Orion East

The Orion East region is located at 2.6 pc to the east of Orion BN/KL, and has a size of $\sim 80'' \times 80''$. Orion East has a cometary shape, and has been neglected in most pervious studies, or treated as an extension part of the Orion BN/KL region. Orion East has been clearly detected in 350 μm continuum emission maps (Houde et al. 2004), and also in the [O I] 145.5 μm, [O II] 63.2 μm and [C I] 158 μm lines (Stacey et al. 1993; Herrmann et al. 1997), which indicate that it is probably a PDR also powered by θ^1 Ori C ($\sim 2''$ to the southwest). However, it is worth noting that there is no detection of the NH_3 $(J, K) = (1, 1)$ and $(2, 2)$ and 1.3 mm continuum emission (Wiseman & Ho 1998; Plambeck, Wright, & Carlstrom 1990). Our measurements of the CO isotopologues are summarized in Table 8.13, and the spectra are shown in Figure 8.39. The CO isotopologue ratios are listed in Table 8.14.

As shown in Table 8.13 and Figure 8.39, the average $V_{\rm LSR}$ of CO isotopologic lines in Orion East is ~ 10.5 km s^{-1}. The line widths are 4–5 km s^{-1} for ^{12}CO, and ~ 2 for ^{13}CO and C^{18}O, similar to the Orion Bar. Therefore, Orion East is a relatively quiescent region, but contains highly excited CO isotopologic emission. Besides, the redshifted and blueshifted ^{12}CO $J = 6 - 5$ line wing emission shown in Figure 8.38 reveals a very different emission morphology with the blueshifted line wing emission looking very similar to the straight shape in the Orion Bar and Orion South regions (see the channel maps in Fig. 8.37). The straight shape of the blueshifted ^{12}CO emission in the Orion Bar, South, and East regions probably indicates that the PDRs generated by θ^1 Ori C are located closer to us than the Trapezium stars. In other words, the Trapezium stars are actually

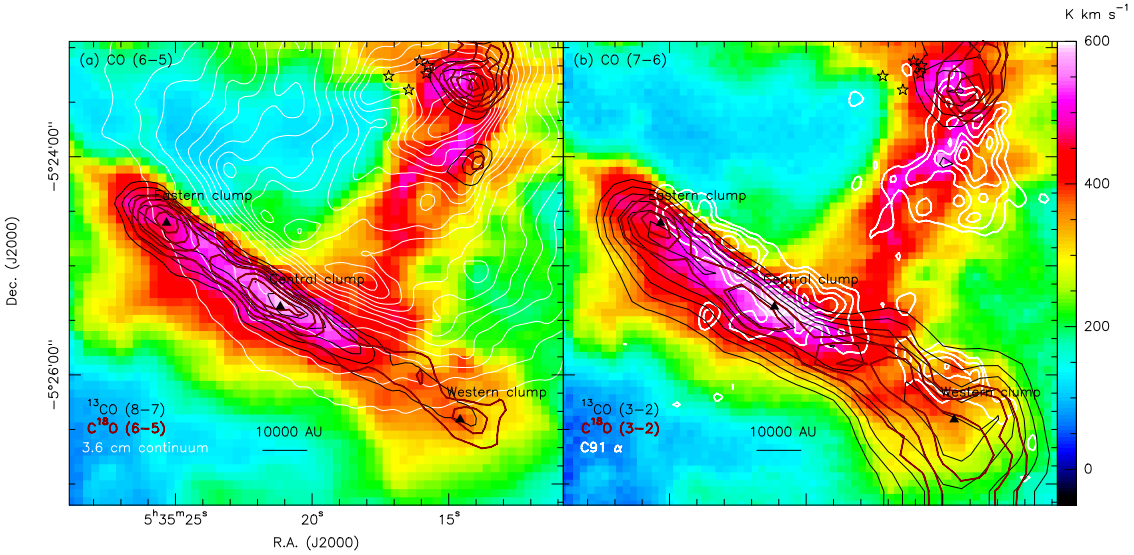

Figure 8.32 The CO isotopologue emission in the Orion Bar and Orion South regions. (a) The ^{12}CO $J = 6 - 5$ integrated intensity image is overlaid with the 3.6 cm VLA-GBT continuum emission in white contours running from 15% to 95% in steps of 5% of the peak intensity (1.82 Jy beam^{-1}). The ^{13}CO $J = 8 - 7$ emission is shown in black contours running from 100 to 200 K km s^{-1} in steps of 20 K km s^{-1}. The C^{18}O $J = 6 - 5$ emission in green contours denote from 25 to 55 K km s^{-1} in steps of 5 K km s^{-1}. (b) The CO $J = 7 - 6$ integrated intensity image is overlaid with the VLA C91α emission (Wyrowski et al. 1997) in thick white contours (30%, 45%, 60%, 75% and 90% of the peak intensity 37.8 mJy beam^{-1}). The black contours of ^{13}CO $J = 3 - 2$ are plotted in steps of 20 K km s^{-1} from 100 to 200 K km s^{-1}, and green contours of C^{18}O $J = 3 - 2$ are plotted in steps of 5 K km s^{-1} from 20 to 35 K km s^{-1}. The three clumps are marked in the both images, and the Trapezium stars are marked in the top-right corner.

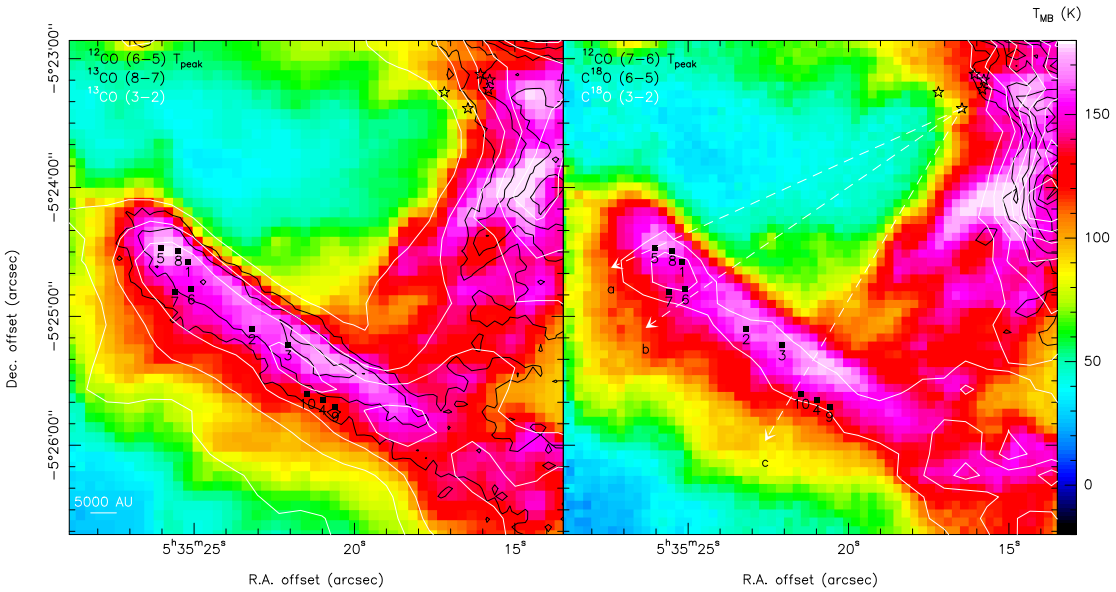

Figure 8.33 The CO isotopologue emission in the Orion Bar and Orion South regions. The left image shows the ^{12}CO $J = 6 - 5$ peak temperature overlaid with the ^{13}CO $J = 8 - 7$ emission in black contours running from 100 to 700 K km s^{-1} in steps of 50 K km s^{-1}, and the ^{13}CO $J = 3 - 2$ emission is shown in white contours running from 70 to 670 K km s^{-1} in steps of 50 K km s^{-1}. The right image shows the ^{12}CO $J = 7 - 6$ peak temperature overlaid the C^{18}O $J = 6 - 5$ emission in black contours running from 30 to 260 K km s^{-1} in steps of 10 K km s^{-1}, and the C^{18}O $J = 3 - 2$ emission is shown in white contours running from 20 to 90 K km s^{-1} in steps of 10 K km s^{-1}. The H^{13}CN clumps from Lis & Schilke (2003) are marked in black filled squares.

Table 8.11. The CO isotopologue measurements of the selected clumps in the Orion Bar region

Line	Central clump			Eastern clump			Western clump		
	$T_{\rm peak}$[a] (K)	$V_{\rm LSR}$ (km s^{-1})	ΔV[b] (km s^{-1})	$T_{\rm peak}$[a] (K)	$V_{\rm LSR}$ (km s^{-1})	ΔV[b] (km s^{-1})	$T_{\rm peak}$[a] (K)	$V_{\rm LSR}$ (km s^{-1})	ΔV[b] (km s^{-1})
^{13}CO $(8-7)$	75.9±3.3	10.7	2.7	66.4±3.8	10.0	2.3	50.4±3.7	9.6	1.7
^{12}CO $(7-6)$	179.9±2.6	10.5	4.0	143.3±2.3	10.2	3.6	136.1±3.3	9.4	3.6
^{12}CO $(6-5)$	180.9±0.9	10.4	3.8	170.2±1.2	10.0	3.4	154.9±1.7	9.1	3.8
C^{18}O $(6-5)$	23.9±2.2	10.9	1.8	28.8±1.7	10.0	1.8	21.4±2.2	9.6	1.8
^{13}CO $(3-2)$	90.1±1.1	10.8	2.4	92.6±1.1	10.1	2.1	88.0±1.4	9.4	2.4
C^{18}O $(3-2)$	13.4±1.0	10.8	1.7	20.2±0.8	9.8	1.3	21.6±1.4	9.2	1.7

[a]Temperatures shown here are corrected to the main beam temperature unit.

[b]Line widths are measured in FWHM.

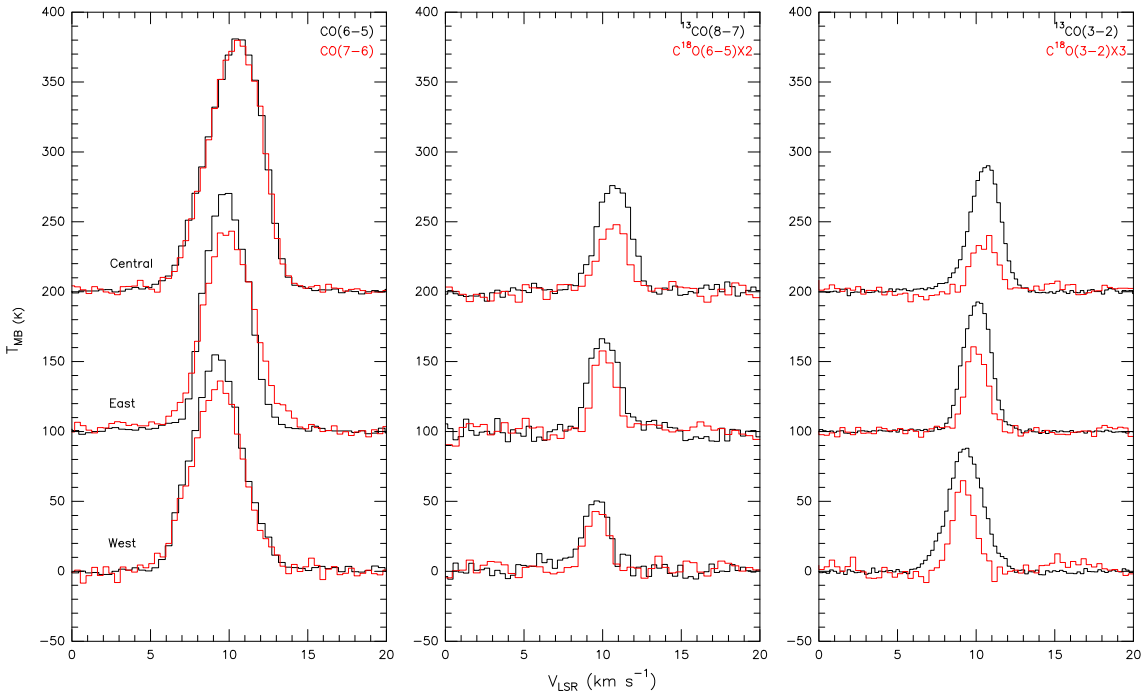

Figure 8.34 The selected spectra of ^{12}CO, ^{13}CO, and C^{18}O in the Orion Bar region corresponding to the three clumps in Figure 8.32.

Table 8.12. The CO isotopologue line ratios in the Orion Bar region

Line ratio	Central clump	Eastern clump	Western clump	$\theta_{\rm HPBW}$
$^{12}CO_{6-5}/^{12}CO_{7-6}$	1.06±0.03	1.13±0.03	1.18±0.04	10″
$^{13}CO_{8-7}/C^{18}O_{6-5}$	3.00±0.27	2.43±0.20	2.59±0.33	10″
$^{13}CO_{3-2}/^{13}CO_{8-7}$	0.93±0.04	1.12±0.04	1.43±0.08	21″
$C^{18}O_{3-2}/C^{18}O_{6-5}$	0.37±0.06	0.85±0.11	0.78±0.09	21″
$^{13}CO_{3-2}/C^{18}O_{3-2}$	6.73±0.51	4.59±0.18	4.07±0.28	21″

[a]Line ratios are derived using the peak temperatures smoothed to the same resolution.

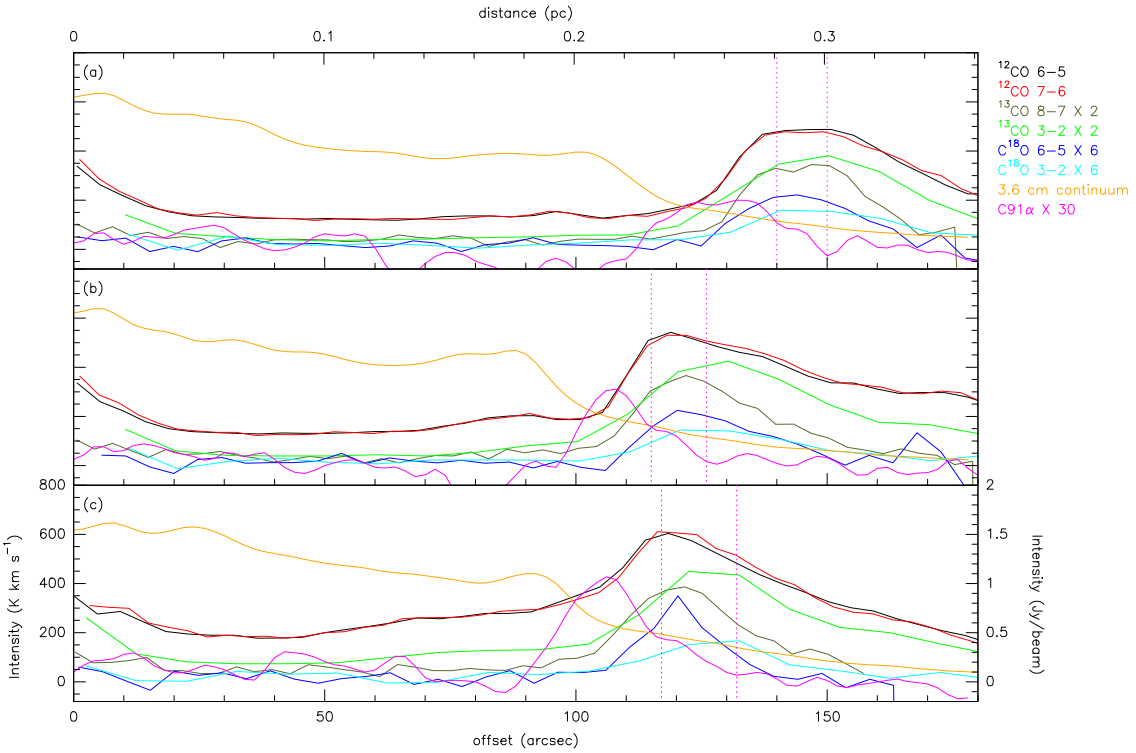

Figure 8.35 Three position-intensity diagrams through θ^1 Ori C of the isotopologue CO emission (in K km s^{-1}) together with the VLA-GBT 3.6 cm continuum and C91α emission from Wyrowski et al. (1997), in the unit of Jy beam^{-1}. The position angles of the cuts are corresponding to the slices a, b, and c shown in Figure 8.33. The zero offset represents the position of θ^1 Ori C. The magenta dotted-lines indicate the two local minimums of the C91α emission in the Bar.

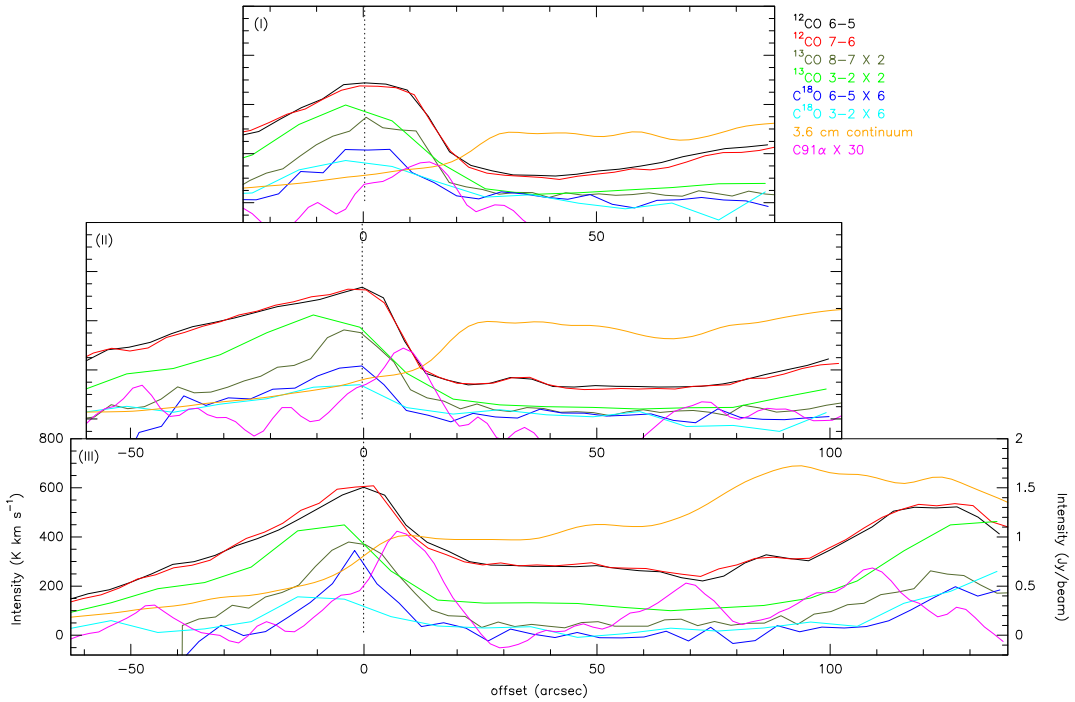

Figure 8.36 Three position-intensity diagrams of the isotopologue CO emission (in K km s^{-1}) together with the VLA-GBT 3.6 cm continuum and the C91α emission from Wyrowski et al. (1997). The 3.6 cm continuum emission and C91α emission are shown in the unit of Jy beam^{-1}. The position angle of the cuts are corresponding to the PV slices I, II, and III perpendicular to the Bar (Fig. 8.30). The zero positions are chosen at the ^{12}CO $J = 6 - 5$ intensity peaks.

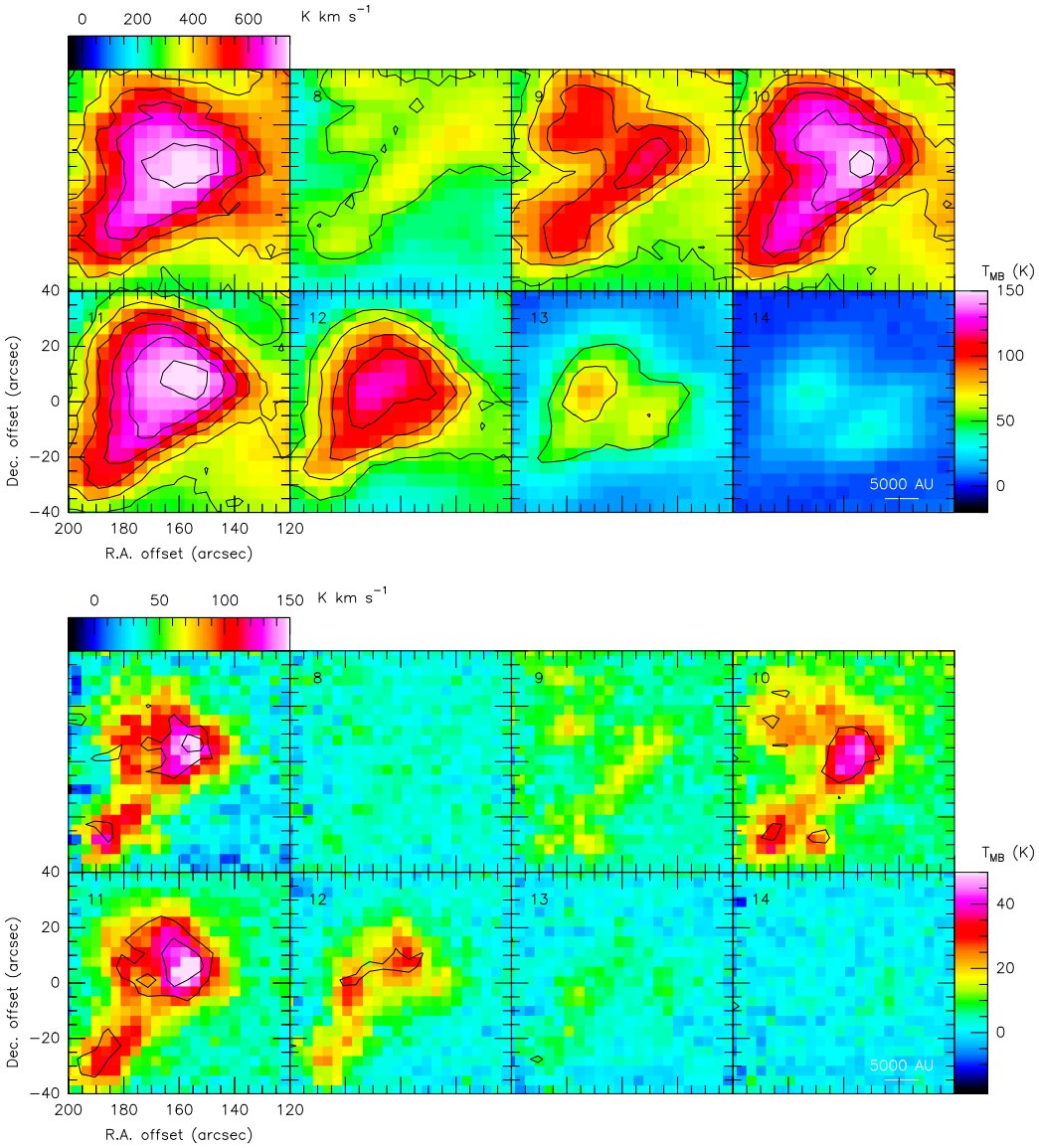

Figure 8.37 Upper panel shows the ^{12}CO $J = 6 - 5$ channel maps in Orion East with the ^{12}CO $J = 7 - 6$ contours. Upper-left map is the ^{12}CO $J = 6 - 5$ [−25, +30] km s^{-1} image overlaid with the $J = 7 - 6$ contours running from 250 to 750 K km s^{-1} in steps of 125 K km s^{-1}. The contours in the rest velocity channel maps are running from 50 to 150 K in steps of 20 K. Lower panel shows the ^{13}CO $J = 8 - 7$ channel maps overlaid with the C^{18}O $J = 6 - 5$ contours. Upper-left map is the ^{13}CO $J = 8 - 7$ [3+, +14] km s^{-1} image overlaid with the C^{18}O $J = 6 - 5$ [+4, +12] contours in values of 12 K km s^{-1} (3 σ level) and 18 K km s^{-1}. The contours in the rest velocity channel maps represent 3.6 K (3 σ level) and 6.6 K.

Table 8.13. The CO isotopologue measurements in Orion East

Line	$T_{\rm peak}$ [a] (K)	$V_{\rm LSR}$ (km s^{-1})	ΔV [b] (km s^{-1})
^{13}CO $(8-7)$	55.7±2.5	10.6	2.3
^{12}CO $(7-6)$	156.2±3.1	10.5	4.0
^{12}CO $(6-5)$	156.7±1.2	10.4	4.7
C^{18}O $(6-5)$	8.2±1.3	10.4	2.2
^{13}CO $(3-2)$	41.6±1.1	10.6	2.3
C^{18}O $(3-2)$	3.9±1.0	10.4	2.3

[a]Temperatures shown here are corrected to the main beam temperature unit.

[b]Line widths are measured in FWHM.

Table 8.14. The CO isotopologue line ratios in Orion East

Line ratio	Orion East	$\theta_{\rm HPBW}$
$^{12}CO_{6-5}/^{12}CO_{7-6}$	1.06±0.03	10″
$^{13}CO_{8-7}/C^{18}O_{6-5}$	6.10±1.34	10″
$^{13}CO_{3-2}/^{13}CO_{8-7}$	0.94±0.06	21″
$C^{18}O_{3-2}/C^{18}O_{6-5}$	0.39±0.13	21″
$^{13}CO_{3-2}/C^{18}O_{3-2}$	10.75±2.87	21″

[a]Line ratios are derived using the peak temperatures smoothed to the same resolution.

enclosed by OMC-1 instead of lying in front of OMC-1 as many authors assumed, e.g., Pellegrini et al. (2009).

The cone-like structure of the red- and blueshifted ^{12}CO line wing emission shown in Figure 8.40 probably is caused by FUV photons from θ^1 Ori C shaping Orion East. The redshifted $[+15, +20]$ km s^{-1} emission is part of the bar-like PDR similar to the blueshifted $[+6, +10]$ km s^{-1} emission, and the cone-like redshifted $[+12, +15]$ km s^{-1} emission has a counterpart in the blueshifted $[+2, +6]$ km s^{-1} emission. A similar structure is also seen in the ^{13}CO $J = 8-7$ emission (Fig. 8.41). Therefore, the redshifted $[15, 20]$ km s^{-1} and blueshifted $[+2, +6]$ km s^{-1} line wing emission shown in Figure 8.40 is not a bipolar outflow, but part of the cone-like structure instead. Besides, the PV diagram in this direction (Fig. 8.42 Cut III) shows no clear outflow signature. However, one weak outflow is found close to the ^{12}CO $J = 6-5$ emission peak shown in Figure 8.42 Cut II.

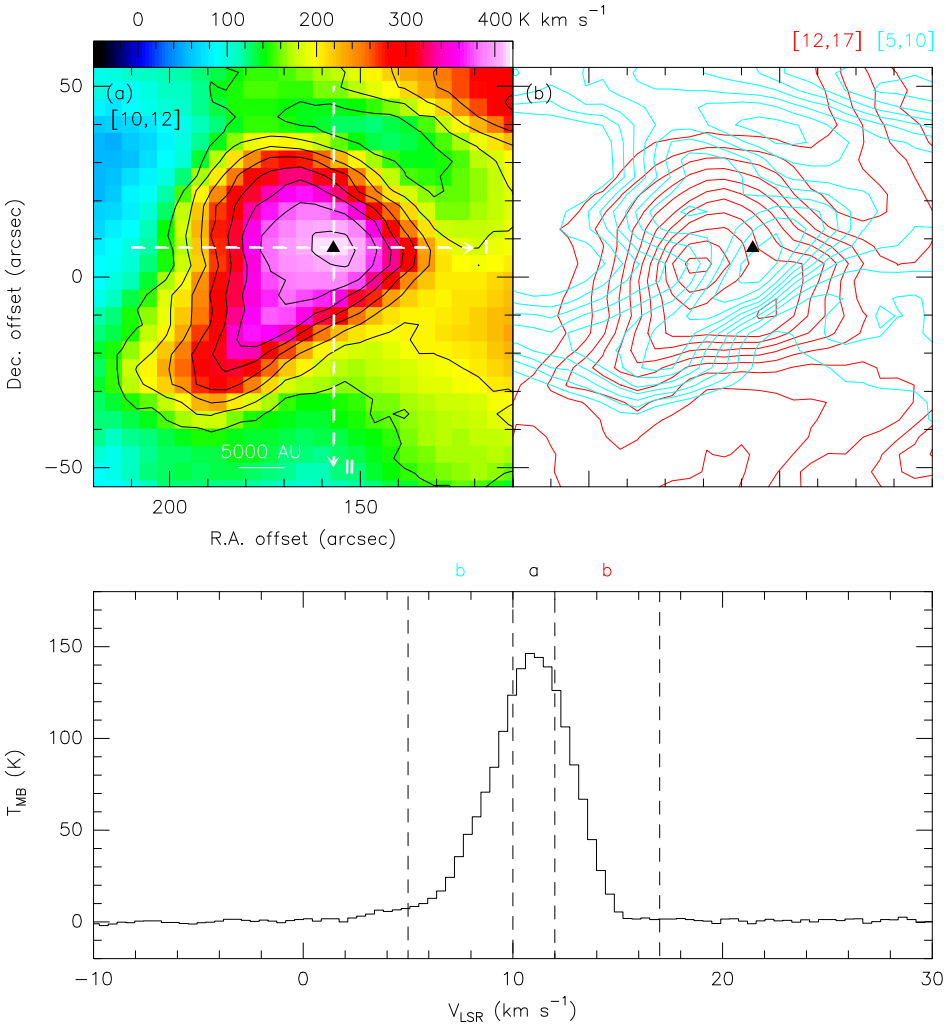

Figure 8.38 The velocity structure of Orion East. Upper panel shows the different velocity intervals corresponding to the spectrum shown in the lower panel.(a) The ^{12}CO $J = 6 - 5$ [+10, +12] km s^{-1} image is overlaid with the ^{12}CO $J = 7 - 6$ contours in steps of 40 K km s^{-1} from 140 to 420 K km s^{-1}. (b) The red- and blueshifted line wings of ^{12}CO $J = 6 - 5$ in Orion East. The red contours are plotted in steps of 20 K km s^{-1} from 50 to 250 K km s^{-1}, and the blue contours are plotted from 200 to 400 K km s^{-1} in steps of 20 K km s^{-1}. The black triangle marks the ^{12}CO $J = 6 - 5$ and $J = 7 - 6$ emission peaks.

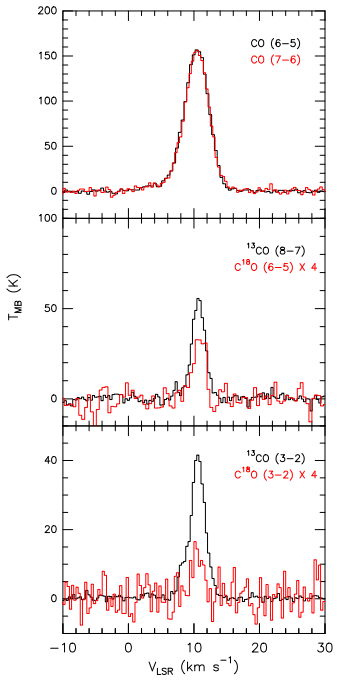

Figure 8.39 The spectra of ^{12}CO, ^{13}CO, and C^{18}O in Orion East.

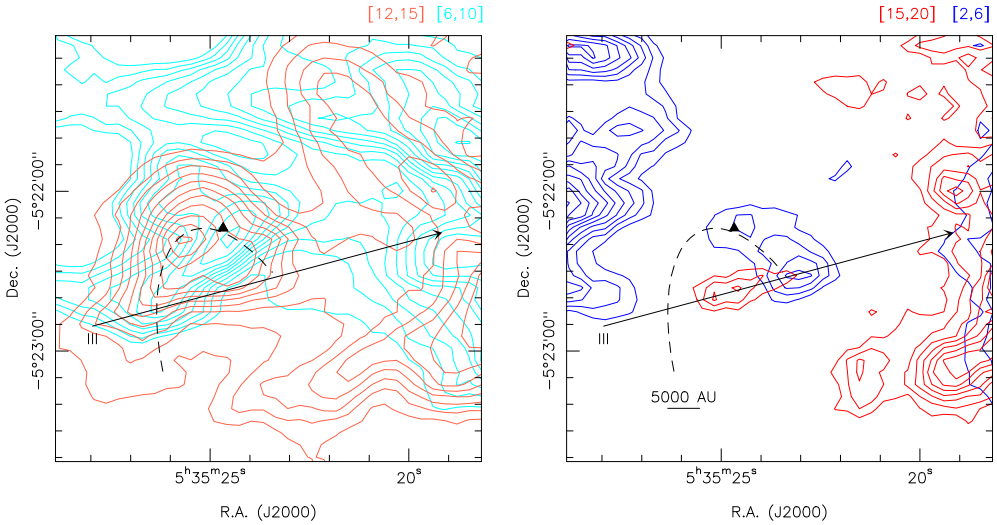

Figure 8.40 Left image shows the ^{12}CO $J = 6 - 5$ [+6, +10] km s^{-1} emission in light blue contours running from 200 to 480 K km s^{-1} in steps of 20 K km s^{-1}, and the [+12, +15] km s^{-1} emission in the light red contours running from 50 to 250 K km s^{-1} in steps of 20 K km s^{-1}. Right image shows the ^{12}CO $J = 6 - 5$ [+2, +6] km s^{-1} emission in blue contours running from 35 (3 σ level) to 125 K km s^{-1} in steps of 10 K km s^{-1}, and the ^{12}CO $J = 6 - 5$ [+15, +20] km s^{-1} emission in red contours running from 18 (3 σ level) to 60 K km s^{-1} in steps of 6 K km s^{-1}. The black dashed-lines indicate the cone-like structure.

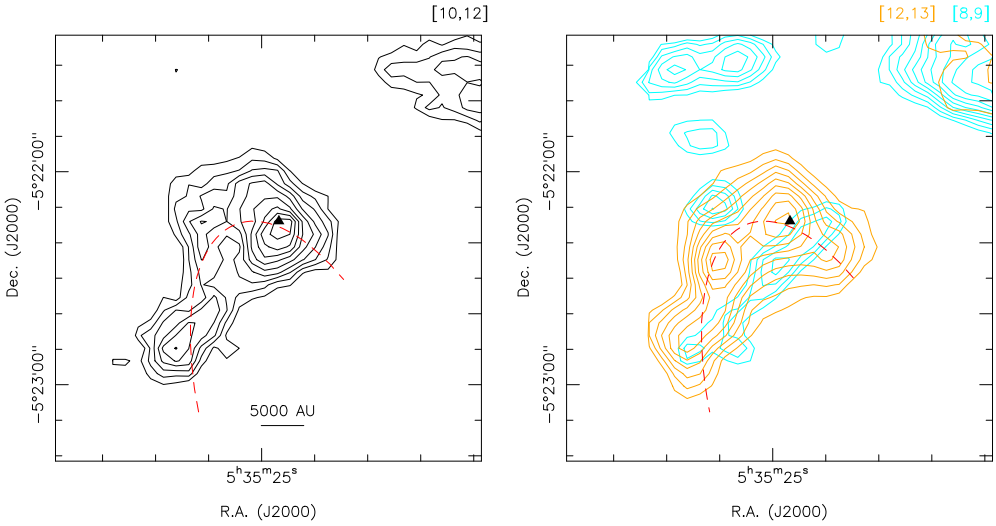

Figure 8.41 Left image shows the ^{13}CO $J = 8 - 7$ [+10, +12] km s^{-1} emission in black contours running from 40 (3 σ level) to 130 K km s^{-1} in steps of 10 K km s^{-1}. Right image shows the ^{13}CO emission image smoothed in two Gaussian beams. The [+8, +9] km s^{-1} emission is shown in blue contours running from 15 (3 σ level) to 30 K km s^{-1} in steps of 1.5 K km s^{-1}, and [+12, +13] km s^{-1} emission is shown in orange contours running from 9 (3 σ level) to 33 K km s^{-1} in steps of 3 K km s^{-1}. The red dashed-lines indicate the cone-like structure.

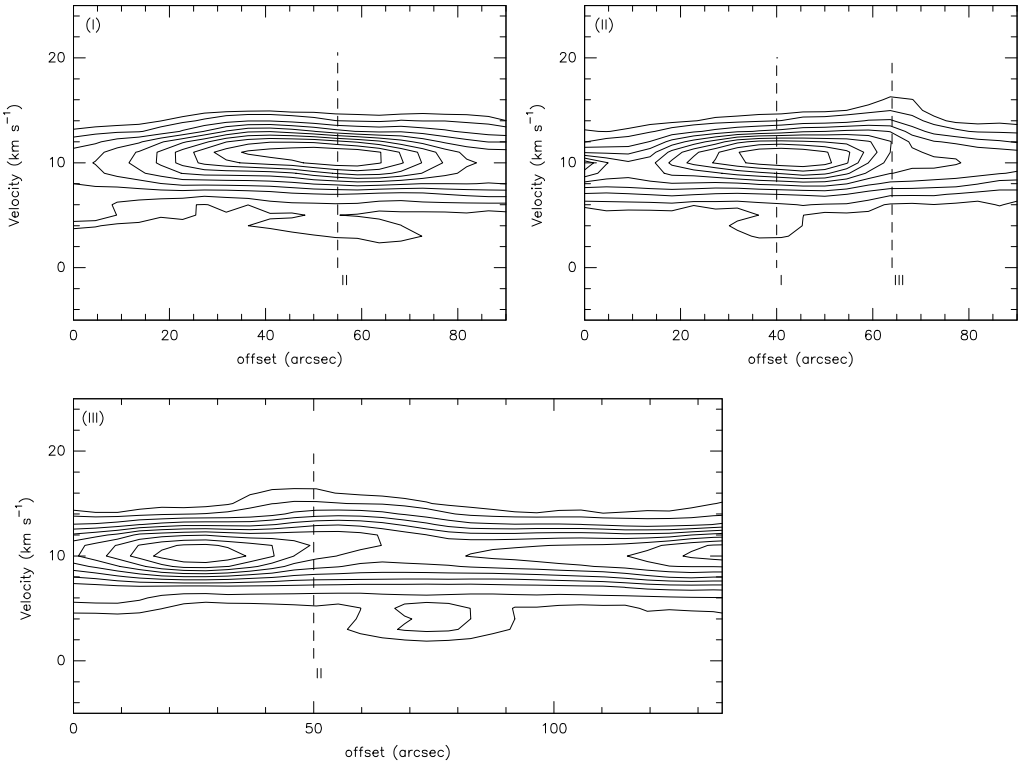

Figure 8.42 Three position-velocity slices in the Orion East region shown in Figures 8.38 and 8.40. Panel (I) shows the eastwestern slice through Orion East, and the northsouthern slice is shown in Panel (II). The contours in Cut I and II represent 5% and from 10% to 90% in steps of 10% of the peak temperature (155 K). The contours in Cut III represent 5% and from 10% to 90% in steps of 10% of the peak temperature (127 K).

9

RADEX Modeling of OMC-1

9.1 The excitation temperature and the density estimation

The ^{12}CO $J = 6 - 5$ and C^{18}O $J = 6 - 5$ data are used here to derive the excitation temperature and density of OMC-1. In the submillimeter regime where the Rayleigh-Jeans approxmation is often not valid, the observed radiation temperature in LTE can be expressed as

$$T_{\rm R}^{*} = (\frac{h\nu}{k})\frac{1 - e^{-\tau_\nu}}{e^{h\nu/kT_{\rm ex}} - 1}, \tag{9.1}$$

where $T_{\rm ex}$ is the excitation temperature, and τ_ν is the optical depth in a specific molecular transition. The background radiation of 2.73 K was neglected assuming $T_{\rm bg} \ll T_{\rm ex}$. By making the assumption of the same excitation temperatures for ^{12}CO and C^{18}O $J = 6 - 5$, the optical depths of ^{12}CO and C^{18}O $J = 6 - 5$ can be determined from the relation

$$\frac{T_{\rm R}^{*}(^{12}{\rm CO})}{T_{\rm R}^{*}({\rm C}^{18}{\rm O})} \approx \frac{1 - e^{-\tau(^{12}{\rm CO})}}{1 - e^{-\tau({\rm C}^{18}{\rm O})}}. \tag{9.2}$$

Since the optical depth of ^{12}CO $J = 6 - 5 \gg 1$, the optical depth of C^{18}O $J = 6 - 5$ can be directly obtained by assuming that the optical depth ratio is approximated to the isotopologic abundance ratio, and here we adopted [^{12}CO]/[C^{18}O] of 490 (e.g. Boreiko & Betz 1996; Wilson & Matteucci 1992) and a beam filling factor of unity ($T_{\rm R}^{*} = T_{\rm MB}$). The excitation temperatures of ^{12}CO and C^{18}O $J = 6 - 5$ can be estimated via

$$T_{\rm ex} = E_{\rm u}\left[\ln\left(1 + \frac{E_{\rm u}}{T_{\rm MB}(^{12}{\rm CO})}\right)\right]^{-1}, \tag{9.3}$$

where $E_{\rm u}$ is the energy level of the upper state, and is 116.2 K for the ^{12}CO $J = 6 - 5$ transition. Using Eqs. B.22 and B.28 (see Appendix B), the total C^{18}O column density can be derived from

$$N({\rm C}^{18}{\rm O}) \simeq 1.33 \times 10^{12}\ (T_{\rm ex} + 0.88)\ e^{\frac{E_{\rm u}}{T_{\rm ex}}} \int T_{\rm MB} dV\ {\rm cm}^{-2}, \tag{9.4}$$

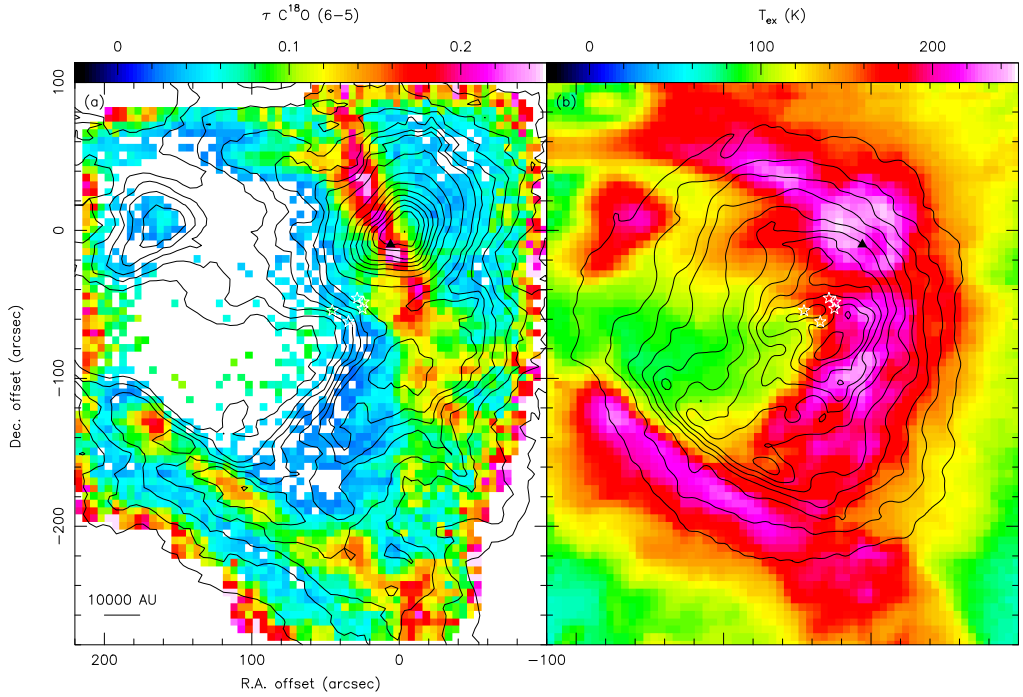

Figure 9.1 (a) The $C^{18}O$ optical depth image of OMC-1 overlaid with the ^{12}CO $J = 6 - 5$ emission in black contours running from 300 to 900 K km s^{-1} in steps of 100 K km s^{-1} and the subsequent contours running from 1200 to 7200 K km s^{-1} in steps of 800 K km s^{-1}. (b) The excitation temperature image for ^{12}CO and $C^{18}O$ overlaid with 3.6 cm VLA-GBT continuum emission in black contours running from 15% to 95% in steps of 10% of the peak intensity (1.82 Jy beam^{-1}). The stars mark the five Trapezium stars (θ^1 Ori A, B, C, D, and E), and the black triangle represents the Orion Hot Core.

where E_u is 110.6 K for the $C^{18}O$ $J = 6-5$ transition. The results of the optical depth and excitation temperature distributions are shown in Figure 9.1, and the $C^{18}O$ and H_2 column density maps are shown in Figure 9.2, where a north-south dense ridge near the Trapezium cluster and the Orion Bar in the southeast are clearly seen. The average $\tau(C^{18}O)$ in the $J = 6 - 5$ transition over the whole OMC-1 region is about 0.08, and the kinetic temperature is about 145 K, which is consistent with the ^{12}CO $J = 9 - 8$ observations of Kawamura et al. (2002). Besides, the minimum kinetic temperature in OMC-1 is $\sim$ 50 K, which indicates a generally warm environment. The average $C^{18}O$ column density in OMC-1 is about 9.6×10^{15} cm^{-2}, corresponding to an H_2 column density of 5.9×10^{22} cm^{-2} assuming a ^{12}CO abundance of 8×10^{-5} (Wilson & Matteucci 1992). Therefore, the dense gas mass is ~ 150 $M_\odot$ in an area of 1.26×10^{36} cm^2 (0.13 pc^2). The H_2 column density agrees with the density of $5 \times 10^{21} - 7 \times 10^{22}$ cm^{-2}, derived from the mid-J CO isotopologue observations (Wirström et al. 2006).

It is interesting that the dense ridge has an offset from the peak temperatures especially in

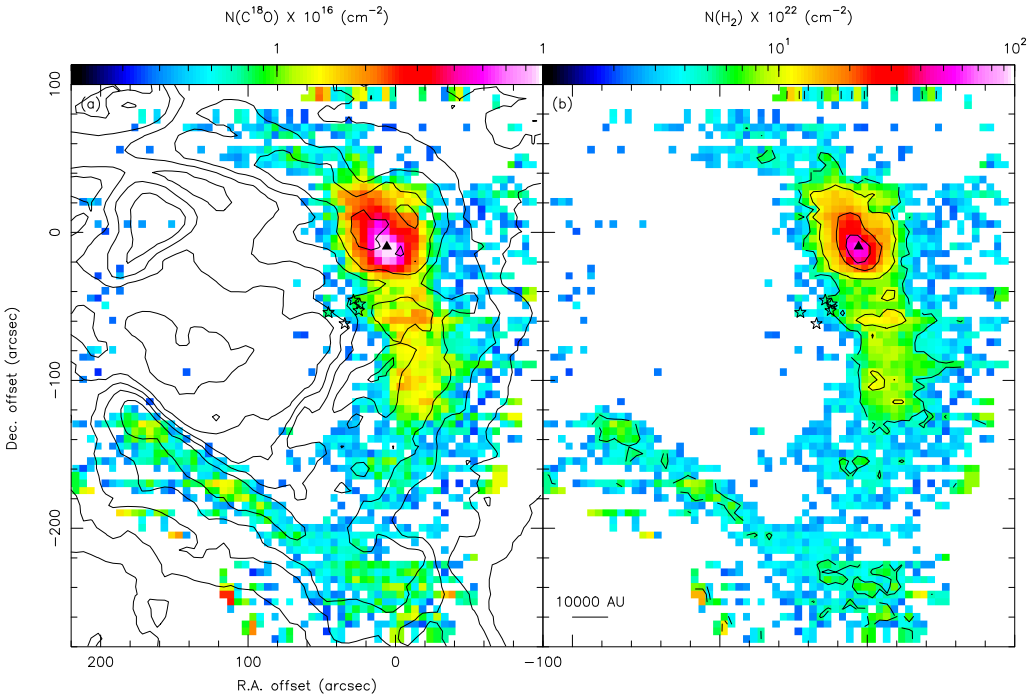

Figure 9.2 (a) The $C^{18}O$ column density image of OMC-1 overlaid with the kinetic temperature map in black contours running from 60 to 240 K in steps of 30 K. (b) The H_2 column density image of OMC-1. Contours represent 5×10^{22} cm^{-3}, 10×10^{22} cm^{-3}, 20×10^{22} cm^{-3}, and 40×10^{22} cm^{-3}. The stars mark the five Trapezium stars (θ^1 Ori A, B, C, D, and E) and the black triangle represents the Orion Hot Core.

the Orion South region and the north of the Orion BN/KL region. The dense ridge seems to extend to the north of OMC-1, and is probably related to the OMC-2/3 filamentary structure, another active star forming region.

9.2 RADEX modeling

The non-LTE radiative transfer program RADEX (van der Tak et al. 2007, see also §4.2) was used to investigate the accuracy of the temperature and density calculation in LTE shown above. The optical depth effects are taken into account by RADEX using the escape probability approximation, where a uniform sphere geometry (Eq. 4.6) was chosen. The different transitions of ^{12}CO, ^{13}CO, and $C^{18}O$ were taken into account in the modeling, and their line widths were fixed at 5.0 km s^{-1}, 4.5 km s^{-1}, 4.0 km s^{-1}, respectively, which are the average values from the observations. In addition, only H_2 was chosen as a collision partner, and 2.73 K was adopted as the background temperature. The input parameters are kinetic temperature and H_2 number density. Each model was iterated with a kinetic temperature ranging from 50 to 450 K, and an H_2 number density ranging from 10^4 to 10^8 cm^{-3}. The input column densities of these three molecules were fixed, so that their ratios were

Table 9.1. The estimates of the average optical depths, excitation temperatures, and $C^{18}O$ and H_2 column densities in OMC-1

Source	$\tau(^{18}CO)^a$	T_{ex} (K)	$N(C^{18}O)^a$ (cm^{-2})	$N(H_2)^a$ (cm^{-2})
Orion BN/KL	0.10	200	1.7×10^{16}	1.0×10^{23}
Orion South	0.09	190	9.3×10^{15}	5.7×10^{22}
Orion Bar	0.09	175	6.7×10^{15}	4.1×10^{22}
Orion East	0.06	140	4.0×10^{15}	2.5×10^{22}
OMC-1	0.08	145	9.6×10^{15}	5.9×10^{22}

[a]The H_2 column density is estimated by assuming the ^{12}CO to $C^{18}O$ abundance ratio of 490 and the ^{12}CO to H_2 abundance ratio of 8×10^{-5}.

fixed at the isotopologic abundance ratios of 490 for $[^{12}CO]/[C^{18}O]$ and of 60 for $[^{12}CO]/[^{13}CO]$ (e.g. Boreiko & Betz 1996; Wilson & Matteucci 1992). Three models were iterated with three different ^{12}CO column densities of 1×10^{18} cm^{-2}, 5×10^{18} cm^{-2}, and 1×10^{19} cm^{-2}. Since these models did not take outflows into account, the output molecular line radiation temperatures (T_R) were directly compared to the peak temperatures from the observations instead to the integrated intensities. The modeling results are shown in Figures 9.3 and 9.4.

Figure 9.3 reveals that most regions in OMC-1 have an H_2 number density of $\sim 10^4 - 10^6$ cm^{-3}. The Orion Bar and Orion East emission peaks (Fig. 9.3 a), however, show higher densities. The distribution of the H_2 number density in the Bar is consistent with $10^4 - 10^5$ cm^{-3} for a homogeneous medium (Wyrowski et al. 1997) and $10^6 - 10^7$ cm^{-3} assuming clumping (Lis & Schilke 2003). The modeling results in the Orion BN/KL, Orion South, and Orion Bar regions (Fig. 9.3) all show similar trends of diverse kinetic temperature distribution from about 80 K to a high temperature of few hundred Kelvin. Noteworthily, the Orion BN/KL region and part of the Orion South region (Fig. 9.3 a) show very high kinetic temperatures (> 350 K) which indicate an extra heating mechanism, e.g. outflow/shock heating. The suggestion of outflow/shock heating is supported by the larger ^{12}CO line widths (Fig. 8.1) and a great amount of known outflows in these regions. In addition, the high kinetic temperatures (≥ 250 K) in the Orion Bar and Orion East regions (Fig. 9.3 a) are hardly explained by the outflow/shock heating for the lack of outflow activities or a broad ^{12}CO line width. Instead, as PDRs, the Orion Bar and Orion East are expected to be heated by FUV photons from OB stars. Moreover, a recent study of the Orion Bar (Pellegrini et al. 2009) suggests an extra heating by the excess density of cosmic rays, which are trapped in the compressed magnetic field.

Figure 9.4 shows the same model results and the correlations between ^{12}CO $J = 6 - 5$ and ^{12}CO $J = 7 - 6$ in OMC-1, where both ^{12}CO transitions have similar intensities. The results from

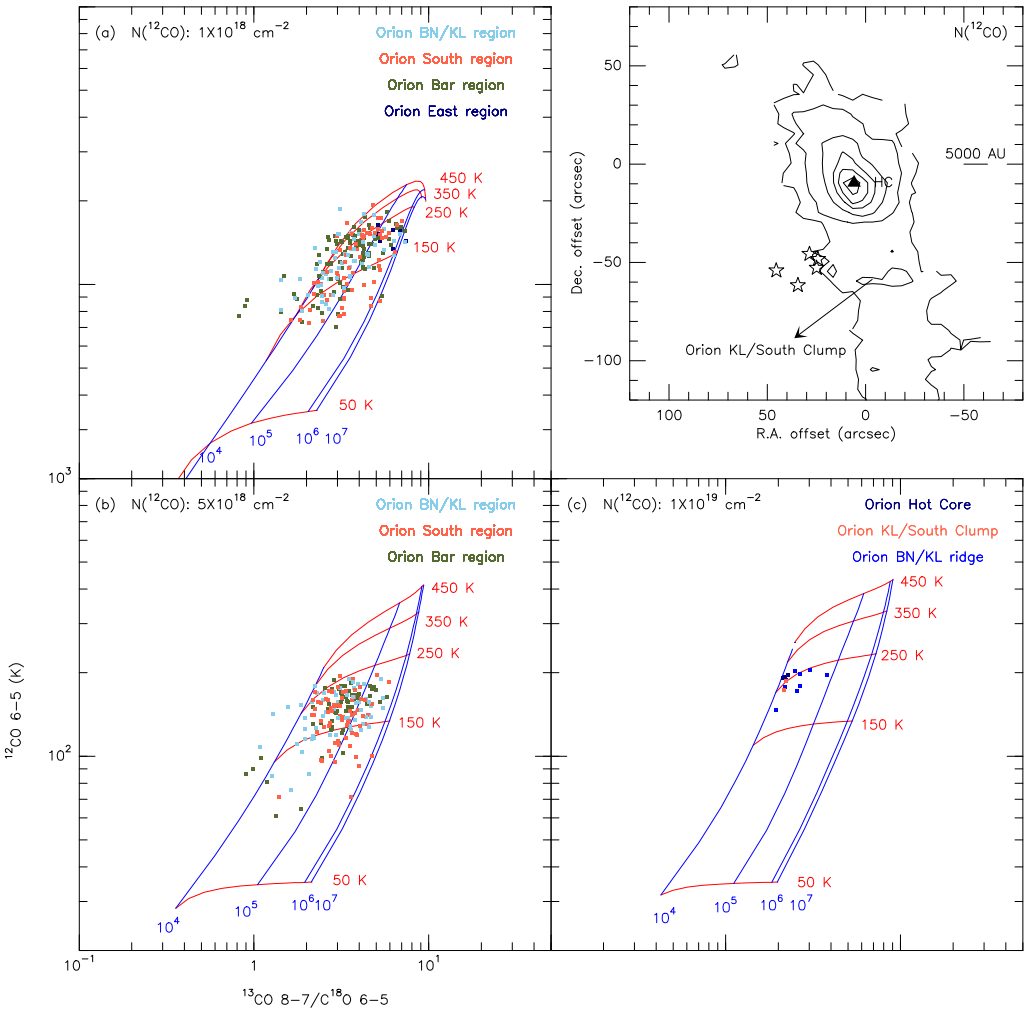

Figure 9.3 The RADEX modeling results shown in the ^{12}CO $J = 6 - 5$ peak temperatures and the ^{13}CO/C^{18}O ratios for three different ^{12}CO column densities. The column densities of ^{13}CO and C^{18}O are fixed at the isotopologic abundance ratio of 1/60 and 1/490 of the ^{12}CO column density. The line width of ^{12}CO, ^{13}CO, and C^{18}O is fixed at 5.0, 4.5, and 4.0 km s^{-1}, respectively. The red and blue contours denote the temperature and H_2 number density, repsectively, and the color points represent the data in the different regions of OMC-1. Each point represents a peak ^{12}CO $J = 6 - 5$ temperture and a temperature ratio between ^{13}CO $J = 8 - 7$ and C^{18}O $J = 6 - 5$ from a single pixel with a resolution of 20″. (a) The column density of ^{12}CO is 1×10^{18} cm^{-2}, and the data are plotted in a ^{12}CO column density density of $7.5 \times 10^{17} - 2.5 \times 10^{18}$ cm^{-2} (b) The column density of ^{12}CO is 5×10^{18} cm^{-2}, and the data are plotted in a density range of $2.5 \times 10^{18} - 7.5 \times 10^{18}$ cm^{-2}. (c) The column density of ^{12}CO is 1×10^{19} cm^{-2}, and the data are plotted in the density of $\geq 7.5 \times 10^{18}$ cm^{-2}. Upper right panel shows the ^{12}CO column density map in contours of $0.9, 1.8, 3.0, 5.0, 7.0, 9.0 \times 10^{18}$ cm^{-2}. The stars mark the five Trapezium stars (θ^1 Ori A, B, C, D, and E), and the Orion Hot Core and Orion KL/South clump are marked.

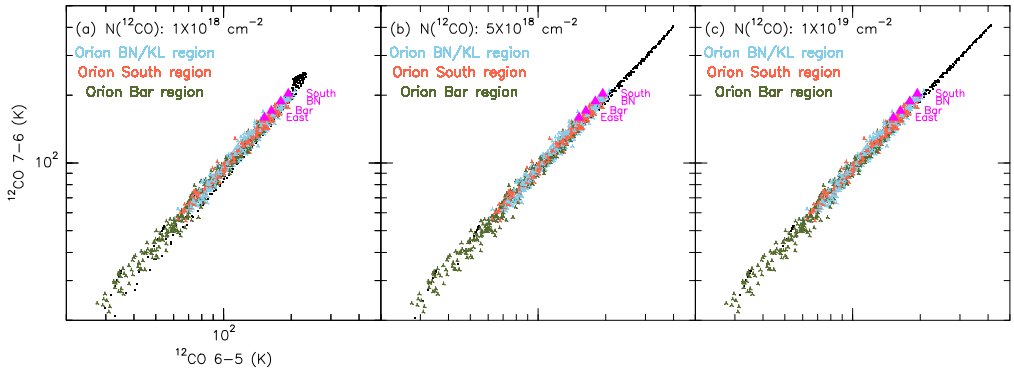

Figure 9.4 The same RADEX modeling as in Figure 9.3 but only shown for the correlations between ^{12}CO $J = 6-5$ and $J = 7-6$. The modeling results are shown in black points and are compared to the data shown in different colors represented for different regions in OMC-1. The peak temperatures of Orion BN, Orion South, Orion Bar, and Orion East are marked in magenta triangles.

the RADEX modeling also suggest a similar linear correlation in a log-log space. Since the opacity of the ^{12}CO emission is very high, the density difference is difficult to distinguish in Figure 9.4.

If we adopted a radius of 50″ and an H_2 density of 10^5 cm^{-3} for Orion BN/KL, we can estimate a gas mass of 24 $M_\odot$ with the assumption of a spherical volume and a distance of 414 pc (Menten et al. 2007). In a similar way, the gas mass in Orion South is 12 $M_\odot$ with a 40″ radius and an H_2 density of 10^5 cm^{-3}. For Orion East, the H_2 density is $\sim 10^5 - 10^6$ cm^{-3} with a 20″ radius, and the gas mass is $\sim 2 - 16$ $M_\odot$. In contrast, it is very difficult to estimate the gas mass in the Orion Bar because of its geometry. We adopted a cylindrical geometry and an H_2 density of 10^6 cm^{-3} as the lower limit since an edge-on plane might contain much more gas. With a length of 300″ and a radius of 15″, the gas mass of the Orion Bar is ~ 99 $M_\odot$. The estimated total dense H_2 gas mass in OMC-1 is ~ 150 $M_\odot$ within a radius of 0.3 pc. This is also consistent with the mass estimated from the LTE calculation above. If we include the warm diffuse gas (10^4 cm^{-3}) in the same volume, the total warm gas mass is ~ 215 $M_\odot$ in OMC-1, where the PDRs (the Orion Bar and East) contribute more than half of the total mass. The OMC-1 total mass estimation is close to the result from the Odin ^{12}CO and ^{13}CO $J = 5-4$ observations (Wirström et al. 2006) where they derived 320 $M_\odot$ in the molecular ridge for a farther distance of 500 pc. A paper by Wilson et al. (2001) also shows a similar estimate of a warm gas mass of $310 - 430$ $M_\odot$ from the observations of ^{12}CO $J = 7-6$ and $J = 4-3$ adopting an OMC-1 distance of 500 pc.

10

OMC-1 Discussion

The three-dimensional overview of the OMC-1 velocity structure is shown in Figure 10.1, which is produced with 3D Slicer[1]. The four prominent sources, Orion BN/KL, Orion South, Orion Bar, and Orion East are clearly seen. In this chapter, the characteristics of individual sources will be discussed.

10.1 Orion BN/KL

The Orion BN/KL region is one of the most active and densest region in OMC-1. The average H_2 column density is about 1×10^{23} cm^{-2} from the LTE calculation, corresponding to an H_2 number density of few times 10^5 cm^{-3} assuming a size of about $50''$. The RADEX modeling results also show a consistent estimate of the H_2 density in this region (see §9.2). The kinetic temperature derived from ^{12}CO $J = 6 - 5$ in the Orion BN/KL region is about 200 K, which indicates hot gas in this region. The densest part in Orion BN/KL follows the NE-SW dense ridge shown in Figures 9.1 and 9.2, and has a density peak at the Orion Hot Core.

The explosive outflow and shell structure

The high-velocity outflow in Orion BN/KL is well-known for its finger-like morphology detected in the infrared H_2 emission (Taylor et al. 1984; Allen & Burton 1993). The origin of this outflow has been debated by many authors (see e.g., Menten & Reid 1995; Beuther & Nissen 2008). Recently, the high resolution ^{12}CO $J = 2 - 1$ observations of Zapata et al. (2009) have revealed a tight correlation between the H_2 fingers and the molecular bullets. Zapata et al. (2009) propose that this explosive outflow is likely produced by a close dynamical interaction involving IR sources BN, n, and radio source I. Figure 10.2 shows the circular PV diagrams of the CO isotopologues in Orion BN/KL,

[1] 3D Slicer (http://www.slicer.org) is a free open source software for visualization and image computing especially in Medicine. This program is coordinated to display astronomical images in the Astronomical Medicine Project (http://astromed.iic.harvard.edu).

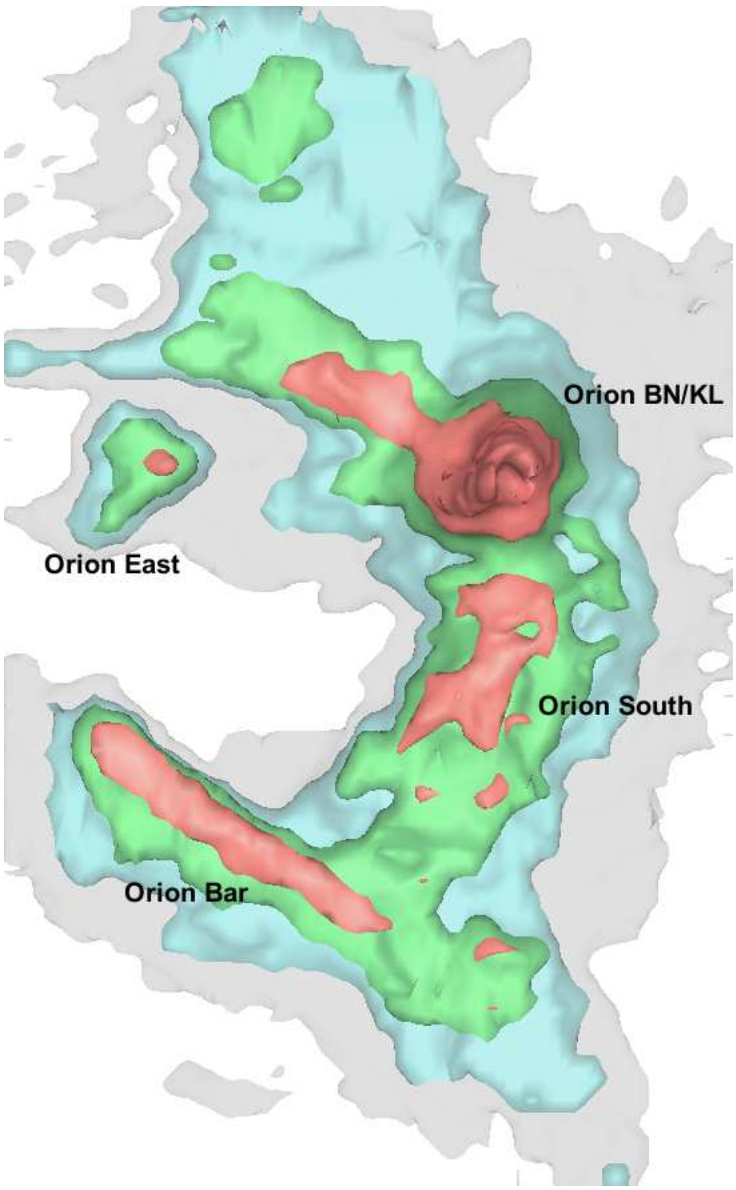

Figure 10.1 A 3D view (R.A., Dec., and velocity) of OMC-1 with four isothermal surfaces marked in different colors. The grey, blue, green, and red surfaces represent $T_{\rm MB}$ of 60 K, 90 K, 120 K, and 150 K, respectively. This image is produced with 3D Slicer.

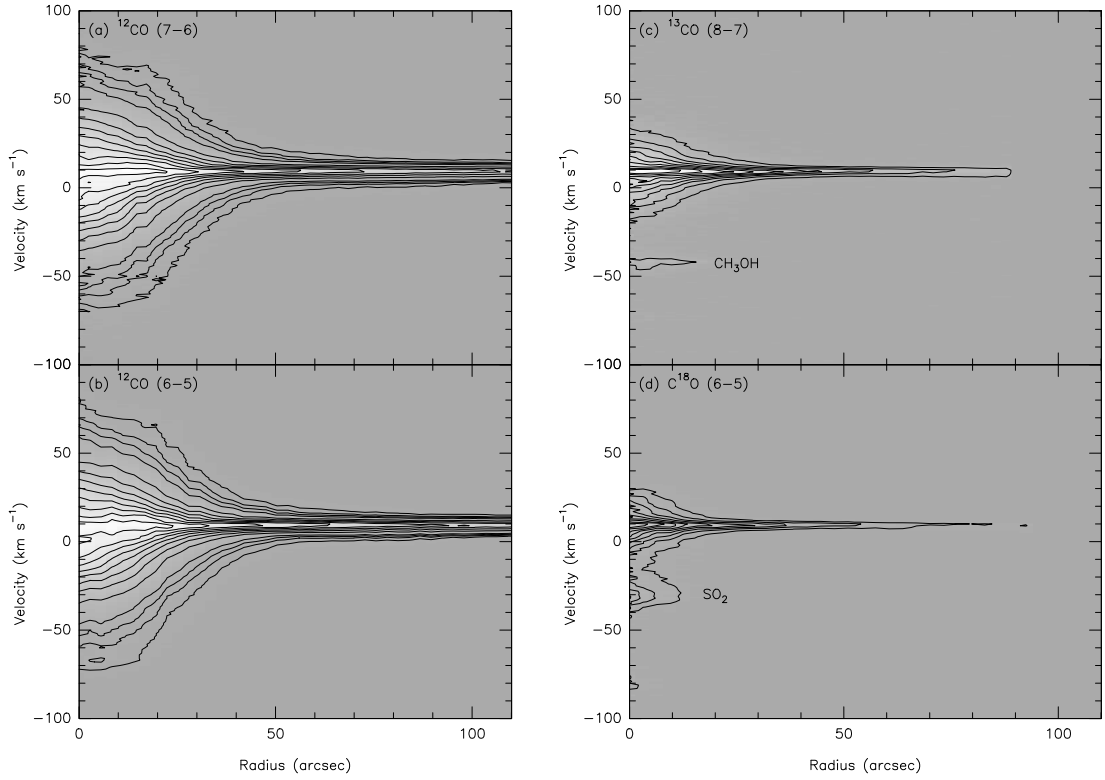

Figure 10.2 The circular PV diagrams in the Orion BN/KL region. The central position of the circular PV diagrams is chosen at the explosive outflow center. (a)-(b) The ^{12}CO $J = 7 - 6$ and $J = 6 - 5$ emission is shown in contours of 3%, 5%, 7%, and from 10% to 90% in steps of 10% of the peak temperature (182 K for $J = 7 - 6$ and 175 K for $J = 6 - 5$). (c)-(d) The ^{13}CO $J = 8 - 7$ and C^{18}O $J = 6 - 5$ emission is shown in contours from 10% to 90% in steps of 10% of the peak temperature (74 K for ^{13}CO $J = 8 - 7$ and 31 K for C^{18}O $J = 6 - 5$). The emission contributed by CH$_3$OH $11_{1,10} - 10_{0,10}$ and SO$_2$ $37_{1,37} - 36_{0,36}$ is indicated.

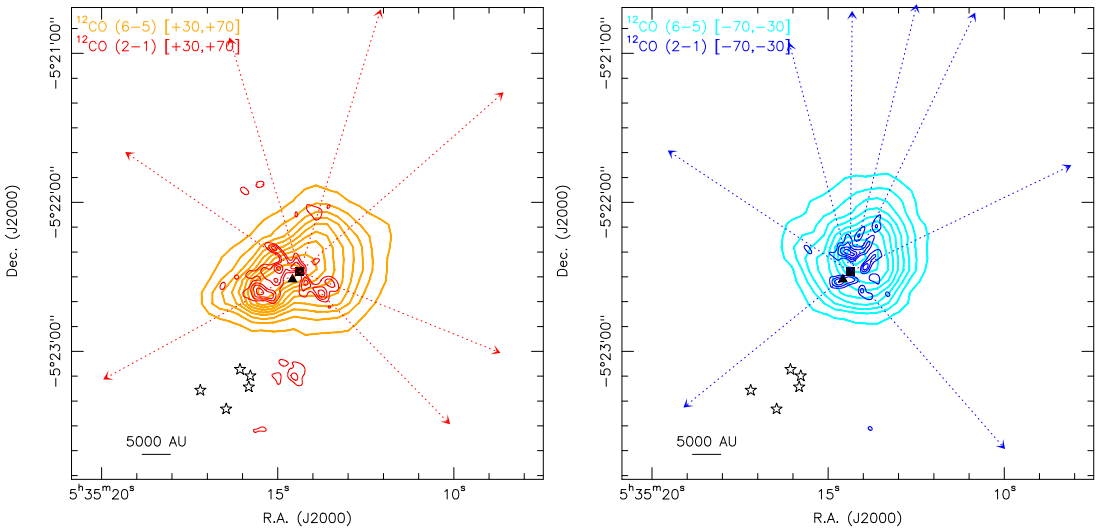

Figure 10.3 The high-velocity outflow emission in the ^{12}CO $J = 6 - 5$ transition overlaid with the SMA ^{12}CO $J = 2 - 1$ emission (Zapata et al. 2009). Left panel shows the redshifted ^{12}CO emission integrated from +30 to +70 km s^{-1}, and right panel shows the blueshifted ^{12}CO emission integrated from −70 to −30 km s^{-1}. The ^{12}CO $J = 6 - 5$ emission is plotted in orange and light blue contours running from 10% to 90% in steps of 10% of the peak intensity. The ^{12}CO $J = 2 - 1$ emission is plotted in red and blue contours running from 30% to 90% in steps of 20% of the peak intensity. The black square represents the explosive outflow center, and the black triangle represents the Orion Hot Core. The black stars mark the five Trapezium stars (θ^1 Ori A, B, C, D, and E).

where the ^{12}CO $J = 6 - 5$ and $J = 7 - 6$ emission reveals a strong and somehow symmetric velocity gradient centered on the origin of the outflow.

In Figure 10.3, the high-velocity ^{12}CO $J = 6 - 5$ emission from the APEX telescope is overlaid with the high-resolution SMA ^{12}CO $J = 2 - 1$ image (Zapata et al. 2009), where the finger-like structure is presented, and the morphology between these two transitions also shows good agreement. In addition, the very high velocity ^{12}CO $J = 2 - 1$ emission (Fig. 10.4) shows clear emission counterparts in the APEX ^{12}CO $J = 6 - 5$ emission, where the redshifted emission lies mostly in the NW-SW direction and the blueshifted one lies mostly in the N-S direction. Noteworthily, the dense ridge peaking at the Orion Hot Core is located at the east of the explosion center. In Figure 10.5, as mentioned in §8.2, a high temperature shell structure is seen in Orion BN/KL, enclosing Orion BN and the Hot Core.

The column density of the outflow can be estimated using Eq. 8.1 assuming optically thin emission of ^{12}CO $J = 6 - 5$ at high velocities (see also §4.3), and an excitation temperature of 80 K. The beam filling factor was estimated to be about 0.05 for the redshifted bullets and about 0.11 for the blueshifted bullets by comparing the outflow FWHM size of the ^{12}CO $J = 2 - 1$ interferometry data with the APEX ^{12}CO $J = 6 - 5$ emission size, given that this outflow is resolved in the SMA

Table 10.1. The Orion BN/KL explosive outflow parameters

Component	f[a] (%)	$M_{\rm outflow}$ ($M_\odot$)	Momentum[b] ($M_\odot$ km s^{-1})	Energy[b] (10^{46} erg)
B $[-100, -70]$	~ 11	$0.4 - 0.5$	$29.6 - 40.5$	$2.2 - 3.0$
R $[+70, +100]$	~ 5	$0.7 - 0.8$	$63.6 - 75.1$	$6.0 - 7.1$

[a]Filling factor is estimated by comparing the emission sizes with the SMA ^{12}CO $J = 2 - 1$ emission sizes.

[b]The energy and momentum are calculated by adopting the velocity of 75 km s^{-1} and 95 km s^{-1} for blue- and redshifted component, respectively.

observations ($3\farcs28 \times 3\farcs12$). The outflow mass and the kinetic energy then can be calculated by adopting an isotopologic abundance ratio $[^{12}{\rm CO}]/[{\rm H_2}]$ of 8×10^{-5} in OMC-1 (Wilson & Matteucci 1992). The derived parameters of this outflow are summarized in Table 10.1. The total kinetic energy associated with this explosive outflow in Orion BN/KL is $\sim 1 \times 10^{47}$ erg, close to the value derived by Kwan & Scoville (1976).

The shell structure seen in the kinetic temperature map (e.g., Fig. 10.5) in the Orion BN/KL region is probably due to the optically thick ^{12}CO emission. Figure 10.6 shows the CO isotopologic spectra in the different offset positions in Orion BN/KL. There are clear absorptions in the north, northwest, and southwest direction from the $(0'', 0'')$ position. However, the absorptions in the north and northwest are redshifted, while the absorption in the southwest is blueshifted according to the ambient velocity of $\sim 9 - 10$ km s^{-1} of Orion BN/KL. Besides, these features are also seen in the PV diagrams (Fig. 8.20) that both red- and blueshifted absorptions appear around the Orion Hot Core and Orion BN. Therefore, it is likely that these absorption features are not only due to self-absorption but also reflect the velocity structure in Orion BN/KL. The three-dimensional views of Orion Bn/KL in Figures 10.7 and 10.8 both show the shell structure in Orion BN/KL extending even to the outflow, where the shell seems to rotate or twist in the red- and blueshifted components. This twist-like motion is shown in the clockwise direction.

It is not clear if this shell structure we seen in Orion BN/KL is associated with the explosive outflow, but it is possible that this explosion event occurs together with the outflow and removes gas from the center of the cloud, where gas in turn accumulates peripherally. However, we do not see clear void inside the Orion BN/KL cloud but dense gas instead. That means the shell structure probably exists before the explosive outflow event occurs, then the gas in the shell structure is heated by the outflow. Moreover, the cause for the shell rotation is not clear. If the shell structure is related to the natal cloud where the radio or IR sources (e.g., BN, source n, and source I) were born, the shell rotation might result from the accretion process in the early star-forming stage. Nevertheless, this shell rotation might be also related to the explosive outflows, but more detailed investigations

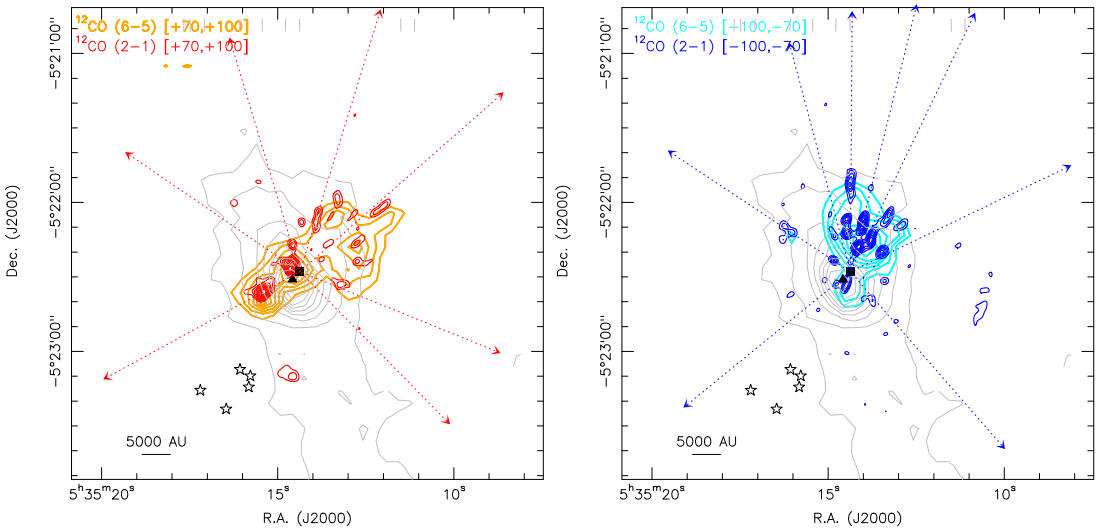

Figure 10.4 The very high velocity outflow emission in the ^{12}CO $J = 6 - 5$ transition overlaid with the SMA ^{12}CO $J = 2 - 1$ emission (Zapata et al. 2009) and the H_2 column density. Left panel shows the redshifted ^{12}CO emission integrated from +70 to +100 km s^{-1}, and right panel shows the blueshifted ^{12}CO emission integrated from −100 to −70 km s^{-1}. The ^{12}CO $J = 6 - 5$ emission is plotted in the orange and light blue contours running from 10% to 90% in steps of 10% of the peak intensity. The ^{12}CO $J = 2 - 1$ emission is plotted in red and blue contours from 30% to 90% in steps of 20% of the peak intensity. The H_2 column density is plotted in grey contours running from 10% to 90% in steps of 10% of the peak density (5.1×10^{22} cm^{-2}). The black square represents the explosive outflow center, and the black triangle represents the Orion Hot Core. The black stars mark the five Trapezium stars (θ^1 Ori A, B, C, D, and E).

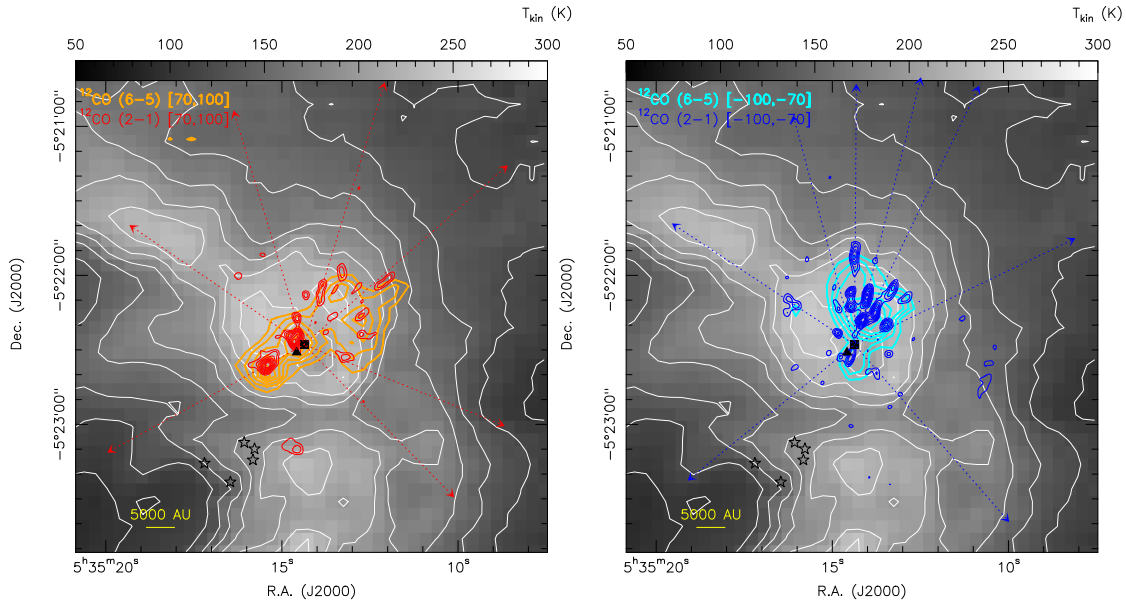

Figure 10.5 The very high velocity outflow emission in the ^{12}CO $J = 6 - 5$ transition overlaid with the SMA ^{12}CO $J = 2 - 1$ emission (Zapata et al. 2009) and the kinetic temperature images. Left panel shows the redshifted ^{12}CO emission integrated from +70 to +100 km s^{-1}, and right panel shows the blueshifted ^{12}CO emission integrated from −100 to −70 km s^{-1}. The ^{12}CO $J = 6 - 5$ emission are plotted in the orange and light blue contours running from 10% to 90% in steps of 10% of the peak intensity. The ^{12}CO $J = 2 - 1$ emission is plotted in red and blue contours running from 30% to 90% in steps of 20% of the peak intensity. The kinetic temperature is shown in the grey scale image and plotted in white contours from 100 to 240 K in steps of 20 K. The black square represents the explosive outflow center, and the black triangle represents the Orion Hot Core. The black stars mark the five Trapezium stars (θ^1 Ori A, B, C, D, and E).

are needed.

The age of this explosive outflow system is estimated to be about 500–1000 yr (Zapata et al. 2009; Lee & Burton 2000), similar to the age estimate for the stellar sources encounter event (see e.g., Rodríguez et al. 2005). Therefore, it is worth checking the voluminous chronicles of the ancient Chinese, where many sudden appearances of stellar activities were recorded. The book, *The History of Chinese Astronomy Volume III*[1], was consulted for this purpose. In addition, only the events whose positions are directly related to Orion are taken into account.

As a result, we found ten related events in the category of Comets and Ke-Sings (strange stars or guest stars), and seven of them are related to comets which are described to have clear tails and motions in a period of time. There are two events related to comets without clear descriptions,

[1]This book is written by Zun-Gui Chen, and the ages of the collected records in this book cover from about 2000 BCE to the early 20th century. The third volume of this book describes the astronomical events including eclipses, comets, planetary motions, and some unknown events.

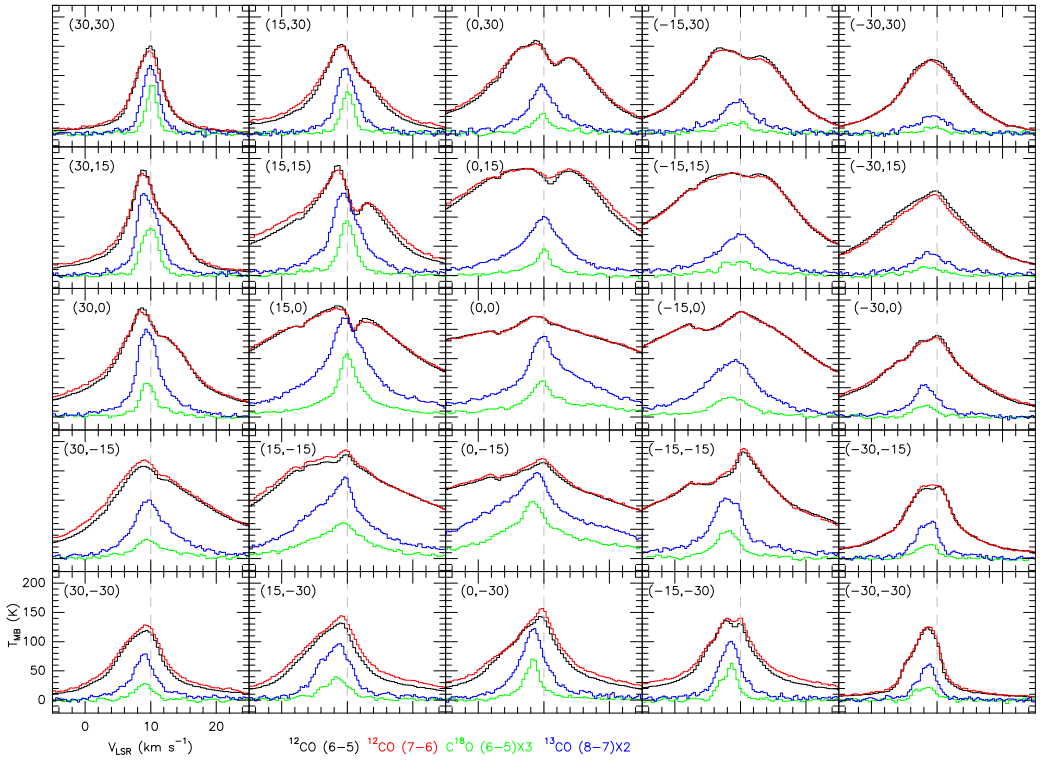

Figure 10.6 The CO isotopologic spectra in the Orion BN/KL region.

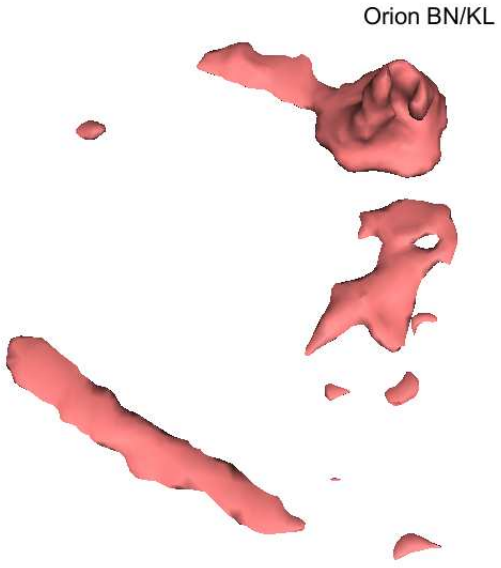

Figure 10.7 The OMC-1 3D view similar to Figure 10.1 but only shown in one isothermal surfaces of 150 K, where the shell structure in Orion BN/KL is clear.

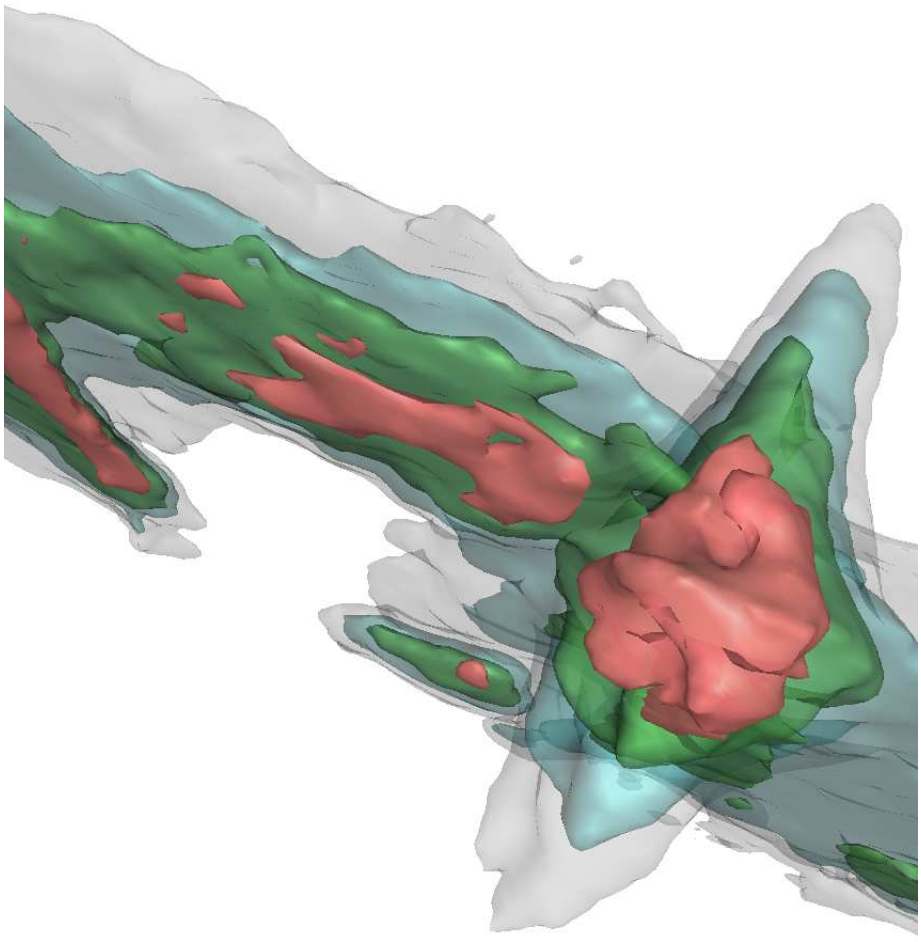

Figure 10.8 The same 3D view as Figure 10.1 with a different angle of view toward Orion BN/KL. The grey, blue, green, and red surfaces represent $T_{\rm MB}$ of 60 K, 90 K, 120 K, and 150 K, respectively. The redshifted component is shown in upper-right, and blueshifted one is shown in bottom-left.

Figure 10.9 Various types of Ke-Sings (strange stars or guest stars) in the ancient Chinese astronomical records (adopted from *The History of Chinese Astronomy Volume III*).

Table 10.2. The possible events associated with the explosive outflow in Orion BN/KL

Year	Description	Note
483 CE	In October, there is a cloud-like[a] Ke-Sing (guest star) as big as a dipper appeared in the east of Shen.[b]	might be a supernova
852 CE	In March, a comet[c] appears in the regions of Zi[d] and Shen.	
1639 CE	In fall, a comet[c] appears in Shen.	

[a] A gaseous or cometary shape.

[b] The ancient Chinese constellations are divided by 31 regions, including 28 "mansions" and 3 enclosures. "Shen", which literally means "three stars", is referred to the three bright stars of the Orion's Belt (ζ Ori, ϵ Ori, and δ Ori) at the beginning, and later includes another four stars (α Ori, β Ori, γ Ori, and κ Ori).

[c] It generally refers to cometary or gaseous objects.

[d] Three stars (e.g., λ Ori) located in the head of Orion.

and one suspicious event is shown in Table 10.2. Since the ancient Chinese records of comets and some other objects (e.g., novae, Lundmark 1921) are sometimes mixed together, it is difficult to distinguish those objects without a clear description of their shapes or motions in the sky (e.g., Fig. 10.9). The event in 483 CE (Table 10.2) is likely resulted from a supernova explosion suggested by Chen (1998) because this object seems to be very bright and extended. However, the Orion Nebula (M42) is usually located in the south of the Orion's Belt from an angle of an observer at a latitude of $\sim 40^\circ$ N, assuming that one observed from the Datong city, the capital of Northern Wei Dynasty ($386-534$ CE). Therefore, the event in 483 CE probably has nothing to do with the explosive outflow in Orion BN/KL. In a similar way, the event in 852 CE, which is also located differently in the sky from M42, is ruled out. As for the event in 1639 CE, this event occurred 370 years ago, and is close to the outflow start time of about 500 years estimated by Zapata et al. (2009). Nevertheless, since this event provided too little information, caution must be taken to connect two events together. Thus, from this investigation in ancient Chinese records, no conclusive events but one suspected event in 1639 CE is directly associated to the explosive outflow in Orion BN/KL. However, more evidence is needed to confirm the relation between this event and the outflow in Orion BN/KL. In addition, it is also possible that this explosion is not optically visible because of its relatively low energy of 10^{47} erg compared with the energy released by a supernova explosion ($\sim 10^{51}$ erg).

10.2 Orion South

Orion South is another highly active star-forming region in OMC-1, and seems to associated with many outflows in optical and radio molecular emission (see, e.g., O'Dell et al. 2009; Henney et al. 2007; Zapata et al. 2005; Schmid-Burgk et al. 1990). As shown in Figure 10.10, the average

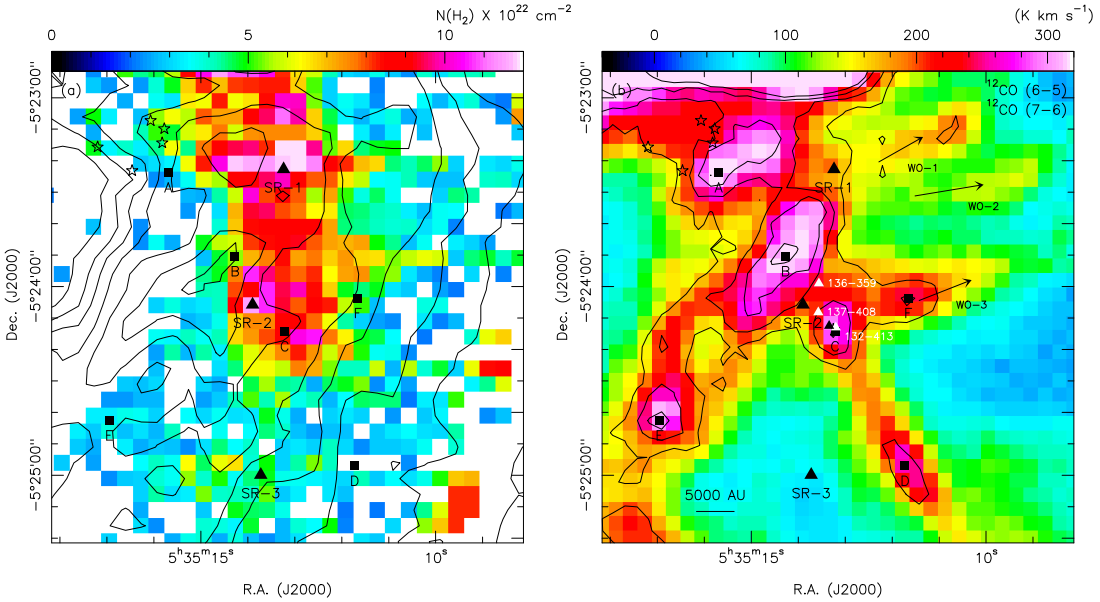

Figure 10.10 (a) The H_2 column density image of the Orion South region overlaid with the kinetic temperature contours running from 100 to 240 K in steps of 20 K. The Orion Sout Ridge components 1 to 3 are marked (SR-1, SR-2, SR-3) in black triangles, and the sources A−F are marked in black squares. (b) The same ^{12}CO $J = 6 - 5$ $[+11, +25]$ km s^{-1} image as Figure 8.24 overlaid with the $J = 7 - 6$ contours. Sources 137-408, 136-359, and 132-413 are marked in white triangles, and the associated outflows (WO-1, WO-2, and WO-3) are also marked.

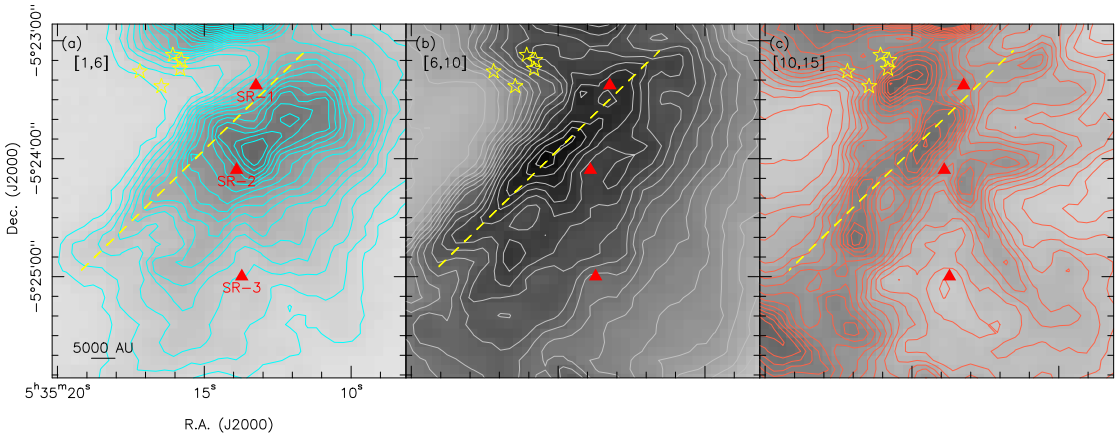

Figure 10.11 The ^{12}CO $J = 6 - 5$ channel maps of Orion South. (a) The ^{12}CO $J = 6 - 5$ emission integrated from 1 to 6 km s^{-1} shown in light blue contours running from 40 to 480 K km s^{-1} in steps of 20 K km s^{-1}. (b) The ^{12}CO $J = 6 - 5$ emission integrated from 6 to 10 km s^{-1} shown in grey contours running from 40 to 760 K km s^{-1} in steps of 40 K km s^{-1}. (c) The ^{12}CO $J = 6-5$ emission integrated from 10 to 15 km s^{-1} shown in light blue contours running from 40 to 480 K km s^{-1} in steps of 20 K km s^{-1}. The Orion Sout Ridge components 1 to 3 are marked in red triangles, and the yellow dashed-lines represent the suggestive PDR interface in Orion South.

H_2 column density in this region is $\sim 5 \times 10^{22}$ cm^{-2} with a temperature of ~ 180 K in the LTE calculation. The average H_2 number density is estimated to be $\sim 2 \times 10^5$ cm^{-3} assuming a size of $40''$, which also agrees well with the RADEX modeling result (Fig. 9.3). However, the difference in the distribution of dense and warm gas is obvious from Figure 10.10 (a), where the high kinetic termperature area (i.e., source B) appears to form a straight shape facing the O type star θ^1 Ori C, but the high density regions simply follow the north-south dense ridge. The offset between the dense and high temperature areas in Orion South indicates that θ^1 Ori C illuminates the surface of Orion South and has developed an inclined PDR there, e.g., the temperature decreases toward the southwest, and three dense ridge components (SR-1, SR-2, and SR-3) lie in the southwest of the temperature peaks.

PDR in Orion South

Figure 10.11 shows the channel maps of ^{12}CO $J = 6 - 5$ in Orion South, and the straight shape of the ^{12}CO emission facing θ^1 Ori C is clearly seen. It is thus possible that this straight structure is part of the PDR $H^+/H^0/H_2$ interface. This suggestive PDR interface is most pronounced in the ^{12}CO emission at $V_{\rm LSR}$ of ~ 8 km s^{-1}. In addition, the stratified structure of this PDR is also seen in Figure 10.12, where the emission from the carbon recombination C91α line is offset from the ^{12}CO emission, and is close to θ^1 Ori C. Furthermore, the offset of the C^{18}O emission is also clear around SR-2. Figure 10.13 shows the position-intensity diagrams corresponding to the two cuts in Figure

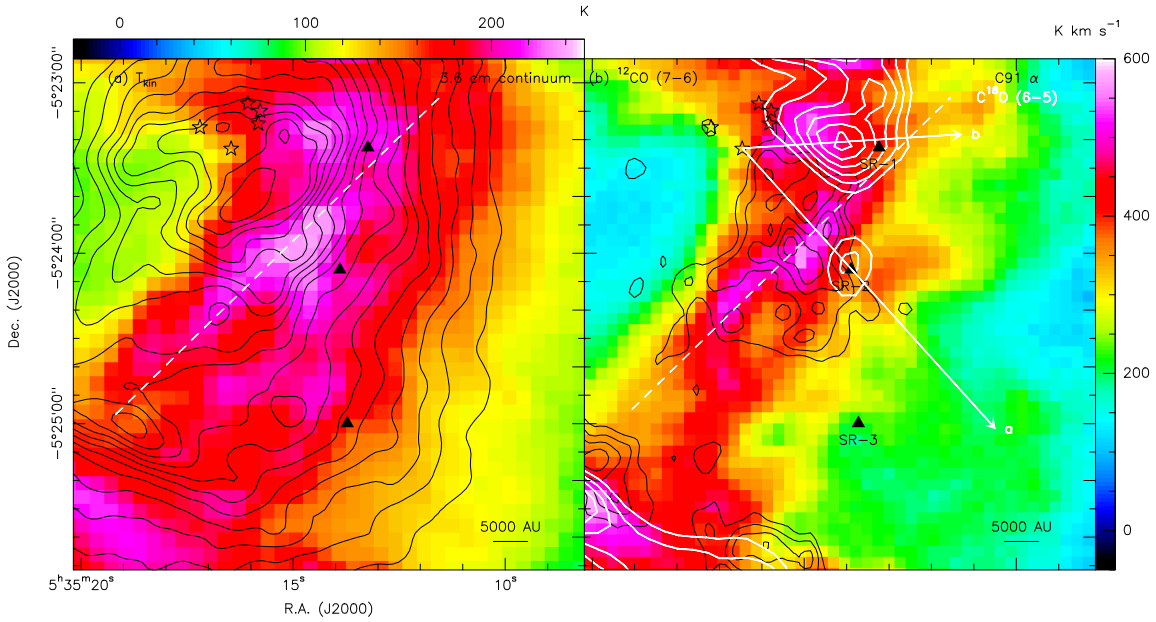

Figure 10.12 (a) The kinetic temperature image overlaid with the VLA-GBT 3.6 cm continuum emission in black contours running from 15% to 95% in steps of 5% of the peak intensity (1.82 Jy beam^{-1}). (b) The ^{12}CO $J = 7 - 6$ [+9,+12] km s^{-1} image overlaid with the VLA C91α emission (Wyrowski et al. 1997) in black contours (30%, 45%, 60%, 75% and 90% of the peak intensity 37.8 mJy beam^{-1}), and the smoothed C^{18}O $J = 6 - 5$ emission ($\sim 17''$) in white contours running from 20 to 55 K km s^{-1} in steps of 5 K km s^{-1}.

10.12, in which most lines show multiple peaks. In Figure 10.12 (a), the 3.6 cm continuum emission has two peaks that coincide with the peaks of the C91α line and ^{12}CO lines at offsets of $43''$ and $63''$, respectively. The ^{13}CO and C^{18}O emission, however, has an offset about $5'' - 8''$ from the second peak of the ^{12}CO lines. The offsets among these lines in cut (b) are less obvious. Because of outflow activities, the line widths in Orion South are wider compared to that in the Orion Bar. Therefore, the PDR in Orion South covers a much broader velocity range and becomes more complicated due to its geometry. For example, Figure 10.14 shows the two position-intensity cuts according to different velocity ranges of the ^{12}CO emission. For both cuts, the redshifted ^{12}CO emission has a very tight correlation with the C91α carbon recombination line, which suggests a mixed-up H^0/H_2 zone in the Orion South region. Additionally, the ^{12}CO emission peak is shifted $\sim 60''$ from the blueshifted emission toward the redshifted emission. This shift indicates a tilted illuminated surface around the Orion South Ridge 1.

Outflows in Orion South

As described in §8.3, there are three dense components (i.e., SR-1, SR-2, and SR-3) along the north-south ridge in the Orion South region. For SR-1, the clear shift at $\sim 7 - 11$ km s^{-1} for the ^{12}CO,

^{13}CO, and C^{18}O emission peaks is likely due to the emission stratification in the PDR interface with an inclination angle, as discussed above. In addition, the western outflows WO-1 and WO-2 seem to have emanated from this region, and are likely associated with the western larger-scale filament seen in the 350 μm dust continuum (Lis et al. 1998) and NH_3 emission (Wiseman & Ho 1998). The SR-2 region, which is associated with a cluster of radio sources (Zapata et al. 2004) and NIR sources (Gaume et al. 1998), coincides with a CS clump (source CS3 in Mundy et al. 1986) within $\sim 5''$, and contains at least two hot molecular cores, sources 139-409 and 134-411 (Zapata et al. 2007). The peak H_2 column density in the SR-2 region is 1.2×10^{22} cm^{-2} with a kinetic temperature about 210 K. The outflow WO-3 seems to come from this dense region, and is probably the origin of the Herbig-Haro (HH) object HH 269 seen in the [O III] line (Henney et al. 2007; Walter, O'dell, Hu, & Dufour 1995). Source B is located at one side of SR-2 in the PDR interface (Figs. 10.10 and 10.11), and is likely an illuminated part of the clump in SR-2. In addition, source C, which is part of SR-2, coincides with sources 132-413 and 134-411, and an FIR source FIR4 (Mezger, Zylka, & Wink 1990).

It has been proposed that the outflow Ori-S6 is emanating from the region of CS3/FIR4 (Schmid-Burgk et al. 1990). However, a recent SO observation by (Zapata et al. 2010) suggests that the radio source 139-409, which is $5\farcs5$ in the southwest of source 137-408, is the origin of this collimated outflow. However, there is a difference in a position angle of $\sim 15^\circ$ between the ^{12}CO outflow and the SO emission, which means that a deflection is needed to explain that they are the same outflow. Zapata et al. (2010) proposed that the dense clump (source C) might cause the deflection of Ori-S6, but the interaction between them is not clear.

10.3 Orion Bar

Figure 10.15 shows the density and temperature distribution of the Orion Bar region, where three clumps are seen. The eastern and central clumps are clearly associated with the dense clumps showing the H^{13}CN emission. The average H_2 column density in the Orion Bar region is 4×10^{22} cm^{-2} with an average kinetic temperature of about 160 K. The H_2 column density is close to the value of 6.8×10^{22} cm^{-2} estimated by van der Wiel et al. (2009) using the C^{18}O $J = 2 - 1$ line, adopting a higher ^{12}CO abundance of 1.1×10^{-4}. Our kinetic temperature is also consistent with the result of Batrla & Wilson (2003) who estimated a kinetic temperature of ~ 150 K using the inversion lines of ammonia. The RADEX modeling results (Fig. 9.4) show a relatively high temperature due to larger line widths (i.e., 5 km s^{-1} for ^{12}CO $J = 6 - 5$) adopted in the model compared to the observed ^{12}CO line width of $\sim 3 - 4$ km s^{-1}. Besides, most of gas in the Orion Bar region has an H_2 number density of $10^4 - 10^5$ cm^{-3}, and some clumps have densities up to $\sim 10^6$ cm^{-3} (Fig. 9.4), which is also consistent with the densities of interclump and clump gas (Hogerheijde, Jansen, & van Dishoeck 1995).

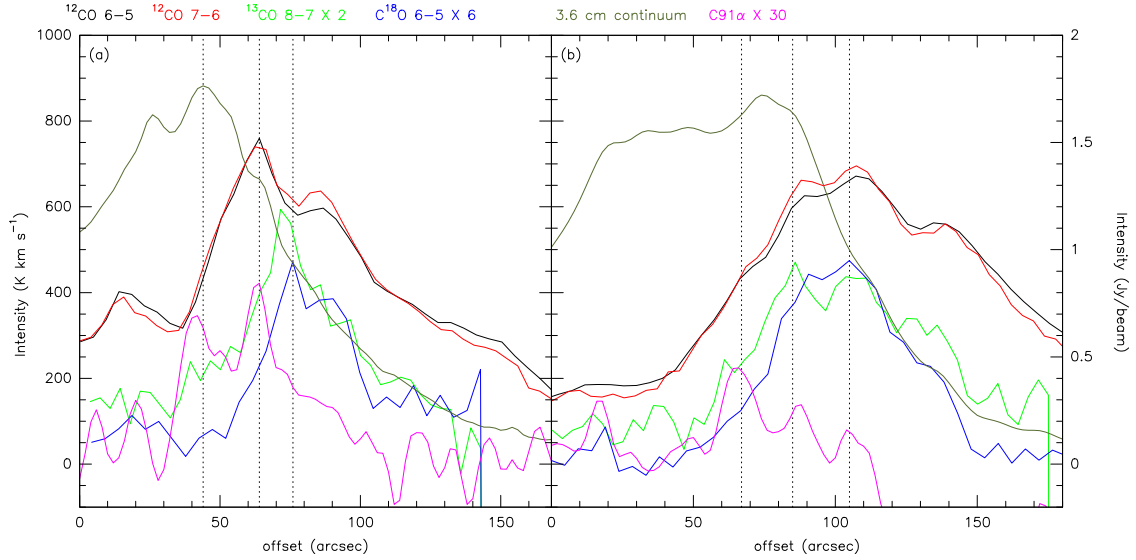

Figure 10.13 Two position-intensity diagrams of the CO isotopologic emission (in K km s^{-1}) together with the VLA-GBT 3.6 cm continuum and the C91α emission from Wyrowski et al. (1997). The ^{12}CO lines are integrated from 6 to 10 km s^{-1}. The ^{13}CO and C^{18}O lines are shown in $[+5, +15]$ and $[+4, +12]$ km s^{-1}, respectively. The 3.6 cm continuum and C91α emissions are shown in the Jy beam^{-1} unit. The position angles of the cuts correspond to the slices shown in Figure 10.12. The zero offsets are chosen at θ^1 Ori C.

The Meudon/RADEX modeling

As mentioned in §8.3, we have seen a clear stratified structure in different emission lines in the Orion Bar. Therefore, it is of interest to investigate this feature by using a code developed for the modeling of PDRs. We first used the Meudon PDR code (Le Petit et al. 2006) to solve the radiative transfer in UV; at the meantime, the thermal balance is also computed by the program, where both heating and cooling processes are taken into account. Chemistry is calculated, and the abundances of different species are derived by the program. Hence, with the density, temperature, and abundance information, we can compute the line intensities for different species using the RADEX program. Then, the modeling results can be directly compared with our data.

Only general description of the Meudon PDR code is given here. And, see Le Petit et al. (2006) for the code structure and numerical details. The Meudon PDR code is only computed in one-dimensional steady-state approximation with a plane-parallel slab geometry, where gas and dust are illuminated by UV photons coming from both sides of the cloud. The computation is carried out iteratively at each point of the cloud by solving radiative transfer in UV, chemistry, and thermal balance, and will proceed until a convergence criterion is reached. In the thermal balance calculation, both the heating from the photoelectric effect on grains and the cooling from the radiative transition of various species are considered. In addition, this program considers mainly

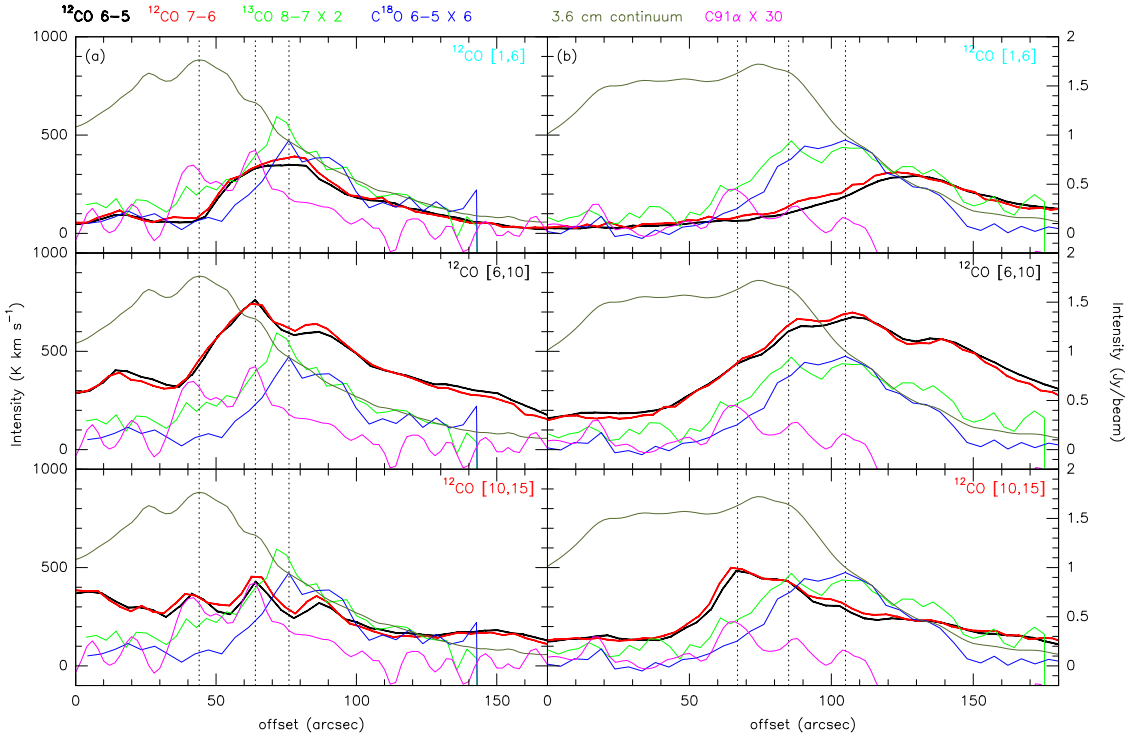

Figure 10.14 The similar position-intensity diagrams as Figure 10.13 compared with the red- and blueshifted ^{12}CO emission. The ^{13}CO and C^{18}O line emission is the same as Figure 10.13, and the ^{12}CO lines are shown in [+1, +6], [+6, +10], and [+10, +15] km s^{-1}. The 3.6 cm continuum and C91α emission are shown in the Jy beam^{-1} unit. The position angles of the cuts correspond to the slices shown in Figure 10.12. The zero offsets are chosen at θ^1 Ori C.

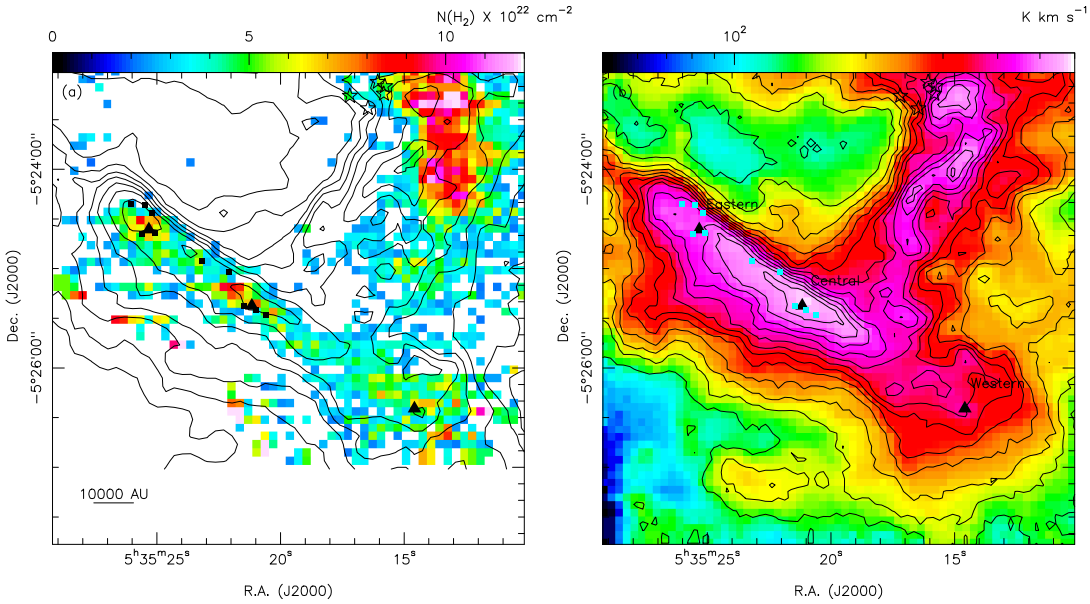

Figure 10.15 (a) The H_2 column density image of the Orion Bar and South regions overlaid with the kinetic temperature contours running from 100 to 240 K in steps of 20 K. The three main clumps are marked in black triangles, and the squares represent the $H^{13}CN$ clumps from Lis & Schilke (2003). (b) The same ^{12}CO $J = 6 - 5$ $[+9, +12]$ km s^{-1} image overlaid with the $J = 7 - 6$ contours running from 120 to 480 K km s^{-1} in steps of 40 K km s^{-1}.

two-body reactions or three-body reactions involving two atomic hydrogen atoms in chemistry. H_2 formation and photodestruction processes are also taken into account. The spatial coordinate used in the Meudon code is the dust optical depth τ_V, and path length can be calculated via

$$L = \frac{N_H}{n_H} = \frac{C_D}{n_H} \times \frac{A_V}{R_V}, \tag{10.1}$$

where N and n_H is the total hydrogen column density and number density, respectively. C_D is the ratio between the quantity of gas on dust in the cloud, and a standard Galactic value of 5.8×10^{21} cm^{-2} mag^{-1} is adopted. R_V is the ratio between total extinction and color excess ($R_V = A_V/E_{B-V}$), and the standard value of 3.1 is adopted in the program.

In our Orion Bar models, the distance from the Orion Bar to θ^1 Ori C is fixed at 0.18 pc, which is estimated from the 3.6 cm free-free continuum emission by adopting the OMC-1 distance of 414 pc (Menten et al. 2007). The radiation fields are determined by θ^1 Ori C (O6 star) from one side, and the diffuse interstellar radiation field from the other side. The Galactic line-of-sight extinction curve is used, and the dust-to-gas mass ratio is 100, where a grain mass density of 3 g cm^{-3} is adopted. The $[^{16}O]/[^{18}O]$ ratio is fixed at 490, and $[^{12}C]/[^{13}C]$ is fixed at 60 (e.g. Boreiko & Betz 1996; Wilson & Matteucci 1992). The purpose of these modelings is not to look for an exact fitting to the data but to have a general understanding for the future modeling. Therefore, several different density profiles are tested, which include both constant density profiles and Gaussian density profiles.

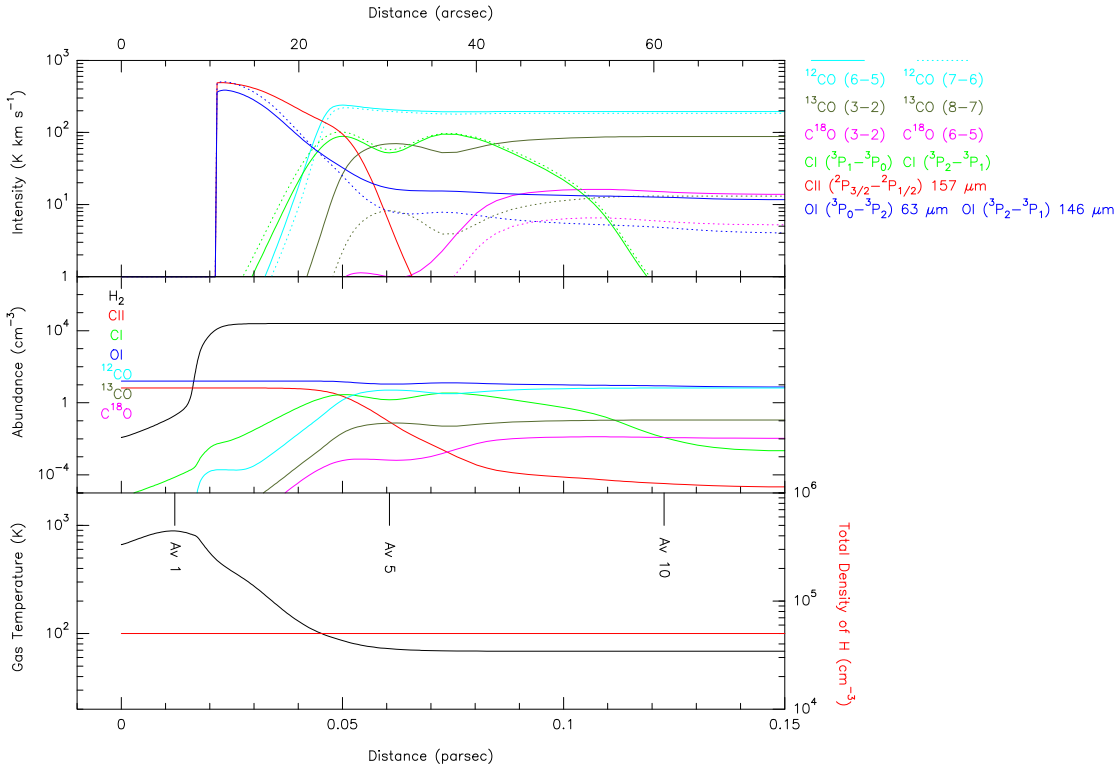

Figure 10.16 The results of the Meudon/RADEX modeling with a constant density of 5×10^4 cm^{-3}. The gas temperature and total H density are shown in the lower panel. The abundances of various species are shown in the middle panel, and the calculated line intensities are shown in the upper panel.

The main output results of gas temperatures, H_2 number densities, and abundances (in cm^{-3}) of various species from the Meudon program will be used as input parameters in the following RADEX calculation. The geometry of a homogeneous slab is chosen for the RADEX modeling, assuming that the thickness of the Bar is 0.1 pc (Pellegrini et al. 2009). Once the column densities for various species at a given position are known, then the line intensities are calculated by the RADEX program. The Meudon/RADEX modeling results are shown in Figures 10.16–10.17 and E.1–E.5.

The Meudon/RADEX results for a constant density profile (5×10^4 cm^{-3}) are shown in Figure 10.16, where a clear emission stratification is seen. We clearly see the C$^+$/C/CO interface at $A_V \simeq 4$ and the H_2-CO region at $A_V \gtrsim 5$. The ^{12}CO intensity attains its maximum around 25″ from the ionization front, and the [C I] emission shows two peaks due to self-shielding (see e.g., Hollenbach & Tielens 1997). The ^{12}CO self-shielding (see the abundance figure) is less pronounced in the line intensity. Similar self-shielding feature is seen in the ^{13}CO and C^{18}O lines, where the first peak of the C^{18}O emission is barely seen. The offset between the ^{12}CO emission peak and the first peak of the ^{13}CO emission is about 5″, and the second peak of the ^{13}CO and C^{18}O emission lies $\sim$ 15″ deeper in the cloud. However, the flat emission profiles of CO isotopologues at large A_V

is mainly due to a constant gas temperature of about 70 K and a constant density. The reason for a constant gas temperature deep inside the cloud is probably because the Meudon code does not compute a detailed energy balance for grains but uses an empirical expression (Le Petit et al. 2006).

Figure 10.17 shows the Meudon results for a Gaussian density profile. The stratification is similar as in the constant density model shown in Figure 10.16, but the second peaks of the ^{13}CO and C^{18}O emission are dominated by the density peak at $A_V = 20$. In addition, it is noteworthy that the [O I] 146 μm emission shows two peaks at where the second peak is stronger than the 63 μm emission. It seems that the increasing intensity of the 63 μm line is also due to the increase of density. The offset of the ^{12}CO peak emission from the ionization front is close to our data (Fig. 8.35 c) at $\sim 20''$, and the offset of the emission peak between ^{12}CO and its isotopologues (i.e., ^{13}CO and C^{18}O) is $\sim 10''$ which also agrees with our data. However, this model does not show any position offset between the low-J and higher-J transitions of ^{13}CO and C^{18}O, probably because the thermal balance is not well-modeled inside the dense region. Besides, according to our data (Fig. 8.35 c), the higher-J intensities for both ^{13}CO and C^{18}O are stronger than the low-J intensity, which indicates a high excitation in the Orion Bar. However, the Meudon results show a relatively low temperature of about 70 K, which is only half of the estimated kinetic temperature ($\sim$ 160 K) of the Orion Bar. The model by van der Wiel et al. (2009) using a different PDR code shows an even lower temperature of $\sim 20 - 40$ K. Because of the lower temperatures, their calculated line intensities are three times smaller in our data. Even though the thickness of the Bar increases to 0.2 pc, the intensities of various species only increase by less than 10% (not shown). Therefore, it seems the temperature here is more critical than the density in the intensity comparison.

In short, the Meudon/RADEX modeling results reveal a clear emission stratification in the Orion Bar, but the model with a Gaussian density profile shows better agreement with the data. However, the intensities calculated in the model are smaller than the data due mainly to the low temperature predicted for the Orion Bar. Therefore, more investigations and detailed modeling are needed to understand the temperature problem mentioned above, and the higher-J transitions of CO isotopologues will be essential to constrain the excitation in future modeling.

Last but not least, it is interesting to compare the Orion Bar with Orion South, where many star-forming activities are seen. Orion South and the Bar have an average H_2 density of $\sim 10^5$ cm^{-3} and a similar kinetic temperature of $160 - 180$ K. It seems that θ^1 Ori C has a strong influence on both regions creating PDRs. The biggest difference is that, while Orion South is located at the north-south ridge of OMC-1, and the Orion Bar seems to extend 1.5 pc to the southwestern part of the Orion Nebula seen in the optical image (see e.g., Henney et al. 2007). It is also known that some dense clumps with densities up to $\sim 6 \times 10^6$ cm^{-3} are found in Orion Bar (Lis & Schilke 2003), but it is not clear whether those clumps will collapse. Therefore, the lack of star-forming activity in the Orion Bar is probably just a matter of time. There is a time lag for star formation in the Orion Bar compared with Orion South, which is unlikely due to the influence from θ^1 Ori C, given a similar distance. Therefore, the location of Orion South in the ridge is probably the key to understand the

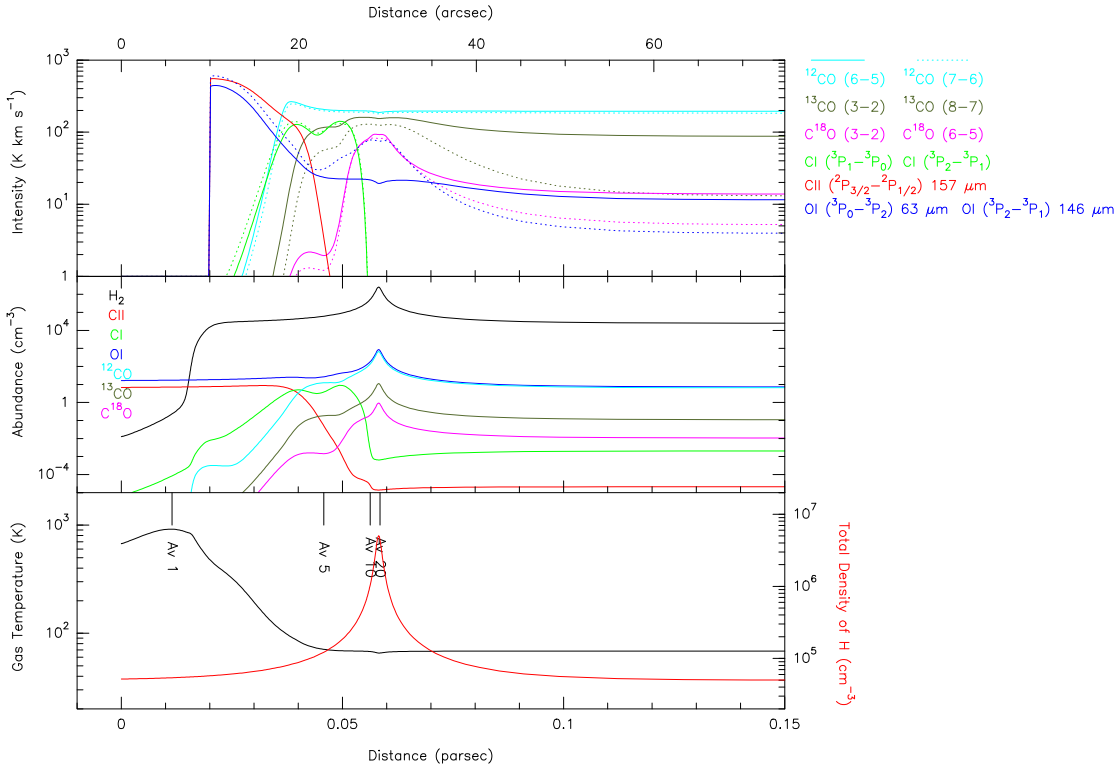

Figure 10.17 The results of the Meudon/RADEX modeling with a Gaussian density profile whose minimum and maximum density is 5×10^4 cm^{-3} and 5×10^6 cm^{-3}. The density peak is located at $A_{\rm V} = 20$. The gas temperature and total H density are shown in the lower panel. The abundances of various species are shown in the middle panel, and the calculated line intensities are shown in the upper panel.

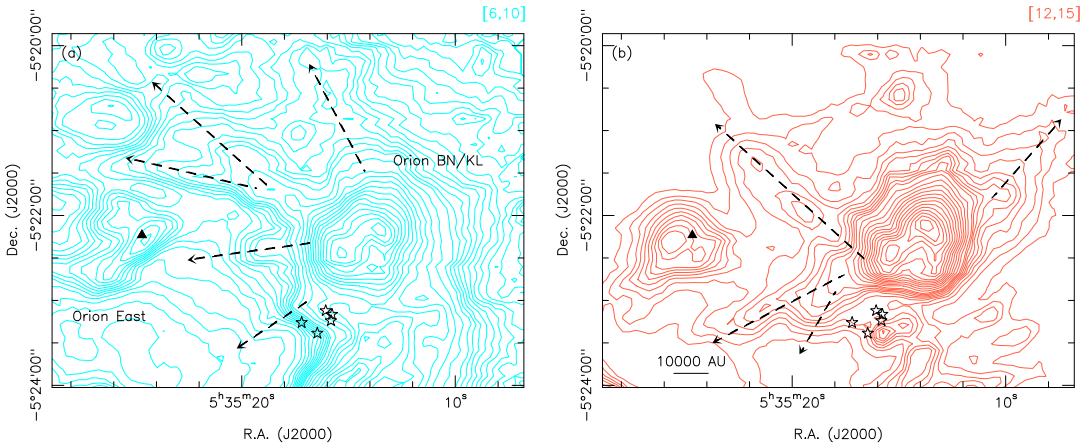

Figure 10.18 (a) The ^{12}CO $J = 6 - 5$ $[+6, +10]$ km s^{-1} emission of the northern part of OMC-1 shown in blue contours running from 40 to 400 K km s^{-1} in steps of 20 K km s^{-1}, and the subsequent contours running from 420 to 1000 K km s^{-1} in steps of 40 K km s^{-1}. (b) The ^{12}CO $J = 6 - 5$ $[+12, +15]$ km s^{-1} emission of the northern part of OMC-1 shown in red contours running from 40 to 220 K km s^{-1} in steps of 20 K km s^{-1}, and the subsequent contours running from 260 to 800 K km s^{-1} in steps of 40 K km s^{-1}. The black triangle represents the ^{12}CO $J = 6 - 5$ emission peak in Orion East, and the black dashed-lines represent the suggestive outflows.

different star-forming behaviors in both regions. On the other hand, if the clumps in the Orion Bar are not going to form stars in the future, then the similar question raises itself : Why does the Orion Bar fail to form stars even if its density and temperature are similar to the values found in Orion South? It is important to have more detailed study in the Orion Bar and South, and to seek a link between these two regions.

10.4 Orion East

Orion East has a peak H_2 column density of $\sim 2 - 3 \times 10^{22}$ cm^{-2} with a temperature of about 150 K. This indicates a less dense but still warm environment. As mentioned in §8.4, Orion East is also a PDR heated by FUV photons from θ^1 Ori C. The H_2 number density of Orion East is estimated to be $\sim 1 \times 10^5$ cm^{-3} assuming a size of 30″. However, the RADEX modeling results show a high density of $10^5 - 10^6$ cm^{-3} (Fig. 9.4).

Figure 10.18 shows several outflows emanating from the Orion BN/KL region, some of them seem to affect Orion East. However, it is not clear if these large-scale outflows are associated with the explosive outflow discussed before, since the ^{12}CO $J = 2-1$ emission excited by the latter outflow has only been detected in a range of $\sim 60''$ from the explosion center (see Zapata et al. 2009). However, the HH objects associated with the H_2 fingers extend more than 2′ from the explosion center. Hence, it is possible that the ^{12}CO outflows we see are actually related to the explosive outflow in Orion

BN/KL, and these outflows might interact with Orion East. Apart from the straight shape seen in the ^{12}CO emission, a cone-like structure is also shown inside Orion East (see §8.5). This cone-like structure might result from the explosive outflow in the Orion BN/KL region. The high temperature of Orion East is likely due in large part to its PDR nature, since there is no evidence that Orion East has embedded heating sources. However, a high-resolution observation is needed to better understand this interesting region in which both strong UV radiation and outflows play important roles.

11

OMC-1 Conclusions

The structure of OMC-1 consists of two main parts: One is the north-south dense ridge where most of the present star-forming activities take place (i.e., Orion BN/KL and Orion South). The other component includes most of the PDRs where the gas is heated by FUV photons from θ^1 Ori C (i.e., the Orion Bar and Orion East). For these two different reasons, outflows, FUV heating, and highly excited ^{12}CO emission are seen thoughout the whole OMC-1 region with an H_2 density of $10^4 - 10^6$ cm^{-3} and a kinetic temperature of $\sim 150 - 200$ K. The gas mass in OMC-1 is estimated to be about $200 - 300$ M$_\odot$.

In Orion BN/KL, the explosive outflow is well seen in the APEX ^{12}CO mid-J emission, and the high-velocity ^{12}CO $J = 6 - 5$ emission agrees well with the shock excited CO emission seen in the high angular SMA images. A shell structure around the Orion BN/KL region is also seen, due in part to self-absorption, but mainly reflecting the true structure of the shell. Besides, evidence for the rotation of this shell is presented which might be related to the natal cloud where BN, source n, and source I are born. However, it is not clear whether the shell structure is associated with the explosive outflow, but it seems possible that the shell was formed earlier and heated by the outflow later. Besides, ancient Chinese records are investigated, and one suspicious event in 1639 CE is found. Although the age of 370 years is close to 500 years estimated for a disintegration of a massive star system and from the SMA high-resolution observations, a conclusion cannot be drawn due to the little information on this event provided in the historical record. Therfore, more investigations are needed to determine the starting time of this outflow. In addition, the energy released in this outflow is estimated to be $\sim 10^{47}$ erg.

Orion South is also an active star-forming region which contains several outflows, and most of the outflows seem to be associated with the dense ridge. The famous outflow Ori-S6 is seen in the ^{12}CO $J = 6 - 5$ and $J = 7 - 6$ images, and the highly excited ^{12}CO emission results from the shock heating. The highly collimated outflow located at SR-2 is also seen in the highly excited ^{12}CO emission, and has an outflow velocity up to about ± 80 km s^{-1} with a kinetic energy of $\sim 10^{47}$ erg

comparable to the energy of the explosive outflow in Orion BN/KL. Besides, Orion South is also a PDR illuminated by FUV photons from θ^1 Ori C. Since the emission in Orion South covers a larger velocity range, the emission stratification of different molecules also changes in different velocities. Besides, the different distributions of the gas density and the kinetic temperature in Orion South indicate that this region is strongly heated by θ^1 Ori C, where the temperature peaks are closer to θ^1 Ori C compared to the density peaks.

As for the well-studied PDR, the Orion Bar, we carried out some general modelings using the Meudon code together with the RADEX program to investigate the stratified structure seen in the data. Both constant density and Gaussian density profiles are modeled, and the results from a Gaussian density profile ($5 \times 10^4 - 5 \times 10^6$ cm^{-3}, $A_{\rm V} = 20$) agree well with the data. However, the calculated line intensities are about three times lower than the measured values due to a lower gas temperature (about 70 K). Therefore, more detailed modelings are needed to investigate the temperature issue in the Orion Bar.

Apart from the three well-known regions mentioned above, the less-studied Orion East is a small patch of cloud located in the northeast of the Trapezium stars. Orion East is shown to have a cone-like structure, and seems to be influenced heavily by θ^1 Ori C and probably also the explosive outflow in Orion BN/KL. The straight edges seen in the ^{12}CO emission of Orion East are likely due to FUV photons shaping this region. In addition, the cone-like structure might result from the explosive outflow extending about two arcminutes. More observations will help to clarify the roles played by the UV radiation and outflows in this region.

12

Summary

In this thesis, a detailed molecular line study of the Galactic starburst template W49A ($d = 11.4$ kpc) and the well-known massive star forming region OMC-1 ($d = 414$ pc) is presented. In W49A, a pronounced shell-structure has been identified in the MIR and molecular emission. The observations imply that these expanding shells trigger the formation of massive stars in a short period of time ($\sim 10^5$ yr). A further feature of large-scale gas ejections is seen in the W49 complex, and it seems to share a common center with the expanding shells. However, the cause of both events which release a total energy of few times 10^{50} erg is not clear, and more observations are thus needed. In addition, several kinds of molecular emission are obtained toward W49A. In close examination, together with the RADEX modeling, the HCO^+/HCN and HNC/HCN intensity ratios are found to be highly dependent on the angular resolution and the source environment. Besides, the intensity ratios among these molecular emissions do not directly probe their abundance ratios. Hence, one must bear in mind these caveats when using their intensity ratios to distinguish between PDRs and XDRs. Furthermore, no clear correlation between the hard X-ray emission and SiO emission is seen in W49A, which indicates that the mechanism responsible for the hard X-ray emission is different from the shock/outflow activities which enhance the SiO gas phase abundance.

As for OMC-1, highly excited CO emssion is detected, and the calculated temperature and density reveal a generally warm (50–200 K) and dense ($10^4 - 10^6$ cm^{-3}) environment. The high temperature of this region is determined mainly by FUV photons from the O6 star θ^1 Ori C which heats the cloud and creates PDRs in the region, i.e., in Orion South, the Orion Bar, and Orion East. Several outflows which have been detected in low-J molecular emission in Orion BN/KL and South are also seen in the higher-J CO emission, i.e., explosive outflows in Orion BN/KL and Ori-S6 in Orion South. This proves the ubiquitous role of outflows/shocks in star-forming regions. Very different morphologies of these outflows reveal a complex mechanism responsible for them.

Hence, the study in these two sources provides a clear picture of triggered massive star formation and the strong feedbacks, e.g., associated outflows, stellar winds, and UV radiation, from

the newly born stars into their environments on different scales.

Bibliography

Aalto, S., Polatidis, A. G., Hüttemeister, S., & Curran, S. J. 2002, A&A, 381, 783

Aalto, S., Spaans, M., Wiedner, M. C., üttemeister, S. 2007, A&A, 464, 193

Allen, D. A., & Burton, M. G. 1993, Nature, 363, 54

Alves, J., & Homeier, N. 2003, ApJ, 589, L45

Baan, W. A., Henkel, C., Loenen, A. F., Baudry, A., & Wiklind, T. 2008, A&A, 477, 747

Bachiller, R., Pérez Gutiérrez, M., Kumar, M. S. N., & Tafalla, M. 2001, A&A, 372, 899

Bally, J., O'Dell, C. R., & McCaughrean, M. J. 2000, AJ, 119, 2919

Bally, J., & Zinnecker, H. 2005, AJ, 129, 2281

Batrla, W., & Wilson, T. L. 2003, A&A, 408, 231

Beaumont, C. N., & Williams, J. P. 2009, arXiv:0912.1852

Bechtel, H. A., Steeves, A. H., & Field, R. W. 2006, ApJ, 649, L53

Becker, R. H., White, R. L., & Proctor, D. D. 1992, AJ, 103, 544

Becklin, E. E., & Neugebauer, G. 1967, ApJ, 147, 799

Beckwith, S., Persson, S. E., Neugebauer, G., & Becklin, E. E. 1978, ApJ, 223, 464

Benjamin, R. A., et al. 2003, PASP, 115, 953

Beuther, H., & Nissen, H. D. 2008, ApJ, 679, L121

Beuther, H., Churchwell, E. B., McKee, C. F., & Tan, J. C. 2007, Protostars and Planets V, 165

Beuther, H., et al. 2004, ApJ, 616, L31

Beuther, H., et al. 2005, ApJ, 632, 355

Boreiko, R. T., & Betz, A. L. 1996, ApJ, 467, L113

Brogan, C. L., & Troland, T. H. 2001, ApJ, 550, 799

Buckley, H. D., & Ward-Thompson, D. 1996, MNRAS, 281, 294

Chen, Z.-G. 1998, The History of Chinese Astronomy Volume III, by Zun-Gui Chen. ISBN 957-9364-27-3. Published by Wen Hai Foundation for Culture & Education, Taipei, Taiwan, 1998.,

Churchwell, E., et al. 2006, ApJ, 649, 759

Cohen, R. J., Gasiprong, N., Meaburn, J., & Graham, M. F. 2006, MNRAS, 367, 541

De Pree, C. G., Mehringer, D. M., & Goss, W. M. 1997, ApJ, 482, 307

De Pree, C. G., Wilner, D. J., Goss, W. M., Welch, W. J., & McGrath, E. 2000, ApJ, 540, 308

Dickel, H. R., & Goss, W. M. 1990, ApJ, 351, 189

Doeleman, S. S., Lonsdale, C. J., & Pelkey, S. 1999, ApJ, 510, L55

Fazio, G. G., et al. 2004, ApJS, 154, 10

Friedel, D. N., & Snyder, L. E. 2008, ApJ, 672, 962

Gao, Y., & Solomon, P. M. 2004, ApJ, 606, 271

García-Burillo, S., et al. 2006, ApJ, 645, L17

Gaume, R. A., Wilson, T. L., Vrba, F. J., Johnston, K. J., & Schmid-Burgk, J. 1998, ApJ, 493, 940

Genzel, R., et al. 1978, A&A, 66, 13

Genzel, R., Reid, M. J., Moran, J. M., & Downes, D. 1981, ApJ, 244, 884

Genzel, R., & Stutzki, J. 1989, ARA&A, 27, 41

Graciá-Carpio, J., García-Burillo, S., Planesas, P., & Colina, L. 2006, ApJ, 640, L135

Graciá-Carpio, J., García-Burillo, S., Planesas, P., Fuente, A., & Usero, A. 2008, A&A, 479, 703

Graf, U. U., Genzel, R., Harris, A. I., Hills, R. E., Russell, A. P. G., & Stutzki, J. 1990, ApJ, 358, L49

Greaves, J. S., Ohishi, M., & Nyman, L.-A. 1996, A&A, 307, 898

Greenhill, L. J., Gezari, D. Y., Danchi, W. C., Najita, J., Monnier, J. D., & Tuthill, P. G. 2004, ApJ, 605, L57

Greenhill, L. J., Gwinn, C. R., Schwartz, C., Moran, J. M., & Diamond, P. J. 1998, Nature, 396, 650

Greve, T. R., Papadopoulos, P. P., Gao, Y., & Radford, S. J. E. 2009, ApJ, 692, 1432

Gómez, L., Rodríguez, L. F., Loinard, L., Lizano, S., Poveda, A., & Allen, C. 2005, ApJ, 635, 1166

Güsten, R., et al. 2006, Proc. SPIE, 6267,

Gwinn, C. R., Moran, J. M., & Reid, M. J. 1992, ApJ, 393, 149

Henney, W. J., O'Dell, C. R., Zapata, L. A., García-Díaz, M. T., Rodríguez, L. F., & Robberto, M. 2007, AJ, 133, 2192

Herrmann, F., Madden, S. C., Nikola, T., Poglitsch, A., Timmermann, R., Geis, N., Townes, C. H., & Stacey, G. J. 1997, ApJ, 481, 343

Hogerheijde, M. R., & van der Tak, F. F. S. 2000, A&A, 362, 697

Hogerheijde, M. R., Jansen, D. J., & van Dishoeck, E. F. 1995, A&A, 294, 792

Hollenbach, D. J., & Tielens, A. G. G. M. 1997, ARA&A, 35, 179

Homeier, N. L., & Alves, J. 2005, A&A, 430, 481

Houde, M., Dowell, C. D., Hildebrand, R. H., Dotson, J. L., Vaillancourt, J. E., Phillips, T. G., Peng, R., & Bastien, P. 2004, ApJ, 604, 717

Ishii, K., Tajima, A., Taketsugu, T., & Yamashita, K. 2006, ApJ, 636, 927

Jackson, J. M., et al. 2006, ApJS, 163, 145

Juneau, S., Narayanan, D. T., Moustakas, J., Shirley, Y. L., Bussmann, R. S., Kennicutt, R. C., & Vanden Bout, P. A. 2009, ApJ, 707, 1217

Kasemann, C., et al. 2006, Proc. SPIE, 6275,

Kawamura, J., et al. 2002, A&A, 394, 271

Kennicutt, R. C., Jr. 1998, ApJ, 498, 541

Kennicutt, R. C. 2005, Massive Star Birth: A Crossroads of Astrophysics, 227, 3

Kewley, L. J., Geller, M. J., Jansen, R. A., & Dopita, M. A. 2002, AJ, 124, 3135

Klein, B., Philipp, S. D., Krämer, I., Kasemann, C., Güsten, R., & Menten, K. M. 2006, A&A, 454, L29

Kleinmann, D. E., & Low, F. J. 1967, ApJ, 149, L1

Knudsen, K. K., Walter, F., Weiss, A., Bolatto, A., Riechers, D. A., & Menten, K. 2007, ApJ, 666, 156

Kohno, K. 2005, The Evolution of Starbursts, 783, 203

Krips, M., Neri, R., García-Burillo, S., Martín, S., Combes, F., Graciá-Carpio, J., & Eckart, A. 2008, ApJ, 677, 262

Krügel, E. 2008, An introduction to the physics of interstellar dust / Endrik Krügel; Taylor & Francis, c2008.xiii, 387 p. : ill. ; 25 cm. Series in astronomy and astrophysics. Includes bibliographical references (p. 377-380) and index. ISBN : 9781584887072 (alk. paper) 1584887079 (alk. paper)

Krumholz, M. R., & Matzner, C. D. 2009, ApJ, 703, 1352

Krumholz, M. R., & Thompson, T. A. 2007, ApJ, 669, 289

Kurtz, S., Churchwell, E., & Wood, D. O. S. 1994, ApJS, 91, 659

Kwan, J., & Scoville, N. 1976, ApJ, 210, L39

Lacy, J. H., Knacke, R., Geballe, T. R., & Tokunaga, A. T. 1994, ApJ, 428, L69

Lada, C. J., & Lada, E. A. 2003, ARA&A, 41, 57

Langer, W. D., & Penzias, A. A. 1990, ApJ, 357, 477

Le Petit, F., Nehmé, C., Le Bourlot, J., & Roueff, E. 2006, ApJS, 164, 506

Lee, J.-K., & Burton, M. G. 2000, MNRAS, 315, 11

Lis, D. C., Schilke, P., & Keene, J. 1997, IAU Symposium, 170, 128

Lis, D. C., Serabyn, E., Keene, J., Dowell, C. D., Benford, D. J., Phillips, T. G., Hunter, T. R., & Wang, N. 1998, ApJ, 509, 299

Lis, D. C., & Schilke, P. 2003, ApJ, 597, L145

Loenen, A. F., Spaans, M., Baan, W. A., & Meijerink, R. 2008, A&A, 488, L5

Lundmark, K. 1921, PASP, 33, 225

Marrone, D. P., et al. 2004, ApJ, 612, 940

Martín-Pintado, J., de Vicente, P., Rodríguez-Fernández, N. J., Fuente, A., & Planesas, P. 2000, A&A, 356, L5

Martín, S., Martín-Pintado, J., & Viti, S. 2009, ApJ, 706, 1323

Martín, S., Mauersberger, R., Martín-Pintado, J., Henkel, C., & García-Burillo, S. 2006, ApJS, 164, 450

Matthews, H., et al. 2009, AJ, 138, 1380

McGrath, E. J., Goss, W. M., & De Pree, C. G. 2004, ApJS, 155, 577

McKee, C. F., & Ostriker, E. C. 2007, ARA&A, 45, 565

McMullin, J. P., Mundy, L. G., & Blake, G. A. 1993, ApJ, 405, 599

Meijerink, R., & Spaans, M. 2005, A&A, 436, 397

Meijerink, R., Spaans, M., & Israel, F. P. 2007, A&A, 461, 793

Menten, K. M., Reid, M. J., Forbrich, J., & Brunthaler, A. 2007, A&A, 474, 515

Menten, K. M., & Reid, M. J. 1995, ApJ, 445, L157

Mezger, P. G., Zylka, R., & Wink, J. E. 1990, A&A, 228, 95

Minh, Y. C., Irvine, W. M., McGonagle, D., & Ziurys, L. M. 1990, ApJ, 360, 136

Minh, Y. C., Ziurys, L. M., Irvine, W. M., & McGonagle, D. 1991, ApJ, 366, 192

Mufson, S. L., & Liszt, H. S. 1977, ApJ, 212, 664

Mundy, L. G., Scoville, N. Z., Baath, L. B., Masson, C. R., & Woody, D. P. 1986, ApJ, 304, L51

Murray, N., Quataert, E., & Thompson, T. A. 2010, ApJ, 709, 191

Nguyen, Q.-R., Jackson, J. M., Henkel, C., Truong, B., & Mauersberger, R. 1992, ApJ, 399, 521

Nissen, H. D., Gustafsson, M., Lemaire, J. L., Clénet, Y., Rouan, D., & Field, D. 2007, A&A, 466, 949

Norris, R. P. 1984, MNRAS, 207, 127

O'Dell, C. R., Henney, W. J., Abel, N. P., Ferland, G. J., & Arthur, S. J. 2009, AJ, 137, 367

Pardo, J. R., Cernicharo, J., & Phillips, T. G. 2005, ApJ, 634, L61

Pellegrini, E. W., Baldwin, J. A., Ferland, G. J., Shaw, G., & Heathcote, S. 2009, ApJ, 693, 285

Pérez-Beaupuits, J. P., Spaans, M., van der Tak, F. F. S., Aalto, S., García-Burillo, S., Fuente, A., & Usero, A. 2009, A&A, 503, 459

Plambeck, R. L., Wright, M. C. H., & Carlstrom, J. E. 1990, ApJ, 348, L65

Plambeck, R. L., Wright, M. C. H., Mundy, L. G., & Looney, L. W. 1995, ApJ, 455, L189

Reach, W. T., et al. 2005, PASP, 117, 978

Risacher, C., et al. 2006, A&A, 454, L17

Rodríguez, L. F., Poveda, A., Lizano, S., & Allen, C. 2005, ApJ, 627, L65 s

Rodríguez-Franco, A., Martín-Pintado, J., & Wilson, T. L. 1999, A&A, 344, L57

Sanders, D. B., & Mirabel, I. F. 1996, ARA&A, 34, 749

Schilke, P., Walmsley, C. M., Pineau Des Forets, G., Roueff, E., Flower, D. R., & Guilloteau, S. 1992, A&A, 256, 595

Schmid-Burgk, J., et al. 1989, A&A, 215, 150

Schmid-Burgk, J., Guesten, R., Mauersberger, R., Schulz, A., & Wilson, T. L. 1990, ApJ, 362, L25

Schmidt, M. 1959, ApJ, 129, 243

Schöier, F. L., van der Tak, F. F. S., van Dishoeck, E. F., & Black, J. H. 2005, A&A, 432, 369

Schuller, F., et al. 2009, A&A, 504, 415

Schulz, A., et al. 1995, A&A, 295, 183

Schuster, K.-F., et al. 2004, A&A, 423, 1171

Scoville, N. Z., Sargent, A. I., Sanders, D. B., Claussen, M. J., Masson, C. R., Lo, K. Y., & Phillips, T. G. 1986, ApJ, 303, 416

Seaquist, E. R., & Frayer, D. T. 2000, ApJ, 540, 765

Serabyn, E., Guesten, R., & Schulz, A. 1993, ApJ, 413, 571

Shuping, R. Y., Morris, M., & Bally, J. 2004, AJ, 128, 363

Sievers, A. W., Mezger, P. G., Bordeon, M. A., Kreysa, E., Haslam, C. G. T., & Lemke, R. 1991, A&A, 251, 231

Simon, R., Jackson, J. M., Clemens, D. P., Bania, T. M., & Heyer, M. H. 2001, ApJ, 551, 747

Siringo, G., et al. 2009, A&A, 497, 945

Smith, N., Bally, J., Shuping, R. Y., Morris, M., & Hayward, T. L. 2004, ApJ, 610, L117

Smith, N., et al. 2000, ApJ, 540, 316

Stacey, G. J., Jaffe, D. T., Geis, N., Grenzel, R., Harris, A. I., Poglitsch, A., Stutzki, J., & Townes, C. H. 1993, ApJ, 404, 219

Sugai, H., et al. 1994, ApJ, 420, 746

Taylor, K. N. R., Storey, J. W. V., Sandell, G., Williams, P. M., & Zealey, W. J. 1984, Nature, 311, 236

Tsujimoto, M., Hosokawa, T., Feigelson, E. D., Getman, K. V., & Broos, P. S. 2006, ApJ, 653, 409

Usero, A., García-Burillo, S., Martín-Pintado, J., Fuente, A., & Neri, R. 2006, A&A, 448, 457

Vacca, W. D., Garmany, C. D., & Shull, J. M. 1996, ApJ, 460, 914

van der Tak, F. F. S. 2005, Massive Star Birth: A Crossroads of Astrophysics, 227, 70

van der Tak, F. F. S., Black, J. H., Schöier, F. L., Jansen, D. J., & van Dishoeck, E. F. 2007, A&A, 468, 627

van der Wiel, M. H. D., van der Tak, F. F. S., Ossenkopf, V., Spaans, M., Roberts, H., Fuller, G. A., & Plume, R. 2009, A&A, 498, 161

Walmsley, C. M., Natta, A., Oliva, E., & Testi, L. 2000, A&A, 364, 301

Walter, D. K., O'dell, C. R., Hu, X., & Dufour, R. J. 1995, PASP, 107, 686

Watson, C., Araya, E., Sewilo, M., Churchwell, E., Hofner, P., & Kurtz, S. 2003, ApJ, 587, 714

Watson, C., et al. 2008, ApJ, 681, 1341 2004, A&A, 423, 1171

Weaver, R., McCray, R., Castor, J., Shapiro, P., & Moore, R. 1977, ApJ, 218, 377

Welch, W. J., Dreher, J. W., Jackson, J. M., Terebey, S., & Vogel, S. N. 1987, Science, 238, 1550

Whitworth, A. P., Bhattal, A. S., Chapman, S. J., Disney, M. J., & Turner, J. A. 1994, A&A, 290, 421

Williams, J. A., Dickel, H. R., & Auer, L. H. 2004, ApJS, 153, 463

Wilner, D. J., De Pree, C. G., Welch, W. J., & Goss, W. M. 2001, ApJ, 550, L81

Wilson, T. L., & Matteucci, F. 1992, A&A Rev., 4, 1

Wilson, T. L., & Rood, R. 1994, ARA&A, 32, 191

Wilson, T. L., Muders, D., Kramer, C., & Henkel, C. 2001, ApJ, 557, 240

Wirström, E. S., Bergman, P., Olofsson, A. O. H., Frisk, U., Hjalmarson, Å., Olberg, M., Persson, C. M., & Sandqvist, A. 2006, A&A, 453, 979

Wiseman, J. J., & Ho, P. T. P. 1998, ApJ, 502, 676

Wiseman, J. J., & Ho, P. T. P. 1996, Nature, 382, 139

Wright, M., Sandell, G., Wilner, D. J., & Plambeck, R. L. 1992, ApJ, 393, 225

Wu, J., Evans, N. J., II, Gao, Y., Solomon, P. M., Shirley, Y. L., & Vanden Bout, P. A. 2005, ApJ, 635, L173

Wyrowski, F., Schilke, P., Hofner, P., & Walmsley, C. M. 1997, ApJ, 487, L171

Zapata, L. A., Schmid-Burgk, J., Muders, D., Schilke, P., Menten, K., & Guesten, R. 2010, A&A, 510, A2

Zapata, L. A., Schmid-Burgk, J., Ho, P. T. P., Rodríguez, L. F., & Menten, K. M. 2009, ApJ, 704, L45

Zapata, L. A., Ho, P. T. P., Rodríguez, L. F., Schilke, P., & Kurtz, S. 2007, A&A, 471, L59

Zapata, L. A., Ho, P. T. P., Rodríguez, L. F., O'Dell, C. R., Zhang, Q., & Muench, A. 2006, ApJ, 653, 398

Zapata, L. A., Rodríguez, L. F., Ho, P. T. P., Zhang, Q., Qi, C., & Kurtz, S. E. 2005, ApJ, 630, L85

Zapata, L. A., Rodríguez, L. F., Kurtz, S. E., O'Dell, C. R., & Ho, P. T. P. 2004, ApJ, 610, L121

Zinnecker, H., & Yorke, H. W. 2007, ARA&A, 45, 481

Ziurys, L. M., & Turner, B. E. 1986, ApJ, 300, L19

Ziurys, L. M., Snell, R. L., & Dickman, R. L. 1989, ApJ, 341, 857

A

Position-velocity diagrams of the shells in W49A

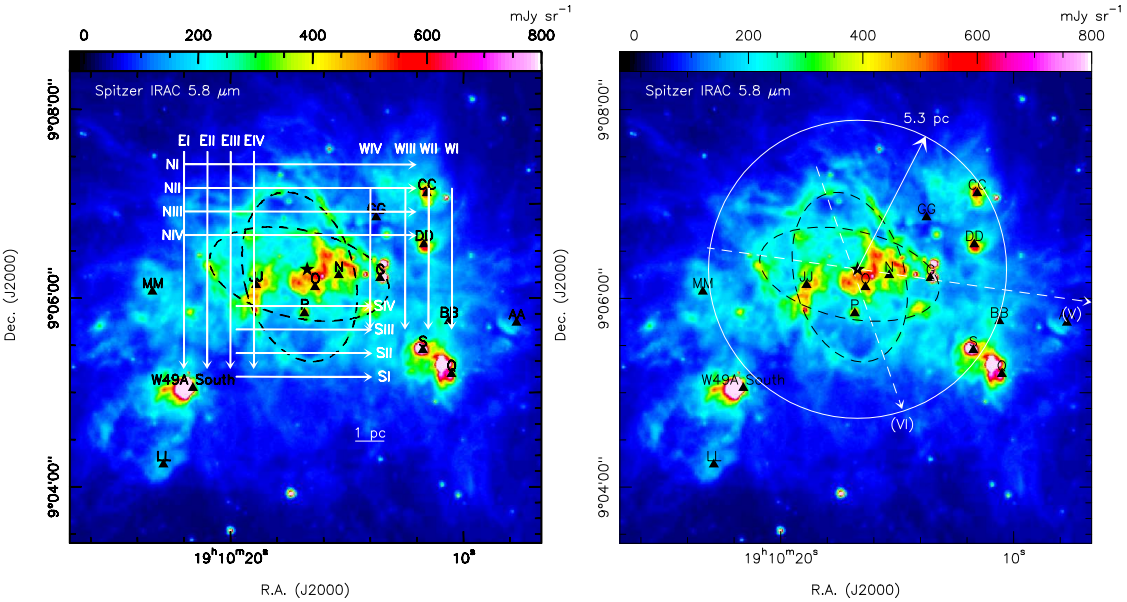

Figure A.1 The same Spitzer IRAC 5.8 μm image of W49A as shown in Figure 5.2. Left image shows four groups of PV cuts in different colors denoted by E, S, N, and W, respectively. The PV diagrams for ^{13}CO, C^{18}O, HCN, HCO$^+$ are shown in Figures A.2 to A.13. Right image shows the circular PV cut (5.3 pc radius) centered on the shell expansion center (black star). Two additional PV cuts through the shells are indicated (Cut V and VI).

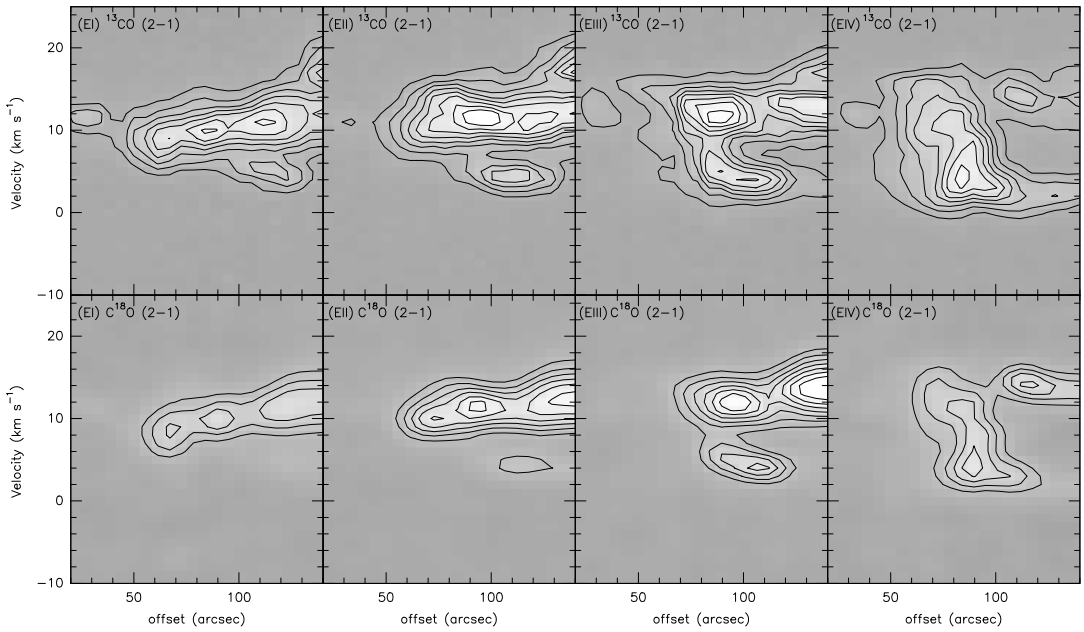

Figure A.2 The PV diagrams of the ^{13}CO and C^{18}O $J = 2 - 1$ emission in the eastern part of the shell structure shown in Figure A.1. The contours in ^{13}CO $J = 2 - 1$ are plotted from 3 to 24 K in steps of 3 K, and the contours in C^{18}O $J = 2 - 1$ are plotted from 1 to 4 K in steps of 0.5 K. The images are smoothed by a Gaussian with a width of two pixels.

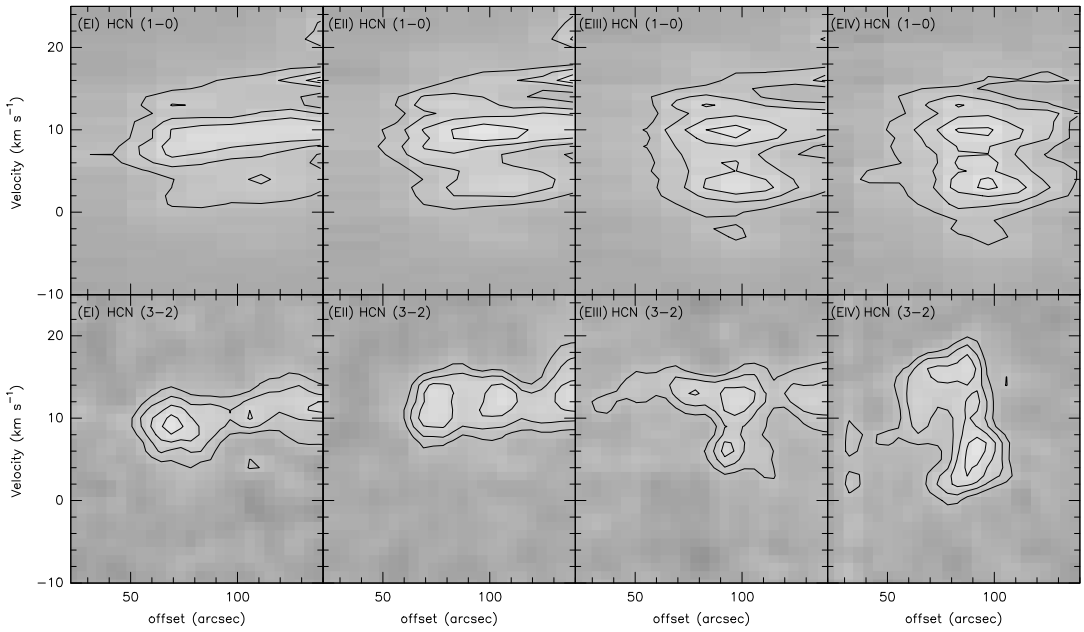

Figure A.3 The PV diagrams of the HCN $J = 1 - 0$ and $J = 3 - 2$ emission in the eastern part of the shell structure shown in Figure A.1. The contours are plotted from 1 to 4 K in steps of 0.5 K. The HCN $J = 3 - 2$ images are smoothed by a Gaussian with a width of two pixels.

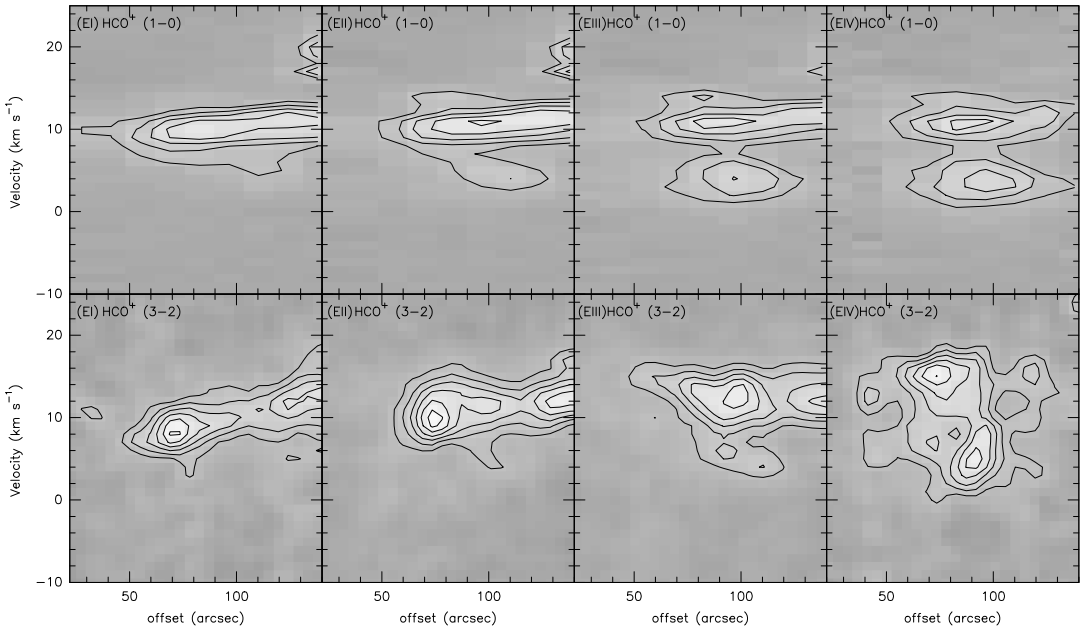

Figure A.4 The PV diagrams of the HCO^+ $J = 1 - 0$ and $J = 3 - 2$ emission in the eastern part of the shell structure shown in Figure A.1. The contours are plotted from 1 to 4 K in steps of 0.5 K. The HCO^+ $J = 3 - 2$ images are smoothed by a Gaussian with a width of two pixels.

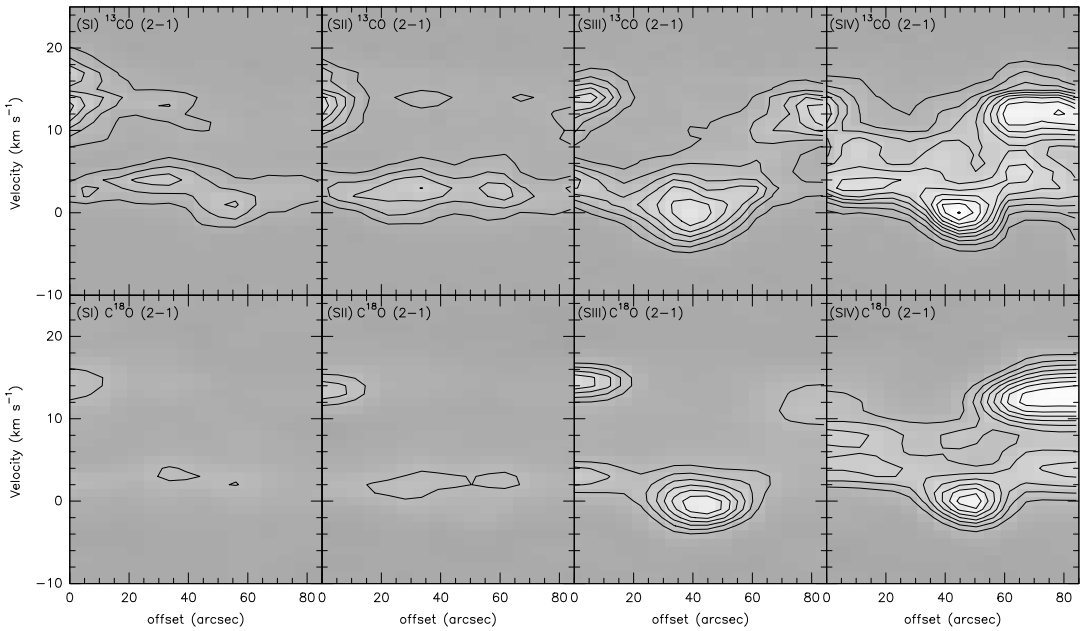

Figure A.5 The PV diagrams of the ^{13}CO and $C^{18}O$ $J = 2 - 1$ emission in the southern part of the shell structure shown in Figure A.1. The contours in ^{13}CO $J = 2 - 1$ are plotted from 3 to 30 K in steps of 3 K, and the contours in $C^{18}O$ $J = 2 - 1$ are plotted from 1 to 4 K in steps of 0.5 K. The images are smoothed by a Gaussian with a width of two pixels.

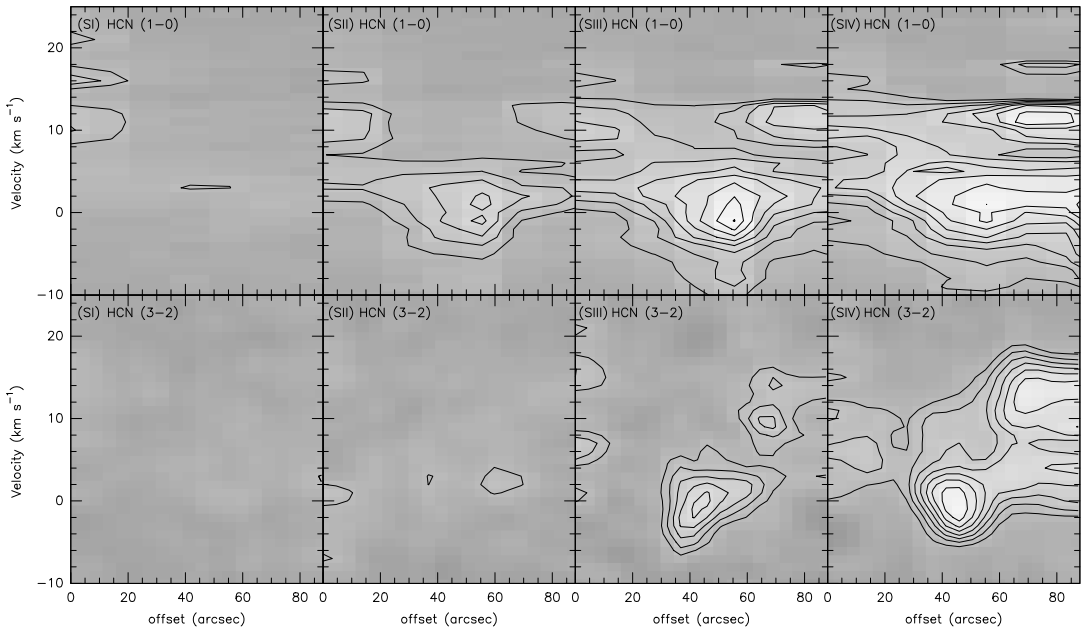

Figure A.6 The PV diagrams of the HCN $J = 1 - 0$ and $J = 3 - 2$ emission in the southern part of the shell structure shown in Figure A.1. The contours are plotted from 1 to 5.5 K in steps of 0.5 K. The HCN $J = 3 - 2$ images are smoothed by a Gaussian with a width of two pixels.

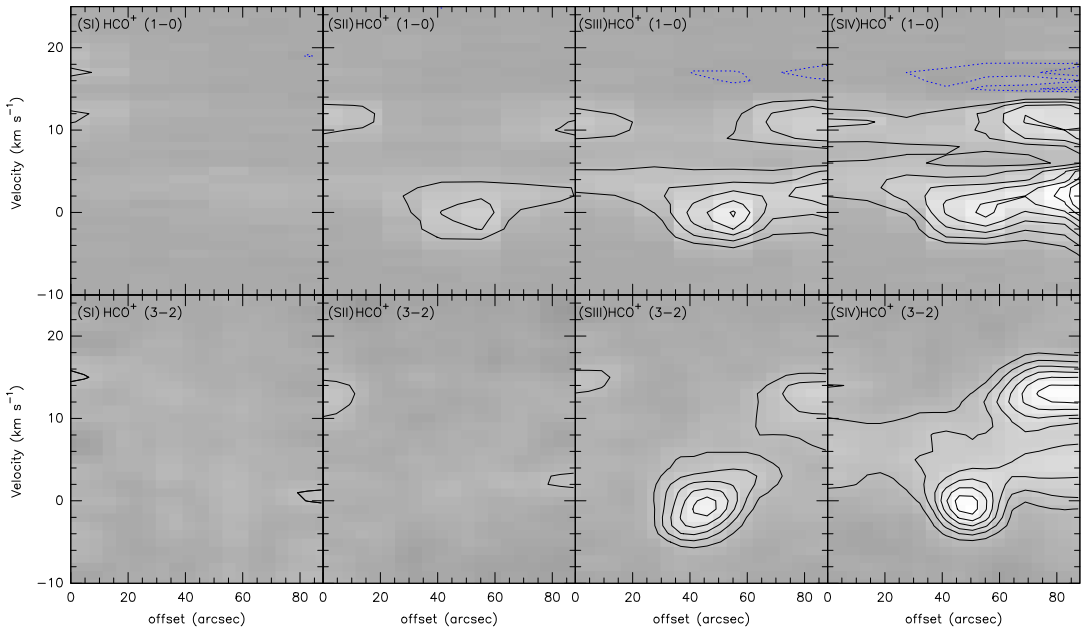

Figure A.7 The PV diagrams of the HCO^+ $J = 1 - 0$ and $J = 3 - 2$ emission in the southern part of the shell structure shown in Figure A.1. The contours are plotted from 1.5 to 7.5 K in steps of 1 K. The dotted blue contours represent -0.2 K and -0.6 K absorption. The HCO^+ $J = 3 - 2$ images are smoothed by a Gaussian with a width of two pixels.

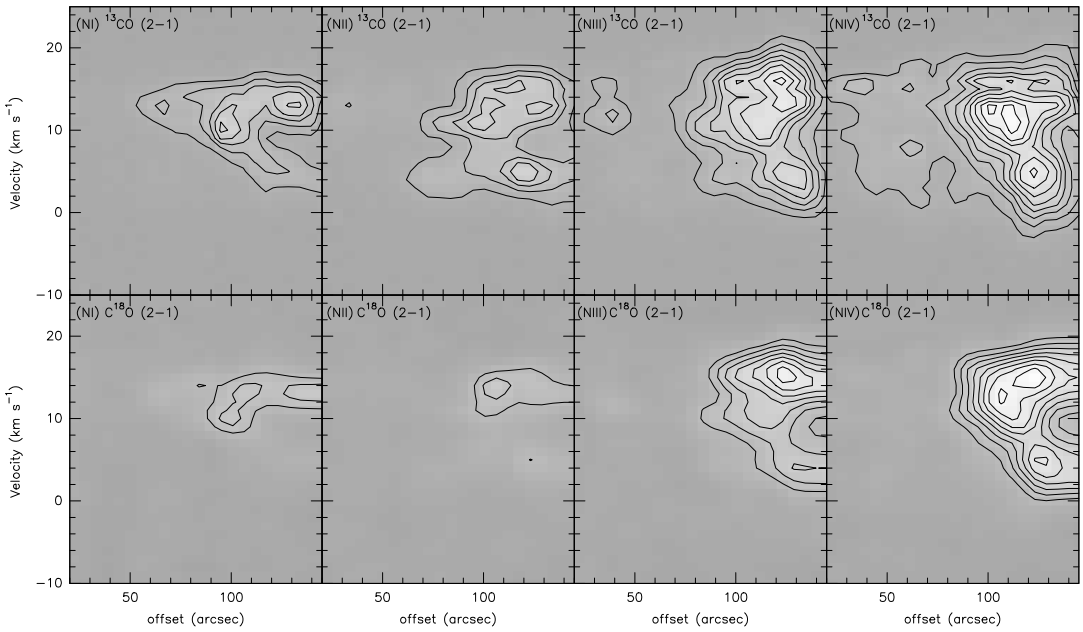

Figure A.8 The PV diagrams of the ^{13}CO and C^{18}O $J = 2 - 1$ emission in the northern part of the shell structure shown in Figure A.1. The contours in ^{13}CO $J = 2 - 1$ are plotted from 3 to 30 K in steps of 3 K, and the contours in C^{18}O $J = 2 - 1$ are plotted from 1 to 5 K in steps of 0.5 K. The images are smoothed by a Gaussian with a width of two pixels.

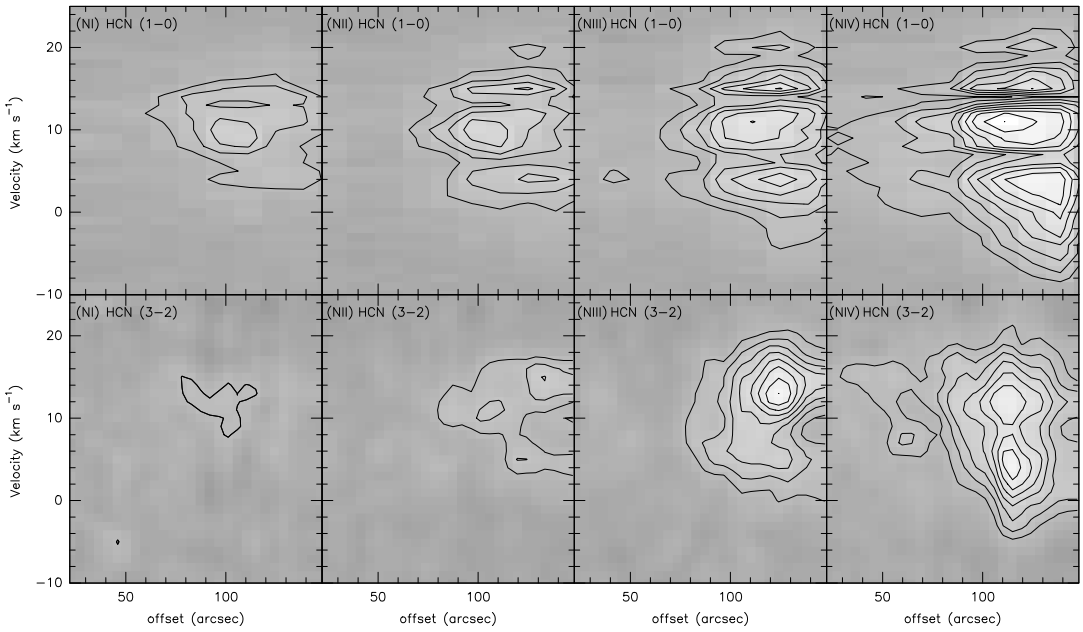

Figure A.9 The PV diagrams of the HCN $J = 1 - 0$ and $J = 3 - 2$ emission in the northern part of the shell structure shown in Figure A.1. The contours are plotted from 1 to 5.5 K in steps of 0.5 K. The HCN $J = 3 - 2$ images are smoothed by a Gaussian with a width of two pixels.

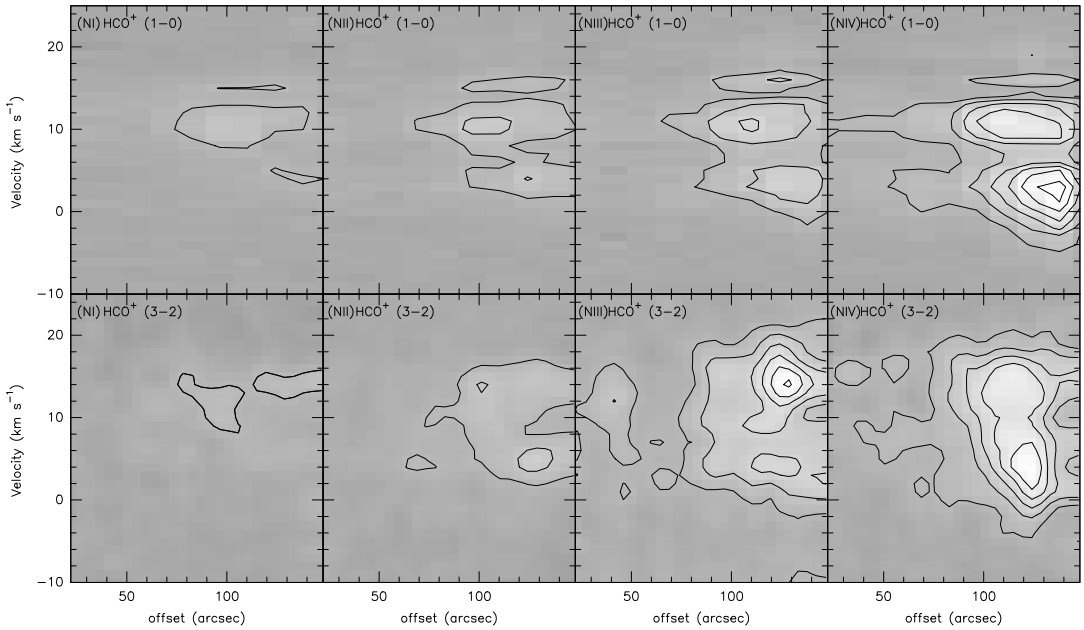

Figure A.10 The PV diagrams of the HCO^+ $J = 1 - 0$ and $J = 3 - 2$ emission in the northern part of the shell structure shown in Figure A.1. The contours are plotted from 1 to 6 K in steps of 1 K. The HCO^+ $J = 3 - 2$ images are smoothed by a Gaussian with a width of two pixels.

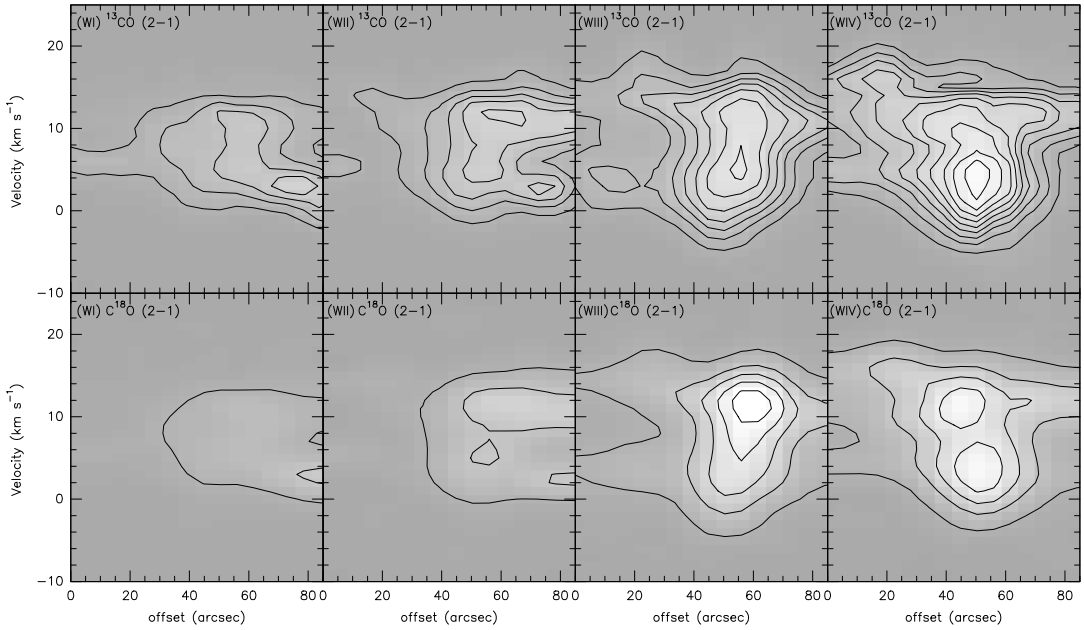

Figure A.11 The PV diagrams of the ^{13}CO and $C^{18}O$ $J = 2 - 1$ emission in the western part of the shell structure shown in Figure A.1. The contours in ^{13}CO $J = 2 - 1$ are plotted from 5 to 50 K in steps of 5 K, and the contours in $C^{18}O$ $J = 2 - 1$ are plotted from 1 to 9 K in steps of 2 K. The images are smoothed by a Gaussian with a width of two pixels.

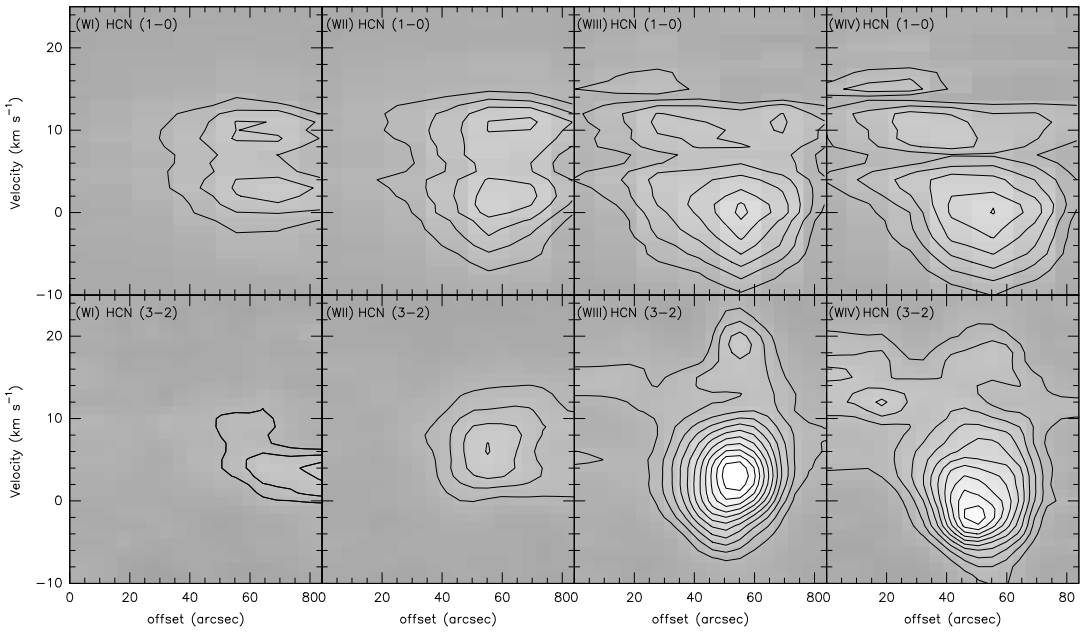

Figure A.12 The PV diagrams of the HCN $J = 1 - 0$ and $J = 3 - 2$ emission in the western part of the shell structure shown in Figure A.1. The contours are plotted from 2 to 12 K in steps of 1 K. The HCN $J = 3 - 2$ images are smoothed by a Gaussian with a width of two pixels.

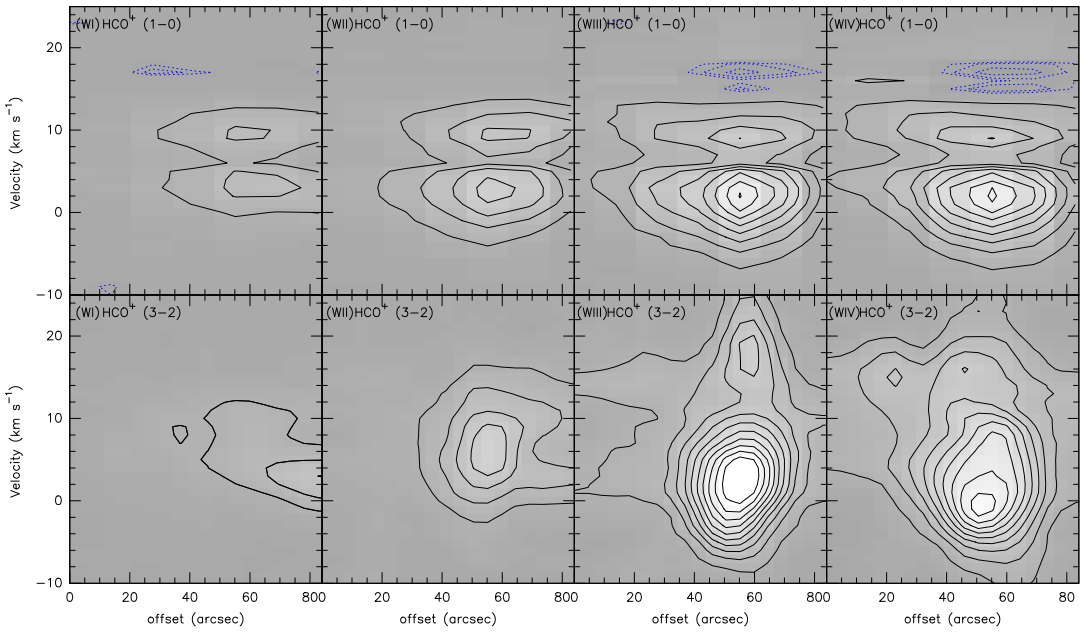

Figure A.13 The PV diagrams of the HCO^+ $J = 1 - 0$ and $J = 3 - 2$ emission in the western part of the shell structure shown in Figure A.1. The contours are plotted from 2 to 20 K in steps of 2 K. The dotted blue contours represent -0.2 K, -0.5 K and -1.0 K absorption. The HCO^+ $J = 3 - 2$ images are smoothed by a Gaussian with a width of two pixels.

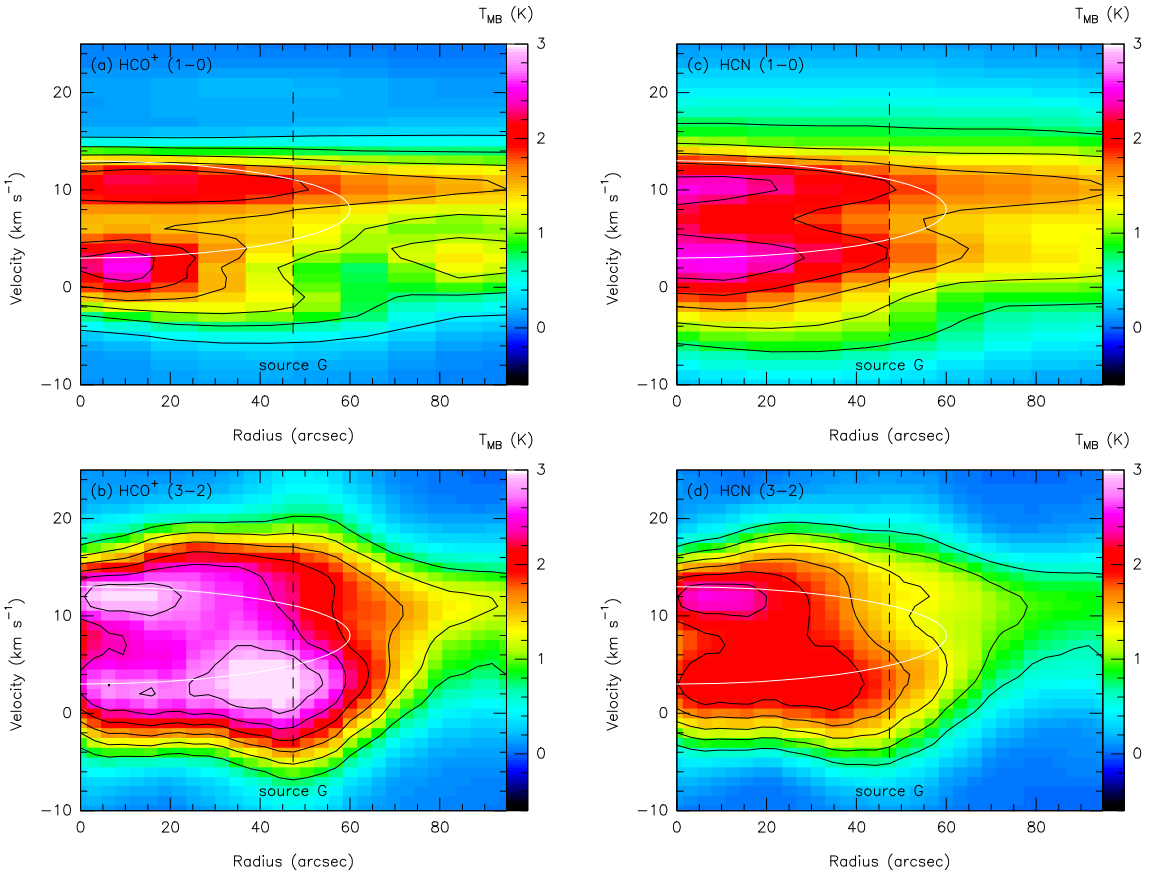

Figure A.14 The circular PV diagrams of the HCO^+, HCN $J = 1 - 0$ and $J = 3 - 2$ lines in the molecular shell shown in Figure A.1. The white lines represent a shell with a velocity centered at ~ 8 km s^{-1} with an expanding speed of 5 km $^{-1}$.

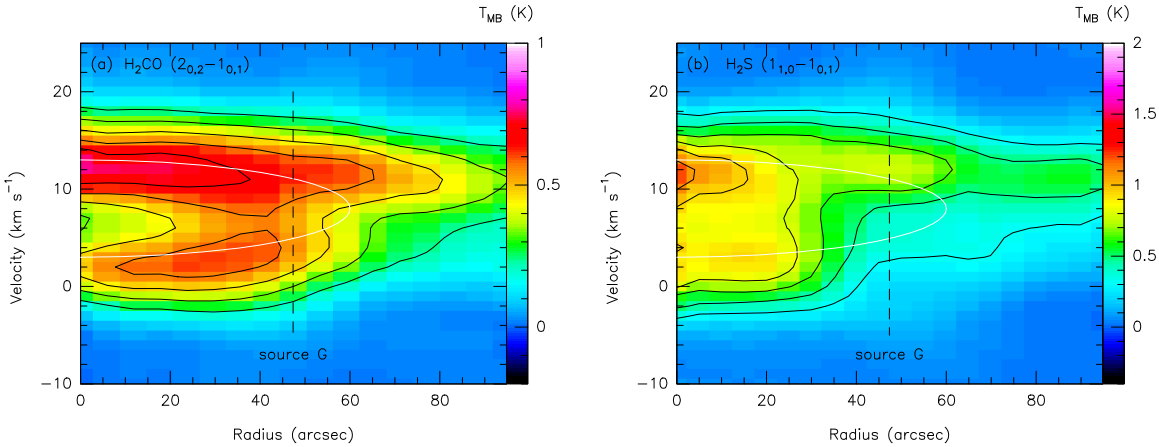

Figure A.15 The circular PV diagrams of the H_2CO $2_{0,2} - 10,1$ and H_2S $1_{1,0} - 1_{0,1}$ lines in the molecular shell shown in Figure A.1. The white lines represent a shell with a velocity centered at ~ 8 km s^{-1} with an expanding speed of 5 km $^{-1}$.

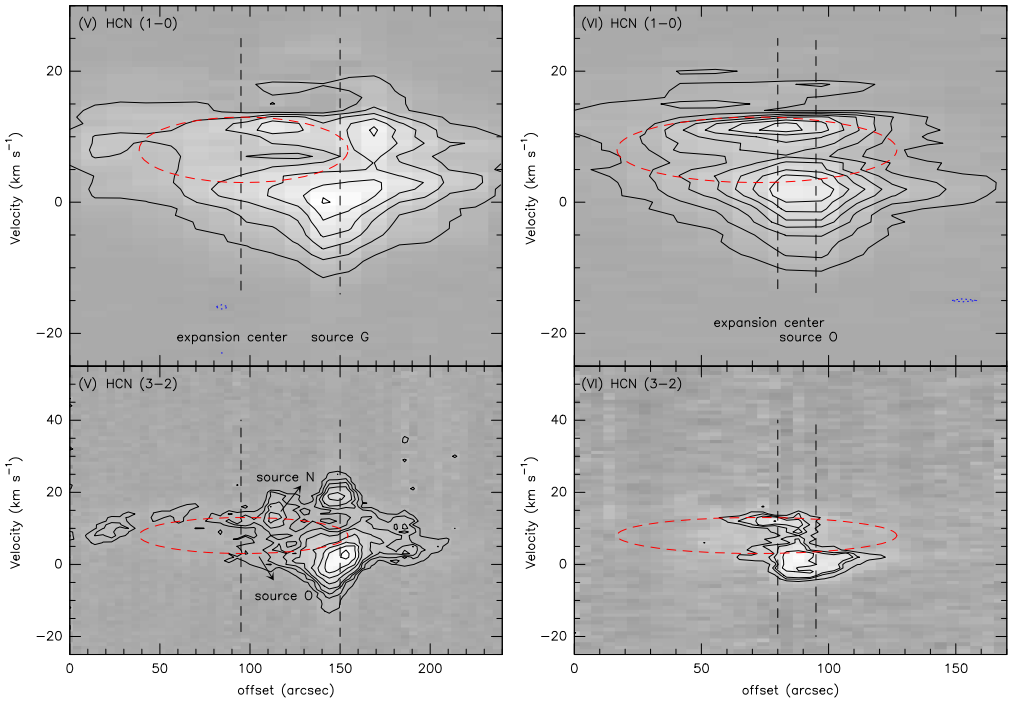

Figure A.16 The PV diagrams of the HCN $J = 1 - 0$ and $J = 3 - 2$ lines corresponding to the two cuts shown in Figure A.1. (V) The contours in HCN $J = 1 - 0$ are plotted from 1 to 6 K in steps of 1 K, and the contours in HCN $J = 3 - 2$ are plotted from 2 to 5 K in steps of 1 K, and the subsequent contours are running from 7 to 13 K in steps of 2 K. (VI) The contours in HCN $J = 1 - 0$ are plotted from 0.5 to 4.5 K in steps of 0.5 K, and the contours in HCN $J = 3 - 2$ represent 1.9 K, 2.6 K, 3 K, 4 K, and 5 K. The red dashed-lines correspond to the MIR shells seen in Figure A.1 with an expansion speed of 5 km $^{-1}$. The shell expansion center and sources O and N are indicated.

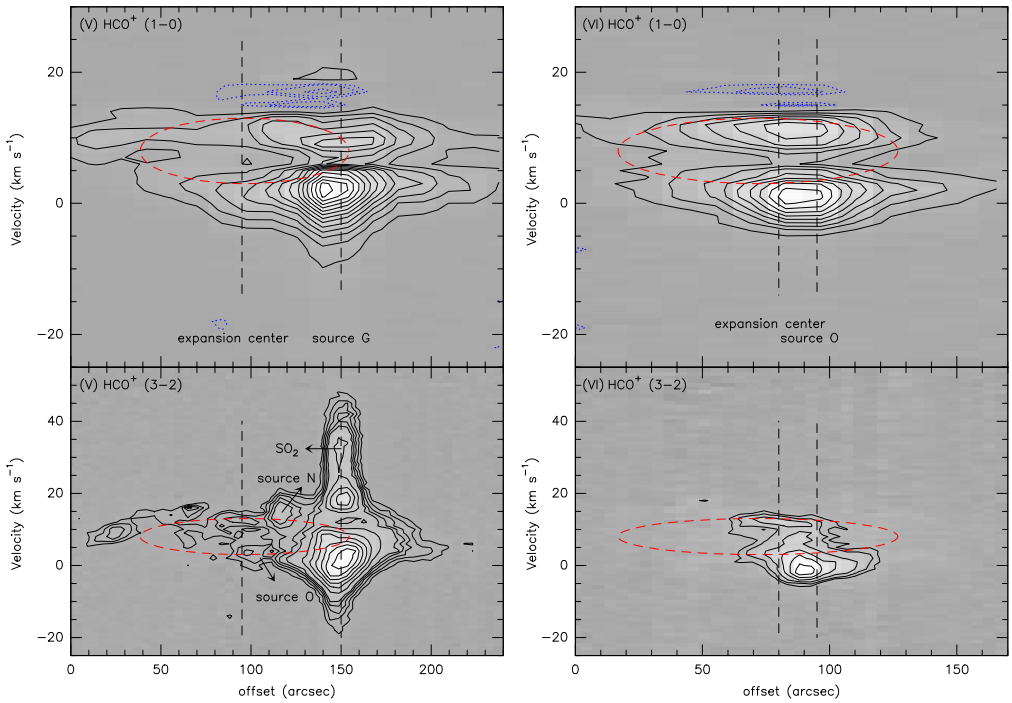

Figure A.17 The PV diagrams of the HCO^+ $J = 1 - 0$ and $J = 3 - 2$ lines corresponding to the two cuts shown in Figure A.1. (V) The contours in HCO^+ $J = 1 - 0$ are plotted from 1 to 15 K in steps of 1 K, and the contours in HCO^+ $J = 3 - 2$ are plotted from 2 to 5 K in steps of 1 K, and the subsequent contours are running from 6 to 27 K in steps of 3 K. The blue dotted lines represent absorptions at -0.2 K, -0.5 K, and -1 K. (VI) The contours in HCO^+ $J = 1 - 0$ are plotted from 0.5 to 5.5 K in steps of 0.5 K, and the contours in HCO^+ $J = 3 - 2$ represent 1.9 K, 2.6 K, 3 K, and run from 4 to 10 K in steps of 2 K. The red dashed-lines correspond to the MIR shells seen in Figure A.1 with an expansion speed of 5 km $^{-1}$. The blue dotted lines represent absorptions at -0.2 K and -0.3 K. The shell expansion center and sources O and N are indicated.

B

B.1 Column Density Calculation

Beginning with the radiative transfer equation, photons travel in a straight line along a distance ds, and the change of I_ν equals

$$\frac{dI_\nu}{ds} = -\kappa_\nu I_\nu + j_\nu, \tag{B.1}$$

where I_ν is the specific intensity (erg s^{-1} cm^{-2} ster^{-1} Hz^{-1}). κ_ν is the absorption coefficient (cm^{-1}), and j_ν is the emission coefficient (erg s^{-1} cm^{-3} ster^{-1} Hz^{-1}). In addition, optical depth τ_ν is defined as

$$d\tau_\nu = -\kappa_\nu ds, \tag{B.2}$$

and is dimensionless. For positive κ_ν, I_ν can be integrated from the observer (τ_ν=0) to the source ($\tau_{\nu r}$) then yields

$$I_\nu = I_\nu(0)e^{-\tau_{\nu r}} + \int_0^{\tau_{\nu r}} \frac{j_\nu}{\kappa_\nu} e^{-\tau_\nu} d\tau_\nu. \tag{B.3}$$

In the local thermodynamic equilibrium (LTE) assumption, the source function, defined as

$$S_\nu = \frac{j_\nu}{\kappa_\nu}, \tag{B.4}$$

is equal to the Planck function

$$B_\nu(T) = \frac{2h\nu^3}{c^2} \frac{1}{e^{h\nu/kT} - 1}. \tag{B.5}$$

Assuming $B_\nu(T)$ is constant through the region, Eq. B.3 becomes

$$I_\nu = I_\nu(0)e^{-\tau_{\nu r}} + B_\nu(T)(1 - e^{-\tau_{\nu r}}). \tag{B.6}$$

In radio spectrum measurements, Eq.B.6 can be rewritten with brightness

$$B_\nu(T_\mathrm{B}) = B(T_\mathrm{bg})e^{-\tau} + B_\nu(T_\mathrm{k})(1 - e^{-\tau}), \tag{B.7}$$

where $T_{\rm B}$ is the observed brightness temperature of the source. $T_{\rm bg}$ is the temperature of the background (usually 2.7 K), and $T_{\rm k}$ stands for the kinetic temperature of the source.

Considering the transitions between two energy levels, the number of emission and absorption should be equal:

$$n_u A_{ul} + n_u B_{ul} u_\nu = n_l B_{lu} u_\nu, \tag{B.8}$$

where A_{ul} is the Einstein spontaneous emission coefficient ($\rm s^{-1}$). B_{ul} is the Einstein stimulated emission coefficient, and B_{lu} is the Einstein induced absorption coefficient. u_ν is the energy density of radiation which is given by the Planck function (Eq. B.5) in the LTE condition. Relative population of states can be described by the Boltzman equation in LTE,

$$\frac{n_u}{n_l} = \frac{g_u}{g_l} e^{-\frac{h\nu}{kT}}. \tag{B.9}$$

Besides, u_ν can be also given by the Planck funcation

$$u_\nu = \frac{4\pi}{c} B_\nu(T) = \frac{8\pi h\nu^3}{c^3} \frac{1}{e^{\frac{h\nu}{kT}} - 1}, \tag{B.10}$$

and we can solve Eq. B.8 using Eqs. B.9 and B.10 to get

$$g_l B_{lu} = g_u B_{ul}, \tag{B.11}$$

$$A_{ul} = \frac{8\pi h\nu^3}{c^3} B_{ul}. \tag{B.12}$$

Combined with the radiative transfer equation (Eq. B.1) and doing some algebra, the absorption coefficient is

$$\kappa_\nu = \frac{h\nu}{c}[n_l B_{lu} - n_u B_{ul}]\varphi(\nu) = \frac{c^2}{8\pi\nu^2} \frac{g_u}{g_l} n_l A_{ul} \left[1 - e^{-\frac{h\nu}{kT}}\right] \varphi(\nu), \tag{B.13}$$

where $\varphi(\nu)$ is the line profile. In the assumption of optically thin condition ($\tau \ll 1$) together with the Planck function (Eq. B.5) and the absorption coefficient (Eq. B.13), and subtracting $B(T_{\rm bg})$ from the observations by chopping on the sky, Eq. B.7 becomes

$$B_\nu(T_{\rm B}) = \tau B_\nu(T_{\rm k}) = B_\nu(T_{\rm k}) \int \kappa_\nu ds, \tag{B.14}$$

$$= \frac{h\nu}{4\pi} n_u A_{ul} \varphi(\nu). \tag{B.15}$$

Therefore, in the Rayleigh-Jeans limit ($h\nu \ll kT$),

$$B_\nu(T_{\rm B}) = \frac{2k\nu^2}{c^2} T_{\rm B} = \frac{h\nu}{4\pi} n_u A_{ul} \varphi(\nu), \tag{B.16}$$

$$T_{\rm B} = \frac{hc^2}{8k\pi\nu} n_u A_{ul} \varphi(\nu). \tag{B.17}$$

In addition, what we measure is integrated intensities

$$\int T_{\rm B} d\nu = \frac{\nu}{c} \int T_{\rm B} dV = \frac{hc^2}{8k\pi\nu} n_u A_{ul} \int \varphi(\nu) d\nu, \tag{B.18}$$

and the integration of line profile with frequency can be normalized to unity. We can get the column density of the upper state, N_u (cm^{-2}), for a single transition:

$$N_u = \frac{8k\pi\nu^2}{hc^3}\frac{1}{A_{ul}}\int T_{\mathrm{B}}dV. \tag{B.19}$$

The Einstein spontaneous emission coefficient A_{ul} can be related to the average strength of the dipole moment,

$$A_{ul} = \frac{64\pi^4}{3hc^3}\nu^3|\mu_{ul}|^2 = \frac{64\pi^4}{3hc^3}\nu^3\frac{S\mu^2}{g_u}, \tag{B.20}$$

where μ^2 is the component of the dipole moment responsible for the transition, and S is the line strength

$$S_{ul} = (2J+1)\frac{|\mu_{ul}|^2}{\mu^2}. \tag{B.21}$$

Given the rotational partition function Q_{rot} with Eqs. B.20 and B.21, the total column density N is

$$N = \frac{Q_{\mathrm{rot}}}{g_u e^{-\frac{E_u}{kT_{\mathrm{rot}}}}}N_u = \frac{3kQ_{\mathrm{rot}}}{8\pi^3\nu S\mu^2}e^{\frac{E_u}{kT_{\mathrm{rot}}}}\int T_B dV. \tag{B.22}$$

For more than one transition, the rotation diagram can be plotted, and the excitation temperature and total column density can be derived by taking the logarithm of Eq. B.22:

$$ln\frac{N_u}{g_u} = ln\frac{3k\int T_{\mathrm{B}}dV}{8\pi^3\nu S\mu^2} = ln\frac{N}{Q_{\mathrm{rot}}} - \frac{E_u}{kT_{\mathrm{rot}}}. \tag{B.23}$$

The rotation of a diatomic molecule, e.g., CO, CS, SO, and SiO, can beapproximatedd by a rigid rotator and the energy levels of the rotational states are given by the solution to the Schrödinger equation for a rigid rotator:

$$E_{\mathrm{J}} = \frac{h^2}{8\pi^2 I}J(J+1), \tag{B.24}$$

where $I = \mu {r_0}^2$ is the moment of inertia with a reduced mass μ and an internuclear separation r_0, and J is the rotational quantum number. Eq. B.24 can be written in terms of the rotational constant B,

$$E_{\mathrm{J}} = hBJ(J+1), \tag{B.25}$$

where

$$B = \frac{h}{8\pi^2 I}. \tag{B.26}$$

The rotational partition function for diatomic and linear polyatomic molecules is

$$Q_{\mathrm{rot}} = \sum_{i=0}^{\infty} g_i e^{-E_i/kT} = \sum_{J=0}^{\infty}(2J+1)g_I e^{-hBJ(J+1)/kT}, \tag{B.27}$$

where g_I is the nuclear statistical weight. For example, the B_0 is 54891.42 MHz for $C^{18}O$ and the partition function is

$$Q_{\mathrm{rot}}(C^{18}O) = \frac{kT}{hB_0} + \frac{1}{3} \simeq 0.38(T + 0.88). \tag{B.28}$$

B.2 Dust Mass Calculation

The dust opacity τ_ν at the frequency ν is defined by the dust absorption coefficient κ_ν:

$$\tau_\nu = \int \kappa_\nu \rho \; ds = \kappa_\nu \int \frac{M_{\rm dust}}{V} \; ds = \frac{\kappa_\nu M_{\rm dust}}{D^2 \Omega_{\rm s}}, \tag{B.29}$$

where D is the distance of the source, and $\Omega_{\rm s}$ is the source solid angle. Therefore, the total mass of dust can be estimated using

$$M_{\rm dust} = \frac{\tau_\nu D^2 \Omega_{\rm s}}{\kappa_\nu}, \tag{B.30}$$

and τ_ν is given by the radiative transfer equation (Eq. B.6) and Planck function (Eq. B.5). The Rayleigh-Jeans approxmation is not used here since it does not hold anymore in the submm regime. The average intensity is related to the received flux by

$$\langle I_\nu \rangle = \frac{S_\nu}{\Omega_{\rm s}}. \tag{B.31}$$

Therefore, the total dust mass can be obtained via

$$M_{\rm dust} = \frac{D^2 \Omega_{\rm s}}{\kappa_\nu} \left\{ -ln \left[1 - \frac{S_\nu}{(B_\nu(T_{\rm d}) - B_\nu(T_{\rm bg}))\Omega_{\rm s}} \right] \right\}^{-1}, \tag{B.32}$$

where one can use the more useful form of B_ν

$$B_\nu(T) = 6.04 \times 10^{10} \Big(\frac{\nu}{345 \text{ GHz}} \Big)^3 \frac{1}{e^{1.66(\nu/345 \text{ GHz})(T/10 \text{ K})} - 1} \text{ Jy}. \tag{B.33}$$

Besides, the dust optical depth is related to the column density, the H_2 column density can be thus derived via

$$N_{\rm H_2} = \int \frac{\rho}{\mu m_{\rm p}} \; ds = \frac{1}{\mu m_{\rm p} \kappa_\nu} \int \kappa_\nu \rho \; ds = \frac{\tau_\nu}{\mu m_{\rm p} \kappa_\nu}, \tag{B.34}$$

where $\mu = 2.33$ is the mean molecular weight per H_2, and $m_{\rm p}$ is the proton mass of 1.67×10^{-24} g.

C

The RADEX modeling results of W49A

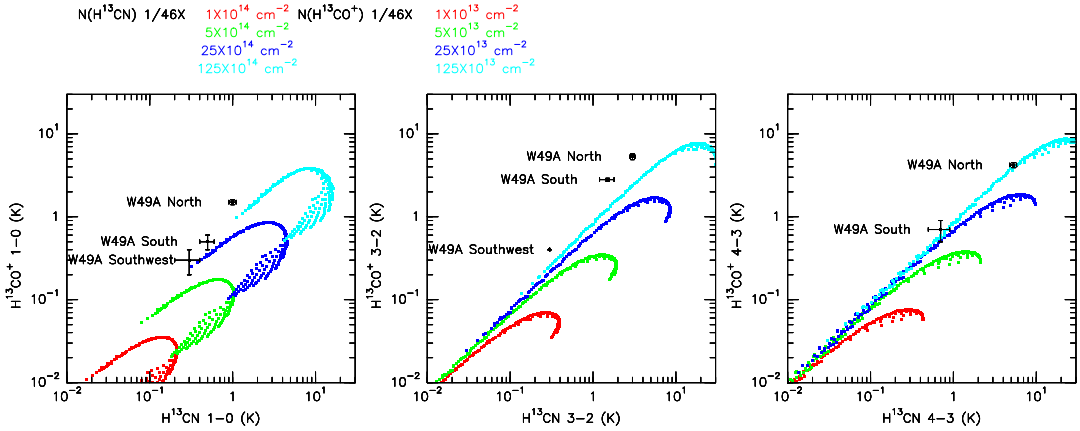

Figure C.1 The similar modeling as in shown Figure 4.7 with a different $H^{13}CN/H^{13}CO^{+}$ column density ratio of 10 : 1. The four different colors are the RADEX results for different column densities plotted in an H_2 density range of $10^4 - 10^7$ cm^{-3} and a temperature range of 20–150 K. The data of W49A North, South, and Southwest are denoted.

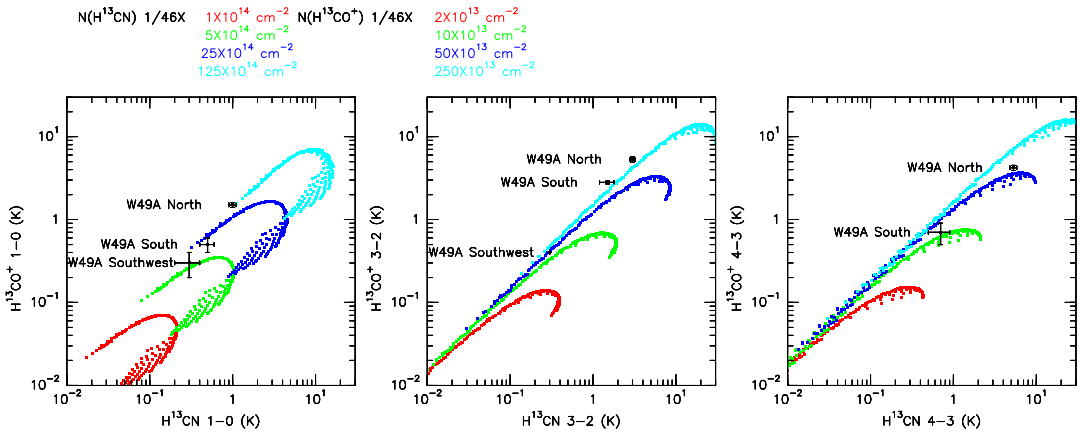

Figure C.2 The similar modeling as shown in Figure 4.7 with a different $H^{13}CN/H^{13}CO^{+}$ column density ratio of 5 : 1.

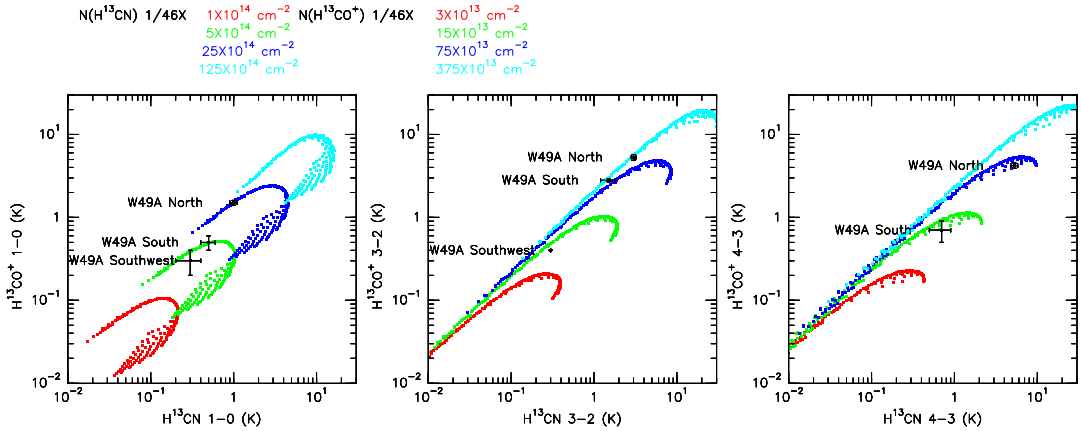

Figure C.3 The similar modeling as in shown Figure 4.7 with a different $H^{13}CN/H^{13}CO^+$ column density ratio of 10 : 3.

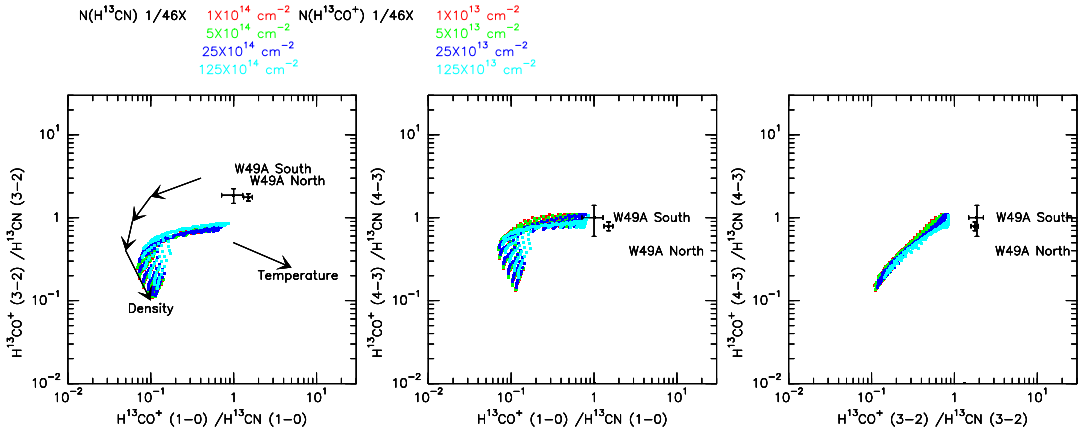

Figure C.4 The same RADEX modeling as in Figure C.1. The four different colors are the RADEX results for different column densities plotted in an H_2 density range of $10^4 - 10^7$ cm^{-3} and a temperature range of 20–150 K. The relative column density ratio among $H^{13}CN$ and $H^{13}CO^+$ is fixed at 10 : 1. The data of W49A North, South and Southwest are denoted.

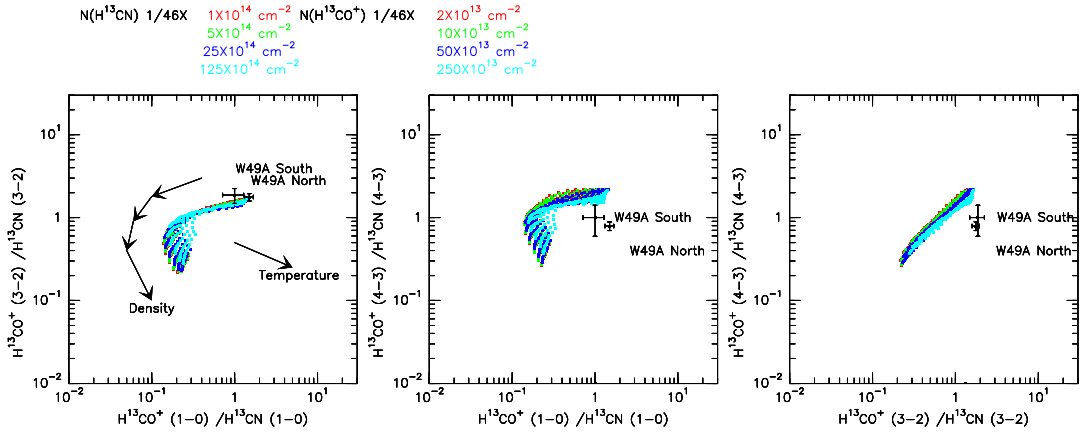

Figure C.5 The same RADEX modeling as in Figure C.2. The four different colors are the RADEX results for different column densities plotted in an H_2 density range of $10^4 - 10^7$ cm^{-3} and a temperature range of 20–150 K. The relative column density ratio among $H^{13}CN$ and $H^{13}CO^+$ is fixed at 5 : 1. The data of W49A North, South and Southwest are denoted.

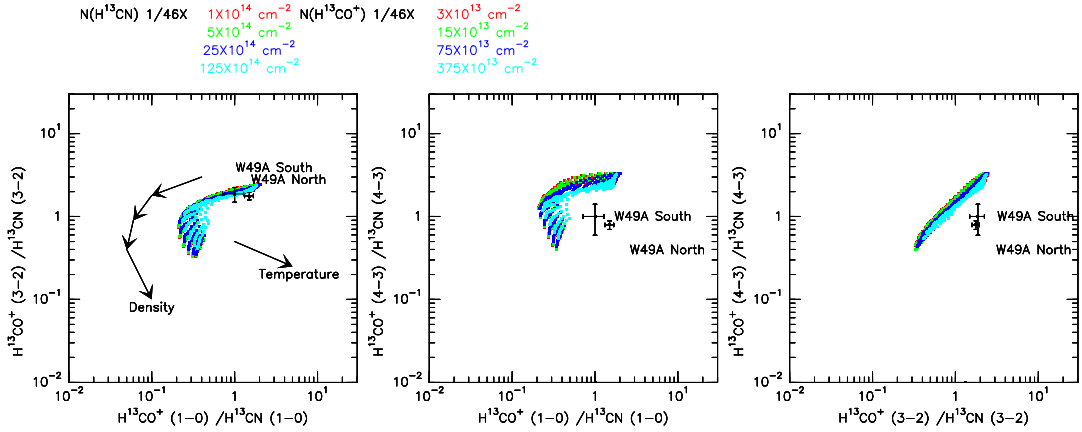

Figure C.6 The same RADEX modeling as in Figure C.3. The four different colors are the RADEX results for different column densities plotted in an H_2 density range of $10^4 - 10^7$ cm^{-3} and a temperature range of 20–150 K. The relative column density ratio among $H^{13}CN$ and $H^{13}CO^+$ is fixed at 10 : 3. The data of W49A North, South and Southwest are denoted.

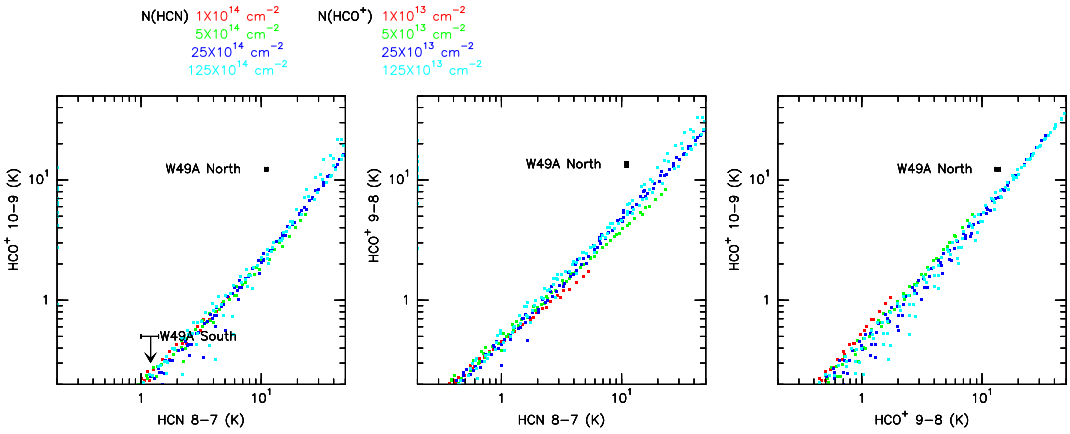

Figure C.7 The RADEX modeling for the brightness temperature correlation between the high-J HCN and HCO^+ transitions. The four different colors are the RADEX results for different column densities plotted in an H_2 density range of $10^4 - 10^7$ cm^{-3} and a temperature range of 20–150 K. The relative column density ratio between HCN and HCO^+ is fixed at 10 : 1. The data of W49A North are denoted.

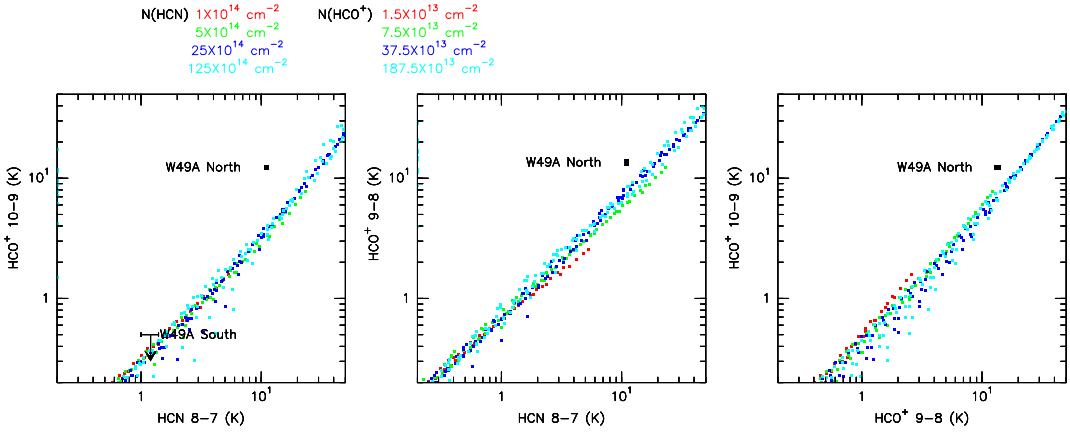

Figure C.8 The similar modeling as in Figure C.7 with different HCN/HCO^+ column density ratio of 20 : 3.

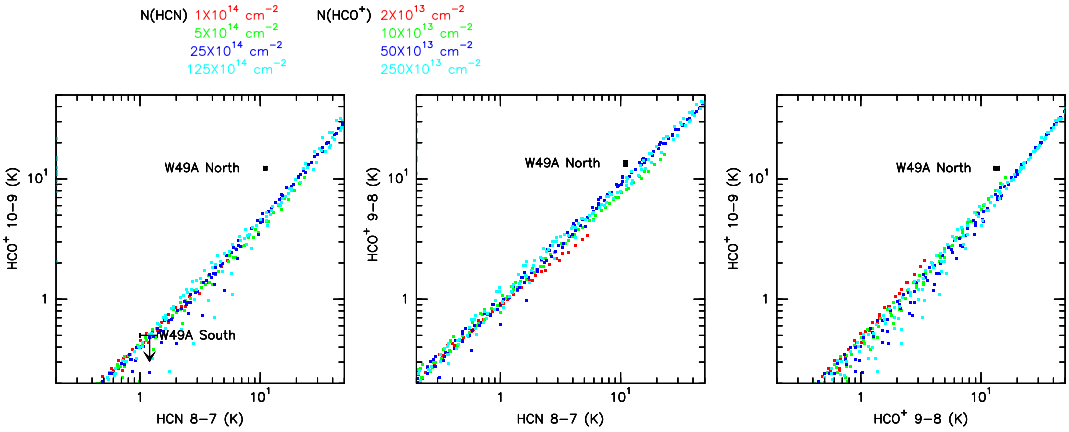

Figure C.9 The similar modeling as in Figure C.7 with different HCN/HCO^+ column density ratio of 5 : 1.

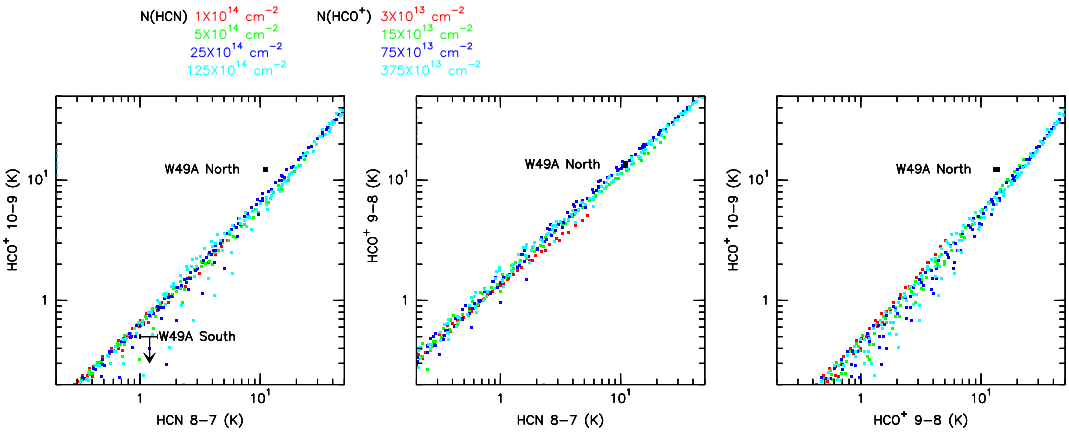

Figure C.10 The similar modeling as in Figure C.7 with different HCN/HCO^+ column density ratio of 10 : 3.

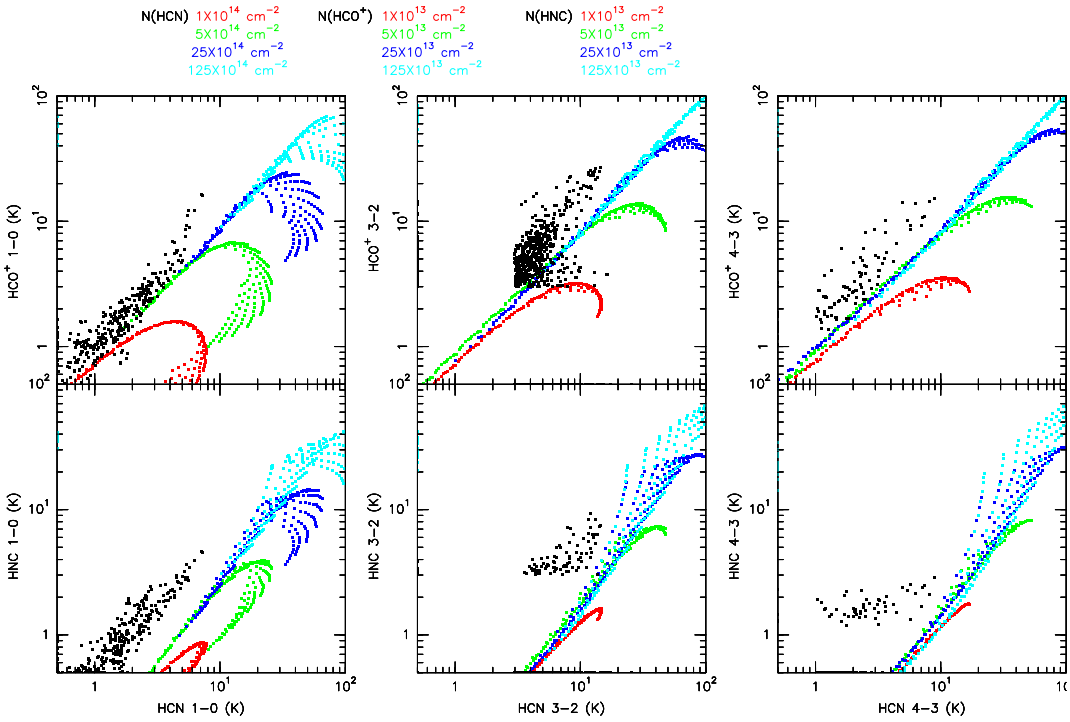

Figure C.11 The similar RADEX modeling as in Figure 4.11 with different column densities ratio of $10 : 1 : 1$, for HCN, HCO^+, and HNC, respectively.

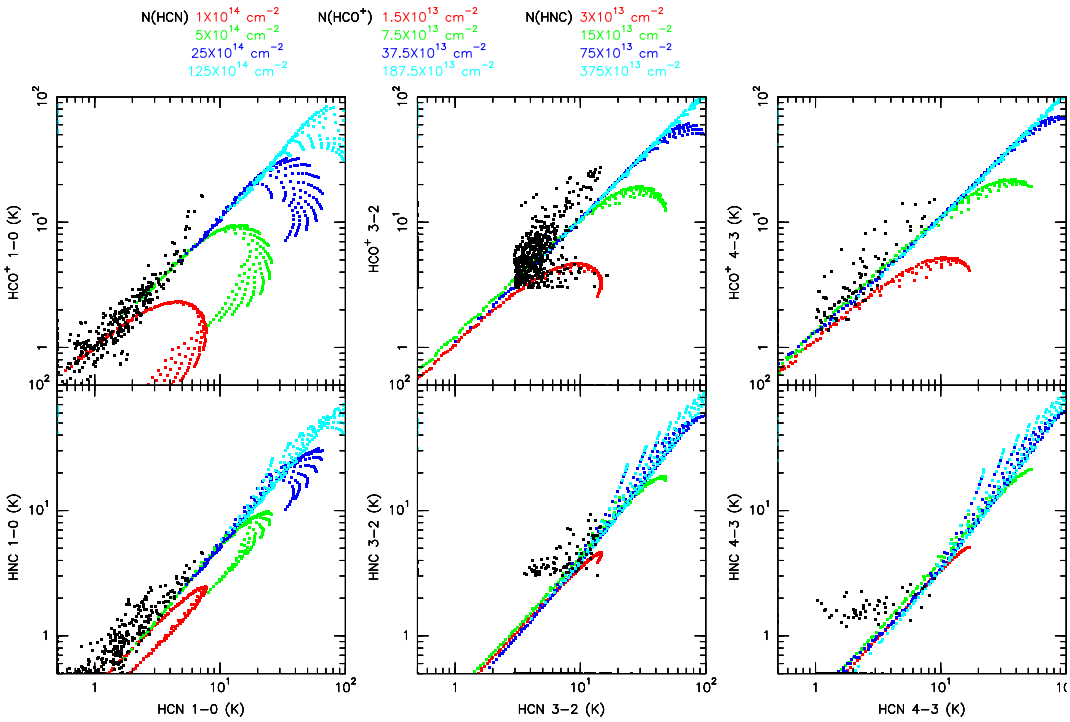

Figure C.12 The similar RADEX modeling as in Figure 4.11 with different column densities ratio of $10 : 1.5 : 3$, for HCN, HCO^+, and HNC, respectively.

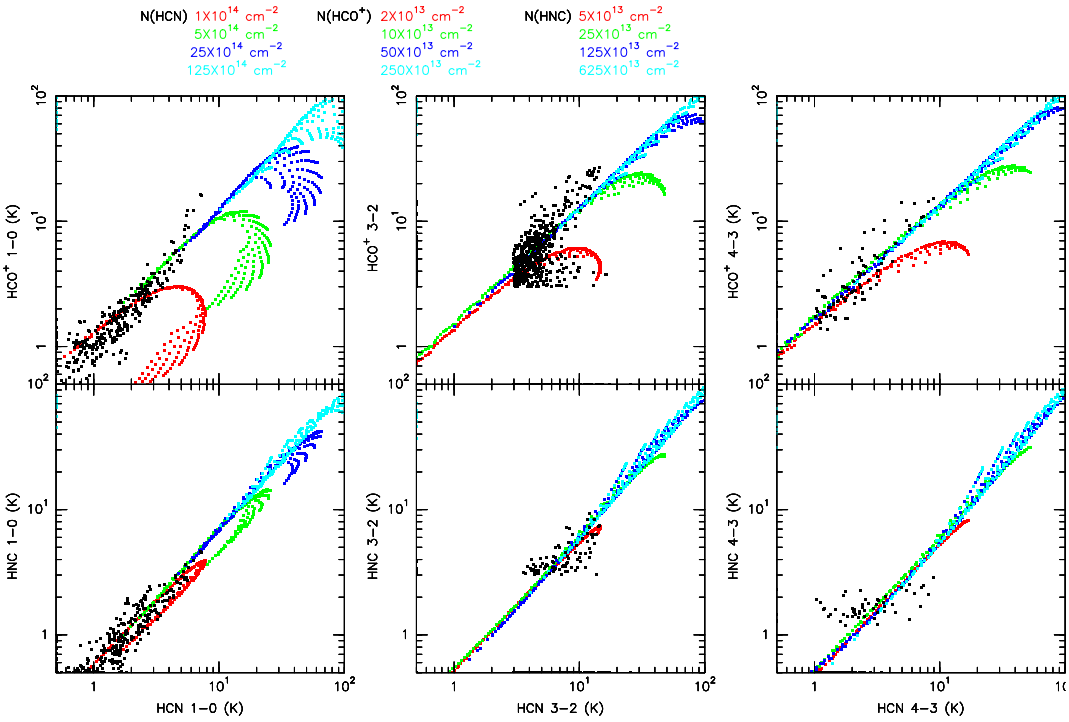

Figure C.13 The similar RADEX modeling as in Figure 4.11 with different column densities ratio of 10 : 2 : 5, for HCN, HCO^+, and HNC, respectively.

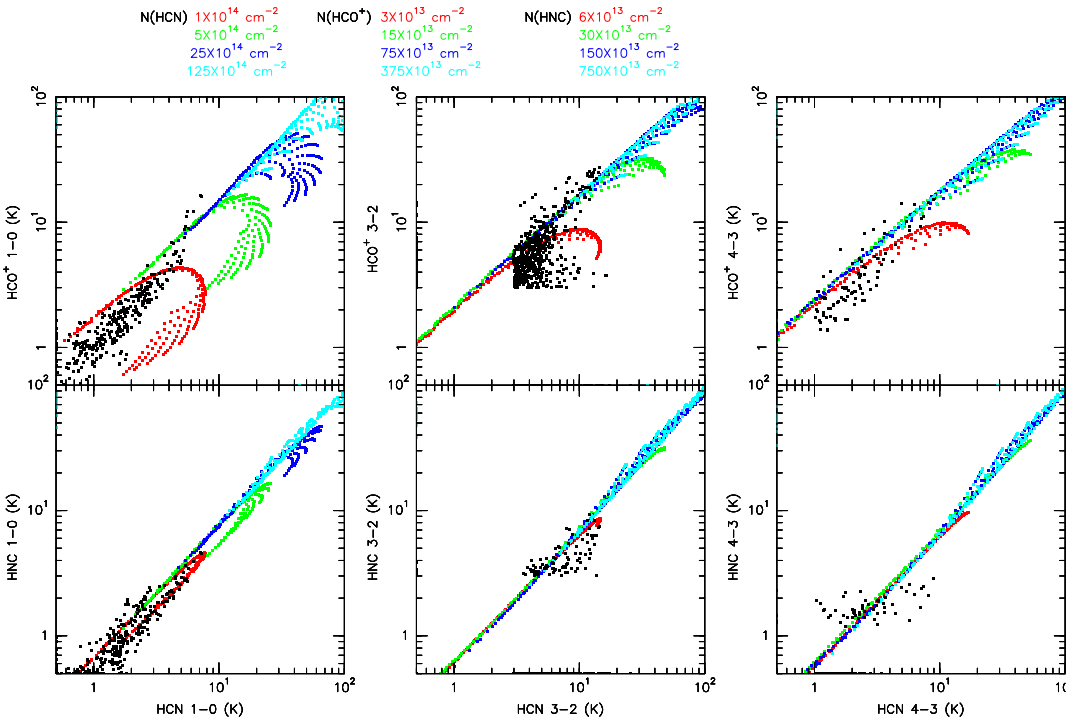

Figure C.14 The similar RADEX modeling as in Figure 4.11 with different column densities ratio of 10 : 3 : 6, for HCN, HCO^+, and HNC, respectively.

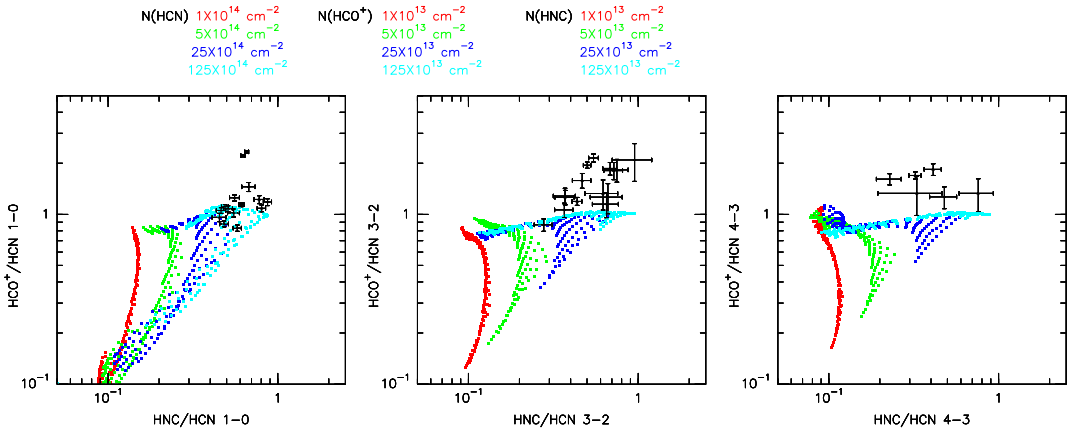

Figure C.15 The RADEX modeling of the ratios between HCN, HCO^+ and HNC from the same results in Figure C.11. The four different colors are the RADEX results for different column densities plotted in an H_2 density range of $10^4 - 10^7$ cm^{-3} and a temperature range of 20–150 K. The relative column density ratio among HCN, HCO^+, and HNC is fixed at 10 : 1 : 1. The data of selected clumps in W49A are marked.

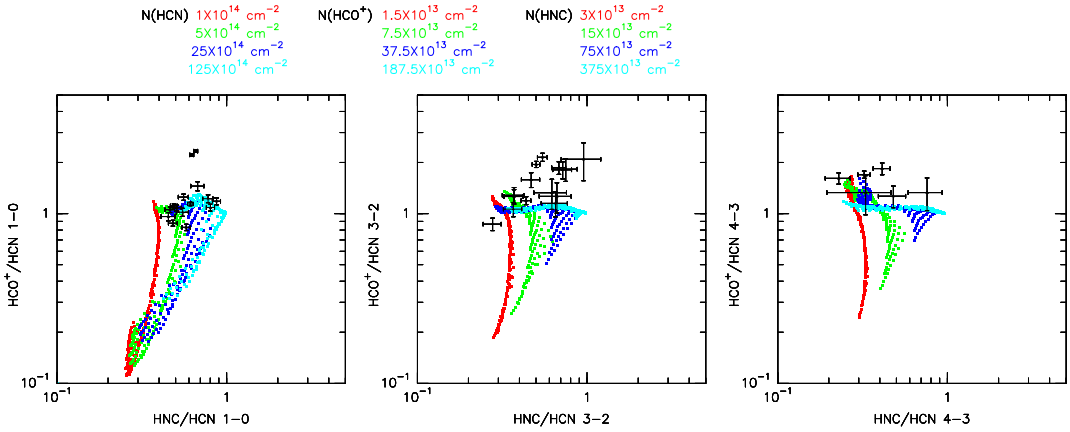

Figure C.16 The RADEX modeling of the ratios between HCN, HCO^+ and HNC from the same results in Figure C.12. The four different colors are the RADEX results for different column densities plotted in an H_2 density range of $10^4 - 10^7$ cm^{-3} and a temperature range of 20–150 K. The relative column density ratio among HCN, HCO^+, and HNC is fixed at 10 : 1.5 : 3. The data of selected clumps in W49A are marked.

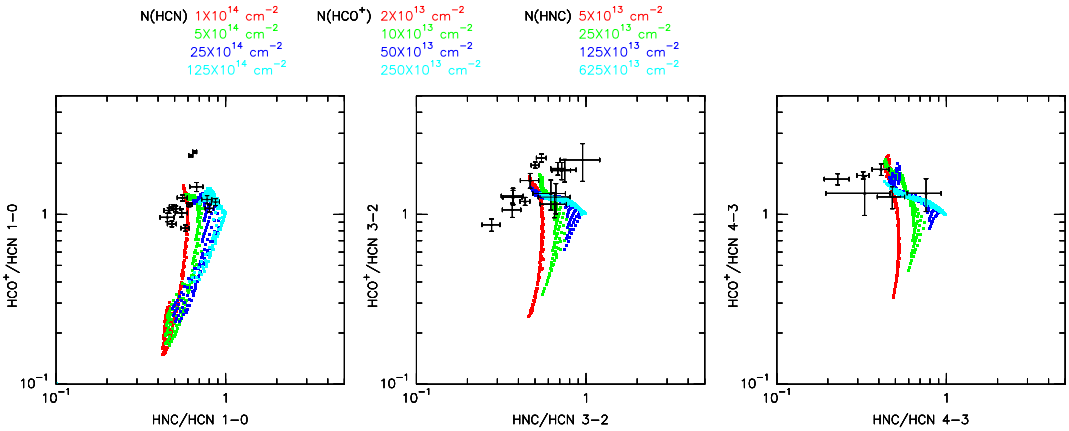

Figure C.17 The RADEX modeling of the ratios between HCN, HCO^+ and HNC from the same results in Figure C.13. The four different colors are the RADEX results for different column densities plotted in an H_2 density range of $10^4 - 10^7$ cm^{-3} and a temperature range of 20–150 K. The relative column density ratio among HCN, HCO^+, and HNC is fixed at 10 : 2 : 5. The data of selected clumps in W49A are marked.

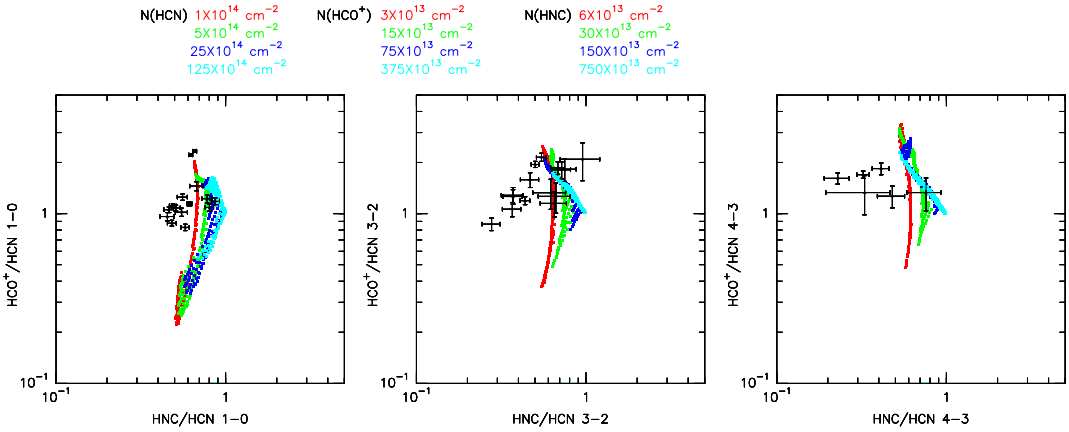

Figure C.18 The RADEX modeling of the ratios between HCN, HCO^+ and HNC from the same results in Figure C.14. The four different colors are the RADEX results for different column densities plotted in an H_2 density range of $10^4 - 10^7$ cm^{-3} and a temperature range of 20–150 K. The relative column density ratio among HCN, HCO^+, and HNC is fixed at 10 : 3 : 6. The data of selected clumps in W49A are marked.

D

Spitzer color-color images of W49A

The color index is used in the following expression:

$$m_1 - m_2 = 2.5 \log(F_2/F_1) + C_{12}, \tag{D.1}$$

where $C_{12} = 2.5 \log(F_{10}/F_{20})$ is the difference in magnitude between the zero points of two filters. The calibration values for the Infrared Array Camera (IRAC) from Reach et al. (2005) are adopted. The zero-point flux is 280.9 ± 4.1 Jy, 179.7 ± 2.6 Jy, 115.0 ± 1.7 Jy, and 64.1 ± 0.9 Jy, for 3.6 μm, 4.5 μm, 5.8 μm, and 8.0 μm, respectively. Therefore, the color-color indexes used here are

$$[3.6] - [4.5] = 2.5 \log(F_{4.5}/F_{3.6}) + 0.485 \tag{D.2}$$

$$[4.5] - [5.8] = 2.5 \log(F_{5.8}/F_{4.5}) + 0.485 \tag{D.3}$$

$$[5.8] - [8.0] = 2.5 \log(F_{8.0}/F_{5.8}) + 0.634. \tag{D.4}$$

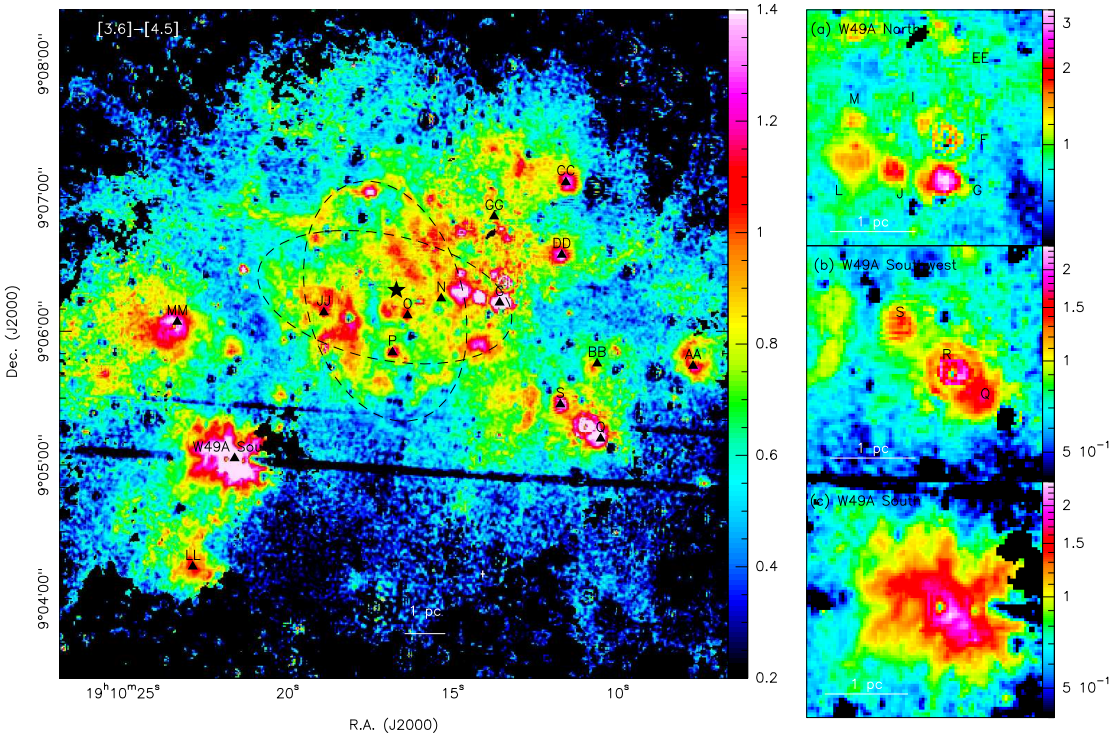

Figure D.1 The IRAC color-color ($[3.6]-[4.5]$) image of W49A. The corresponding radio sources are marked in black triangles. The suggestive shells are represented by black dashed-contours, and the shell center is denoted by a black star. The right panel shows the close-up images of W49A North, Southwest, and South.

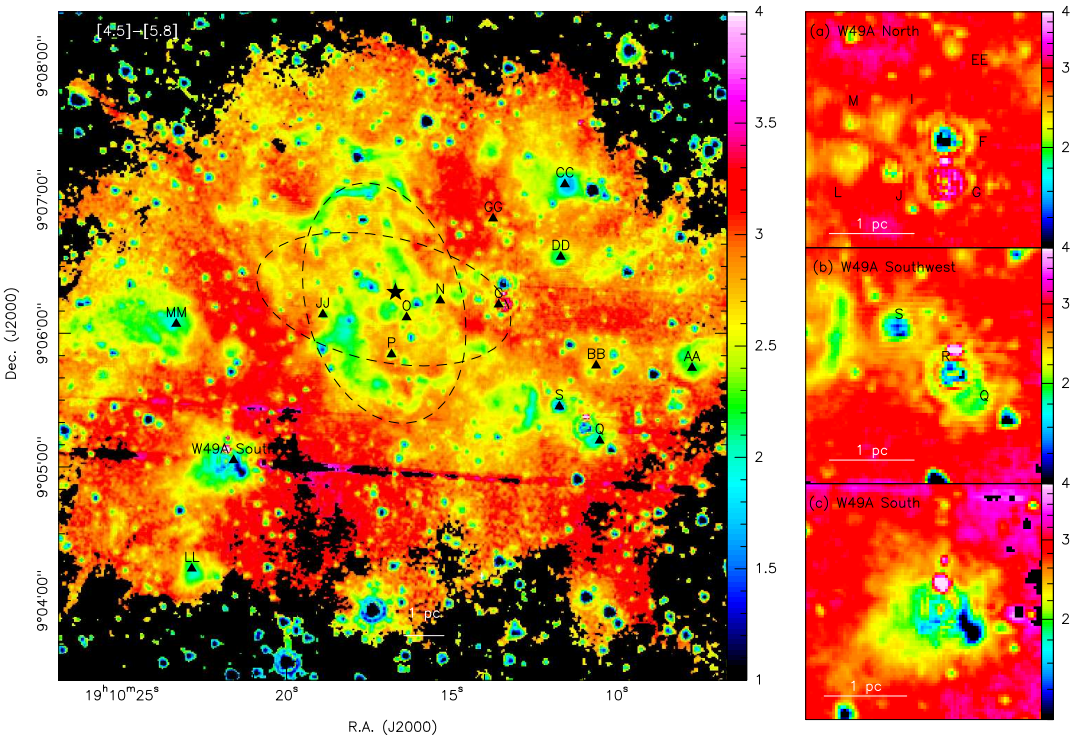

Figure D.2 The IRAC color-color ([4.5] − [5.8]) image of W49A. The corresponding radio sources are marked in black triangles. The suggestive shells are represented by black dashed-contours, and the shell center is denoted by a black star. The right panel shows the close-up images of W49A North, Southwest, and South.

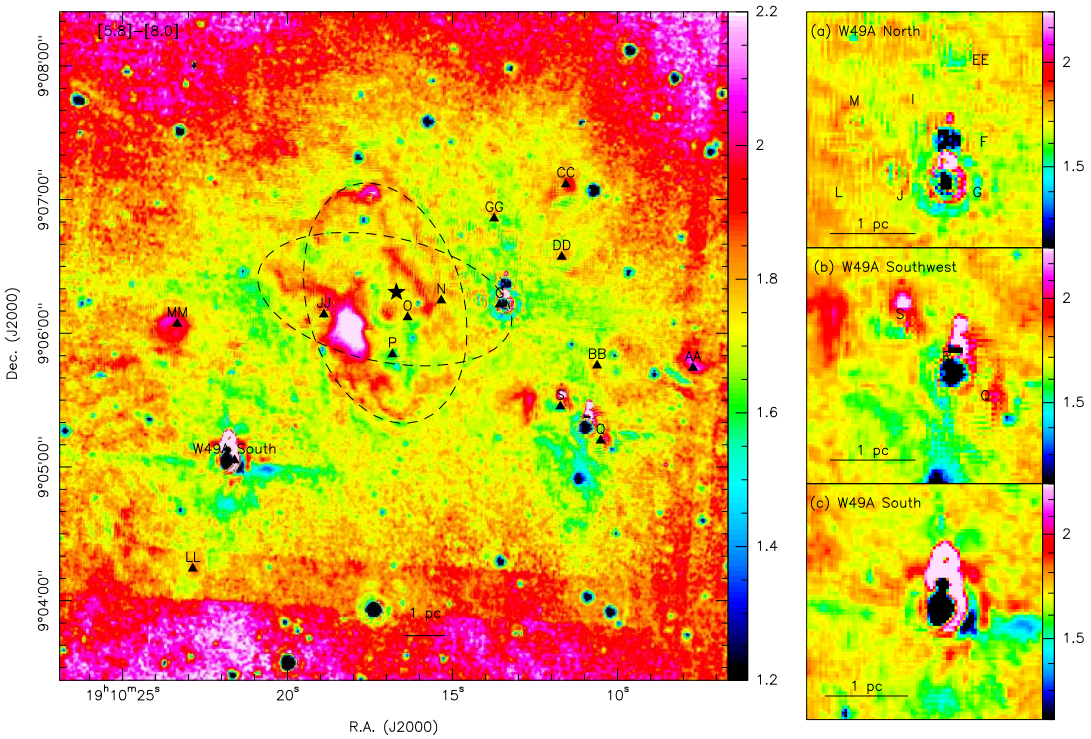

Figure D.3 The IRAC color-color ($[5.8]-[8.0]$) image of W49A. The corresponding radio sources are marked in black triangles. The suggestive shells are represented by black dashed-contours, and the shell center is denoted by a black star. The right panel shows the close-up images of W49A North, Southwest, and South.

E

The Meudon/RADEX results of the Orion Bar

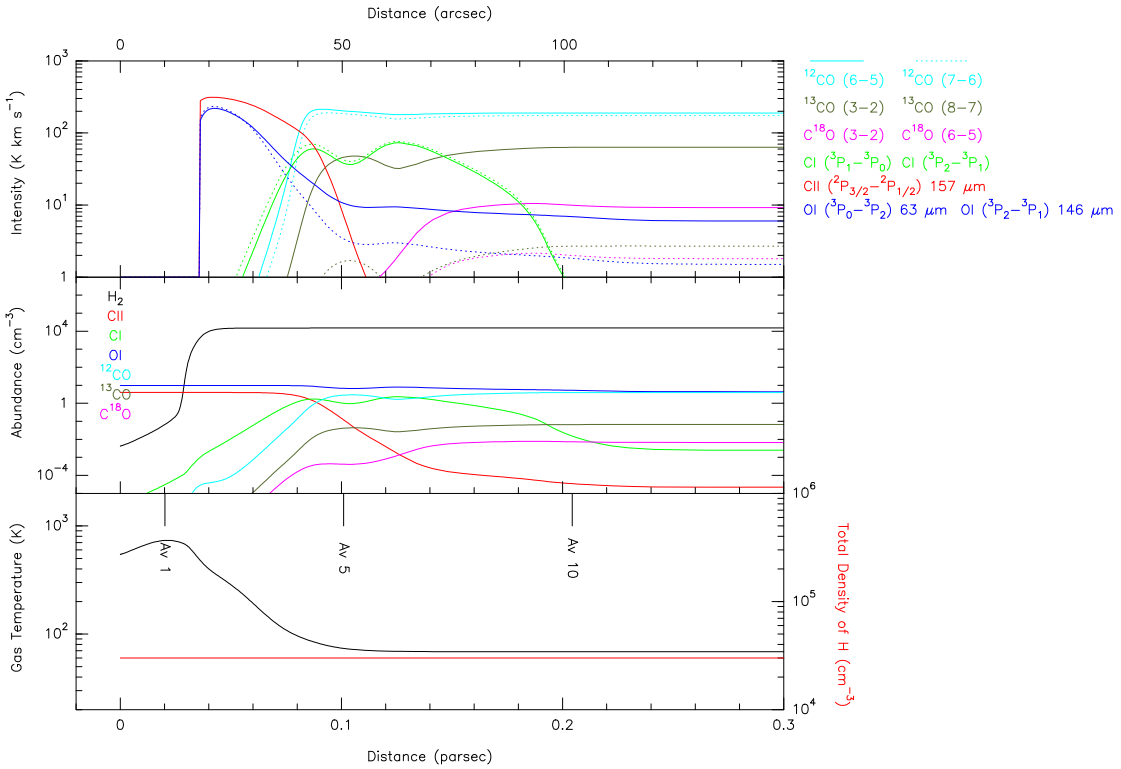

Figure E.1 The results of the Meudon/RADEX modeling with a constant density of 3×10^4 cm^{-3}. The gas temperature and total H density are shown in the lower panel. The abundances of various species are shown in the middle panel, and the calculated line intensities are shown in the upper panel.

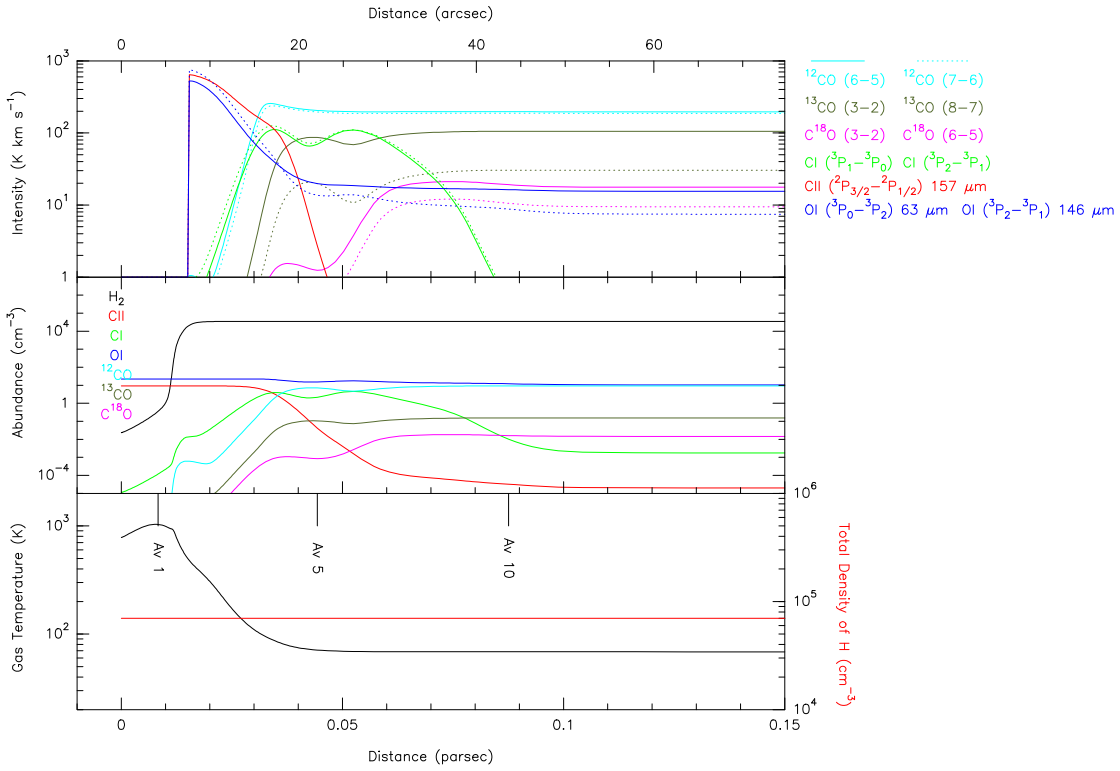

Figure E.2 The results of the Meudon/RADEX modeling with a constant density of 7×10^4 cm^{-3}. The gas temperature and total H density are shown in the lower panel. The abundances of various species are shown in the middle panel, and the calculated line intensities are shown in the upper panel.

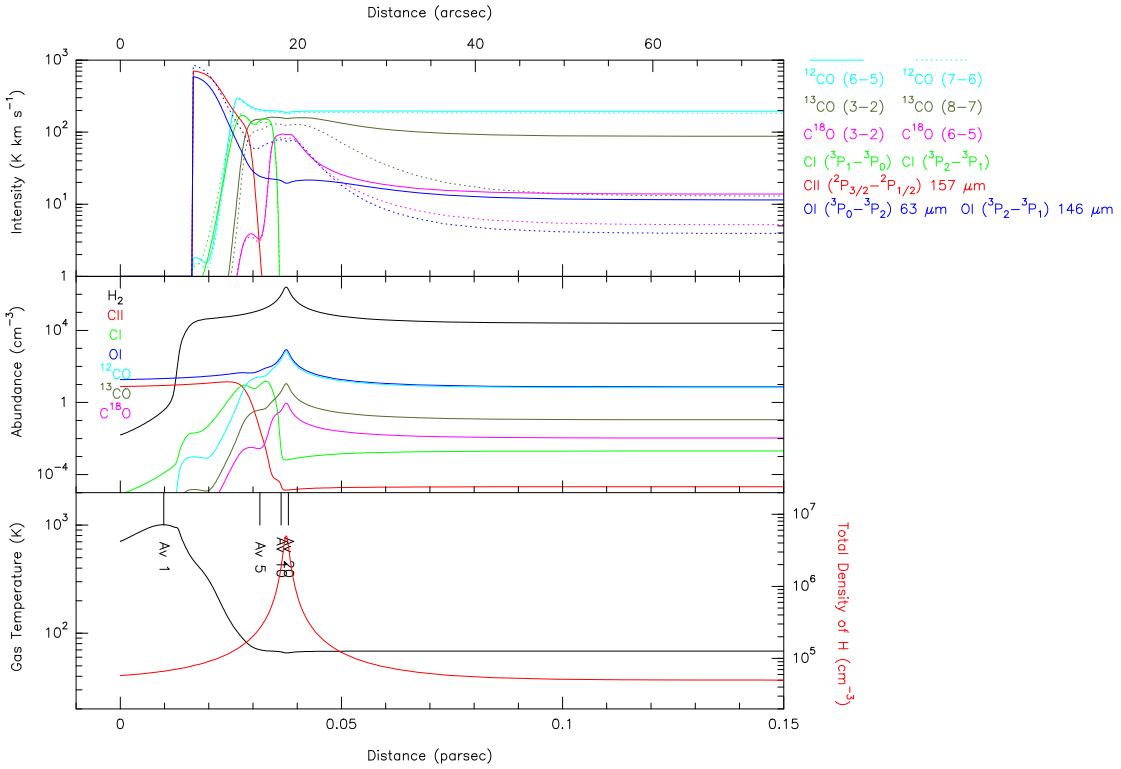

Figure E.3 The results of the Meudon/RADEX modeling with a Gaussian density profile whose minimum and maximum density is 5×10^4 cm^{-3} and 5×10^6 cm^{-3}, respectively. The density peak is located at $A_V = 18$. The gas temperature and total H density are shown in the lower panel. The abundances of various species are shown in the middle panel, and the calculated line intensities are shown in the upper panel.

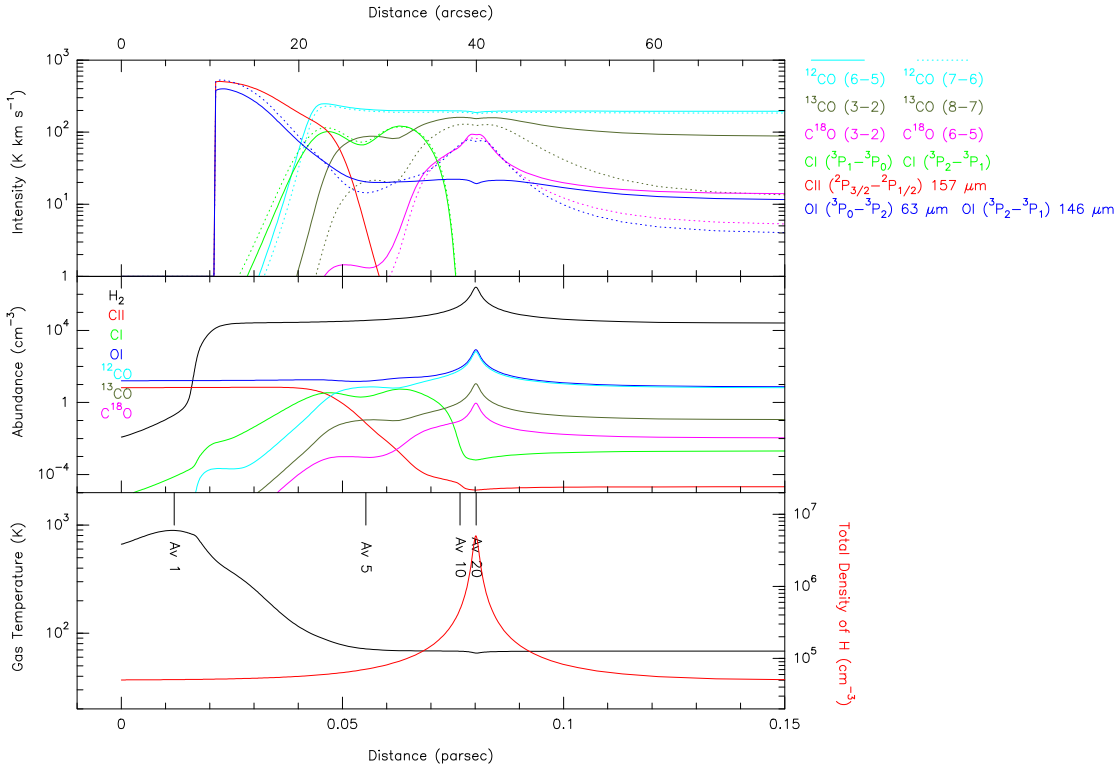

Figure E.4 The results of the Meudon/RADEX modeling with a Gaussian density profile whose minimum and maximum density is 5×10^4 cm^{-3} and 5×10^6 cm^{-3}, respectively. The density peak is located at $A_V = 22$. The gas temperature and total H density are shown in the lower panel. The abundances of various species are shown in the middle panel, and the calculated line intensities are shown in the upper panel.

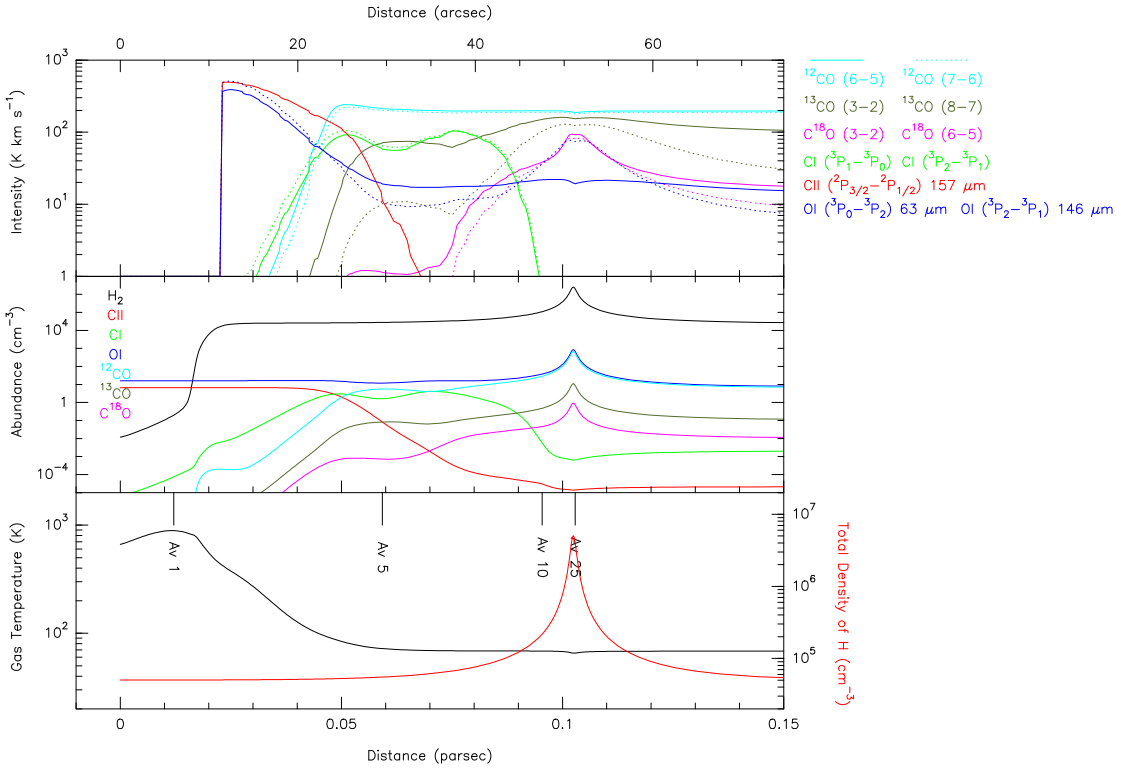

Figure E.5 The results of the Meudon/RADEX modeling with a Gaussian density profile whose minimum and maximum density is 5×10^4 cm^{-3} and 5×10^6 cm^{-3}, respectively. The density peak is located at $A_V = 24$. The gas temperature and total H density are shown in the lower panel. The abundances of various species are shown in the middle panel, and the calculated line intensities are shown in the upper panel.